TRANSPORT OF PASSIVE AND ACTIVE SCALARS IN MICROFLUIDICS: DEVICE DESIGN FOR SOLUTE DELIVERY TO RAT HIPPOCAMPAL NEURONS, IMPROVED ANALYTICAL EXPRESSIONS FOR ELECTROKINETIC TRANSPORT IN POROUS AND CHARGED LAYERS, AND ELECTROKINETIC INTERROGATION OF PERFLUORINATED IONOMERIC (NAFION) THIN FILMS

A Dissertation

Presented to the Faculty of the Graduate School

of Cornell University

in Partial Fulfillment of the Requirements for the Degree of

Doctor of Philosophy

by

Alexander C. Barbati

Jan 2014

© 2014 Alexander C. Barbati

ALL RIGHTS RESERVED

TRANSPORT OF PASSIVE AND ACTIVE SCALARS IN MICROFLUIDICS: DEVICE DESIGN FOR SOLUTE DELIVERY TO RAT HIPPOCAMPAL NEURONS, IMPROVED ANALYTICAL EXPRESSIONS FOR ELECTROKINETIC TRANSPORT IN POROUS AND CHARGED LAYERS, AND ELECTROKINETIC INTERROGATION OF PERFLUORINATED IONOMERIC (NAFION) THIN FILMS

Alexander C. Barbati, Ph.D.
Cornell University 2014

First, we outline the design, modeling, and fabrication of a glass-polymer microdevice for the spatio-temporal delivery of neutral solutes to coherently grown rat hippocamapal neurons. In the design and modeling of this device, we incorporate biological constraints of the neurons and relate them to engineering parameters like solute delivery/clearing time and the fluid shear incumbent on the neurons. Next, we describe the effects of porous and charged interfaces on transport in microdevices. Porous and charged interfaces exhibit a fixed charge in a region of increased mechanical resistance. I will present approximate analytical relations to describe forces (gradients of pressure and electrical potential) and fluxes (mass and current) in a microfluidic device coated with porous and charged layers. These relations improve upon existing expressions in the literature. We demonstrate the efficacy of our results by comparison with numerical values. Finally, we execute streaming potential, conductivity, and other measurements on Nafion polymer films in a parallel-plate cell. I show that the charging of Nafion is relatively independent of pH, but that electrokinetic outputs are strongly dependent on the ionic strength of solution. These results are interpreted using our approximate analytical expressions predicting forces and fluxes.

BIOGRAPHICAL SKETCH

Alexander was born in Stoneham, Massachusetts on September 10, 1984 to Joseph and Michelle Barbati. The eldest child, he was later joined by his brother Matthew and sister Cora. Since childhood, Alex has shown an interest in science and engineering, although he did not know this at the time. His interests were nurtured by his parents and family, through patience with ‘disassembled’ VCR’s, making space for a ‘lab’ in the basement, and their selection of Halloween costumes.

He attended Winthrop elementary school, Melrose Middle School, and Melrose High School where his interests in science, first chemistry and then physics, matured. Alex took nearly every science course offered before graduating and entering the University of Massachusetts at Amherst in the fall of 2003. While at UMass, Alex studied mechanical engineering and minored in mathematics, graduating *summa cum laude* in the spring of 2007. He relocated to Ithaca, NY that summer and began study in the Sibley School of Mechanical and Aerospace Engineering at Cornell in the fall. Shortly after beginning his graduate work, he joined Brian Kirby’s research group.

At Cornell Alex rekindled his interests in physics and chemistry, encouraged by an invigorating academic and social environment formed by his instructors and colleagues. Eventually, Alex synthesized these interests with his engineering background, studying fluid mechanics and interface science in microfluidic devices.

ACKNOWLEDGEMENTS

I would like to thank my parents, Joseph and Michelle, above all others for their encouragement and support. I could not have done this without them. Along with my brother Matthew, sister Cora, and extended family, they have given me sense of balance and perspective for life and work. I thank Mekala Krishnan for her countenance and support; Her kindness in and beyond graduate school has (and continues to be) both encouraging and remarkable.

I thank my advisor, Prof. Brian Kirby, for his efforts guiding me through all aspects of the academy. His conveyance of matters both technical and nontechnical has helped me immensely. I will be forever grateful for his tutelage; I hope he has enjoyed this process as much as I have.

I also thank Professors Donald Koch and Héctor Abruña for serving on my thesis committee. Their enthusiasm and advice has been much appreciated.

My time at Cornell has been enriched by friends and colleagues. I have been fortunate to work with thoughtful and capable peers since my earliest days in Ithaca. I thank all members of the KirbyLab, but in particular Sowmya Kondapalli, Ben Hawkins, Vishal Tandon, Erica Pratt, Tim Lannin, Jim Smith, Mike Bono, and Steven Santana. Also, thanks to Bernardo Cordovez, Michael Kalontarov, Edgar Cuji, and Juan Salazar for helpful discussions (and many cups of coffee).

Finally, I would like to thank Marcia Sawyer for her help with all things administrative, and for her commitment to her students.

TABLE OF CONTENTS

Biographical Sketch iii
Acknowledgements iv
Table of Contents v
List of Tables viii
List of Figures ix

1 Introduction 1

2 Culture of Primary Rat Hippocampal Neurons: Design, Analysis, and Optimization of a Microfluidic Device for Cell Seeding, Coherent Growth, and Solute Delivery 3

2.1 Abstract 3
2.2 Introduction 3
2.3 Device Design 8
2.4 Design Analysis and Discussion 16
2.5 Device Fabrication 20
2.6 Demonstration of Cell Culture 22
2.7 Conclusions 25
2.8 Acknowledgments 26

3 Soft Diffuse Interfaces in Electrokinetics - Theory and experiment for transport in charged diffuse layers 27

3.1 Abstract 27
3.2 Introduction 27
3.3 Theoretical Electrokinetics at Hard and Soft Interfaces 30
  3.3.1 Fundamentals of Electrokinetics at Hard and Soft Interfaces . . 30
  3.3.2 The Electrokinetic Coupling Matrix 34
  3.3.3 Electrokinetics and Soft Interfaces 36
  3.3.4 Theoretical descriptions of Soft Interfaces in Electrokinetics . . 37
  3.3.5 Charge Transport: χ_{12} and χ_{21} 42
  3.3.6 Film and Fluid Conductivity: χ_{22} 49
  3.3.7 Film Property Variation 55
3.4 Experiments 58
3.5 Discussion and Conclusions 67
3.6 Acknowledgements 70

4 Force and Flux Relations for Flows of Ionic Solutions between Parallel Plates with Porous and Charged Layers 71

4.1 Abstract 71
4.2 Introduction 71
4.3 Fluid Physics in Porous Layers 77
4.4 Generating integral formulas for EKCM Coefficients 81

4.5 Coupling terms for systems with rigid interfaces 82
4.5.1 Remarks on Coupling Terms for Rigid Interfaces 85
4.6 Coupling Terms for Systems with Porous and Charged Interfaces 85
4.6.1 χ_{11} with Porous and Charged Interfaces 86
4.6.2 χ_{21} with Porous and Charged Interfaces 88
4.6.3 χ_{12} with Porous and Charged Interfaces 92
4.7 Analysis and Limiting forms of $\chi_{21}^{(\mathrm{soft})}$ and $\chi_{12}^{(\mathrm{soft})}$ 93
4.8 Numerical Representation of $\chi_{ij}^{(\mathrm{soft})}$ for Arbitrary Values of α, β, γ, and Validation of Approximate Analytical Formulas 99
4.9 Conclusion 105
4.10 Acknowledgments 106
4.11 Supplementary Information 107
4.11.1 Brief Details on the Numerical Scheme 107
4.11.2 $\chi_{12}^{(\mathrm{soft})}$ for Porous and Charged Interfaces 107
4.11.3 The Potential at the Porous Layer Boundary 111
4.11.4 Additional Approximations for $\chi_{ij}^{(\mathrm{soft})}$ 113

5 Surface Conductivity in Electrokinetic Systems with Porous and Charged Interfaces: Benchmarking Analytical Approximations vs. Numerical Results 115
5.1 Abstract 115
5.2 Introduction 115
5.3 Electrokinetic Descriptions of Systems with Porous and Charged Layers 119
5.3.1 Momentum and Potential Distributions in Sytems with Porous and Charged Layers 120
5.3.2 General Conductivity Expressions 124
5.3.3 The Dukhin Model for Conductivity in Systems with Porous and Charged Layers 127
5.4 Numerical Representation of the Conductivity 130
5.4.1 Conductivity at Low Potential, $\phi_D^*, \phi_o^* \ll 1$ 130
5.4.2 Conductvity at High Potential, $\phi_D^*, \phi_o^* > 1$ 131
5.5 An Improved Conductivity Approximation 133
5.6 Streaming Potential and Electroviscosity in Systems with Porous and Charged Layers 136
5.6.1 Streaming Potential in Systems with Porous and Charged Layers 138
5.6.2 Electroviscosity in Systems with Porous and Charged Layers . . 139
5.7 Conclusion 142
5.8 Supplementary Information 143
5.8.1 Electroosmotic velocity and flow in the porous layer 143
5.8.2 Descriptive Ability of the Maximum and Minimum Approximations for χ_{22}^* 145

6 Electrokinetic Characterization of Thin Nafion Films 147
- 6.1 Abstract 147
- 6.2 Introduction 147
- 6.3 Materials and Methods 152
- 6.4 Results and Discussion 157
  - 6.4.1 Streaming Potential 157
  - 6.4.2 Conductivity 161
- 6.5 Conclusions 167
- 6.6 Acknowledgemens 168
- 6.7 Supplementary Information 169
- 6.8 XPS 169
  - 6.8.1 XPS spectra showing removal of sodium peak with acid treatment 170
- 6.9 Ellipsometry 170
- 6.10 Ionic Mobilities Expressed as Potentials 171

7 Conclusion 173

Bibliography 175

LIST OF TABLES

2.1 Geometric parameters tabulated for particular channel aspect ratios. The parameters were computed from ca. 1000 summands, at which point the sum had converged. 15

3.1 Collected electrokinetic characterization experiments with flows orthogonal, and parallel (★) to the surface normal of the diffuse interface. Here, materials with homogeneous microstructure on the scale of the electrostatic screening length are stressed; we do not include macroporous membranes. † C – system/surface conductivity, CA – contact angle, E – ellipsometric film thickness, PT – potentiometric titration, SC – streaming current, SP – streaming potential. 68

5.1 Mobilities [1] and tabulated potentials for ions, at 25 [C]. $\phi^*_{\text{ion}} = \frac{F\phi_i}{RT}$ . . 126

6.1 Optical constants extracted from ellipsometry data and model of Nafion film. 171

6.2 Mobilities [1] and tabulated potentials for ions, at 25 [C]. $\phi^*_{\text{ion}} = \frac{F\phi_i}{RT}$ . . 172

LIST OF FIGURES

2.1 Various schematics of the device showing relevant features to specify momentum and mass transfer. Top Right: The layout of the device in two tones. The fluid delivery layer is shown in red (dark), and the culture layer is shown in blue (light). Bottom Right: A demonstration of the operating mechanism. Fluid flows easily through low-resistance channels and is retarded in high-resistance channels. Arrows denote directions of flow. Left: A dissected view of the device describing variables explained in the text. 9

2.2 Device layout recast as a network of hydraulic resistances (resistors) and fixed pressure zones (outlined by dashed lines). 11

2.3 Concentration isocontours as a function of time and Péclet number for various positions along the axonal channel (x*). 17

2.4 Transient response of device from steady-state operation with non-zero boundary conditions to solute clearing state with zero concentration boundary conditions at both ends of the culture channel. 18

2.5 Maximum shear in the device, normalized by Péclet number (left) and pressure gradient (right), as a function of absolute channel height and channel aspect ratio. Dimensional quantities are plotted for simplicitiy in device design. The inset (at right) provides the collapsed curves for shear when appropriately normalized. 19

2.6 Phase contrast image of cells within device at DIV 1 (left) and DIV 7 (right). Cells at DIV 7 display healthy morphology evidenced by the absence of clumping and the outgrowth and development of both dendrites and axons. Images were captured on an inverted microscope, enabled by the coverslip-thin device substrate. The scale bar in both figures is 140 [μm] 24

2.7 Frame A: Demonstration of entrained neural axons within culture channels. Fluoresence micrographs (middle right and bottom), with corresponding device locations hightlighted at top, show stained (Calcein AM, Invitrogen) cells indicating the presence of axons within the channels. Growth of axons proceeds from the somal chamber to the first fluidic channel. Frame B: Micrographs (top) and diagram (bottom) of axons in a device *without* guide lines. In the bottom diagram, three zones are specificed: (I) the somal chaber, (II) partially enclosed culture channels, and (III) completely enclosed culture channels. Shown above are micrographs of axons failing to enter the channels in zone (III), having been stalled in zone (II). The micrographs at top were captured using fluoresence microscopy on cells treated with MitoTracker Green dye, visualizing the mitochondria within the cells. 25

3.1 Diagram of charge-generated potential profiles at an impermeable charged interface. Bound wall charge (here negative) generates an immobile (Stern) layer of ions and a diffuse layer. Schematic potential and velocity profiles, as a result of forcing by pressure and potential fields, illustrate characteristic length scales and behaviors. The velocity profiles at left are comparable in shape but not magnitude. 31
3.2 Schematic of electrokinetic cell used in theoretical modeling and experimental investigations (top). The configuration here is not drawn to scale; typically $w >> d$ to approximate parallel plates. (Below) A typical velocity profile produced by an applied pressure difference. The hydrodynamic penetration distance, λ_o, is also shown. 38
3.3 Diagrams of charge (ρ_f) and potential (ϕ) profiles for various wall boundary conditions. (A): Neumann boundary condition with fixed potential slope at wall. (B): Dirichlet boundary condition with fixed potential at the wall. In both cases, characteristic decay lengths are indicated for the fluid (λ_d) and diffuse charge layers (λ_δ), with ϕ_δ is the electrical potential at the film edge. 41
3.4 Schematic of potential and velocity profiles for a negatively charged polymer film. Various momentum and potential decay scales are displayed, which mitigate both pressure and electric field actuated transport. In the velocity–position plot at left, the u_p and u_{EO} plots are not comparable in magnitude, but do indicate differences in spatial velocity gradients; pressure–driven flow changes continuously until the channel center, and local to the film varies linearly when the size of the channel is large as compared to the film thickness. The E-field generated (electroosmotic) flow establishes on scales comparable to the Debye length. 42
3.5 Potential profiles for various charge distributions derived from equation (3.25). The film extends a distance $10\lambda_d$ into the domain from the wall ($x^* = 0$). The inset figures (at right) show the various charge distributions, ρ, considered. In all cases, the total charge is conserved across the film of thickness δ^*. 45

4.1 Diagrammatic representation of the system under consideration. (A): Geometric definition of the parallel-plate system studied; plates of width w and length L are separated by a distance $2h$. Included are shapes of pressure-driven and electrically forced flows for (left) a channel with rigid surfaces and (right) a channel with a porous lining. In (B) and (C), magnified diagrams at the surface detail distributions of velocity and potential for a bare, rigid surface (B) and a surface with a porous layer of thickness δ (C). 73

4.2 Velocity profiles about the channel centerline for varying layer resistance parameter α and relative channel height β. At left, $\beta = 2$, the velocity profile is strongly perturbed from parabolicity by large and moderate values of α. At right, $\beta = 10$, the channel is large relative to the porous layer thickness, and retarding effects are mainly confined to the porous layer and do not interfere strongly with momentum transport in the pure fluid region. 87

4.3 Plots of $\chi_{11}^{(\mathrm{soft})}$ normalized by the $\alpha \to 0$ limit (left) and the $\alpha \to \infty$ limit (right). In both cases, porous layer effects are small when the channel height is large relative to the porous layer thickness ($\beta \gg 1$). 89

4.4 Behavior of the filter-like function $-\frac{1}{\beta}H(y^*;\alpha,\beta)$ as function of space over a range of α (columns) and β (rows). The horizontal axes in all plots range over $0 \leq y^* \leq 1$. 92

4.5 Numerical results for electrical potential distributions, and comparison against exact results. For all results, $\beta = 10$ with a $1:1$ electrolyte; the uniform porous layer terminates at $y = 1$. (A) Potential profiles for various values of potential and γ (as indicated); the extents of the data are truncated to highlight the porous layer edge. Panes (B) and (C) highlight the change in potential near the porous layer edge at $y = 1$. The legend in (A) also applies to (B) and (C). (D) and (E) display a comparison between the computed potential at the porous layer edge and the analytical result. The legend in (E) applies to (D) as well. . . . 100

4.6 Behavior of the coupling coefficients $\chi_{12}^{(\mathrm{soft})}$ and $\chi_{21}^{(\mathrm{soft})}$ over 7 decades of α for $\beta = 1$ (red lines in (A) and (B)), $\beta = 100$ (black lines in (A) and (B)), and various values of γ, indicated with various line styles. Pane (C) compares numerical values and analytical approximations of $\chi^{(\mathrm{hard})}$ in the $\alpha \ll 1$ limit as a function of γ (x-axis) and β for $\phi_D = 5$, showing excellent agreement. 101

4.7 Upper and lower limit forms of $\chi_{12}^{(\mathrm{soft})}$ for $\alpha = 100$. 104

4.8 Leftmost four plots: Large α limit applied over the entire range of α. Rightmost four plots: Errors (as percent) in $\chi_{12}^{(\mathrm{soft})}$ applied over the entire range of α. The non-monotonicity observed in the errors is results from taking the maximum error of the difference between the numerical value and upper and lower estimations of $\chi_{ij}^{(\mathrm{soft})}$. 105

5.1 Schematic of the parallel-plate cell considered in this work. In (A), the geometric definition of the cell with sample electroosmotic velocity profile u_{EO} resulting from an applied potential gradient, $-\nabla\phi_{\text{ext}}$. The velocity profile is retarded near the wall by the the porous and charged layer, shown in (B) with associated lengths and the free charge density resulting from mobile charges in the bulk and porous and charged regions. In (C) and (D), diagrams of the electroosmotic and Ohmic conduction mechanisms, respectively. Electroosmotic conduction results from the transport of charge by bulk fluid motion, Ohmic conduction results by electrophoresis of the ions; excess free (positive) charges in the porous layer are balanced by bound fixed charge to maintain electroneutrality. 122

5.2 Ohmic and electroosmotic conductivies for $\phi_o^* = \phi_D^* = {}^1/_{10}$ for $\beta = 5$ and 60 as a function of α and γ. The computed Ohmic conductivity in all cases is equal to 1, and is invariant to α, β, and γ. The legend at left applies for both plots. 131

5.3 Above: χ_{22}^* computed numerically and from the Dukhin theory ($\chi_{22,D}^*$, equation (5.39)) for a $1:1$ electrolyte with $\phi_o^* = \phi_D^* = 2$ over a range of α and γ. $\beta = 5$ for frame (A), and $\beta = 60$ for (B). In (C), a selection of the data in (B) for $10^0 \leq \alpha \leq 10^2$, with the percent error between the Dukhin and numerically computed conductivities in (D). Note the logarithmic scale. 132

5.4 Comparison of the improved analytical aproximation (equation (5.49)) for $\beta = 5$ ((A) and (B)) and $\beta = 60$ ((C) and (D)). The fits in both limits of β show excellent agreement over the entire range of α and γ. Computed errors between the approximate and exact numerical results in (C) and (D) are superior to the errors reported in figure 5.3 136

5.5 The streaming potential ratio, equation (5.50), for $\phi_D^* = 2$ (left four plots) and $\phi_D^* = 5$ (right four plots) over a range of parameters α, β, and γ, as indicated. 139

5.6 The magnitude of electroviscous effects for $\phi_D^* = 2$ plotted over $\frac{1}{\gamma}$ for a range of α (weakly resisting, moderately resisting, and strongly resisting) and β. 141

5.7 Magnitude of the electroviscous coefficient for a porous and charged layer with $\phi_D^* = 8$ plotted over the same parameters as in figure 5.6. The limiting behavior of $\Gamma\left(\phi_D^* = 8\right)$ is nearly identical to $\Gamma\left(\phi_D^* = 2\right)$. . . 141

5.8 Plots of the maximum and minimum estimates of the conductivity vs. numerically computed values as a function of the parameters α, β, and γ for $\phi_D^* = 2$. In pane (A), χ_{22}^* for $\beta = 5$ with associated errors in (B). In pane (C), χ_{22}^* for $\beta = 60$ with errors in (D). In both cases, the maximum limit displays suprior perforamance. Note the logarithmic scale in panes (B) and (D). 146

6.1 Picture and schematic of the electrokinetic cell with sample data. The assembled cell is shown in (A), with current leads disconnected for clarity, highlighting the various inputs and outputs of the device. The dimensions of the sample slides and shim are shown diagrammatically in (B); the plate separation (cell height, $2h$) is approximately 57 [μm]. In (C), we present a component-level diagram of the components involved in the streaming potential and conductivity experiments, with sample data from a streaming potential experiment shown in pane (D). 155
6.2 Data and model fit (from equation (6.5)) for χ_{21} and ζ as a function of pH and ionic strength. The model is a function of ionic strength, charge density, and the momentum penetration length λ_o, only. 158
6.3 Left: Cell conductivity as a function of solution pH and ionic strength measured using the four-electrode technique. Right: Cell to bulk conductivity ratio. Bulk conductivities are obtained using a commercial conductivity meter in a 50 [mL] flask, absent surface effects. 162
6.4 Experimental conductivity data (symbols, as indicated) in the Nafion film with lines from the model presented in equation (6.10). The error bars represent propagation of standard deviations from the various measurements determining σ_{Nafion}. 163
6.5 A comparison of conductivities measured in Nafion membranes as a function of ionic strength, with the nature of the electrolyte indicated in the marker type. Shown are the data of Slade, et al. [2], Verbrugge, et al. [3] (for two thicknesses), Kolde, et al.(from Slade [2]), Perez, et al.(from Slade [2]), Okada, et al. [4], Yeo, et al. [5], Stenina, et al. [6], Narebska, et al. [7], and Silva, et al. [8] 166
6.6 XPS spectra of a thin Nafion film following treatment in 70% nitric acid. 169
6.7 XPS spectra of a Nafion film after contact with a 100 [mM] NaCl solution. The film was initially in proton form. 170
6.8 Psi (amplitude) of measured light as a function of wavelength [nm] for a nanoscale Nafion polymer film. The data at various incident angles (green lines) shows an excellent match to the model (red lines). 171

CHAPTER 1

INTRODUCTION

Microscale fluid mechanics, or microfluidics, is applicable to a wide variety of problems across many disciplines. A hallmark of microfluidics is the dominance of novel forces that are absent at larger scales [9]. Linear and nonlinear electrokinetic, van der Waals, surface tension, and other forces can govern flows and device behavior [10, 11]. Since these forces come to dominate at small scales, their effects may be studied more clearly in microdevices without interference from, for example, inertia. Additionally, microfluidic devices may be designed to exploit these physics, leading to the creation of new and novel methods for materials fabrication [12] and cellular analysis [13].

In this thesis, microfluidics and microfluidic phenomena are exploited to study two distinct problems: (1) delivery of solutes to neural cells in culture, and (2) theory and experiment for electrokinetic effects in porous and charged layers. While distinct in scope, these problems are fundamentally about the transport of species, momentum, and charge.

Microscale devices are similarly sized to the fundamental biological unit: the cell. This coincidence enables novel manipulation, stimulation, and observation of mammalian (and other) cells. In chapter two we present our efforts on the design, fabrication, and optimization of a microfluidic device for seeding, growth and solute delivery to primary rat hippocampal neurons. This work is motivated by the hypothesis that defects in transport of organelles and other components along the cell are mediated by reactive species like peroxynitrite. In particular, we describe a novel method to direct neural cell growth without chemical gradients or surface patterns, and identify a geometry to achieve solute delivery while reducing shear stresses on the cells under study.

Porous and charged layers are present in a variety of natural [14] and synthetic [15, 16] systems. Engineering of these systems requires a framework to predict fluxes of momentum and current in response to various forcing conditions. In preparation for our contributions to the electrokinetics of porous and charged layers, we review the available literature on the theory and experimental techniques of porous (or soft) and charged layers in chapter three. This work provides an overview of past research, with emphasis on techniques that aid in the analysis of observed electrokinetic phenomena in these systems.

We improve upon the available descriptions of electrokinetics in porous and charged layers in chapters four and five. By deriving approximate analytical result for all electrokinetic coupling coefficients, our results provide a framework to interpret forces and fluxes in porous and charged layers. Since exact expressions for forces and fluxes in porous and charged layers are available only for a limited range of system parameters, we validate our approximate analytical results against numerical solutions of the exact equations.

In chapter six we implement the theory developed in chapters four and five to examine thin ($\sim$ 300 [nm]) Nafion films in a parallel-plate electrokinetic cell with conductvity and streaming potential measurements. Nafion is a perfluorinated ionomer that forms a network of channels and nodes lined with negative charges within a semi-crystalline teflon-like matrix when cast as a membrane or film. We explore the electrokinetic properties of Nafion in a new experimental configuration and in a novel region of solution ionic strength.

Finally, we close with conclusions drawn from the results of our study.

CHAPTER 2

CULTURE OF PRIMARY RAT HIPPOCAMPAL NEURONS: DESIGN, ANALYSIS, AND OPTIMIZATION OF A MICROFLUIDIC DEVICE FOR CELL SEEDING, COHERENT GROWTH, AND SOLUTE DELIVERY

2.1 Abstract

We present the design, analysis, construction, and culture results of a microfluidic device for the segregation and chemical stimulation of primary rat hippocampal neurons. Our device is designed to achieve spatio temporal solute delivery to discrete sections of neurons with mitigated mechanical stress. We implement a geometric guidance technique to direct axonal processes of the neurons into specific areas of the device to achieve solute segregation along routed cells. Using physicochemical modeling, we predict flows, concentration profiles, and mechanical stresses within pertiment sections of the device. We demonstrate cell viability and growth within the closed device over a period of 11 days. Additionally, our modeling methodology may be generalized and applied to other device geometries.

2.2 Introduction

Neurobiological systems are immensely intricate and complex: exhibiting vastness in extent, variety, and connectivity. Analyses of these systems under well-constrained user-defined conditions is necessary to extract mechanisms of disease, and to develop and

---

The content of this chapter was submitted and published as a research article that is reproduced here with permission from *Biomedical Microdevices*. This is the pre-peer reviewed version of the following article: “Culture of Primary Rat Hippocampal Neurons: Design, Analysis, and Optimization of a Microfluidic Device for Cell Seeding, Coherent Growth, and Solute Delivery”.

screen targeted therapies for acute and chronic diseases. Interrogation of these systems performed at the single- and multi-cell level enables relevant extracellular cell-scale change and control. Micro- and nanofluidic technologies, developed over the past few decades [9, 11], are uniquely suited to extract information at the cell level [17], as these technologies provide devices with length scales comparable to the length scales of the cell(s) under analysis.

Although micro- and nanofluidic systems demonstrate many advantages over traditional techniques, a variety of challenges remain in the design and fabrication of these devices before neurobiological questions can be answered. Most importantly, neurons are extremely sensitive to chemical and mechanical changes in their environment. Mechanical and chemical effects can be mitigated or eliminated at the design stage by considering the bio- and physicochemical implications of the design.

Here, we present, analyze, construct, and qualify a novel microfluidic device to deliver soluble factors to specific locations on an array of coherently grown rat hippocampal neurons with temporal control. Our device improves on the current state-of-the-art by providing for both coherent arrays of neurons in concert with a delivery scheme providing spatial and temporal control of solutes at specific locations along the axon of the cell, while leaving the cell soma undisturbed. Furthermore, our device design approach stresses well-characterized mass and momentum transport to enable neurobiological experiments.

Deficiencies of the intracellular transport mechanism in neurobiological systems are putative causes of neurobiological damage and disease [18]. The biological transport mechanism within the neuron may fail at several levels with the same result. Cargo-carrying molecular motors, energy-producing mitochondria, microtubules (upon which the molecular motors move), and the mechanism of cargo attachment are all succeptible to damage resulting in transport breakdown and cell damage or death [18]. Species such as sodium azide [19] (NaN_3) and peroxynitrite [20]($ONOO^-$) have been shown to damage cells under culture conditions. In these instances, the supposed mechanism for cell death is mitochondrial damage imparted by unchecked reactive oxygen species, such as superoxide [21]. Damage to mitochondria by such species is the suspect of many human maladies, including aging, neurodegenerative disorders, and diabetes [22].

Many important aspects of neural function are mediated by local signals that impinge on only one part of the cell. For example, growth cones at the tips of axons are sensitive to directional cues provided by gradients of chemoattractants and chemorepellants, which guide the axons to their targets [23]. Axons are also susceptible to local damage, a common cause of neurodegeneration. Axons are subject to mechnical damage following an injury or by local chemical insults, as lesions that occur in neuroinflammatory diseases like multiple sclerosis. These chambers provide a means to mimic local signaling in vitro.

Several culture systems have been used to tackle seeding-stimulation-response problems to observe axonal transport deficiencies and highlight the root cause of cell damage and death. Neurons are typically studied *in vitro*, as *in vivo* studies are difficult, involving access and stimulation of a live animal. *In vitro* neurobiological studies of multi-cell systems have historically been implemented on bare or modified culture dishes and coverslips. Although a lab standard, coverslips [24] do not segregate soma and axon and they cannot clearly delineate axonal ownership or polarity. Culture systems using a modified petri dish, Campenot chambers [25–27], improve upon coverslips by providing for multi-chamber (typically three-chamber) segregation of neural cells, which are grown in collagen grooves. The chamber is formed by a teflon divider and sealed to the collagen surface with silicone grease. These chambers are prone to leaks, and the dimension of the smallest chamber is approximately 1mm, limiting the degree to which the solute is localized.

Recently, microfabrication techniques have been implemented to segregate or deterministically order neural cells in predetermined configurations for analysis. Steric approaches dominate in their ubiquity and simplicity: cells are ordered by providing narrow channels though which axons propagate. Generally, channel size and geometry [28, 29] are chosen to permit access and passage to the protruding axon but block migration of cell soma. Once within these channels, the cells can be directed to a second compartment and exposed to a solute, subjected to a gradient within the channel, or both. A popular and influential culture device exploiting this approach is that constructed by Taylor, et al., [30, 31]. This ladder-type device consists of two chambers separated by an array of microchannels shaped to permit axons to grow from the seeding (or somal) chamber to a second (axonal) chamber. By controlling the fluid height between axonal and somal chambers, a hydrostatic head is generated to drive flow from the somal to axonal chambers, and vice versa. By adding a solute to the axonal reservoir, flow induced by the hydrostatic head acts counter to diffusion, establishing a stable, distally directed gradient. The system built by Peyrin, et al. [29] uses similar geometry to generate oriented neural networks for studying neural disease. Kunze, et al. [32] generated opposing groups of somal cells with mixing neurites from microfluidically shaped hydrogel compartments. Both of these approaches also permit fluid segregation similar to the Taylor, et al. approach. To create more complicated solute gradients, Wang, et al., [33] combined laminar flow patterning and neuron culture. Establishing strong gradients required high rates of flow, generating large mechanical shear at the cell-fluid boundary. For their turning assay, Wang, et al. shelter the neurons in grooves to mitigate damage to sensitive cellular components. This gradient generator provides for controlled solute profiles both spatially and temporally, but, as the authors are interested in the response of the cell growth cone to stimuli, arrays of neurons are not generated in which axons are separated from soma.

Other approaches, such as photolithographic and microcontact printing (μCP) methods are also used in which a surface is prepared such that cells exhibit a preference for patterned or unpatterned regions of the culture substrate. The photolithographic approach [34] (1980s) predates the contemporary microtechniques for cell culture, with the drawbacks that harsh chemicals are used in the preparation of the pattern (photoresist and photoresist solvent), photolithographic tools are required to produce each device, and it is difficult to increase patterns in complexity. In contrast, microcontact printing [12] generates devices from the same microcontact 'stamp', the 'ink' is generally aqueous and non-cytotoxic, and many patterns can be overlayed as the chemistry permits. The primary difficulties in forming μCP patterns stem from chemical and physical affinities between the material to be attached and the surface (e.g., keeping chemistry wet [23]), and the alignment of overlayed patterns [35]. μCP patterns effectively guide axons, but intial placement of soma is generally at random, requiring additional structures to block or promote adhesion on the pattern as desired.

Many reviews summarize cell culture methods relevant to neurobiological systems. Banker and Goslin [36] have described a useful collection of traditional culture methods and procedures, including a discussion of early lithographic patterning approaches and the Campenot chamber. More recent reviews on general microfluidic cell culture systems have been conducted by Meyvantsson and Beebe [37], as well as Keenan and Folch [13] with the latter stressing the role of biomolecular gradients. Both works are aimed at general problems in cell biology. Addressing the problem of neural culture, Gross, et al., [38] and Wang, et al., [39] provide reviews on recent work combining microfluidics and neural culture.

In general, neural microfluidic culture systems with solute delivery fall within two broad categories: cells within channels or gels, and cells on a surface. Neurons within channel- and gel-type systems are subjected to chemicals acting at either the distal or proximal end, with a gradient in between and fairly low shear stresses. In surface-type systems, cells are typically probed with a laminar-flow patterning type gradient generator which produces rather large shear stresses transverse to the neuron. The modeling of both these systems is generally straightforward, as cells in both systems are exposed to steady, uniform flows with large Peclet numbers, and diffusion can be ignored. Variations in geometry introduce modeling difficulties, and can be analyzed with finite element techniques [33].

Here, we present the design, development, and culture results of a microfluidic device to deliver solutes to rat hippocampal neurons with spatial and temporal resolution. We begin with a discussion of the device design, including its principle of operation, layout, selection of parameters, and design specifications. The design presentation is followed by a procedure for device fabrication and demonstrations of stable cell culture within the constructed device. We close with conclusions drawn from the design, as well as implications of our design for future neuron studies.

2.3 Device Design

Our design consists of two layers: an upper fluid delivery layer, and a lower culture and growth layer for the cells, as shown in Figure 2.1. The top, delivery layer consists of three fluid channels, each connected to a unique inlet reservoir, and a common outlet. A culture layer for cell attachment and directed cell growth sits below this delivery layer. This bottom layer holds an array of axonal channels, vertically offset and perpendicular to the fluid delivery channels, with mismatched hydraulic resistance to confine the delivered solute. Cells are introduced to the culture layer by holes cut through the delivery layer.

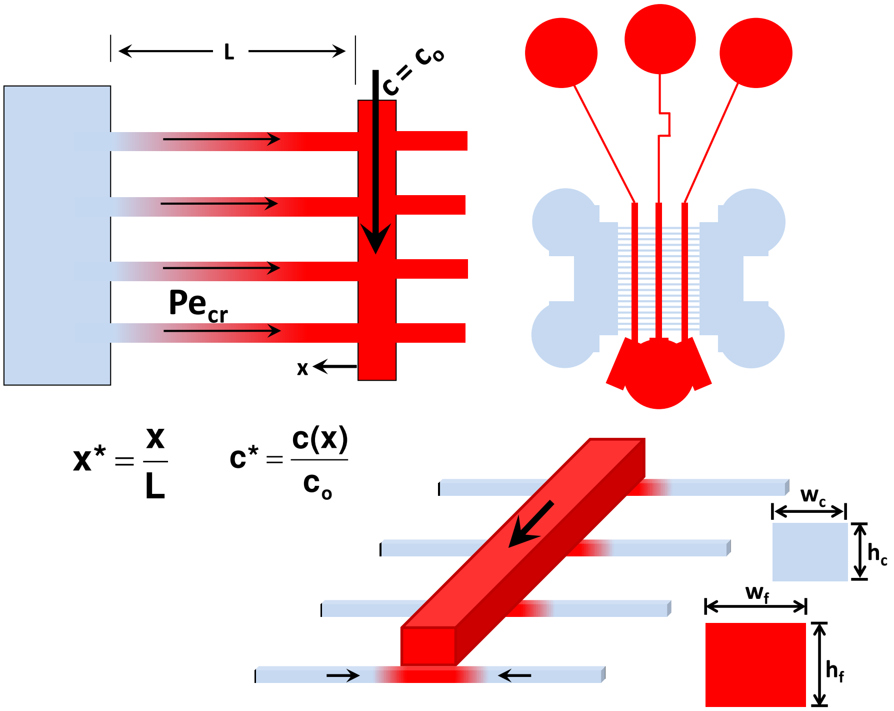

Figure 2.1: Various schematics of the device showing relevant features to specify momentum and mass transfer. Top Right: The layout of the device in two tones. The fluid delivery layer is shown in red (dark), and the culture layer is shown in blue (light). Bottom Right: A demonstration of the operating mechanism. Fluid flows easily through low-resistance channels and is retarded in high-resistance channels. Arrows denote directions of flow. Left: A dissected view of the device describing variables explained in the text.

This design has several advantages. The footprint of the device is small (~15 mm^2), reducing required volumes of reagents and cells, but is still easy to manipulate without specialized equipment. Because neurons attach to the bottom surface of the device, growth and transport are easily visualized with an inverted microscope. Actuation by hydrostatic head obviates syringe pumps and tubing; perfusion and solute delivery is prompted by pipetting of reagents/media into one of the seven open reservoirs.

The intersection of the large flud delivery channels in the upper layer and the small axonal channels in the lower culture layer is important. The axonal channels function by allowing the axon to enter and preventing the passage of the cell soma. We confine solutes from the fluid delivery channels to segments of the axonal channels, through a mismatch of the hydraulic resistances in both the delivery and axonal channels. At the intersection of a large delivery and small axonal channel, mass and momentum are easily transferred across the large delivery channel, but the small axonal channel, exhibiting a much larger hydrualic resistance, retards streamwise convection of fluid from the large channel. By controlling the direction and magnitude of flow in this fluid network, solutes can be confined to segments of the axon.

For a steady, laminar flow, the pressure drop and flow along a channel of uniform geometry are related linearly by a hydraulic resistance:

$$\Delta P = R_h Q \tag{2.1}$$

Where ΔP is the pressure drop, Q the flowrate, and R_h the resistance along the channel. The resistance may be estimated for rectilinear channels [40] by:

$$R_h = 8\eta\ell\frac{(h+w)^2}{h^3w^3} \tag{2.2}$$

Here, η is the viscosity of the fluid, and h, w, and ℓ represent the height, width and length of the channel. For nearly square channels, the resistance scales as $R_h \sim 1/h^4$, giving $Q \sim h^4\Delta P$ where the flow is strongly nonlinear in the characteristic size of the channel, and linear in the pressure difference. The mathematical stiffness of the flow in response to channel dimension communicates a flow that varies drastically between large and small channels, and a comparatively weak dependence on the pressure difference relegates pressure to a minor role. Therefore, flows will vary strongly between large and small channels, so long as the *differential in pressure drop* between the channels remains small relative to $\frac{h_{\text{large.}}}{h_{\text{small}}}$.

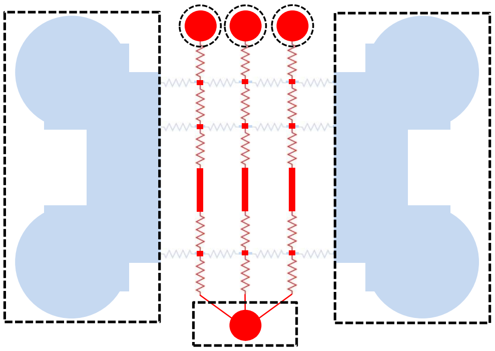

Figure 2.2: Device layout recast as a network of hydraulic resistances (resistors) and fixed pressure zones (outlined by dashed lines).

We determine pressure in the device by solving a system of equations relating the pressure drop, flowrate, and hydraulic resistance, as well as continuity of mass at each fluid node in the device ($\sum_{\text{nodes}} Q = 0$). A schematic of the hydraulic resistnace model of the system is given in figure 2.2. In this model, each channel has a hydraulic resistance given by equation (2.2). For a device with n axonal channels, there are $7n + 3$ unknown flows within the device. To solve this system, we write $3n$ equations enforcing continuity of mass at each node, and $4n + 3$ pressure drop equations of the form $\Delta P = R_h Q$. These pressure-drop equations represent closed fluid circuits (where $\Delta P = 0$), and open-ended circuits incorporating the boundary conditions (here, outlet reservoirs) as endpoints. This system of equations is then solved in MATLAB. The solution yields pressures at each node and flowrates in each channel. This equivalent hydraulic resistance model alone does not predict spatial varation of flow within each channel, and flow velocities are not predicted as a function of position on the channel cross-section; however, the pressure drops combined with later predictions facilitate the three-dimensional velocity distribution far from nodes (i.e., $\ell >> d$ from node).

Mass transfer within the device is well approximated by the one-dimensional convection diffusion equation. This approximation requires that transport along the channel occur at a time scale much greater than similar processes across the channel: $\tau_{||} >> \tau_{\perp}$. The ratio of the dominant lengthwise ($\tau_{||}$) to transverse ($\tau_{\perp}$) transport time scales in the low axial Pe limit , $\frac{\tau_{||}}{\tau_{\perp}} \sim \left(\frac{\ell}{a}\right)^2$, as well as the high axial Pe limit, $\frac{\tau_{||}}{\tau_{\perp}} \sim \left(\frac{\ell}{a}\right)^2 \frac{1}{\mathrm{Pe}}$, show that flow within microchannels of moderate Péclet number satisfy the approximation. Thus,

$$\frac{\partial c}{\partial t} + u_x \frac{\partial c}{\partial x} = D \frac{\partial^2 c}{\partial x^2} \tag{2.3}$$

Where $c(x, t)$ is the local concentration of solute [a.u.], t is time in [sec], x the distance along the channel ($0 < x < \ell$) in [m], and D the diffusivity of solute in [m^2/s].

We solve equation (2.3) in segmented lengths of the axonal channels. We impose fixed concentration boundary conditions at the intersections between axonal and delivery channels, $c(0, t) = c_o$, representing the solute imposed on the cell, and a zero-concentration boundary condition where the axonal channels meet the somal chamber, $c(\ell, t) = 0$. We non-dimensionalize equation (2.2) using scaling defined in Figure 2.1 and a convective temporal scale to non-dimensionalize time $t^* = \frac{t}{\ell/\overline{u}}$. The velocity scale in this case is the average across the channel, $\overline{u} = \frac{Q}{A}$, computed from knowledge of the device geometry (cross-sectional area, A) and the flowrate from (2.1). With this scaling, and noting that $u_x = \overline{u}$ for unidirectional flows, the equation becomes:

$$\frac{\partial c^*}{\partial t^*} + \frac{\partial c^*}{\partial x^*} = \frac{1}{\mathrm{Pe}} \frac{\partial^2 c^*}{\partial x^{*2}} \tag{2.4}$$

The Péclet number, $\mathrm{Pe} = \frac{\overline{u}\ell}{D} = \frac{\tau_{\mathrm{Diff}}}{\tau_{\mathrm{Conv}}}$, relates the timescales of convection and diffuson along the channel. Often, flows in microdevices have large Péclet numbers, limiting mixing (e.g., laminar flow patterning). Here, a large streamwise Péclet number will similarly result in strong solute confinement, whereas a flow with a near-zero streamwise Péclet number yields a linear concentration profile in the steady-state.

This problem is closed by writing a homogeneous initial condition: $c^*(x^*, 0) = 0$. We perform an eigenfunction expansion to obtain a series solution of this boundary-value problem applicable for all non-zero values of Pe:

$$c^*(x^*,t^*) = e^{\frac{Pe}{2}x^*}\sum_{n=1}^{\infty}\frac{2n\pi}{n^2\pi^2+1/4Pe^2}\sin(n\pi x^*)\left(1-e^{-\frac{t^*}{\tau_n^*}}\right) \tag{2.5}$$

with $\tau_n^* = \frac{1}{\frac{n^2\pi^2}{Pe}+\frac{Pe}{4}}$. For an arbitrary intial solution concentration profile, $\phi(x)$, and zero concentration boundary conditions, the concentration evolves in time and space as:

$$c^*(x^*,t^*) = e^{\frac{Pe}{2}x^*}\sum_{n=1}^{\infty}C_n^*\sin(n\pi x^*)e^{-\frac{t^*}{\tau_n^*}} \tag{2.6}$$

With the intial-condition-dependent constants:

$$C_n^* = 2\int_0^1 \phi(x^*)\sin(n\pi x^*)e^{-\frac{Pe}{2}x^*}\,dx^* \tag{2.7}$$

The Péclet number governs the shape of the concentration profile, both at steady and transient states. The nature of the series solution necessarily means that there is not one single time constant, but a time constant for each mode of the solution. The time constant controlling the development of a concentration profile corresponds to the largest time constant, which is the lowest Fourier mode, $\tau_1^* = \frac{4Pe}{4\pi^2+Pe^2}$ or $\tau_1 = \frac{4\ell^2}{D\left(4\pi^2+Pe^2\right)}$; for D = $1e-9$, $\tau = 2.7$ [sec], D = $1e-11$, $\tau = 275$ [sec].

The shear at the interface between the wall and fluid is determined by solving the steady, 2-D Navier–Stokes equation for uniform flow in an asymmetric duct under the action of a pressure gradient $\nabla p = \frac{p_{\text{high}}-p_{\text{low}}}{0-\ell}$:

$$\nabla p = \eta\nabla^2 u_x = \frac{\partial p}{\partial x} = \eta\left(\frac{\partial^2 u_x}{\partial y^2}+\frac{\partial^2 u_x}{\partial z^2}\right) \tag{2.8}$$

This is solved in a rectangular domain: $-\frac{w}{2}\le z\le\frac{w}{2}$, $-\frac{h}{2}\le y\le\frac{h}{2}$, $w>h$ with $u_z=0$ on the boundary. The velocity profile is given by:

$$u(y,z) = \frac{G\left(\frac{h^2}{4}-y^2\right)}{2\mu} - \sum_{\substack{n\\\text{(odd)}}}\frac{4h^2G}{n^3\pi^3\mu}\sin\left(\frac{n\pi}{2}\right)\cos\left(\lambda_n y\right)\frac{\cosh\left(\lambda_n z\right)}{\cosh\left(\lambda_n\frac{w}{2}\right)} \tag{2.9}$$

with $\lambda_n = \frac{n\pi}{h}$ and $G = -\nabla p$. The fluid shear is, in general, a tensor quantity, but the positions of maximal shear reside on the centers of the channel edges. Thus, to identify an upper limit for shear, we need only compute the shear at two points in the domain:

$$\tau_1 = \eta \left.\frac{\partial u}{\partial z}\right|_{z=\pm w/2, y=0} = \sum_{\substack{n \\ (\text{odd})}} \frac{4h^2 G}{n^3\pi^3} \lambda_n \sin\left(\frac{n\pi}{2}\right) \tanh\left(\lambda_n \frac{w}{2}\right) \tag{2.10}$$

$$\tau_2 = \eta \left.\frac{\partial u}{\partial y}\right|_{z=0, y=\pm h/2} = -G\frac{h}{2} + \sum_{\substack{n \\ (\text{odd})}} \frac{4h^2 G}{n^3\pi^3} \frac{\lambda_n}{\cosh\left(\lambda_n \frac{w}{2}\right)} \tag{2.11}$$

Of these, τ_2 is the dominant stress. High shear is present in regions with high fluid velocity gradients, and this is the case on the boundaries of the device; the rectilinear shape of the channel creates points of high shear on the long sides of the channel, as the maximum velocity in the center of the channel must decay to the no-slip value at the wall over a shorter length, increasing the spatial gradient of velocity.

In addition to interfacial stresses, the velocity solution is integrated to give a flowrate, and average velocity:

$$\bar{u} = \frac{Q}{A} = h^2 \frac{G}{4\eta} \left(\frac{1}{3} - \sum_{\substack{n \\ (\text{odd})}} \frac{64}{n^5 \pi^5} \frac{h}{w} \tanh\left(\frac{n\pi}{2} \frac{w}{h} \right) \right) \tag{2.12}$$

For $w/h > 2$, the hyperbolic tangent is approximated as unity for all n, and the remaining sum, $\sum_{n\ (\text{odd})} \frac{1}{n^5}$ can also be approximated as one. Whence,

$$\bar{u} = h^2 \frac{G}{4\eta} \left(\frac{1}{3} - \frac{64}{\pi^5} \frac{h}{w} \right) \tag{2.13}$$

We perform a similar procedure to convert the shear stress from an exact trancendental to an approximate algebraic function. In this case, the hyperbolic function does not approach a convenient limit, so we introduce a parameter, ε, that depends on the ratio of height to width in the device:

$$\tau_2 = -G\frac{h}{2} \left(1 - \sum_{\substack{n \\ (\text{odd})}} \frac{8}{n^2\pi^2} \frac{1}{\cosh\left(\frac{n\pi}{2} \frac{w}{h}\right)} \right) = -G\frac{h}{2}(1 - \varepsilon) \tag{2.14}$$

Table 2.1: Geometric parameters tabulated for particular channel aspect ratios. The parameters were computed from ca. 1000 summands, at which point the sum had converged.

$\frac{h}{w}$	ε	δ
1/2	.6303	3.232
1/4	.8144	1.320
1/6	.8763	0.828
1/10	.9258	0.475

The above expressions (2.12) and (2.13) can be combined to eliminate explicit dependence on pressure, providing a dependence on average velocity in the channel:

$$\tau_2 = \frac{\eta\bar{u}}{h}\left(2\frac{1-\varepsilon}{1/3 - \frac{64}{\pi^5}\frac{h}{w}}\right) = \frac{\eta\bar{u}}{h}\delta = \frac{\eta\mathrm{Pe}\frac{D}{\ell}}{h}\delta \tag{2.15}$$

Equation (2.15) is convenient to quickly estimate the shear as a function of key geometric and fluid parameters. In keeping theme with the mass convection-diffusion analysis of the system, we find it convenient to recast the shear as a function of Péclet number rather than velocity. We tolerate this addition of variables by noting that the diffusivity of species does not change greatly (if interested in only small ions, $D \sim 10^{-9}$ [m^2/s], or only large macromolecules, $D \sim 10^{-11}$ [m^2/s]), and that the length of the device, although it may change, is typically fixed by the demands of the experiment.

From the solutions to mass and momentum transfer relations, we determine the maximal shear stresses and concentration profiles (in time and space) using the hydraulic resistance model of the device from which the pressure drops were obtained. These results do not require multiphysics modeling of mass and momentum transport, and this is a direct result of design decisions enabling simplifications in the governing equations to analytically tractable forms.

2.4 Design Analysis and Discussion

The critical performance and design parameter in the device is the Péclet number, which we have identified as the controlling parameter in the distribution of solutes imposed on the neuron. Below (Figure 2.3), we present six plots detailing the concentration of a solute, as normalized by its input concentration, at positions along the culture channels. Solute concentration at six positions (identified by x^*) along the axonal channel are queried as a function of the Péclet number and time and plotted. By selecting a desired channel location and a fraction of the input concentration, the plots yield the Péclet number required for the desired solute profile for transient and steady-state modes of operation.

These concentration isocontours show that the system equilibrates on the order of ten seconds. For most profiles shown, a time of two minutes is sufficient to achieve steady-state operation. These concentration profiles establish more rapidly than standard solute delivery experiments, which are typically over 15 minutes in duration.

We quantify changes of fluid height analytically with the 1D model presented previously (equation (2.6)). This result is necessary to determine the time required to clear an axonal channel at the conclusion of solute injection, for example. To model device clearing, we introduce a nonzero initial condition for the concentration distribution in the channel, along with homogenous boundary conditions on the edges of the channel. By solving a change in device state from an experiment run at $Pe = 15$ with soluble chemicals (i.e., the delivery state) to a cleared device, we have found a 5-fold (e.g., 10^5) reduction in maximum concentration is achieved 4τ after the system is changed from the delivery to the clearing state. This is visualized in the following figure, where concentration is shown as a function of time and space, decaying from an initial condition.

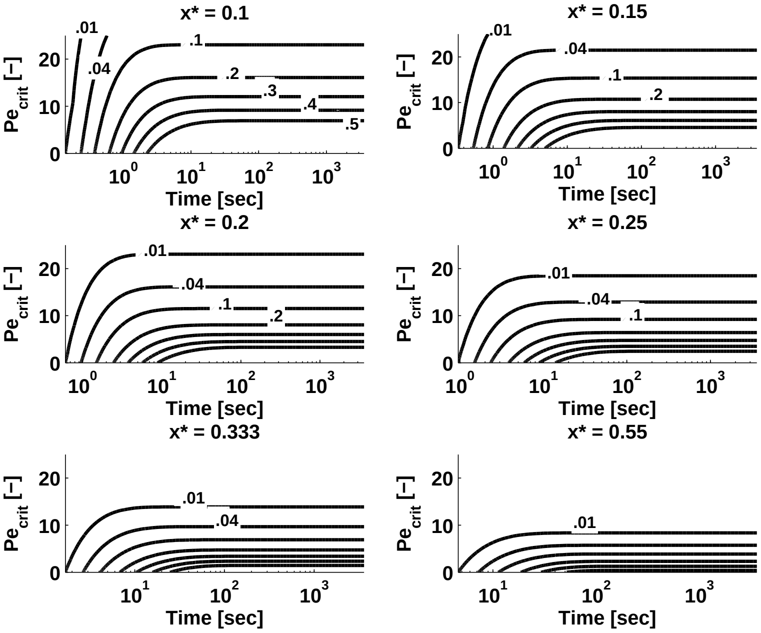

Figure 2.3: Concentration isocontours as a function of time and Péclet number for various positions along the axonal channel (x*).

Here, the time constant is take as that of the lowest Fourier mode, $\tau = \frac{4Pe}{Pe^2+4n^2\pi^2}$.

Out design specifies the Péclet number required such that diffusion is entirely dominated by convection of the fluid from the somal chamber toward the delivery fluidics. Solute confinement is produced at the cost of fluid shear stresses that are imposed along the axon. Fluid shear within the device, as a function of fluid, solute, and geometric parameters, is presented in equation (2.15), and is plotted in Figure 2.5. We present two scalings of the shear to highlight important design considerations: (1) allowable channel dimensions for specific values of $\frac{\tau}{\mathrm{Pe}}$ under the action of a constant fluid velocity (pressure and resistance changing) and (2) allowable channel dimensions for specific values of $\frac{\tau}{G}$ under the action of a constant pressure difference (flow and resistance changing).Of course, these figures will collapse to a single curve with appropriate scaling ($\frac{\tau}{Gh}$), and this is shown as an inset in the figure.

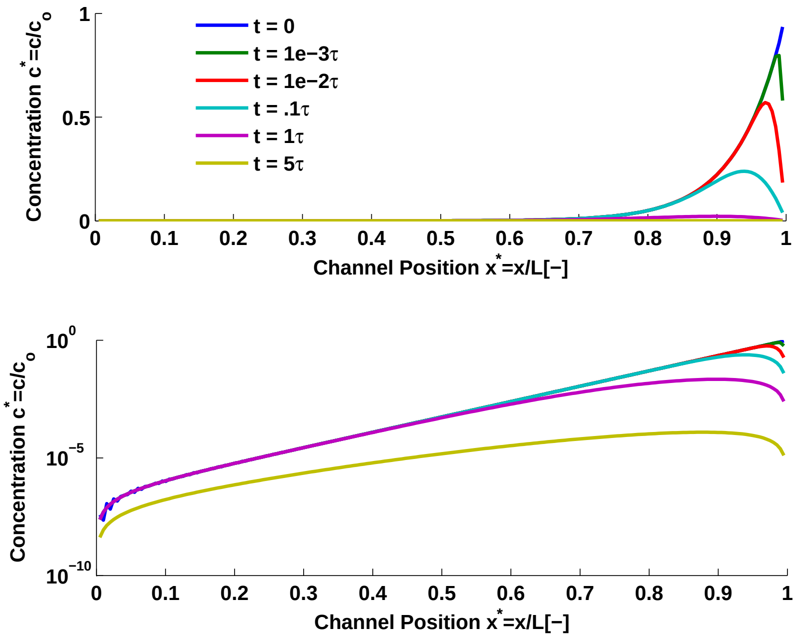

Figure 2.4: Transient response of device from steady-state operation with non-zero boundary conditions to solute clearing state with zero concentration boundary conditions at both ends of the culture channel.

The left pane in Figure 2.4 shows shear normalized by Péclet number to communicate dependence on the ratio of the channel sides, as well as the abolute height of the channel. Normalization by Péclet removes pressure dependence as the geometry is varied; changes in the shear are due purely to dissipation of energy at the walls vs. disspation in the bulk - as the channel area is reduced and the shape made more oblong, the surface area becomes exaggerated and energy dissipation at the boundaries is enhanced.

At fixed Péclet number, increasing h/w, the channel dimension ratio, and the absolute channel height, h, reduce shear but these parameters are limited by engineering constraints. There are fundamental limitations to the selection of both of these design dimensions, typically imposed by the method of device construction. Dry chemical etching of glass is impractical for depths greater than 3 μm as impurities deposit in the channel halting the etch (in these cases, the glass has a frosty appearance). Wet etch-

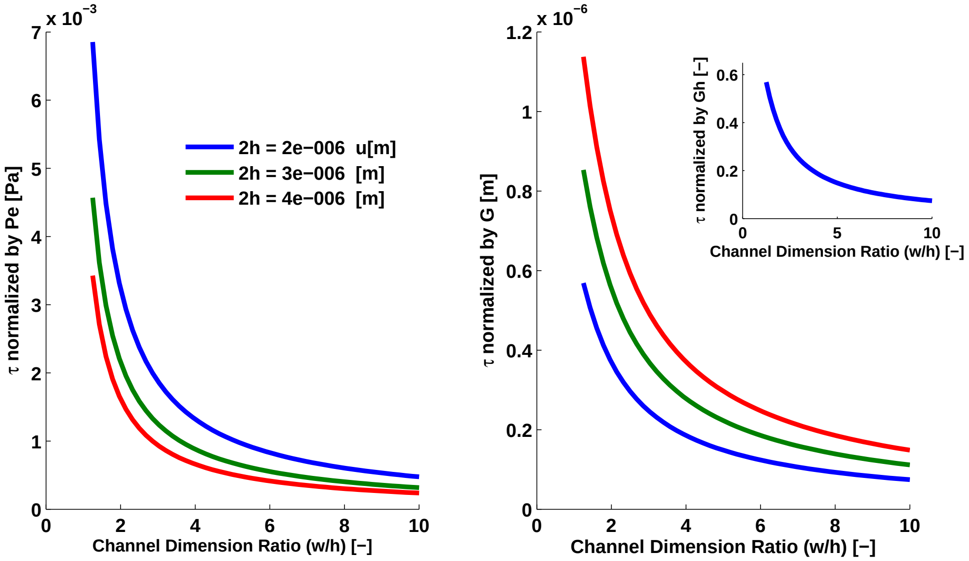

Figure 2.5: Maximum shear in the device, normalized by Péclet number (left) and pressure gradient (right), as a function of absolute channel height and channel aspect ratio. Dimensional quantities are plotted for simplicitiy in device design. The inset (at right) provides the collapsed curves for shear when appropriately normalized.

ing generates channels of arbitrary depth, but semi-circular channels of poor geometric definition. Aside from fabrication constraints, channels with large widths invalidate the arguments used previously to justify a 1-D solute transport model, as enhancement of the channel cross-section decreases $\tau_{\perp}$ while $\tau_{||}$ remains constant.

The presence of axons within the channels perturbs channel geometry. Blockage of the channel by cellular components increases the resistance of the channel, decreasing the average fluid velocity in the presence of a constant pressure drop. The pressure drop can be assumed constant as pressure on the somal side is fixed by the culture reservoir height, and the pressure distal from the soma is fixed by the pressure in the fluidic channel which, owing to the small resistance of this channel, is essentially that of the outlet reservoir located at the bottom of the device. We plot shear normalized by the pressure gradient in the culture channel in the right pane of Figure 2.5. Here, a blockage is easily seen as a change in both the aspect ratio of the channel as well as the absolute height of the channel. For growth along the base of the channel, the aspect ratio will increase and the channel height will decrease. Both these effects decrease the incumbent fluid shear on the cells. For growth along the sidewall of the channel, the height remains constant and the shear increases soley in response to the change in aspect ratio. Since the plot is nonlinear, stronger changes in fluid shear are felt for channels designed with smaller aspect ratios.

Both of these presentations of shear in the device discuss the case of maximal shear occuring a the center of the long wall on the channel cross-section. Locations away from this point will experience lower shear, with a minimum value of zero at the corners of the rectangular cross section.

2.5 Device Fabrication

The two-layer device is constructed from PDMS (for the fluid delivery network) and fused silica (for the culture and growth substrate). PDMS casting masters were fabricated from Silicon wafers (500 [μm] thick) using a Bosch etch process. Prior to etching, wafers are cleaned in Pirahna, dehydrated via heating in a hexamethydisilazane atmosphere (YES Vapor Prime Oven), and patterned photolithographically with Megaposit SPR 220-7.0 positive photoresist spun to a thickness of 7 [μm]. The channels with the smallest aspect ratio (1.3 : 1) in the delivery layer are those residing directly above the axonal channels, having dimensions 135 [μm] x 100 [μm] (height x width), and the channels with the largest aspect ratio (8.4 : 1) construct the resistance network, running from the input reservoir to the large fluid delivery channels. Channels in the reistance network are [16 μm] in width.

After etching the master, we passivate the surface by exposure to a small liquid volume ($\sim$ 80 [μL]) of 1H,1H,2H,2H-perfluorooctyltrichlorosilane (Sigma-Aldrich) under vacuum for $\sim$ 2 hours. PDMS (Sylgard 184, Dow Corning), mixed in a ratio of 10 : 1 (base: curing agent), degassed, is combined with the master, and baked at 60 C for 2 hours to form the fluidic layer. After removing the PDMS from the mold, intlet, outlet, and culture reservoirs are installed using a biopsy punch. We employ the leaching procedure of Millet, et al. [41] to remove uncrosslinked oligomers from the PDMS matix, preventing eventual release of these oligomers during cell culture and device operation. Briefly, a series of solvents swell the PDMS increasing the diffusivity of uncrosslinked polymer. We soak the devices in solutions of pentane (36 [hr]), pentane (7 [hr]), xylenes (16 [hr]), xylenes (7 [hr]), 200 proof Ethanol (2 [hr]), 200 proof ethanol (16 [hr]), 200 proof ethanol (7 [hr]), and a final soak in sterile DI water for a minimum of 12 hours. After the final sterile DI water exposure, we dry the PDMS under vacuum or in a 60 C oven.

The bottom (culture) layer of the device is fabricated from fused silica. Coverslip-thin (170 [μm]), 4-inch fused silica wafers were ordered from Mark Optics, Inc. (Santa Ana, CA). These wafers are washed in concentrated nitric acid, rinsed with DI water and nitrogen spray-dried prior to patterning. We coat the wafers with 70 [nm] of sputtered Chrome, followed by Shipley 1818 photoresist spun at 3000 RPM for 30 sec. We then pattern and develop photoresist to generate a masked array of culture channels, guide lines, and the culture base. Exposed Chrome is removed with CR-14 etchant (Transene Company, Inc. Danvers, MA), and the wafer is again rinsed with DI water and dried in nitrogen.

Using the chrome mask, we perform reactive ion etching to create the culture layer of the device. The chrome mask is etched in CHF_3/Ar plasma (Oxford 100, Oxford Instruments) to a depth of 3 [μm]. After transferring the pattern from the Cr mask to the fused-silica, we remove the remaining photoresist and chrome mask, and clean the wafer in DI water. The cleaned and patterned wafer is then diced with a wafer saw, yielding 24 substrates per wafer.

Both device halves are assembled after activation of the bonding surfaces in air plasma (Harrick Plasma, Ithaca, NY; ~30 [W], 200 [mTorr], 90 [sec]). By attaching both layers on an inspection microscope, using a small drop of water between the fused silica and PDMS, we delay the onset of the bond to increase working time and improve alignment. Post-alignment, we gently pinch the parts together and wick residual water from the device edges using a KimWipe. To ensure a strong bond, the assembled device is cured overnight in a 60 [C] oven.

We then prime the device with sterile DI water by filling inlet and culture reservoirs, submerging the device in sterile DI water, and exposing the device to slighlty negative pressure to remove bubbles trapped within the device [42]. After removing all bubbles, we exchange a solution of 1 [g/L] poly-L-lysine in borate buffer in the device to improve adhesion between the neurons and the wetted surfaces of the device. Typically, we perform two exchanges in total with the second 1.5-2 hours following the first. After the poly-L-lysine deposition, we again flush sterile DI water through the device. Devices are stored wet until used.

2.6 Demonstration of Cell Culture

We perform culture of primary rat hippocampal neurons in the device. These cells are used to study the distribution and trafficking of motor proteins, growth factors, and other biochemical agents. The neurons are sensitive both mechanically and chemically, providing an excellent test platform for our device.

Primary hippocampal cultures were prepared from E18 embryonic rats of either sex as described previously [24, 36, 43]. Cells were plated at 250 cells/mm^2 into the poly-L-lysine-treated somal chamber and maintained in cortical astroglia cells-conditioned NB/B27 medium at 37 degrees incubator with 5% CO2. Due to evaporation, medium was replenished every other day. Cells attached to the surface a few hours after seeding and axons started to grow into the micro-channels 3-5 days after seeding. For visualization of neurite growth, 10uM Calcein AM (Invitrogen), a cell-permeant dye that is converted to a green-fluorescent calcein after acetoxymethyl ester hydrolysis by intracellular esterases, was added to the somal chamber for 15min incubation at 37 degrees followed by gentle rinse with pre-warmed medium. To label mitochondria, 50nM MitoTracker® dye (Invitrogen) was added to the somal chamber for 30min incubation at 37 degree followed by gentle rinse with pre-warmed medium. Cells were maintained at 37 degrees for live imaging. Before acquiring movies, nanochamber was semi-sealed into a heated chamber (Warner instruments, Hamden, CT) containing hibernate A medium (Brainbits LLC, Springfield, IL) kept at 37 degree. Images were captured with a spinning disk confocal microscope setup custom built by Solamere Technology Group (Salt Lake City, Utah). Laser excitation wave length for different fluorophores was 488nm for GFP and 568nm for Mitotracker Red. Mitochondrial transport was acquired using a 40X 1.3 N.A oil objective. Both objective and the imaging stage are heated to 37 degrees.

We image cells using phase constrast microscopy to gauge cell viability and directed growth. Cells are shown at day in vitro (DIV) 1 and DIV 7 in Figure 2.6 below. These images show the growth of cells from a globular to stellated morphology, concurrent with the extension of axons into the culture channels. As described in the previous section, guide lines were fabricated onto the surface of the device where the cells are seeded. These guide lines are marked in Figure 2.6, leading from the seeding area toward the trigonal opening of the culture channels. Neurons were successfully cultured in the closed device for up to 11 DIV, which is sufficient time for cells to reach fluidic channels within the device enabling confined solute delivery.

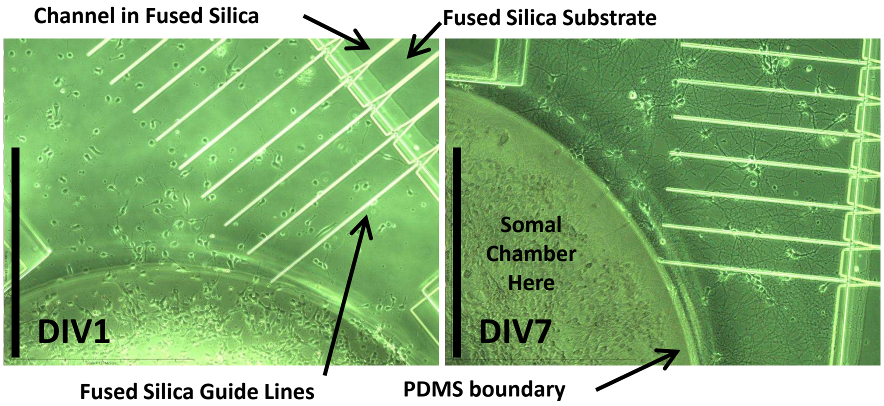

Figure 2.6: Phase contrast image of cells within device at DIV 1 (left) and DIV 7 (right). Cells at DIV 7 display healthy morphology evidenced by the absence of clumping and the outgrowth and development of both dendrites and axons. Images were captured on an inverted microscope, enabled by the coverslip-thin device substrate. The scale bar in both figures is 140 [μm]

We found guide lines into the axonal channel necessary to align the culture channels with the axon of the seeded cells. This observation is, at first glance, inconsistent with the work of Taylor, et al. [30, 31], as they do not require special modification of the entrace region to their channels. There are, however, geometric differences between our work and Taylor, et al. which explain the differences in cell behavior. The interface between the small channels and the culture area is formed by the attachment of the top PDMS cover and the bottom fused-silica base. When attached, the PDMS cover and base form a seal above the culture channels which is not entirely flush and the region between the PDMS top and fused silica base presents the cells with a three-dimensional charged surface (the entire device has been coated with cationic poly-lysine) that is amenable to cell growth and attachment. Both the fabrication of the PDMS cover and the alignment of the PDMS/fused-silica assembly contribute to the geometry of this surface. The edges on the PDMS cover are not perpendicular, but curved owing to the etching of the master; off-edge alignment exaggerates the extent of the bounding surface.

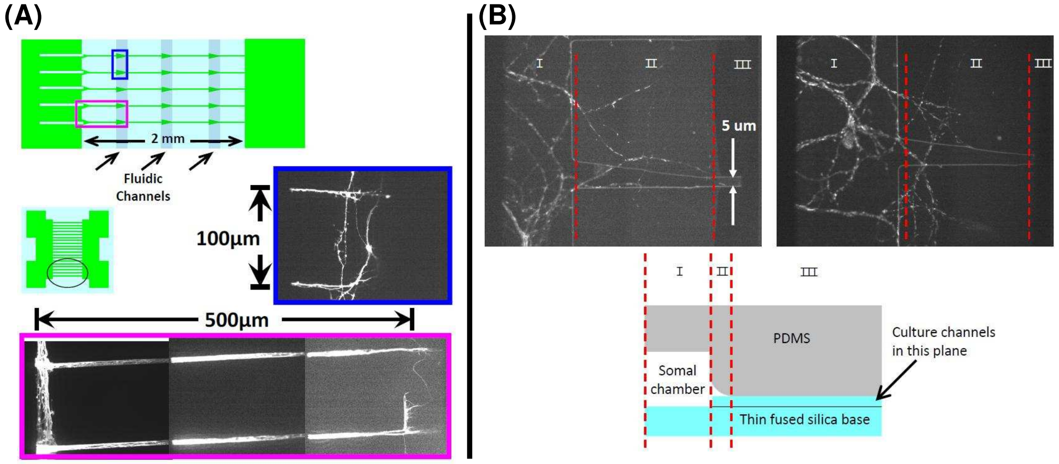

Figure 2.7: Frame A: Demonstration of entrained neural axons within culture channels. Fluoresence micrographs (middle right and bottom), with corresponding device locations hightlighted at top, show stained (Calcein AM, Invitrogen) cells indicating the presence of axons within the channels. Growth of axons proceeds from the somal chamber to the first fluidic channel. Frame B: Micrographs (top) and diagram (bottom) of axons in a device *without* guide lines. In the bottom diagram, three zones are specificed: (I) the somal chaber, (II) partially enclosed culture channels, and (III) completely enclosed culture channels. Shown above are micrographs of axons failing to enter the channels in zone (III), having been stalled in zone (II). The micrographs at top were captured using fluoresence microscopy on cells treated with MitoTracker Green dye, visualizing the mitochondria within the cells.

2.7 Conclusions

We have presented a design methodology quantifying the effects of device geometry on mass transport and fluid shear. These results were used to design a microfluidic device, in which nerve cells were sucessfully cultured. The design methodology presents a two-step process: (1) a hydraulic resistance model is used to predict fluid flow and pressure drops in all channels within the device (2) the pressure drops and flow rates are used to predict fluid shear and solute distribution profiles. This approach obviates implementation of multiphysics or CFD software, requiring only implementation of a matrix solver — mass transport and momentum behavior are straightforwardly communicated via plots and tables to determine shear as a function of flowrate and geometry, along with transient and steady state solute distributions given previously-determined flow behavior. This reduced-order design formulation enables fast and straightforward design of arrayed microfluidic devices for neural culture.

Culture on the device was demonstrated using primary embryonic rat hippocampal neurons. We also describe a geometric guidance scheme to direct axonal processes of the neurons into a linear array of culture channels where the axons may be later analyzed using the fluidic delivery system. Such a system will be useful in neurobiological experiments such as drug screening for prevention of, or solube factor delivery for the encouragement of, transport defects within the axon. Furthermore, the layout of the device enables somal isolation (and therefore known cell polarity) and the multiplexed culture channels of known orientation permit addressable data collection with minimal effort.

2.8 Acknowledgments

The authors thank Barbara Smoody for her expert technical assistance, and acknowledge funding from the National Multiple Sclerosis Society (MS Center Grant CA 1055-A-3); CF is supported by a postdoctoral fellowship from the National Multiple Sclerosis Society. ACB is supported by a Graduate Research Fellowship from the National Science Foundation. This work is based upon work supported by the STC Program of the National Science Foundation under Agreement No. ECS-9876771, and was performed in part at the Cornell NanoScale Facility, which is supported by the National Science Foundation (Grant ECS-0335765).

CHAPTER 3

SOFT DIFFUSE INTERFACES IN ELECTROKINETICS - THEORY AND EXPERIMENT FOR TRANSPORT IN CHARGED DIFFUSE LAYERS

3.1 Abstract

Charged and uncharged soft interfaces are present in a variety of microfluidic and biological systems. The electrokinetic properties of these fixed-diffuse-charge systems are dependent on (1) the components of the working fluid, (2) the bounding surface of the diffuse charge layer, and (3) the chemical and mechanical properties of the film itself. Here, we describe recent and past literature to provide a framework for the interpretation of data, utilizing the electrokineic coupling matrix, and a description of the experimental techniques relevant for microfluidic systems. In this work, we focus on experiments on, and models for, flat surfaces with constant film mass.

3.2 Introduction

Soft materials occur throughout natural and synthetic systems. In biology, soft materials are present inside and outside most multicellular organisms, found at the boundaries of the tissue and vasculature [14]. Less complex organisms, such as bacteria, have diffuse charge layers on their outer surface that are essential for cell adhesion [44–46] and other processes [47]. In the lab, both charged and uncharged polymer layers may be grafted to structures and within capillaries to suppress electroosmosis, [48, 49] or otherwise modify the surface chemistry and charge [49, 50]. Despite the ubiquity of these interfaces,

---

The content of this chapter was submitted and published as a research article that is reproduced here with permission from *Soft Matter*. This is the peer reviewed version of the following article: "Soft Diffuse Interfaces in Electrokinetics - Theory and experiment for transport in charged diffuse layers".

our ability to describe fixed-diffuse-charge systems is limited by ambiguities in the electrostatic and hydrodynamic governing equations and associated boundary conditions.

Descriptions of electrokinetic (EK) phenomena generally depend upon the ζ-potential of the material–solution system. The ζ-potential relates to the surface potential, ϕ_o, which is a critical component of DLVO theory used to characterize the interaction between charged surfaces [10, 51]; ζ is furthermore used to predict electroosmotic fluid actuation in glass and polymer capillaries [52, 53]. Electrokinetic characterization of the ζ-potential for a range of solution conditions is relatively straightforward for rigid-walled systems because the electrostatic and hydrodynamic boundaries coincide; for soft interfaces this is often not the case. Here and throughout we consider a soft interface to be a system composed of a rigid backing wall upon which a fluid permeable layer resides. These layers may be charged or uncharged.

A complete description of soft interfaces requires that we consider four key points:

1. **Chemical interactions between the diffuse-charge layer and the bulk fluid.** We must know film chemistry to predict film charge as a function of pH and ionic strength. Oxides can have poorly-defined dissociation chemistries and charging behavior [52] but polymer and other films can be synthesized or selected to create systems with improved chemical definition, using tuned acid/base dissociation constants. Furthermore, models can be formulated and validated against experiments to extract key chemical parameters (e.g., active site density, pK_a of surface groups). Questions remain, however, with the charge–generating mechanism of chemically inert polymers and underlying rigid film backing.
2. **Mechanical interaction models between the diffuse-fixed-charge layer and the bulk fluid.** Fluid–film interactions govern pressure- and electroosmotically-driven transport. Models of fluid–solid interaction for films as a function of pH,

ionic strength, temperature and other local solvent/film properties must be composed to describe the transport of fluid within the film layer. The solution to this problem will enable descriptions of momentum transfer in films, likely using an effective viscosity or Brinkman-type correction to the Navier–Stokes equations.

3. **Modeling of the surface- and fluid-generated potential field.** Closed-form solution for film potentials are known only in specific limits of relative film size (relative the Debye length) and film potential (relative to the thermal voltage). Films may be described with variable or uniform charge, and coupled to the governing Poisson–Boltzmann equation as a forcing term as a function of space. Potential modeling of the film and fluid are necessary to quantify charge and momentum transport. As in solid-surface electrokinetics, analyses can be simplified in the low-potential linear case, or examined numerically in the nonlinear case.
4. **Experimental methods to extract film/fluid system parameters.** Experiments are required to validate proposed theories. Relevant experimental measurables for films on solid substrates in microfluidic systems are electroosmotic velocity induced by an electric field transverse to the film surface normal, conductance of the film, and measured streaming current and potential. Contemporary advances in microfabrication techniques, metrology tools such as AFM [54], and the wealth of physical and chemical information on polymer films encourages parametric investigations of solid-film-solution systems to test quantitatively proposed models for these systems.

Here, we address these aspects of the solid-film-fluid interface for applications in microfluidic systems; specific attention is paid to the coupling of film properties using the formalism of the electrokinetic coupling matrix. Recently, Pallandre, et al. [55] reviewed aspects of these systems, with regard to the application of surface treatment techniques developed for large surfaces. Zembala reviewed electrokinetics of heterogeneous surfaces [56], examining diffuse charge layers on heterogeneous particles and electrokinetics of particles adsorbed on surfaces. A later review by Adamczyk and coworkers [57] describes work on heterogeneous surfaces, considering more specifically the case of particle covered surfaces with well defined ζ-potentials.

In the first half of this paper, we review fundamental electrokinetics of rigid surfaces, and then incorporate the ideas of diffuse interfaces to compare between the two. In the second half, we review the literature in two parts: (i) theoretical descriptions of diffuse interfaces and (ii) experimental work on diffuse interfaces. We conclude with future directions in diffuse interface research.

3.3 Theoretical Electrokinetics at Hard and Soft Interfaces

3.3.1 Fundamentals of Electrokinetics at Hard and Soft Interfaces

The ζ-potential is of fundamental interest and importance in electrokinetics, representing the observed electrokinetic potential as the result of an experiment. The ζ-potential stands in contrast to the surface potential, ϕ_o (figure 3.1), which is the electrical potential of the coincident plane at the solid surface. Commonly, as in the case of the Gouy–Chapman model [1], the two are taken to coincide. In the Gouy–Chapman–Stern model the two potentials are different; an immobile layer of ions with thickness λ_s offsets the plane of shear and surface potential, as shown in figure 3.1.

The starting point for the analysis of double-layer phenomena is the Poisson–

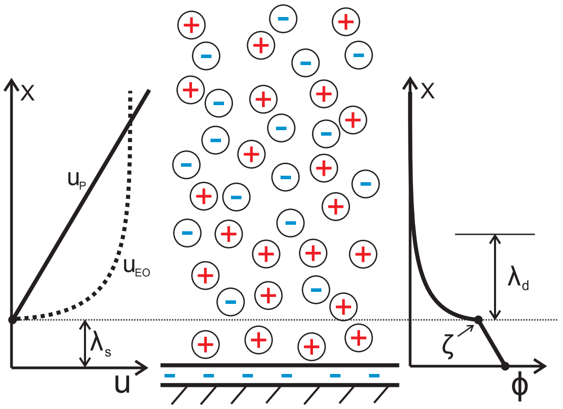

Figure 3.1: Diagram of charge-generated potential profiles at an impermeable charged interface. Bound wall charge (here negative) generates an immobile (Stern) layer of ions and a diffuse layer. Schematic potential and velocity profiles, as a result of forcing by pressure and potential fields, illustrate characteristic length scales and behaviors. The velocity profiles at left are comparable in shape but not magnitude.

Boltzmann equation:

$$\nabla \cdot (-\varepsilon^* \varepsilon_o \nabla \phi) = \rho_e + \rho_f = F \sum_{j=1}^{n} c_{j,\infty} z_j^* e^{\frac{-z_j^* F \phi}{RT}} + \rho_f \tag{3.1}$$

Here, ϕ is the electrical potential, ε_o is the permittivity of free space, ε^* is the dielectric constant in the continuum, F is Faraday's constant, $c_{j,\infty}$ and z_j^* are the bulk concentration and valence for the j^{th} ionic component (from a total of n), R is the molar gas constant, T the temperature, ρ_e is the free charge density (expressed via the Boltzmann distribution in equation (3.1)), and ρ_f is the fixed charge density. Unitless variables are embellished with asterisks; dimensionless functions and non-dimensional parameters (e.g., *Du*) are, however, *not* embellished. The Poisson–Boltzmann equation is nondimensionalized by the Debye length $\lambda_d = \sqrt{\frac{\varepsilon^* \varepsilon_o RT}{2F^2 I_c}}$, the characteristic electrical decay length in the fluid, the thermal voltage $\phi_{\mathrm{T}} = \frac{RT}{F} \sim 25[\mathrm{mV}]$ as the characteristic potential, the ionic strength $I_c = 1/2 \sum_{j=1}^{n} z^{*2}_j c_{j,\infty}$ as a concentration scale, and an arbitrary parameter, β, as a scale for the fixed charge. For a $z^* : z^*$ electrolyte with uniform permittivity, the 1-D Poisson–Boltzmann equation becomes:

$$\frac{d^2 \phi^*}{dx^{*2}} = -\frac{1}{z^*} \sinh(z^* \phi^*) - \rho_f^*(x) \frac{\beta}{2FI_c} \tag{3.2}$$

Equation (3.2) above suggests the scale β be taken as $2FI_c$, which is characteristic of the charge capacity of the ions in solution. Dukhin, et al. [58] has additionally proposed a length scale for characteristic electrical decay *within* the fixed charge layer:

$$\lambda_\delta = \lambda_d \sqrt{\frac{2Fc_\infty}{|\rho_f|}} = \sqrt{\frac{\varepsilon^* \varepsilon_o RT}{F\,|\rho_f|}} \tag{3.3}$$

This relation communicates the importance of the fixed charge on the electrical potential profiles, and is paramount in descriptions of conductivity within the film. In the absence of a charged layer, $\rho_f(x) = 0$, the boundary condition on the solid wall is described with either a fixed charge, $\varepsilon^* \varepsilon_o \left.\frac{d\phi}{dx}\right|_{x=0}$, or a fixed potential, ϕ_o. The second boundary condition in bulk solution or the far field is taken to have zero charge or zero field, or, in the case of symmetrical walls, a second fixed charge or fixed potential.

The ζ-potential is the electrokinetic potential at or near the rigid surface, and it is obtained from an electrokinetic experiment, e.g., streaming current/potential [52, 59, 60], current monitoring [52, 59, 60], or neutral-dye elution [52, 59, 60]. A variety of other techniques may be used, including surface conductance or dielectric spectroscopy measurements [61]. Streaming current/potential and conductance techniques are the most useful for these studies, as the chemistry of the working fluid remains constant and the required equipment is readily available.

Streaming current and streaming potential techniques are straightforward to interpret on rigid surfaces in the thin–EDL limit. In a streaming-type experiment, the test cell is typically a small-bore (diameter typically 25 to 150 μm) capillary [62–65] or parallel plate assembly [66–68]. Fluid is actuated by a pressure difference, Δp, across the channel of length ℓ and uniform area A. The pressure difference generates a flow with velocity field $\mathbf{u}$ that acts to transport the free charge density (ρ_e) as a current:

$$I_{\text{str}} = \int_A \mathbf{u}\rho_e \cdot d\mathbf{A} \tag{3.4}$$

When the hydraulic radius of the channel, $r_h \sim \frac{2\cdot\text{Area}}{\text{Perimeter}}$ is large relative to the Debye length, the streaming current integrates to [59, 69]:

$$I_{\text{str}} = \frac{\zeta \varepsilon^* \varepsilon_o A}{\eta} \frac{\Delta p}{\ell} \tag{3.5}$$

Thus, the channel cross-section and fluid properties are known, and we can measure the streaming current and pressure drop across the channel to yield an expression for the ζ-potential. A similar technique, streaming potential, uses the same experimental setup, but the electrical potential is measured with a high-impedance voltmeter rather than current with a low-impedance ammeter. In enforcing $I = 0$, an adverse current of charged species is conducted through the fluid as caused by an equilibrium E-field.

The mechanism of system conductance is essential to the measured streaming potential. Absent double layer effects, the system conductance is due only to the presence of ions in the bulk fluid, although surface conductance effects can be present owing to the charged surface. The presence of the surface enhances the conductivity of the system. The total effective conductivity of the channel is a combination of the bulk and surface conductivities:

$$\sigma = \sigma_B + \frac{G_s}{r_h} \tag{3.6}$$

Where σ is the system conductivity, σ_B the conductivity of the bulk fluid, and G_s the surface conductance. By recasting the total conductivity, we extract a nondimensional parameter that defines the relative importance of the surface conductance:

$$\sigma = \sigma_B(1 + \text{Du}) \tag{3.7}$$

The Dukhin number is defined as $\text{Du} = \frac{G_s}{\sigma_B r_h}$. As the characteristic dimension of the channel and solution ionic strength increases, surface conductance effects become less apparent — Davies and Rideal remark [70], that capillary ζ-potentials were initially thought to depend on the radius of the capillary directly only to be later understood as enhanced conductivity as the surface to volume ratio of the capillary increased. Attempts at analytical descriptions of the surface conductance tend to underestimate the observed values [71–74].

The surface conductance of a system may be determined in several ways. Common methods are (a) the four-electrode technique of Schwan [75], which is a direct measurement of the cell conductivity, (b) a limiting extrapolation method in which an electrokinetic measurement is performed as the characteristic channel dimension is changed, and (c) sequential streaming current and streaming potential measurements from which the cell conductivity is derived and corrected by the bulk fluid value.

3.3.2 The Electrokinetic Coupling Matrix

The cognate electrokinetic phenomena are well described with formalism of the electrokinetic coupling matrix [59, 76]. Here, the system is forced by a pressure gradient $\nabla p \cdot \vec{n}$, with $\vec{n}$ directed along the channel axis, and/or an electric field E, and the outputs are flow and/or current densities. Generally,

$$\begin{bmatrix} Q/A \\ I/A \end{bmatrix} = \begin{bmatrix} \chi_{11} & \chi_{12} \\ \chi_{21} & \chi_{22} \end{bmatrix} \begin{bmatrix} -\nabla p \cdot \vec{n} \\ E \end{bmatrix} \tag{3.8}$$

This matrix communicates immediately all essential electrokinetic phenomena: fluid flow in the absence of electrical forcing depends on χ_{11} only ($Q/A = -\chi_{11} \nabla p \cdot \vec{n}$), streaming current depends on χ_{21} only ($I/A = -\chi_{21} \nabla p \cdot \vec{n}$), conductivity measurements on χ_{22} only ($I/A = \chi_{22} E$), and streaming potential on a ratio of χ_{22} and χ_{21} ($I/A = 0 \Rightarrow E = \chi_{21}/\chi_{22} \nabla p \cdot \vec{n}$). Other phenomena such as EK pumping ($-\nabla p \cdot \vec{n} = \chi_{11}/\chi_{12} E$) and electroviscosity ($Q/A = -\nabla p \cdot \vec{n}(\chi_{11} - \chi_{12}\chi_{21}/\chi_{22})$) are straightforwardly descried as well. The structure of the electrical double layer (EDL) governs the form of the χ_{12},$\chi 21$ and terms.

For a $z:z$ electrolyte in the thin–EDL limit, the four components of the EK coupling matrix are:

$$\chi_{11} \approx \frac{r_h^2}{8\eta} \tag{3.9}$$

$$\chi_{12} = -\frac{\varepsilon^* \varepsilon_o}{\eta} \phi_o \tag{3.10}$$

$$\chi_{21} = -\frac{\varepsilon^* \varepsilon_o}{\eta} \phi_o \tag{3.11}$$

$$\chi_{22} = \sigma_B + \frac{G_s}{r_h} \tag{3.12}$$

The χ_{11} term is affected only by the channel size and fluid viscosity; the components off the main diagonal depend on electrical and mechanical properties of the fluid and the wall potential. The χ_{22} term is equal to the system conductivity, composed of bulk conductivity, surface conductance, and the hydraulic radius of the channel. There are two commonly recognized sources of surface conductance: (1) an electrophoretic component, similar to the bulk, but increased because of enhanced concentration of ions near the surface and (2) a convective component provided by electroosmotic flow, which carries the net charge in the EDL. These two effects were quantified by Bikerman [71–73]:

$$G_s = \sqrt{8\varepsilon^* \varepsilon_o c_\infty RT} \left(\frac{u_+}{B^* - 1} - \frac{u_-}{B^* + 1} + \frac{4\varepsilon^* \varepsilon_o RT}{\eta z F} \frac{1}{B^{*2} - 1} \right) \tag{3.13}$$

Here, $B^* = \coth\left(\frac{-z\phi_o}{4\phi_T}\right)$ and $u_\pm$ are the ionic mobilities of the counter- and coions in solution (cf. Bard and Faulkner [1] p.68).

We introduce integral formulations of the electrokinetic coupling terms, which generalize the electrokinetic parameters when outside of the thin–EDL limit [76]. Here, the velocity u is a function of both a pressure gradient and electrical potential. Further, the phenomena is reduced to two dimensions – with directions parallel (y) and orthogonal

(x) to the flow:

$$\begin{bmatrix} Q/A \\ I/A \end{bmatrix} = \begin{bmatrix} \frac{1}{-\frac{\partial p}{\partial y}} \frac{1}{\int dx} \int u|_{E=0}\, dx & \frac{1}{E} \frac{1}{\int dx} \int u|_{\frac{\partial p}{\partial y}=0}\, dx \\ \frac{1}{-\frac{\partial p}{\partial y}} \frac{1}{\int dx} \int u|_{E=0}\, \rho_e\, dx & \frac{1}{\int dx} \left(\int \sum_j z_j^* F u_j c_j\, dx + \frac{1}{E} \int u|_{\frac{\partial p}{\partial y}=0}\, \rho_e\, dx \right) \end{bmatrix} \begin{bmatrix} -\frac{\partial p}{\partial y} \\ E \end{bmatrix} \tag{3.14}$$

The quantity u_j denotes the ionic mobility for the j^{th} ion in the system. Representation of this matrix equation in higher dimensions is straightforward, although evaluation of the terms will be complicated by irregularities in geometry. We implement the reduced for above consistent with past work in this field, as well as experimental systems designed to accomodate simplified forms.

3.3.3 Electrokinetics and Soft Interfaces

The electrokinetic coupling matrix is a convenient way to codify the response of the diffuse charge system to external forcing. The integral formulation outlines how such responses will be determined, provided that expressions for the fluid velocity and concentrations are known as a function of applied electric and pressure fields both inside and outside of the surface layer.

The generalized electrokinetic coupling terms described in equation (3.14) are applicable to soft interfaces. The key difference between rigid and diffuse interfaces with respect to these terms is the breakdown of a well-defined and meaningful ζ-potential. For rigid interfaces, ζ represents the potential at the plane of shear, whereas for soft materials, ζ is an integral function of the soft layer charge and hydrodynamic properties.

3.3.4 Theoretical descriptions of Soft Interfaces in Electrokinetics

To analyze and interpret theory and experimental data, we use the system geometry in figure 3.2. Here, the height of the channel is small relative to the width ($d << w$) and thus the channel geometry can be approximated as infinite parallel plates. A fixed charge layer of thickness δ uniformly covers each surface. Depending upon the phenomena of interest, pressure or electric fields may actuate the fluid.

Descriptions of electrokinetics at geometrically well-defined soft interfaces have been proposed and studied by many workers. The genesis for the initial work is a description of membrane surfaces, as they appear in filtration systems and biological applications [77]. Although these studies are useful to frame our current discussion on planar interfaces in electrokinetics, we will not discuss results specific to non-planar geometries. Soft systems have also been analyzed with respect to colloidal mobility [78–80], sharing many aspects of the theory, but these studies are outside of the current discussion owing to the inclusion of complicating factors (e.g., geometry, although this complication vanishes for Debye and diffuse-layer length scales much larger than the characteristic particle size).

Soft interfaces may be divided into two classes: soft interfaces *with* charge and soft interfaces *without* charge. Early attempts at modeling the soft interface without charge were provided by Cohen Stuart, et al. [81, 82]. In their approach, the film completely blocks momentum transfer, yet has electrical properties identical to the bulk fluid. This shifts the shear plane away from the rigid wall into solution by a thickness δ, and is distinct from the Stern layer picture of the interface as the drop within the film layer proceeds exactly as in the bulk, vs. the linear decay demanded by a finite layer of oppositely charged ions. Specifically, Cohen Stuart, et al. assume a solid wall with

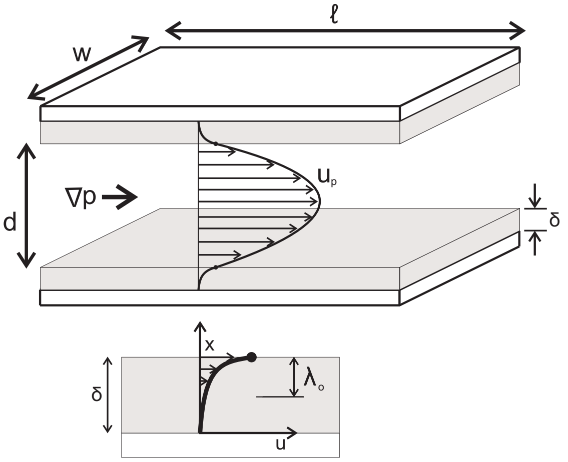

Figure 3.2: Schematic of electrokinetic cell used in theoretical modeling and experimental investigations (top). The configuration here is not drawn to scale; typically $w >> d$ to approximate parallel plates. (Below) A typical velocity profile produced by an applied pressure difference. The hydrodynamic penetration distance, λ_o, is also shown.

potential $\phi_o^* = \frac{F\phi_o}{RT}$ and a film with thickness δ to obtain the potential at the film edge:

$$\phi_\delta = \frac{2RT}{z^*F} \ln\left(\frac{1 + \tanh\left(\frac{\phi_o^*}{4z}\right) e^{-\delta/\lambda_d}}{1 - \tanh\left(\frac{\phi_o^*}{4z}\right) e^{-\delta/\lambda_d}}\right) \tag{3.15}$$

For a $z^* : z^*$ electrolyte in the case described above, the four components of the electrokinetic coupling matrix are:

$$\chi_{11} = \frac{(d/2 - \delta)^2}{8\eta} \tag{3.16}$$

$$\chi_{12} = -\frac{\varepsilon^* \varepsilon_o \phi_\delta}{\eta} \tag{3.17}$$

$$\chi_{21} = -\frac{\varepsilon^* \varepsilon_o \phi_\delta}{\eta} \tag{3.18}$$

$$\chi_{22} = \sigma_B + \sigma_\delta + \frac{G_s}{d/2 - \delta} \tag{3.19}$$

Compared to systems absent the film, the χ_{11} term is affected only by a reduced flow path, and χ_{12} and χ_{21} exhibit reduced electrical potential as the potential drops across the immobile film to the displaced plane of shear. The conductivity term, χ_{22}, now has three components: the bulk conductivity of the channel, σ_B, the conductivity within the stiff film, σ_δ, and a conductivity term accounting for excess and depletion of counter- and coions near the charged surface and an electroosmotic component of the flow, G_s. Here, we take σ_δ to be zero as the film has infinite resistance to flow. Outside the film, we adopt the Bikerman formulation of surface conductivity (equation (3.13)). From equations (3.16)-(3.19) we observe that the EK coupling matrix for a transport-impermeable film of thickness δ is nearly identical to a system without a transport impermeable film. The slight differences originate in a decrease in the hydraulic resistance and apparent ζ-potential for the system with a film.

Although the impact of the momentum-impermeable, electrically-identical film is straightforward to analyze and interpret, the model can be applied to very few systems: Generally, an interfacial layer will exhibit none of these outcomes — grafted layers are seldom impermeable to transport, and films rarely exist completely uncharged. Indeed, there are many reports of surfaces with no inherent chemical charge generation method [48, 65, 83, 84] (i.e., no dissociable groups or groups that may be substituted) that nevertheless generate a local potential and charge attributable to nonspecific adsorption, or other physical and chemical interactions. Studies of charged interfaces present greater difficulties in analysis and interpretation.

Modeling of soft interfaces is grounded in the examination of biological materials. Early efforts by Donath and Pastushenko [85, 86] analyzed the electrophoresis of a cell coated with glycoproteins and glycolipids. The Donath and Pastushenko theory is developed for the linearized Poisson–Boltzmann equation with a uniform fixed charge density in the glycoprotein/lipid layer. Whereas, the biological analytes considered by Donath, et al. [85, 86] are poorly defined geometrically and heterogeneous in extent, the theory developed assumes planar geometry on the assumption that the characteristic length scale for changes in the electrokinetic and flow profiles are much smaller than the characteristic dimension of the cells under study (erythrocytes and bull spermatocytes).

In the Donath and Pastushenko theory, the inner membrane potential is related to the fixed charge through the Donnan potential. The concept of the Donnan potential [70, 87, 88] is central to nearly all studies of diffuse-charge interfaces. A charged membrane will uptake ions from solution, generating a difference in concentration. This is coincident with a difference in potential because the chemical potential of the same species must be equal in both the fluid and film phases [70]. This same relation between bulk fluid and inner membrane potential is obtained from equation (3.1) when $\frac{d^2\phi}{dx^2} = 0$, as a uniform equilibrium is enforced between the salt reservoir and the fixed charge sites. For an ion-permeable membrane with fixed charge density ρ_f and a solution of $z^* : z^*$ electrolyte with concentration c_∞ at equilibrium, the Donnan potential is:

$$\phi_D = -\frac{RT}{|z^*|\,F}\text{arcsinh}\left(\frac{\rho_f}{2\,|z^*|\,Fc_\infty}\right) \tag{3.20}$$

When the potential and charge density are made dimensionless by ϕ_T and $\beta = 2FI_c$, the Donnan potential becomes:

$$\phi_D^* = -\frac{1}{|z^*|}\text{arcsinh}\left(\rho_f^*\right) \tag{3.21}$$

This describes the potential difference between a thick membrane ($\delta >> \lambda_d$) and a point far out in solution; $\delta >> \lambda_D$ implies that the curvature in potential will vanish, leaving a balance between the free and fixed charge densities, as above. Ohshima and Ohki [89] require this condition at the interface between the inner and outer layers of the membrane, and this, in conjunction with zero potential gradient at the membrane midline, requires that the center layer of the film assume a potential equal to the Donnan potential. This Neumann boundary condition appears in nearly all descriptions of diffuse-charge interfaces; notable exceptions are those descriptions that select a potential boundary condition deep within the film of the rigid backing substrate (e.g., a boundary potential of silica for a hydrogel attached to glass). This boundary condition is indicated schematically in frame A of figure 3.3.

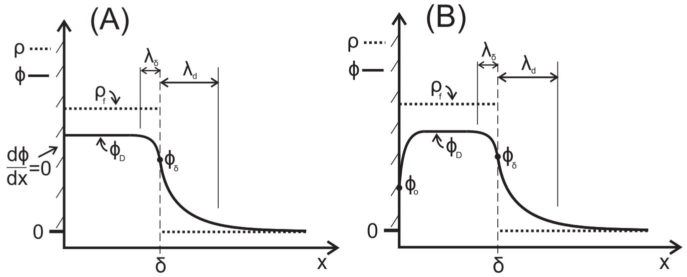

Figure 3.3: Diagrams of charge (ρ_f) and potential (ϕ) profiles for various wall boundary conditions. (A): Neumann boundary condition with fixed potential slope at wall. (B): Dirichlet boundary condition with fixed potential at the wall. In both cases, characteristic decay lengths are indicated for the fluid (λ_d) and diffuse charge layers (λ_δ), with ϕ_δ is the electrical potential at the film edge.

In the Donath and Pastushenko theory, Donath, et al. [85, 86] formulate a three-parameter model varying the thickness of the film, film permeability, and the fixed-charge density of the film. Inherent in their model is the assumption of equal dielectric constant (ε^*) in both the gel layer and solution—an assumption that they assert is justified on the high water content of the film.

Ohshima and Ohki [89] consider the electrical potential profile of a partially charged membrane sandwiched by free solution. In this model, a free membrane in solution has a dry, *uncharged* center and hydrated exterior regions which *are* charged. Their analysis is similar to the prior efforts by Donath et al. [85, 86], although Ohshima and Ohki consider the general nonlinear description of the electrokinetics, and benefit from symmetry conditions at the membrane interior. Considering thin ($2\delta/\lambda_d \sim 1$) and thick ($2\delta/\lambda_d >> 1$) membranes, they derive an expression relating the potential at the outer plane of the diffuse charge layer with an inner, uncharged, layer that is offset from the outer plane by some distance δ_h. Asserting the uncharged inner layer possesses zero curvature in electrical potential $\left(\frac{d^2\phi}{dx^2} = 0\right)$, and defining the center of the membrane as a plane of symmetry $\left(\frac{d\phi}{dx}\Big|_{\text{midpoint}} = 0\right)$, they relate the potential at the outer membrane boundary to points within the inner layer of the membrane [89, 90]:

$$\phi_\delta^* = \phi_D^* - \tanh\left(\frac{\phi_D^*}{2}\right) \tag{3.22}$$

Here, ϕ_δ^* lies on the edge of the membrane/film and ϕ_D^* lies in the plane dividing the charged and uncharged membrane sections; ϕ_D^* is also the potential everywhere *within* the uncharged membrane; both potentials are made dimensionless by ϕ_T.

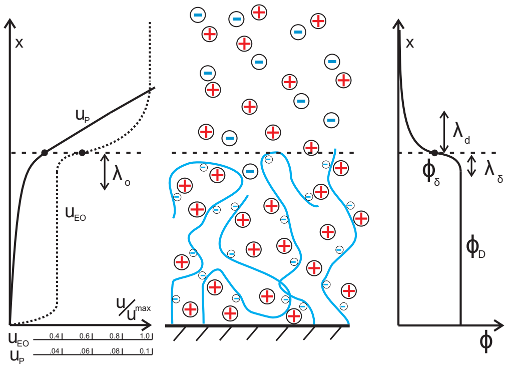

Figure 3.4: Schematic of potential and velocity profiles for a negatively charged polymer film. Various momentum and potential decay scales are displayed, which mitigate both pressure and electric field actuated transport. In the velocity–position plot at left, the u_p and u_{EO} plots are not comparable in magnitude, but do indicate differences in spatial velocity gradients; pressure–driven flow changes continuously until the channel center, and local to the film varies linearly when the size of the channel is large as compared to the film thickness. The E-field generated (electroosmotic) flow establishes on scales comparable to the Debye length.

3.3.5 Charge Transport: χ_{12} and χ_{21}

Studies of electrokinetic behavior on diffuse-charge interfaces have been conducted for planar (or nearly planar) surfaces by Wunderlich [91], Donath and Voigt [92], Ohshima and Kondo [93], and Starov and Solomentsev [94, 95]. Donath and Voigt [92] compute the streaming current and streaming potential of diffuse-charge layers on parallel plates. Their formulation of the system includes fluid mechanical and electrical modeling. They solve a modified Navier–Stokes equation by including a Brinkman-type [96] resistance term:

$$\eta \frac{d^2u}{dx^2} - k(x)u = \frac{\partial p}{\partial y} \tag{3.23}$$

which we nondimensionalize to:

$$\frac{d^2u^*}{dx^{*2}} - \lambda^{*2}u^* = \frac{\partial p^*}{\partial y^*} \tag{3.24}$$

Where $u^* = \frac{u}{U}$ defines a characteristic velocity scale U, $y^* = \frac{y}{\ell}$ and $x^* = \frac{x}{\delta}$ define length scales based on channel length and film thickness, the pressure is nondimensionalized as $p^* = \frac{p}{\eta \ell U/\delta^2}$, and $\lambda^* = \sqrt{\frac{k(x)\delta^2}{\eta}}$ defines the square of the ratio of a characteristic length scale for the penetration of fluid into the film, $\lambda_o = \sqrt{\frac{\eta}{k(x)}}$, which nondimensionalizes the film thickness, δ. The Brinkman (friction) coefficient, $k(x)$, is a function of space and may generally be taken to vary in direct proportion to the charge density of the film, as the density of charge groups on the polymer is presumed to scale linearly with the film volume fraction and hence film resistance. In the Donath and Voigt formulation, the friction coefficient is non-zero and uniform throughout the film $0 \leq x \leq \delta$, and zero in the pure fluid phase $\delta < x \leq d/2$.

The electrical modeling of the planar fixed-charge layer and fluid assumes the form given by equation (3.1), with a spatially varying fixed-charge density ρ_f. Studying the cases of a $z^* : z^*$ electrolyte, the problem is then to solve equation (3.2), with $\beta = 2FI_c$. Since the full equation is nonlinear, most closed-form solutions have been found only for the linearized case. Linearization results in:

$$\frac{d^2\phi^*}{dx^{*2}} = -\phi^* + \rho_f^*(x) \tag{3.25}$$

This now limits the applicable range of study to cases where $\phi^* < 1$ or equivalently $\phi <$ 25 [mV]. Equation (3.25) may be solved both inside and outside of the film, applying a matching condition for electrical potential and electrical field at the film edge. The boundary conditions away from the film are zero potential in the bulk (cell midline) and fixed potential slope at the inner surface of the film:

$$\phi^*\left(\frac{d}{2\delta}\right) = 0 \tag{3.26}$$

$$\left.\frac{d\phi^*}{dx^*}\right|_{x^*=0} = -\sigma^* \tag{3.27}$$

Here, $\sigma^* = \frac{\sigma}{\sqrt{2\varepsilon\varepsilon_o RTI_c}}$. The first condition enforces electroneutrality of bulk solution, and the second fixes the charge of the film interior to that of the bulk film, neglecting any apparent charge at the solid wall that would result from, for example, a charge-generating dissociation reaction. Both of these boundary conditions are indicated in figure 3.3.

The distribution of fixed charge within the film strongly affects the film surface potential and surface-sensitive measurements. In figure 3.5 we plot analytical solutions to equation (3.25) with various charge density profiles, all having the same total charge. These profiles indicate the dependence of profile shape and boundary value on the charge distribution. Considering the effect of charge distribution on film measurements, streaming current preferentially probes the surface of the film, and is sensitive to the charge density at the surface (as determined by the potential). The surface potential varies strongly in for the three charge distributions considered.

Donath and Voigt [92] examine streaming current as a function of system parameters in the low potential limit. These results do not address films having high charge or films bounded by surfaces with electrical boundary conditions that differ from the film boundary conditions. Donath and Voigt [92] also describe a nonlinear treatment of streaming current, streaming potential, and surface conductivity for a volume with uniform charge distribution terminated by a surface with fixed surface charge. A numerical approach was required to produce a solution to the problem of ion transport under the action of pressure and electrical fields.

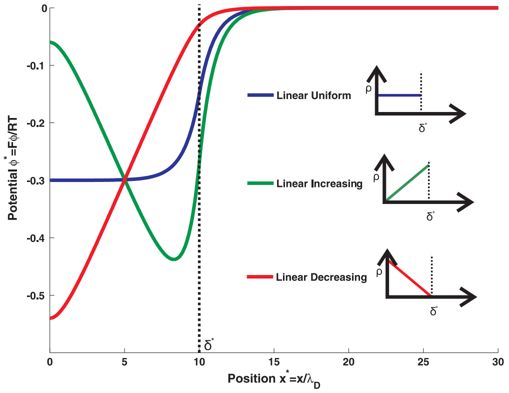

Figure 3.5: Potential profiles for various charge distributions derived from equation (3.25). The film extends a distance $10\lambda_d$ into the domain from the wall ($x^* = 0$). The inset figures (at right) show the various charge distributions, ρ, considered. In all cases, the total charge is conserved across the film of thickness δ^*.

The identical problem was considered by Ohshima and Kondo [93, 97], who additionally show in the limits $\delta/\lambda_d >> 1$ and $\delta/\lambda_o >> 1$ that Onsager reciprocity is satisfied in the system (i.e., $\chi_{12} = \chi_{21}$). In this case, the fixed charge density is distributed uniformly across a distance δ from the wall into the fluid. A closed-form solution is available for the off-diagonal term of the EK coupling matrix:

$$\frac{\chi_{12}}{\mu} = \frac{\chi_{21}}{\mu} = \frac{\lambda^* \phi^*_\delta + \phi^*_D \delta^* \cosh^{1/2}({}^{*}z\phi^*_D)}{\lambda^* + \delta^* \cosh^{1/2}(z^*\phi^*_D)} + \rho^*_f \left(\frac{\delta^*}{\lambda^*}\right)^2 \tag{3.28}$$

Here, the potentials ϕ^*_δ, and ϕ^*_D are uniquely determined by the film charge ρ^*_f; ϕ^*_D is given by equation (3.21), and ϕ^*_δ has been derived in equation (3.22).We introduce a scale for the streaming current term, as suggested by equation (3.10), $\mu \sim \frac{\varepsilon^* \varepsilon_o RT}{\eta F}$; this is equivalent to the electroosmotic or electrophoretic mobility of a wall or particle having a surface potential equal to the thermal voltage. The χ_{12} and χ_{21} terms are a function of the charge density in the film, as well as the parameters λ^* and δ^*.

Extensions and considerations beyond the models of Donath and Voight [92] and Ohshima and Kondo [88, 93, 97] have been made in recent studies. In a pair of papers, Starov and Solomentsev describe the effects of diffusion [94] in the film and consider the interaction between ions in the fluid and the film to develop an apparent electrokinetic potential [95].

Theoretical determinations of surface conductivity have also been considered by Ohshima, et al. [93] and Donath, et al. [92].Ohshima and Kondo [93] describe χ_{22} in terms of the bulk conductivity only, whereas Donath and Voigt [92] describe enhancements of conductivity due to the presence of the film layer (concentration enhancement/depletion as well as electroosmotic effects), although their expression requires knowledge of ϕ^*_δ, which is only known explicitly in specific cases, as discussed by Ohshima and Kondo [93].

The terminating geometry of the adhered film is an important film characteristic, determining both the distribution of fixed charge and the local resistance of the polymer network. Duval [98] and Duval and van Leeuwen [99] pose and examine a distribution of uniform fixed charge that terminates into solution with a linear decay. Their models suppose a film friction that varies proportionately with the fixed charge density profile. Later, a smooth hyperbolic function was used to describe the transition from finite to zero fixed charge [100].

Duval, et al. [98, 99] solve the piecewise-charged film with both linear [98] and nonlinear [99] analyses. In both cases, the parameters δ, λ_o, and the characteristic dimension of the film transition α are essential in the EK description of the film–fluid system. They obtain solutions to the hydrodynamic and electrical profiles in solution, analyze the streaming current produced by an imposed pressure gradient, as well as current produced by a transverse electric field. The piecewise nature of the fixed-charge profile leads to a complicated expressions for the streaming current within the system, we omit this expression here.

The linear Duval, et al. model [98] illustrates the interplay between momentum and potential profile decay from regions of high charge density and low velocity to low charge density and high velocity: films with $\alpha/\lambda_d >> 1$ exhibit *lower* values of streaming potential because of decreases in fluid velocity where a net charge exists — at a flat interface, the decay of electrical potential occurs in the free fluid, whereas a film with a gradual linear decay of charge into solution has simultaneous screening of charge and momentum. For $\alpha/\lambda_d << 1$, the electrical potential dissipates within the region of retarded flow, reducing the net charge convected by the fluid. The linear model presented by Duval and van Leeuwen is restricted to cases where $\delta^* >> 1$, and $\phi_D^* < 1$.

In describing the potential profile and charge transport due to the presence of a soft layer, we remark that many studies do not account for the charge of the bare solid surface when formulating expressions for charge transport. It is only correct to neglect the influence of the solid potential boundary condition when the film is sufficiently thick as compared both to the hydrodynamic penetration length of the film, $1/\lambda_o$, and the Debye length of the fluid. In the case of a $\delta >> 1/\lambda_o$ and λ_d for a film probed with pressure driven flow, charge transport is nearly extinguished near the wall while charge at the outer surface of the membrane is easily convected. If the film is *thin* as compared to $1/\lambda_o$ and λ_d, then the wall potential must be accounted for. Such relations can be derived in the limit of low electrical potentials (Debye-Huckel limit) and numerical simulation is generally required for arbitrary potentials.

Duval used a numerical solution to extend their linear analysis of charged films [99] to the general nonlinear, unrestricted ϕ_D, case with the same geometry. The scaling of the Donnan potential (cf., (3.21)) implies that the nonlinear theory will be applicable at low solution ion concentration, as large concentrations drive the film–solution equilibrium toward low values of interfacial potential difference ($\Delta\phi = \phi_D - \phi(\infty) << 1$). The disparity in streaming potential between the linearized and nonlinear theories is most apparent at low solution concentration and low λ_o/λ_d (cf. Duval [99] figure 7).

In the Duval, et al. [98,99] and subsequently considered models, film hydrodynamics are described with a Brinkman-modified Navier–Stokes equation (3.23). This approach follows Brinkman [96], who proposed a Stokes-like equation to describe the motion of fluid within a dense collection of particles. Debye and Bueche [101] derived a resistance expression applicable to polymer films by assuming the polymer may be described as a string of Stokeslets, with each Stokeslet along the string acting as a resistance center. The Brinkman approach is implemented for flows in porous-media, and descriptions of porous media hydrodynamics are available in the monographs by Scheidegger [102] and Happel and Brenner [103]. As observed by Dukhin, et al., [104] the Brinkman–Debye–Bueche approach is widely used in the description of soft polymer layers. In many cases, the mechanical attributes of the diffuse layer are assumed, assigned, or varied to demonstrate trends in the behavior of the proposed theories [78, 81, 85, 86, 105, 106]. In others, such as Duval, et al. [98, 99], the Debye and Bueche approach [101] is used to correlate the local resistance and local charge of the film, because of the assumption that regions of higher polymer density contain higher charge.

The Debye–Bueche approach leads to a direct expression for the Brinkman friction term. The dimensional resistance is written as [98]:

$$\frac{\lambda^*}{\delta} = \sqrt{\frac{k(x)}{\eta}} = \left(\frac{R^2}{18}\left(3 + \frac{4}{\varphi^*(x) - 3\left(\frac{8}{\varphi^*(x)} - 3\right)^{1/2}}\right)\right)^{-1/2} \tag{3.29}$$

With R the characteristic radius of a spherical polymer segment, and $\varphi(x)$ the volume fraction of polymer in the fluid–film system; for $\varphi^*(x) << 1$, $\lambda^*/\delta \approx 6/R + {\varphi^*}^{1/2}(x)/(3\sqrt{3}R) + O(\varphi^*)\ldots$ Experimental investigations on diffuse charge interfaces (discussion below) typically implement this description for polymer layers with low volume fraction of solids. Duval, et al. [98] cite a limit of $\varphi^*(x) < .6$ for the above expression (and themselves apply it in a dilute limit, $\varphi^*(x) < .05$), although a Stokesian dynamics analysis of the Brinkman equation by Durlofsky and Brady [107] places further limits on this technique, determining that the Brinkman formulation of the system mechanics is applicable only in the limit of dilute solids, $\varphi^*(x) < .05$.

3.3.6 Film and Fluid Conductivity: χ_{22}

With three of the four electrokinetic coupling matrix components already having been discussed, we now turn to χ_{22}. The χ_{11} term describes the impact of the film on the hydraulic resistance of the flow; for systems with $\delta << d/2$, this effect is minimal. The χ_{12} and χ_{21} terms (closed form in specific limits) describe the response of flow and current to lengthwise electrical potential and pressure gradients, respectively; here, the impact of the fixed charge layer depends non-trivially on the charge distribution and density, ion concentration, film thickness, δ^*, and film hydrodynamics, λ^*. The final term χ_{22} relates current to the electric field, E, and is considered presently.

The presence of a surface locally affects the conductivity of a fluid. The standard Bikerman model [71–74] of surface conductivity accounts for the enhancement and depletion of ions in a field-induced convection of counterions and coions produced by a surface charge, as well as the electroosmotic transport of ions produced by actuation of the carrier fluid; both of these phenomena are necessarily actuated by a transverse field gradient E. These same transport processes occur within the soft diffuse-charge layer attached to a rigid surface. Given a precise enough model for these processes, conductance measurements combined with physicochemical measurements of the film and solution provide sufficient information to characterize the electrokinetic potentials of the system. Streaming potential measurements also require the system conductivity, although only the measured value is required to interpret streaming potential data;

analytical expressions are not needed for measurements.

The total conductivity is separated into contributions from the surface (charged film and adjacent layer with net charge) and bulk (no net charge). The conductivity is additive in bulk and surface conductivities:

$$\chi_{22} = \sigma_B + \sigma_s \tag{3.30}$$

It is customary to separate the surface conductivity term into ionic and electroosmotic conductances, along with a length scale, r_h:

$$\sigma_s = \frac{1}{r_h}\left(G_{\mathrm{I}} + G_{\mathrm{EO}}\right) \tag{3.31}$$

For the systems we are examining here, we further decompose each component into parts interior and exterior to the charged layer:

$$G_{\mathrm{I}} = G_{\mathrm{I,i}} + G_{\mathrm{I,o}} \tag{3.32}$$

$$G_{\mathrm{EO}} = G_{\mathrm{EO,i}} + G_{\mathrm{EO,o}} \tag{3.33}$$

Given a film over $0 \leq x \leq \delta$ the ionic component is:

$$G_{\mathrm{I}} = 2F\sum_j \left|z_j^*\right| u_j \int_0^{d/2} \left(c_j(x) - c_{j,\infty}\right) dx \tag{3.34}$$

$$G_{\mathrm{I,i}} = 2F\sum_j \left|z_j^*\right| u_j \int_0^{\delta} \left(c_j(x) - c_{j,\infty}\right) dx \tag{3.35}$$

$$G_{\mathrm{I,o}} = 2F\sum_j \left|z_j^*\right| u_j \int_{\delta}^{d/2} \left(c_j(x) - c_{j,\infty}\right) dx \tag{3.36}$$

here the sum, j, is over all ions in the layer, and u_j denotes the ionic mobility of the j^{th} ion. Similarly for the electroosmotic conductance:

$$G_{\mathrm{EO}} = \frac{2}{E}\int_0^{d/2} u(x)|_{\frac{\partial p}{\partial y}=0}\,\rho_e(x)\,dx \tag{3.37}$$

$$G_{\mathrm{EO,i}} = \frac{2}{E}\int_0^{\delta} u(x)|_{\frac{\partial p}{\partial y}=0}\,\rho_e(x)\,dx \tag{3.38}$$

$$G_{\mathrm{EO,o}} = \frac{2}{E}\int_{\delta}^{d/2} u(x)|_{\frac{\partial p}{\partial y}=0}\,\rho_e(x)\,dx \tag{3.39}$$

Analytical expressions for conductivity are generally available only in systems with thin or thick films with simply specified charge and fluids.

We write a representation for the χ_{22} term, following the work of Dukhin, et al. Several other workers have also presented analytical expressions where available, and have performed numerical analyses when closed-form expressions are unavailable. Donath and Voigt [92] consider the case of a uniform charge distribution producing a uniform potential within the charged layer. Duval, et al. examine surface conductivity in both the linear case [98] with an analytical theory, and the nonlinear case [99] implementing numerical methods for a film with a linear transition from the charged layer to zero charge in solution. Dukhin, et al. [58] relate measurements of surface conductivity to charge and potential characteristics of polyelectrolyte films with a uniform distribution of pH sensitive charged sites.

We describe here the Dukhin, et al. approach for anionic or cationic films that charge as a function of the proton concentration (pH). Supposing an anionic polymer film with a proton dissociation reaction $HA \rightleftharpoons H^+ + A^-$ and the negative logarithm of the acid dissociation constant pK_a, the following charge–pH relation results:

$$\rho^*_f(x) = \frac{\rho^{*\max}_f}{1 + 10^{\mathrm{pK}_a - \mathrm{pH}} e^{-\phi^*(x)}} \tag{3.40}$$

Here, $\rho^{*\max}_f$ is the charge density of acidic groups (with concentration A^-) and is equivalent to $A^-/(2I_c)$ at full dissociation. The fraction of dissociated groups is dependent upon the local pH surrounding the charged site — a potential biases the concentration of hydronium ions, modifying the concentration from the bulk value in solution. This dissociation approach was first discussed by Donath and Voigt [92]. The Donnan potential is calculated as described previously — by combining equation (3.20) with the curvature–free form of the Poisson–Boltzmann equation. For the case of a 1:1 electrolyte, equation (3.40) becomes [58, 108]:

$$\sinh(\phi_D^*) = \frac{-\rho_f^{*\max}}{1 + 10^{\mathrm{pK}_a - \mathrm{pH}} e^{-\phi_D^*}} \tag{3.41}$$

The Donnan potential must necessarily be determined numerically in this form. When coions are excluded within the film, Dukhin, et al. [58, 108] have derived an expression for the Donnan potential:

$$e^{-\phi_D^*} = \frac{10^{\mathrm{pH} - \mathrm{pK}_a}}{2} \left(\sqrt{1 + 8 \left| \rho_f^{*\max} \right| 10^{\mathrm{pK}_a - \mathrm{pH}}} - 1 \right) \tag{3.42}$$

Dukhin, et al. further derives a result analogous to the Ohshima and Okhi relation between the Donnan and surface potentials of a thick film (cf., equation (3.22)):

$$\phi_D^* - \phi_\delta^* + \ln\left(\frac{1 + 10^{\mathrm{pK}_a - \mathrm{pH}} e^{-\phi_D^*}}{1 + 10^{\mathrm{pK}_a - \mathrm{pH}} e^{-\phi_\delta^*}} \right) = \tanh\left(\frac{\phi_D^*}{2} \right) \left(1 + 10^{\mathrm{pK}_a - \mathrm{pH}} e^{-\phi_D^*} \right) \tag{3.43}$$

The surface and Donnan potentials are explicitly related when the film charge is independent of pH, or when the film is fully dissociated. When the film charge is pH dependent and not fully dissociated, equation (3.43) must be solved in a limit of high or low dissociation, where an implicit relationship between ϕ_D^* and ϕ_δ^* has been obtained. For nearly complete dissociation (i.e., high pH):

$$\phi_\delta^* - \phi_D^* = \ln\left(\frac{e^{s^*} + s^* - 1}{s^*} \right) \tag{3.44}$$

For small amounts of dissociation (i.e., acidic groups at low pH):

$$\phi_\delta^* - \phi_D^* = \ln(2 + s^*) \tag{3.45}$$

In both these relationships, $s^{*-1} = 1 + 10^{-\mathrm{pH}\left(1 - \frac{\mathrm{pK}_a}{\mathrm{pH}}\right)} e^{-\phi_D^*}$, which represents the degree of dissociation in the film — for equation (3.44), $s^* \sim 1$ and for equation (3.45) $s^* << 1$.

The surface conductance is then obtained with the assumption that the Donnan potential describes the potential everywhere within the film, which is valid when

$\lambda_\delta/\delta << 1$. The approach is to use equations (3.35) and (3.36) with $c_i(x) = c_{i,\infty}e^{-z_i\phi_D^*}$ in the film and $c_i(x) = c_{i,\infty}e^{-z_i\phi^*(x)}$ in the diffuse layer, where $\phi^*(x)$ solves the Poisson–Boltzmann equation outside the film given the boundary condition ϕ_δ^* at the film edge, and a potential of zero in solution. In both these cases, the solution is known — the integrals vanish inside the film, and outside the film we use the Bikerman expression for the diffuse component side [58]:

$$G_{\mathrm{I,i}} = 2F\sum_j \int_0^\delta \left|z_j^*\right| u_j c_{j,\infty}\left(e^{-z_j^*\phi_D^*} - 1\right) dx = 2\left|z^*\right| F\delta c_\infty\left(u^+\left(e^{-z^*\phi_D^*} - 1\right) + u^-\left(e^{z^*\phi_D^*} - 1\right)\right) \tag{3.46}$$

$$G_{\mathrm{I,o}} = 2F\sum_j \left|z_j^*\right| u_j \int_\delta^{d/2} \left(c_j(x) - c_{j,\infty}\right) dx = 2\left|z^*\right| F\lambda_d c_\infty\left(u^+\left(e^{-z^*\frac{\phi_\delta^*}{2}} - 1\right) + u^-\left(e^{z^*\frac{\phi_\delta^*}{2}} - 1\right)\right) \tag{3.47}$$

Equations (3.46)-(3.47), are written for a $z^* : z^*$ electrolyte. Furthermore, supposing a film excluding coions, the conductance is further simplified, as the migratory conductance within the film depends completely on the counterionic species as [58]:

$$G_{\mathrm{I,i}} = \frac{\sigma_B\delta}{2}e^{-\phi_D^*} \tag{3.48}$$

where $\sigma_B = 2Fc_\infty u^+$ is the bulk conductivity in the same limit of ion exclusion.

Dukhin, et al. [58], following Ohshima [109], examine the relative importance of electroosmotic and migratory components of the surface conductivity, assuming a model for electroosmosis within the film where the electrical body force balances fluid and film induced friction within the diffuse charge layer. Their model is written as:

$$\rho_e E - ku_{EO} = 0 \tag{3.49}$$

where k is, again, the volumetric frictional force constant retarding the convected charge by the polymer film. This limiting form of transport within the film is obtained by examination of the Navier–Stokes–Brinkman equation with zero pressure gradient and nonzero electric field forcing and charge density, $\rho_e E + \eta\nabla^2 u - ku = 0$. Taking the scales $\nabla^{*2} = \delta^2\nabla^2$, $u = u^* \frac{\varepsilon\varepsilon_o\phi_D}{\eta}E$, $\rho_e = \rho_e^* 2FI_c$, $\phi_D = \phi_D^* \frac{RT}{F}$, and assuming a fully-dissociated film with a $1:1$ electrolyte ($\phi_D^* = -\text{arcsinh}(\rho_e^*)$), the nondimensional form is $\left(\frac{\delta}{\lambda_d}\right)^2 \frac{\sinh(\phi_D^*)}{\phi_D^*} - \nabla^{*2}u^* + \lambda^{*2}u^* = 0$. For a thick ($\delta/\lambda_d >> 1$), highly resistive film ($\lambda^* >> 1$), the $\nabla^{*2}u^*$ term is small and the balance is between charge forcing and volumetric film friction.

The limit of the in-line momentum balance leading to equation (3.49) is not unique, but is consistent given the limits in which the momentum balance is applied. Two other velocity scales yield additional balances: $U \sim 2FI_cE\delta^2/\eta$, which is a viscous scaling for velocity, and $U \sim 2FI_cE/k$, which is a Brinkman balance. The viscous balance yields $\rho_e^* + \nabla^{*2}u^* - \lambda^{*2}u^* = 0$. For $\lambda^* >> 1$ this implies a boundary condition contradictory velocity that is additionally independent of charge–potential forcing; neither of these implications is necessarily the case for a resistive film. The Brinkman balance gives $\lambda^{*2}\rho_e^* + \nabla^{*2}u^* - \lambda^{*2}u^* = 0$, which limits to equation (3.49), as expected given the assumed velocity scale. Synthesizing these limits, the Smoluchowski scale is valid for thick films where $\delta >> \lambda_o \sim \lambda_d$., implying that the interface appears as rigid to the bulk flow. The viscous balance is untenable for descriptions of field-forced flow ions within the film, and the Brinkman balance satisfies physical intuition for flow behavior in the film.

Enhanced friction within the diffuse charge layer relegates the electroosmotic component of the surface conductance to a minor role. Extending the analysis introduced previously (equation (3.49)), Dukhin, et al. [58] show that the electroosmotic component of surface conductivity is minimal both in and outside of the film when $\delta >> \lambda_d$, $\delta >> \lambda_\delta$, and $\lambda >> 1$. In a later work, Dukhin, et al. [110] examine effects of diffuse-layer conductance in a film with a variable charge density. In this analysis, the central simplification is a spatially varying interior film potential that matches exactly with the local Donnan potential of the film (derived by the local charge density). Dukhin, et al. [110] require that the characteristic length over which charge density variations occur in the film, λ_e, be large as compared to the characteristic electrical decay length in the charged film:

$$\frac{\lambda_e}{\sqrt{2}\lambda_d} e^{-1/2\phi^*_D} \gtrsim 3 \tag{3.50}$$

For slowly varying charge densities with no coions, Dukhin, et al. [110] discuss procedures to measure the thickness and charge density for fully and partially dissociated films. These approaches require knowledge of the chemistry of the film combined with streaming current measurements at varying states of film dissociation (i.e., pH).

3.3.7 Film Property Variation

Although the discussion in the previous section has presumed that solution properties inside and outside of the fixed-charge layer are identical, we must in general consider that the properties within the fixed charge layer can differ from those in the bulk solution. We have tacitly assumed that the conductivity of the electrolyte acts independently of the volume fraction of the film — that the only effect of the film on the migratory component of the ions in solution lies in the change in local concentration of the ions introduced by fixed charges in the film. Any additional resistance from the space-filling nature of the gel has been neglected in our presentation. Several authors have discussed the effects of diminished conductivity due to the presence of the polymer network [58, 110–113]. The enhanced conductance is related to diffusion, as the two are linked via the mobility of the ions through the Nernst–Einstein equation and Kohlrausch's law [1]. The results discussed here apply to charge carriers small as compared to the microscopic dimensions of the film — typically ions such as Cl^-, Na^+, and the like. Larger molecules, such as proteins or DNA, also feel diminished diffusion, but such theories are not considered here.

Most of the theories, however, exhibit agreement with experiment only at small polymer volume fraction. Masaro and Zhu [114] review many theories for diffusion of species, such as proteins or other polymers, in dilute to concentrated polymer solutions. The first-order correction to the bulk conductivity (or mobility) of ionic species caused by the polymer as presented by Dukhin, et al. [58, 110] is:

$$\frac{\sigma_p}{\sigma_B} = 1 - G^* \varphi^* \tag{3.51}$$

Expressions of this form, in the limit of low concentrations, appear in many theoretical formulations of retarded diffusion (D), electrophoretic (E) and sedimentation (S) measurements. Odijk [115] cites the form of an experimental fitting curve:

$$\frac{E}{E_o} = \frac{D}{D_o} = \frac{S}{S_o} = F^* = e^{K_r a^{\mu^*} c_p^{\nu^*}} \tag{3.52}$$

Where the subscript naught denotes the transport process (diffusion/electrophoresis/sedimentation) of an object with characteristic radius a in free solution; quantities above (E, D, S) represent the same transport processes in a solution with polymer concentration c_p. Here, the constants K_r, μ^*, and ν^* are determined experimentally by a fit of experimental data to the exponential function; several representative values of these parameters are available in Table 1 of Odijk [115], specifically, for the semi-dilute regime. Typical values for ν^* and μ^* are between 0.5 and 1, with a skew toward unity. The small-argument limit of the fitting relation becomes $F^* \sim 1 - K_r a^{\mu^*} c_p^{\nu^*} \sim 1 - G^* \varphi^*$, consistent with the formula used by Dukhin, et al. [58, 110]; G^* is a term of lumped model parameters to stress the scaling of volume fraction.

Several theoretical expressions have the form of equation (3.52), notably a Cukier model accounting for hydrodynamic corrections to the diffusion of Brownian spheres within a polymeric solution [114–116]. In the development of a model for Brownian spheres, Cukier [116] expounds a theory corresponding to a Debye–Bueche type network of entangled polymer. This model describes a collection of Brownian spheres interacting with a series of deformable pearl strings:

$$\frac{D}{D_o} = e^{-\sqrt{\frac{f n_p}{\eta}} R} \sim 1 - G^* \varphi^{*1/2} \tag{3.53}$$

Where the additional variables f and n_p are the monomer friction factor and the number density of polymer segments. Another scaling for the same regime of polymer concentration suggested by de Gennes [115, 117] assumes the form:

$$\frac{D}{D_o} = e^{R/\xi} \sim 1 - G^* \varphi^{*3/4} \tag{3.54}$$

Where $\xi \sim c_p^{-3/4}$ is the correlation distance of the polymer in solution, which represents the length over which the polymers begin to strongly interact. The review by Masaro and Zhu [114] provides a summary of proposed scalings of concentration with the correlation length, and note that despite theoretical and experimental determinations of this value (between .5 and 1); consensus has yet to be reached.

Inhomogeneity in the dielectric constant between the pure fluid and fluid-film phases has been discussed briefly by several researchers [88, 89, 94, 95]. The dielectric constant of water is known to vary in response to strong electric fields [118, 119] ($\frac{d\phi}{dx} \gtrsim 10^9$ [V/m]), although generation of a field large enough is unlikely, and, for the purposes of the model, would only occur in thin regions near the boundary of the film. Finer descriptions of the polymer microstructure would be necessary to discern any impact of local fields on the dielectric constant of water, as is done with polymers for proton exchange in energy applications [120]. In addition to the field strength, the dielectric constant of water is affected by the local concentration of ions. This effect is communicated in the low-concentration limit by the dielectric increment [59, 119] $\frac{d\varepsilon}{dc_i}$, affecting ε to first order in concentration: $\frac{\varepsilon^*(c_1,\ldots,c_n)}{\varepsilon_o} = 1 + \sum_{i=1}^{n} c_i \frac{d\varepsilon^*}{dc_i}$. Here, c_i is the local ion concentration. Investigations of diffuse charge interfaces accounting for the high-field and dielectric increment variation on the dielectric constant have not been found in the literature in the context of electrokinetics.

Changes in bulk mobility (or diffusion) and dielectric constant within the film illustrate uncertainties that may arise when attempting to interpret experimental conductivity data. Other sources of uncertainty within polymer films not captured by the analytical theory include solid-boundary effects in which the potential at the interface between the film and the solid wall differs from the Donnan potential of the film (i.e., $\frac{d\phi}{dx} = 0$), and instead assumes some potential determined by rigid surface and solution chemistry. Similar analytical approaches as discussed previously may be implemented for small wall potential (e.g., via linearized Poisson–Boltzmann equation) and films that exhibit a region of zero curvature, essentially insulating the nonuniform potential regions on either end of the film; this is similar in some respects to the sandwiched membrane description of Ohshima and Ohki [89]. Computational approaches are necessary to determine potentials in systems in which the film is thin compared with the Debye length ($\frac{\delta}{\lambda_d} \lesssim 1$), the Donnan potential of the film is large ($\phi_D^* \gtrsim 1$), or the charge density within the film is nonuniform. Such an approach was taken by Duval [99] to examine a non-uniform diffuse charge interface with a large Donnan potential.

3.4 Experiments

Depending on the theory to be tested and the information desired, a variety of techniques are available to validate soft diffuse-charge interface theory and determine precisely the surface properties of natural and synthetic systems. Many of these techniques were mentioned in the introduction; we focus here on streaming potential and streaming current techniques, along with conductance measurements for these systems. As was discussed in the theory section, an understanding of surface conductance in diffuse charge systems is necessary to move from measurements of streaming current to streaming potential, or to gain information on film properties directly from a conductance measurement when system conductances are unknown. Furthermore, membrane orientation relative to the direction of flow affects measurement outcomes, and must be considered when interpreting experimental data.

We are concerned with surface measurements in which the flow is along the surface of the diffuse charge interface. When combined with the theory outlined previously, these measurements provide information on the Donnan (ϕ_D) and surface (ϕ_δ) potentials of the film. When supplemented by physical and chemical properties of the film (such as film thickness or film charge density), the theories can be tested more rigorously to determine their range of applicability and precision.

Although we have focused in previous sections on film–fluid systems in which the flow direction is perpendicular to the surface normal of the film, many studies have been performed with flow parallel to the surface normal. The parallel technique has a historical pedigree [69], having been used for the determination of electrokinetic potentials of inorganic materials in plug form. This porous plug technique limits to the standard electrokinetic behavior on hard surfaces when the interstices among the packed particles (i.e., the pores of the porous plug) are large relative to λ_d. For polymeric materials, the characteristic flow size in the polymer is poorly defined, and is unlikely to be everywhere large relative to λ_d. Additionally, through-membrane as opposed to over-membrane techniques fail to probe the diffuse layer at the film–fluid interface. Through-membrane techniques do, however, fully probe the inner structure of the membrane (e.g., ϕ_D via conductivity measurements), and may supplement over-membrane measurements if the structure of the membrane is isotropic in both measurement modes.

Through-membrane analysis is well suited to filtration, ion-exchange, or proton conducting membranes [121–126] because the quantity of interest is often the streaming potential coefficient $\Delta V/\Delta P$ rather than a parameter such as ϕ_D or ζ; this distinction is important, as the through-membrane experiments usually result in measurements of a engineering constant only whereas over membrane measurements, when coupled with the theory, can lead to physical material/solution properties.

Streaming current, streaming potential, and conductance measurements must, in general, be taken at multiple solution and film states. In a given electrokinetic experiment, the maximum film charge density, degree of dissociation, film chemistry, and film thickness are generally not known *a priori*. These quantities are required to predict all electrokinetic phenomena. The degree of dissociation and film thickness are properties of solution pH and ionic strength, so electrokinetic determination of film thickness and charge will, in general, require more than two measurements and will typically be done over a range of pH and ionic strength. In some cases, auxiliary measurements, such as film thickness with an ellipsometer, or film charge by potentiometric titration, are performed to further inform the film state. Conductivity measurements provide information on the bulk film state (ϕ_D), and require film dissociation, thickness, and ion mobility information corresponding to each measurement. When these parameters are not measured at each point, a parametric model predicting these values over the experimental range of ionic strength and pH is required.

Several workers have performed conductivity measurements to directly examine charged films. Yezek [127] performed conductivity measurements on sodium-*co*-acrylate gels of varying polymer volume fraction over a range of ionic strength at a pH of 5.8, corresponding to the natural pH of the polymer–solution mixture. In this work, both full- and partial-dissociation models are used to examine the charge density developed in the gel, with the pK$_a$-dependent dissociation model predicting the observed ratio between the bulk and total conductivities. Theoretical predictions of surface conductivity match the experimental data in the limit of high ionic strength. At lower ionic strengths (less than 1mM), the full dissociation model diverges from both the partial dissociation theory and experiment. A similar approach was used in a prior work by Yezek and van Leeuwen [128] where, in addition to conductivity measurements, streaming potential and potentiometric titration measurements were conducted. There, conductivity measurements and potentiometric charge measurements yielded agreeable Donnan potential values over the range of ionic strength tested. Streaming potential measurements, however, failed to predict quantitatively the observed zeta potential. In their streaming potential model, Yezek and van Leeuwen [128] implemented a modified Smoluchowski formula accounting for the additional conductance introduced by the film, but did not account for other transport characteristics in the film. An interesting artifact of both of these studies [127, 128] is the ratio of cell and bulk conductivities at high ionic strength. This artifact of the experimental limits was examined by Yezek [127] and Dukhin [58]; as the ionic strength increases, ϕ_D decreases, $\phi_D \sim q_f/Fc_\infty$, relegating electrokinetic surface conductivity effects to minor roles. The small difference in conductivity is then ascribed to the blocking effects of the polymeric network. This limit of ionic strength can inform experimentalists on the behavior of hindered conductance measurements in polymeric materials. Freudenberg, et al. [129] executed a similar study, performing streaming current, conductance, and ellipsometry studies on crosslinked and uncrosslinked cellulose films. Here, thick-film theory was used to determine ϕ_D within the film from the surface conductivity of the film layer, as determined by the ratio of streaming current and streaming potential measurements, knowing precisely the geometry of the flow cell. The measurements revealed electrokinetic variance in the film between crosslinked and uncrosslinked states, with strong dependence of film conductance on crosslinking state (lower upon crosslinking), and small differences in Donnan potential.

Although the discussed works [127–129] have analyzed the system by assuming a uniformly distributed charge within the film, and a bounding rigid surface having no affect on the film charge distribution or potential, the film–fluid system is not expected to exhibit such uniformity. Duval, et al. [130], for a thermoresponsive thin film, and Yezek, et al. [100], on a previously studied system [100, 128], remove the assumption of a sharp interface between the charged film and the fluid, instead describing the interface with a continuous transition from a uniform charged region to the uncharged bulk fluid. Considering the latter, Yezek, et al. [100] describe a previously studied system [127, 128] with both the Ohshima and Kondo [93] uniform-charge model and a gradual decay model of the interface. There, measurements of streaming current disagree with the Ohshima theory in the low ionic strength region. The best theoretical fit to the data is obtained in regions of high ionic strength — it is in this limit of high ionic strength where the fluid penetration parameter, λ^*, is determined from a fit. The authors reason the inability of the model to match the experimental data over the entire range of ionic strength as an artifact of film rheology; the parameter fit for λ^* does not vary over the range of ionic strength, even as δ is dependent upon the ionic strength of solution [100]. Yezek, et al. further analyzes the data using a continuous transition of charge/polymer volume fraction of the form:

$$\frac{\varphi^*(x)}{\varphi^{*\max}} = \frac{1}{2}\left(1 - \tanh\left(\frac{x-\delta}{\alpha}\right)\right) \tag{3.55}$$

where $\varphi^{*\max}$ is the polymer volume fraction of the bulk gel (also the maximum value) and α is a length scale used to describe the diffuseness of the interface. For a sharp transition, $\alpha \to 0$. The fit of this parameter, α, for the streaming potential data shows a wide scatter over the range of solution concentrations and film densities tested. The parameter does, however, vary inversely with solution salt concentration, suggesting that the layer expands and contracts with changes in ionic strength. The Yezek, et al. [100, 128] studies suggests that $\alpha \rightarrow 0$ at high ionic strength. Thus, for variable property films, the high salt limit provides a subset of experimental space where thickness-independent parameters such as pH-dependent total film charge may be estimated. A drawback in their analysis, however, is the decoupled nature of α and λ^* in the fitted models. In their approach, Yezek, et al. [100] assume a constant λ^* over the entire range of pH and ionic strength, while α is permitted to vary over the same range. Duval, et al. [130] consider hydrodynamic screening with an uncharged temperature-sensitive hydrogel (poly(N-isopropylacrylamide)-*co*-N-(1-phenylethyl) acrylamide) grafted on a Teflon AF surface within an electrokinetic cell. They apply a theory developed in the same work [130] in which flow is permitted within the gel layer and fit streaming current data over a range of pH for films above and below a gel-swelling temperature threshold. Furthermore, the model permits a fixed potential or charge at the solid surface.

The Duval, et al. [130] theory provides a good match to the observed streaming potential data, fitting only the parameters λ_o and α (taken $\rightarrow 0$) for the film over the entire range of pH. As the film is uncharged, there is no need to characterize charge density or dissociation. The potential of the backing Teflon surface, however, was characterized separately, and used as a model input. When varying the ionic strength at fixed pH, Duval, et al. [130] find agreement between the theory and experimental data (except for 15% deviation at low ionic strength), all while using the same value of hydrodynamic penetration within collapsed and expanded films over all values of ionic strength tested (from .01 to 10 mM KCl). This material was later studied with streaming current (and other techniques) by Cordeiro, et al. [131], although the focus there was the polymer film itself and not electrokinetic behavior.

Zimmermann, et al. [132] executed electrokinetic investigations on poly(styrene)–poly(acrylic acid) (PS-PAA, charged) and poly(styrene)–poly(ethylene oxide) (PS-PEO, uncharged) polymer brushes. Here, the authors measure streaming current, streaming potential, and conductivity of the films. Using literature values, the authors calculate the Donnan and surface potentials of the PS-PAA brush at full dissociation and report values of -186 and -161 [mV] (applying the Ohshima and Kondo theory [93]). The authors further implemented a standard Smoluchowski treatment to their streaming current data at high (i.e., fully dissociated) pH and find a value of $\zeta = -60$ [mV], highlighting the inability of the standard theory to capture the potential state of the film. Using the Bikerman surface conductivity formulation, they estimate a 7% contribution of the diffuse layer conductivity to the surface conductivity as a whole. For the uncharged PS–PEO diblock polymer brush, they find a negative surface potential, which they attribute to the polystyrene surface beneath the poly(ethylene oxide) brush layer. In examining this system, they measured the ζ-potential in the presence and absence of the graft poly(ethylene oxide) polymer brush and examined the results using the theory of Cohen Stuart, et al. [81, 82], which assumes a transport-blocking polymer layer.

Understanding the full range of film properties involves deeper analysis than those presented so far — the state of a charged film depends on the pH and ionic strength of solution. In the prior analyses, rheological attributes of the film were assumed invariant upon changes in ionic strength, equivalent to changing the screening of charge within the film. Furthermore, no transition layer was assumed (i.e., $\alpha = 0$), although non-zero values of α are known to play an important role in measurable electrokinetic parameters [98, 99].

Toward resolving the interfacial structure, Zimmermann, et al. [133] and Duval, et al. [134, 135] perform EK measurements on polymer films over a range of pH and ionic strength and relax the constraint of a sharp interface transition. Such an approach has been used previously to analyze human erythrocytes [136]. Zimmermann, et al.

[133] examine poly(N-isopropylacrylamid-*co*-carboxyacrylamid) films with streaming current/potential, conductivity, and ellipsometry measurements. Ellipsometry data was used to determine swelling as a function of pH for each value of salt concentration tested, and an analytical function was fit to these curves to develop an expression for film thickness. This function assumed the form:

$$\frac{\delta(\mathrm{pH}\,)}{\delta_o} = 1 + \frac{\delta_m - \delta_o}{2\delta_o}\left(1 - \tanh\left(\frac{\mathrm{pH}_i^\delta - \mathrm{pH}}{\Delta\mathrm{pH}_i^\delta}\right)\right) \tag{3.56}$$

Here, δ_m and δ_o represent film thickness at greatest and smallest extent, pH_i^δ is the pH at the inflection point of the δ–pH curve, and $\Delta\mathrm{pH}_i^\delta$ is a characteristic width of the transition region at the inflection point. They further describe the diffuseness parameter of the interface (α) with a function having similar form and pH dependence:

$$\alpha = \frac{\alpha_m}{2}\left(1 - \tanh\left(\frac{\mathrm{pH}_i^\alpha - \mathrm{pH}}{\Delta\mathrm{pH}_i^\alpha}\right)\right) \tag{3.57}$$

Thus, the model consists of six fit parameters: one parameter for the film charge density, one parameter for the hydrodynamic resistance of the film, one parameter for the dissociation constant of the charged groups in the film (pK_a), and three parameters to describe the diffuseness of the interface (α_m, pH_i^α, $\Delta\mathrm{pH}_i^\alpha$). A fitting of ($\sim$ 13) pH points for each ionic strength is performed for streaming current coefficients ($\Delta I/\Delta p$) and surface conductivity data. The model fits obtained quantitatively match the relaxation behavior and magnitudes of the data. The authors show sensitivity of their result by displaying the best fit model along with variations in model parameters, which illustrates the necessity of the diffuse interface approach (i.e., non-zero α) to describe an interior extremum in the streaming current. Furthermore, the model recovered very nearly the maximum charge density with the film over three decades of ionic strength considered ($-\rho_f^{\max}/F = 270$, 240, and 240 [mM] for 0.1, 1 and 10 mM of KCl). The approach does require different values of model parameters, however, for fits to streaming current and conductivity data. Values of the acid dissociation constant are higher by nearly one pH unit for conductivity versus streaming potential data. Also, the size of the relaxation in pH (ΔpH_α) varies as a function of ionic strength of the solution. In comparing model fits and parameter values between conductivity and streaming current data, Zimmermann, et al. [133] remark on the measurement differences between the two techniques, specifically, that the pK$_a$ value from streaming current measurements is consistently smaller than the same value inferred from conductivity measurements. In conductivity measurements, the technique is integrative across the entire film, whereas the streaming current measurement probes the film locally and is highly dependent upon the accessible surface layer of the film. This distance is characterized by the hydrodynamic penetration length of the fluid into the film. (The predicted penetration length is between about 1/80th and 1/200th of the measured film thickness.) Hence, the authors argue that the conductivity pK$_a$ represents the bulk value across the entire film, while the streaming current value probes the pK$_a$ of the surface layer. This argument is grounded in the analysis of Dukhin, et al. [58] in which the electroosmotic component (dependent on film friction) is seen to be a small component of the conductivity in the film layer. They further claim that embedded acidic groups exhibit diminished dissociation owing to hydrophobicitiy of the film interior.

Duval, et al. [134] extend the work by Zimmermann, et al. [133] to examine covalently attached anionic poly(acrylic acid) (PAA) and cationic poly(ethylene imine) (PEI) films with similar techniques as before [133]. The authors successfully analyze the PAA and PEI films using the formalism developed previously — the PAA film shares many physical similarities to the previous system. The PEI film, however, possesses many differences that complicates the analysis. Ellipsometric swelling data is qualitatively different from the PAA film as a function of pH; the swelling data does not demonstrate a significant plateau at any extreme of pH. Furthermore, the cationic polymer is polyprotic, with three pK$_a$ values. The complication for the PEI film stems from ambiguity in describing the thickness of the diffuse interface and the rheological parameter for transport within the film, as the rheological parameter is typically estimated in a limit where the transition of the diffuse layer is minimal in size (or absent altogether). Returning to a point mentioned in Zimmermann, et al. [133], Duval, et al. [134] attribute the difference in the conductance and streaming current fits of pK$_a$ values for PEI and PAA films to changes in the chemical environment of the polymer by the plasma immobilization technique used to attach both polymers. The electrostatic model [133, 134] of the interface uses a zero surface charge boundary condition at the solid surface.

We have discussed several experimental results that implemented (or developed) electrokinetic theories to extract physicochemical information on the state of the interface. The discussion is by no means exhaustive, serving mainly to illustrate applications of the theory developed in the previous sections, and regions of the experimental space where measurables of the theory diverge or are otherwise obscured by unknown system processes and parameters. The experiments discussed above, and several others which were not, are summarized in Table 3.1.

3.5 Discussion and Conclusions

We have reviewed theoretical and experimental descriptions of electrokinetics at diffuse charged interfaces. Both theory and experiment reveal the importance of parameter space extrema in the description of these interfaces. In addition to an overview of theoretical and experimental studies, we considered EK coupling matrix formulations of diffuse fixed charge interfaces in specific limits of film thickness and potential.

Many considered theories and experiments rely upon simplifications in the governing physics; absent simplifications, full numerical solutions are often required. Simplifications follow when the Donnan potential $\phi_D^* << 1$, as the Poisson–Boltzmann equa-

Citation	Material type	Measurements Performed†	Remarks
Afonso [137] ⋆	Celgard N30F, Celgard NF-PES-10	SP	High flow rate imposed, ambiguous geometry; Smoluchowski-type ζ calculation
Ariza, et al. [138] ⋆	commercial polysulfone membrane	C, SP	Smoluchowski type theory for measuring ζ, high surface conductivity
Fievet, et al. [139] ⋆	Sandwiched ceramic membranes	C, SP	Demonstrates importance of excess cell conductivity
Cohen Stuart, et al. [82]	poly(vinyl pyrrolidone) on glass	SP	Estimate hydrodynamic thickness of PVP film using a streaming potential measurement
Cordeiro, et al. [131]	Poly(N-isopropylacrylamide-co-N-(1-phenylethyl) acrylamide)	AFM, CA, E, SC	Measure ζ; film exhibits temperature-dependent thickness; variable pH; films has no ionizable groups; attribute observed streaming current to adsorption of hydronium and hydroxide at underlying Teflon surface and subsequent screening of this charge by the polymer film
Duval, et al. [130]	poly(N-isopropylacrylamide)-co-N-(1-phenylethyl) acrylamide	SC	No charge units in hydrogel; show agreement with developed theory for rigid charged layer beneath the hydrogel and solution layers
Duval, et al. [134]	poly(ethylene imine), poly(acrylic acid)	C, E, SC	Extension of Zimmermann, et al. [133] analysis. Poly(ethylene imine) film description is difficult due to swelling characteristics
Duval, et al. [135]	Multilayer: poly(ethylene imine), poly(acrylic acid), bilayer lipid membrane	E, SC	Theory and experiments for non-homogeneous charge layer
Freudenberg, et al. [129]	Cellulose film (native and crosslinked)	C, E, SC, SP	ϕ_D similar for crosslinked and uncrosslinked films, streaming current, swelling, and conductivity measurements differ
Voigt, et al. [140]	Several polymers	SC, SP	Comparison of ζ from streaming current and streaming potential measurements
Yezek, et al. [128]	Polyacrylamide gel	C, PT, SP	Measure ζ and ϕ_D as a function of ionic strength (NaCl), fluid convection within film neglected
Yezek, et al. [100]	Polyacrylamide-co-sodium acrylate	C, SP	Implement non-uniform film charge model to describe experimental data
Yezek, et al. [127]	Polyacrylamide-co-sodium acrylate	C	Extraction of conductance hindrance coefficient, implement of Dukhin, et al. [58, 108] conductivity theory
Zimmermann, et al. [132]	poly(styrene)–poly(acrylic acid); poly(styrene)–poly(ethylene oxide)	C, SC, SP	Charged and uncharged diblock polymer brushes, estimate ϕ_D using charge dissociation model, ϕ_δ estimated with Ohshima theory, ζ based on Smoluchowski theory with Bikerman-type surface conductance
Zimmermann, et al. [133]	Poly(N-isopropylacrylamid-co-carboxyacrylamid)	C, E, SC, SP	Apply diffuse interface model with transition layer, multi-parameter fit describes experimental data

Table 3.1: Collected electrokinetic characterization experiments with flows orthogonal, and parallel (⋆) to the surface normal of the diffuse interface. Here, materials with homogeneous microstructure on the scale of the electrostatic screening length are stressed; we do not include macro-porous membranes. † C – system/surface conductivity, CA – contact angle, E – ellipsometric film thickness, PT – potentiometric titration, SC – streaming current, SP – streaming potential.

tion can be linearized. Low Donnan potentials typically occur when the solution ionic strength is high. Other simplifications occur when the film is thick relative to the characteristic decay length of the electrical potential. Relative film thickness is influential for conductance calculations in the fixed charge layer, as curvature vanishes and the potential is assumed to be uniform in space. For films with electrical potential greater than the thermal voltage, or thickness not large relative to the Debye length, computational approaches must be implemented to analyze the system. Computational approaches are also necessary for systems with pH-dependent charge densities. These systems do simplify in limits of high and low dissociation, but the simplified expressions remain implicit in ϕ_D^*.

Future studies should account, in a more thorough way, for the influence of the electrokinetic boundary condition present at the plane of film attachment. The electrokinetic boundary value at a rigid surface is likely to be important, but is typically assumed to satisfy $\frac{d\phi}{dx}\big|_{\text{wall}} = 0$ (the exception is examined theoretically by Duval, et al. [130].) In general, the ζ-potential of rigid materials responds in non-trivial ways to pH and ionic strength. Thus, the model–fitting method will fail unless the rigid material is well-characterized prior to experimentation with the soft interface (this amounts to the introduction of another free parameter for each combination of ionic strength and pH).

In a majority of the models presented, fluid properties within and outside the film are presumed identical — this assumption is called into question by the near constant potential within the thick film ($\delta^* >> 1$), opportunity for large charge and ion concentration, and the effects of the polymer network itself. Furthermore, the thickness of the film suggests that, in contrast to a thin–EDL on a rigid surface, any inhomogeneity between charged and neutral regions can persist over a great extent (many times λ_d) magnifying the scope of inhomogeneous fluid property effects. Two cited exceptions to this simplification were the hindered mobilities of ionic species, and the dielectric constant of the working fluid. Inhomogeneity in the dielectric constant has been considered in an *ad hoc* manner by some researchers [88, 89, 94, 95], with a range of dielectric constants selected to illustrate possible changes in system potential. These effects, the origin of which are discussed earlier, would be well treated by numerical methods owing to the complexity they introduce into the functional form of the governing equations.

Effects due to physical adsorption of electrolyte or other charge carriers (e.g., hydronium, hydroxide) should also be considered in film layer charge models, especially for films with low dissociable charge densities. These and other field and concentration dependent properties introduce complications primarily through the functional form of the governing equation, and would be likely analyzed numerically. Further, the theories described often make use of a specific solution limit (high/low salt, high/low pH) to extract physical film parameters [127, 133, 134]. This approach is sufficient for cases in which film characteristics reach limiting values at experimental extremum; we communicated experimental evidence where this was not the case, however, and model values for the rheological behavior of the film could not be determined precisely [134]. There is area for improvement, then, in both theory and experiment for physical systems that do not as clearly exhibit constant or slowly varying properties in areas of high and low pH.

3.6 Acknowledgements

ACB acknowledges support from the NSF Graduate Research Fellowship Program.

CHAPTER 4

FORCE AND FLUX RELATIONS FOR FLOWS OF IONIC SOLUTIONS BETWEEN PARALLEL PLATES WITH POROUS AND CHARGED LAYERS

4.1 Abstract

We derive coefficients of the electrokinetic coupling matrix (χ_{11}, χ_{12}, and χ_{21}) for the flow of an ionic solution through a parallel-plate geometry having porous and charged layers grafted onto a solid surface with a known potential, and demonstrate Onsager reciprocity for the cross terms (i.e., $\chi_{12} = \chi_{21}$). Our results enable the prediction of system outputs in the solid–porous–fluid system from parameters that are either known, or may be measured and inferred. These electrokinetic coupling coefficients are in terms of the potential, ϕ, and fixed charge, ρ_f, only, removing dependence on field gradients and fluid velocity. Additionally, we present simplified expressions of these coupling coefficients in limiting regions of the parameter space. Away from these limits, we present numerical results demonstrating the facility of our functional form for facile numerical approximation, and report the utility and accuracy of our analytical approximations.

4.2 Introduction

Porous interfaces are ubiquitous in both natural and industrial systems. In nature, vital and non-vital porous structures exist: organic forms are found within mammalian cells and tissues [14], as biological membranes [141] and cartilage [142, 143]. Inorganic

---

A manuscript based on the content of this chapter has been accepted for publication in the journal *Physical Review E*. This is the pre-publication version of the following article: “Force and Flux Relations for Flows of Ionic Solutions between Parallel Plates with Porous and Charged Layers”.

porous structures are found in natural geophysical systems like packed silicates [144], and in synthetic components like packed-bed reactors and polymer membranes [145].

A mechanistic understanding of ion transport within membrane and soft-layer systems is required to engineer and optimize device performance. Describing transport within the porous membrane layer requires an understanding of the interplay between chemical and physical attributes of the porous layer. Fuel cells [122], filtration assemblies [121], and electrophoretic [49, 146] and chromatography systems with coated surfaces [147] use membranes or membrane-like layers to some extent. Contemporary workers use anionic and cationic exchange membranes in through-flow configuration for the purification of brackish solutions [16], where transport across exchange membranes is essential to solution treatment [121].

We consider transport along a porous and charged layer bounded by a solid wall and pure fluid, as shown in figure 4.1. In this figure, the plates are separated by dimension $2h$ and the channel cross-section is given by the area $A = 2wh$, with dimension w defining the channel width. The porous layer maintains an immobile charge owing to the presence of active chemical groups through its wetted volume, and Ohmic conduction results from the electrophoretic motion of cations and anions in the fluid subsumed in the porous layer. Furthermore, the porous layer exhibits a Brinkman-type hydraulic resistivity.

Gradients in pressure and electrical potential combined with a distribution of net free charge give rise to electrokinetic phenomena such as electrophoresis, electroosmosis, streaming potential, streaming current, electrical conductivity, and electroviscosity. Gravitational effects may be included in the pressure [148], i.e., the so-called modified pressure [149] but we do not consider gravitational effects here as they are complicated by the porosity of the medium. These phenomena are linear and additive, and are

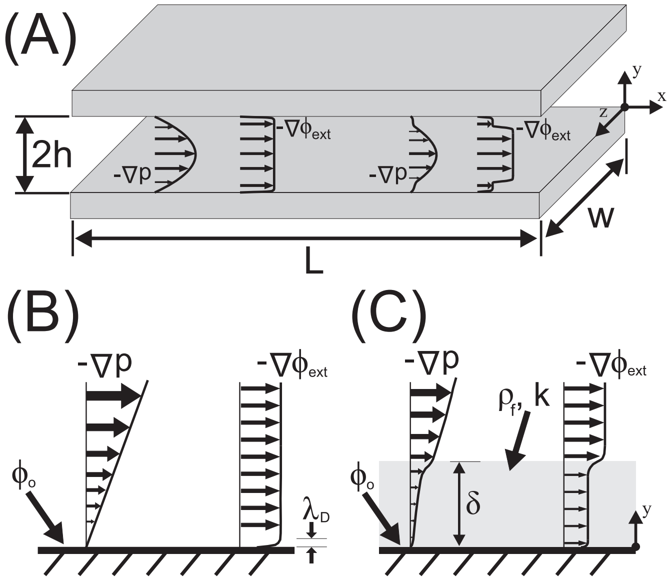

Figure 4.1: Diagrammatic representation of the system under consideration. (A): Geometric definition of the parallel-plate system studied; plates of width w and length L are separated by a distance $2h$. Included are shapes of pressure-driven and electrically forced flows for (left) a channel with rigid surfaces and (right) a channel with a porous lining. In (B) and (C), magnified diagrams at the surface detail distributions of velocity and potential for a bare, rigid surface (B) and a surface with a porous layer of thickness δ (C).

succinctly communicated by the electrokinetic coupling matrix (EKCM). The EKCM describes flux densities of volume and charge through a surface of area A and normal $\vec{n}$ in response to linear gradients in pressure (∇p) and electrical potential ($\nabla\phi_{\text{ext}}$).

$$\begin{bmatrix} Q/A \\ I/A \end{bmatrix} = \begin{bmatrix} \chi_{11} & \chi_{12} \\ \chi_{21} & \chi_{22} \end{bmatrix} \begin{bmatrix} -\langle\nabla p\rangle \\ -\langle\nabla\phi_{\text{ext}}\rangle \end{bmatrix} \tag{4.1}$$

The brackets surrounding gradients of pressure and electrical potential in equation (4.1) denote the averaged values of the normal component of vector fluxes taken over the channel cross section: $\langle\nabla\phi_{\text{ext}}\rangle = \frac{1}{A}\int_S \nabla\phi_{\text{ext}}\cdot\vec{n}\,dA$ and $\langle\nabla p\rangle = \frac{1}{A}\int_S \nabla p\cdot\vec{n}\,dA$. For the remaining terms in equation (4.1), χ_{11} is the hydraulic conductivity term relating the area-averaged (using the channel cross-section) velocity and the pressure gradient; similarly, χ_{12} is the hydraulic conductivity term describing the response to a gradient in electrical potential. The electrical conductivity (both Ohmic and electroosmotic) is given by χ_{22}, and the current produced by a pressure gradient is related through χ_{21}. Exact forms of these coefficients are determined from the geometry and boundary conditions of the system under consideration.

For linear and microscopically reversible processes, the electrokinetic coupling matrix is symmetric. This is a statement of Onsager reciprocity [150–153]; holding so long as, for a near-equilibrium system, the forces and the fluxes relate linearly, and the system remains symmetric upon time reversal. These requirements for Onsager reciprocity generally hold; broken only, for example, when the system considered is placed under the action of a magnetic field or subject to a Coriolis force. Systems so exposed will not reverse in time and will not exhibit reciprocity in the coefficients describing forces and fluxes [153].

Statements of Onsager reciprocity applied to electrokinetic systems are known in the interface and microfluidic literature. Similar to thermoelectric phenomena, reciprocal relationships were known long before the phenomena were codified theoretically. In 1892 Saxén demonstrated the equivalence between electroosmosis and streaming potential [154], showing $\chi_{12} = \chi_{21}$ experimentally. This work was followed by contributions [155, 156] examining the equivalence between porous diaphragms and networks of capillaries. More contemporary work by Gross and Osterle [76] discusses coupling relationships in capillary flow, contributing general integral expressions for pressure, electrical, and chemical potential gradients driving fluxes of volume, current, and mass; with attention to electrodialysis and energy conversion. Extending these ideas to arbitrarily shaped ducts, Mortensen, et al. [157] develop expressions for the EKCM coefficients using a Hilbert space, also showing Onsager reciprocity for the cross terms. The early history of equivalence between electroosmosis and streaming potential is discussed in a review by Wall [158].

More recent investigations have moved beyond pure fluids bounded by rigid, non-reacting surfaces. Brunet and Ajdari [159] have developed a general derivation proving the symmetry property of a coupling matrix for systems with arbitrary microstructure. In their formulation, the system need only obey the no-slip boundary condition, exhibit Newtonian Stokes flow, and obey the Poisson equation for potential in response to a spatial free charge density. They simplify their general results for a periodic isotropic medium and show that the Onsager reciprocal relation holds. Brunet and Adjardi do not, however, present functions for the coupling coefficients. In fact, their proof omits definition of electrical boundary conditions (charge and/or potential) on the system walls. Berli and Olivares [160] develop expressions for electrokinetic coupling coefficients in systems where the working fluid is non-Newtonian. They report symmetry in the electrokinetic coupling matrix, although their model prohibits non-linear viscosity in regions of non-zero electrical potential; the assertion being that the depletion zone of a polymer additive causing the nonlinear flow effects is thicker than the region of net charge. Also, their system ceases to be strictly linear for non-Newtonian fluids, as coefficient χ_{11} will contain a pressure dependence. van Leeuwen and Duval [161] describe effects of a conductive substrate, where faradaic reactions are permitted, on the form of Onsager relations.

Previous works have considered coupling coefficients in channels with charged and porous layers. Donath and Voigt [92] present a 1D formulation of the system we consider, although their approach assumes a low-potential limit and incorrectly predicts a divergence in streaming current as the Debye length of the solvent approaches the characteristic penetration length of the free fluid into the porous region (in our notation, $\lambda_D \rightarrow \lambda_o$). A similar approach was taken by Ohshima and Kondo [93], deriving approximate forms for χ_{12} and χ_{21} (confirming Onsager reciprocity) for a channel many times larger than both the fluid Debye length and the penetration depth of fluid into the porous region. Keh and Liu [162] derive exact analytical expressions for coupling coefficients for the linearized Poisson–Boltzmann equation in a cylindrical geometry. A pair of articles, by Duval and van Leeuwen [98] and Duval [99], develop electrokinetic theories for porous regions of nonuniform charge and resistance, relaxing an assumption of previous workers; results are presented for the small-potential (linearized) regime [98], as well as the nonlinear regime [99]. In a recent publication, we have reviewed electrokinetics of soft and charged layers from both theoretical and experimental viewpoints [163].

In this work, we develop general, closed-form integral expressions describing electrokinetic transport over and within porous layers of uniform resistance and arbitrary fixed charge density; these integral expressions require only physicochemical porous layer properties such as porous layer resistance, porous layer thickness, the distribution of the fixed charge, and the electrical potential in the system. Our results do not require knowledge of the potential gradient or velocity within the channel (other than velocity boundary conditions). Often, these required quantities may be approximated. Generally, the values of potential and charge can be reliably computed. In contrast to previously published results, our expression for the cross-coupling term applies for arbitrary values of the fixed charge density, and geometric and resistive parameters, without regard to the magnitude of the electrical potential in the system. This general integral formulation also facilitates our derivation of simple limiting forms that apply accurately across a wide range of parameter space.

The manuscript is organized as follows: in section 2, we describe fluid physics in porous layers. In section 3, we describe generating formulas for all electrokinetic phenomena, incorporating domain inhomogeneities introduced in the previous section. Coupling formulas are then applied to systems with a hard surface in section 4. These results are contrasted with (and used to motivate) the porous layer coupling coefficients we derive and present in section 5. In section 6, we derive limiting cases of porous layer coefficients, and in section 7, we present numerical representations of coefficients for cases not described by simplifying limits.

4.3 Fluid Physics in Porous Layers

We consider momentum transport at low Reynolds number, governed by the Stokes equation of motion. Fluid forcing in the Stokes equations is linear and additive: gradients in pressure or external electrical potential actuate the fluid independently, and solutions for flows driven by gradients of pressure or electric fields may be superimposed. In the pure-fluid region:

$$0 = \eta \nabla^2 \mathbf{u} - \nabla p - \rho_e \nabla \phi_{\text{ext}} \tag{4.2}$$

Here, η is the fluid viscosity, $\mathbf{u}$ is the velocity field, and ρ_e is the free charge density. Equation 4.2 holds outside of the porous layer. Within the porous layer, we add a term linear in the velocity which accounts for the added resistance of the porous layer beyond the unbounded fluid:

$$0 = \eta \nabla^2 \mathbf{u} - k\mathbf{u} - \nabla p - \rho_e \nabla \phi_{\text{ext}} \tag{4.3}$$

The constant, k, describes the resistivity of the porous region. In both equations (4.2) and (4.3), gradients in pressure and external electrical potential are equivalent in the porous layer and pure fluid.

Multiple schemes have been proposed to connect porous layer and pure fluid flows; we use the Brinkman approach because of the ability to obey both boundary conditions in the porous layer, as well as the ubiquity of the Brinkman approach for the type of problem that we consider here. The Brinkman approach to the momentum distribution is widely used for planar (or nearly planar) porous layers between a solid surface and pure fluid [92, 94, 95, 98–100, 130, 133, 134, 162], and has been reviewed in this context by Dukhin, et al. [104]. Although we work with the Brinkman-modified Stokes equation to connect the porous-layer and pure-fluid flows, coupling between free-fluid and porous layer flows may also be done using the Beavers-Joseph boundary condition [164]; both approaches are approximate and exhibit deficiencies in predicting the velocity profile at the interface between the porous and pure-fluid phases, and have been the subject of much discussion [148, 165–169]. Although the Beavers-Joseph condition matches the velocity at the porous layer–fluid interface, it assumes a Darcian flow inside the porous layer and does not explicitly obey the no-slip condition at the solid wall–porous medium boundary. Although this may be unimportant for macroscale systems (porous layer thickness $\ll \sqrt{\frac{\eta}{k}}$) with low porosity, we consider systems with porous layers that may be thin relative to $\sqrt{\frac{\eta}{k}}$, requiring that the no-slip condition at the solid boundary be obeyed.

Equations (4.2) and (4.3) are typically solved in response to a single momentum source. We indicate forcing with superscripts: $\mathbf{u}^{(p)}$ for pressure-driven flow and $\mathbf{u}^{(e)}$ for flows driven by electric fields. Furthermore, we label the velocity in the porous layer with subscript 1, i.e., $\mathbf{u}_1^{(p)}$, and in the fluid with subscript 2, as $\mathbf{u}_2^{(p)}$.

Momentum distributions in the porous layer and in the pure fluid connect via boundary conditions. For the one-dimensional geometry we consider (figure 4.1), a no-slip condition is applied at the fluid–solid interface, and a symmetry condition is imposed at the channel centerline.The boundary conditions at the interface between the porous and pure-fluid regions require continuity of velocity and stress:

$$\begin{aligned} u_1(0) &= 0 & u_1(\delta) &= u_2(\delta) \\ \left.\frac{du_1}{dy}\right|_{y=\delta} &= \left.\frac{du_2}{dy}\right|_{y=\delta} & \left.\frac{du_2}{dy}\right|_{y=h} &= 0 \end{aligned} \tag{4.4}$$

Here, the Brinkman resistance term $-ku$ is absent, as the boundary conditions are dominated by the tangential stresses; the Brinkman resistance acts on a fluid volume and is lost in the limiting process.

The free charge distribution is determined from the Poisson equation with a fixed-charge that is zero in the pure fluid and nonzero in the porous layer. In general:

$$\nabla\left(-\varepsilon\varepsilon_o\nabla\phi\right) = \rho_e(\mathbf{x}) + \rho_f(\mathbf{x}) \tag{4.5}$$

Here, the distribution of fixed charge is given by $\rho_f(\mathbf{x})$, and may exhibit a dependence on the potential. The electrical potential distribution is determined by the form of the free charge density, ρ_e, the distribution of fixed charge in the domain, ρ_f, and boundary conditions. The dielectric constant of the solvent is given by ε, and ε_o is the vacuum permittivity. The pure-fluid phase cannot support a fixed charge distribution, so $\rho_f = 0$ in this region of the domain:

$$\nabla\left(-\varepsilon\varepsilon_o\nabla\phi_2\right) = \rho_e(\mathbf{x}) \tag{4.6}$$

Again, we use the subscript 2 to indicate quantities in the pure-fluid region of the domain. The porous layer is the only region with non-zero fixed charge density. Fixed charges reside throughout the wetted volume of the porous material. In the porous region:

$$\nabla\left(-\varepsilon\varepsilon_o\nabla\phi_1\right) = \rho_e(\mathbf{x}) + \rho_f(\mathbf{x}) \tag{4.7}$$

The potential distributions in equations (4.6) and (4.7) also couple through boundary conditions. We prescribe a fixed potential on the hard boundary at $y = 0$, and zero potential slope at the channel centerline. At the interface between the fluid and porous layer, continuity in potential and electric flux density, for uniform permittivity, implies matching potential and potential gradient:

$$\begin{aligned} &\phi_1(0) = \phi_o && \phi_1(\delta) = \phi_2(\delta) \\ &\left.\frac{d\phi_1}{dy}\right|_{y=\delta} = \left.\frac{d\phi_1}{dy}\right|_{y=\delta} && \left.\frac{d\phi_2}{dy}\right|_{y=h} = 0 \end{aligned} \tag{4.8}$$

Equality between dielectric constants in the pure-fluid and porous regions is implicitly assumed in the field gradient relation. This constraint was relaxed by Ohshima and Ohki [89] in their analysis of potential profiles across charged biological membranes.

The free-charge density depends upon the local concentration of ions. Typically, a mean-field approximation is used to relate the free-charge density to the potential. By further considering the free ions as point charges, we arrive at the Boltzmann relation for the free-charge density [59]:

$$\rho_e(\mathbf{x}) = F \sum_i z_i c_{i,\infty} e^{-\frac{z_i F \phi(\mathbf{x})}{RT}} \tag{4.9}$$

Here, R is the ideal gas constant, T the absolute temperature, F is Faraday's constant, and z_i and $c_{i,\infty}$ are the valence and bulk concentration of the i^{th} ionic component.

The potential within a porous layer at a point where free and fixed charges exactly balance is known as the Donnan potential [70], and implies that the potential is curvature-free. The functional form connecting the Donnan potential to the fixed-charge distribution depends upon the form of the free- and fixed-charge densities. For a fixed charge density that is independent of the local potential, and a free charge determined by (4.9):

$$0 = F \sum_j z_j c_{j,\infty} e^{-\frac{z_j F \phi_D}{RT}} + \rho_f(\mathbf{x}) \tag{4.10}$$

For a $z : z$ electrolyte, equation (4.10) has the form $\phi_D = \frac{RT}{zF} \text{arcsinh}\left(\frac{\rho_f(\mathbf{x})}{2zFc_\infty}\right)$, where ϕ_D denotes the Donnan potential in the porous layer.

4.4 Generating integral formulas for EKCM Coefficients

All electrokinetic coupling coefficients may be expressed in a general integral form. Typically, the EKCM coefficients are calculated with direct integration in only the simplest systems, but these forms are the starting point for expressions that we derive in later sections. We write an integral expression for χ_{11} for a pressure-driven flow that proceeds through a surface S with unit normal $\vec{n}$ and corresponding flow field $\mathbf{u}^{(p)}(\mathbf{x})$:

$$\chi_{11} = \frac{1}{\int_S -\nabla p \cdot \vec{n}\, dA} \int_S \mathbf{u}^{(p)}(\mathbf{x}) \cdot \vec{n}\, dA \tag{4.11}$$

Terms χ_{12} and χ_{21} relate the area-averaged volume and current fluxes to the application of external electrical potential and pressure gradients, respectively. The general forms of these expressions are given by:

$$\chi_{12} = \frac{1}{\int_S -\nabla \phi_{\text{ext}} \cdot \vec{n}\, dA} \int_S \mathbf{u}^{(e)}(\mathbf{x}) \cdot \vec{n}\, dA \tag{4.12}$$

$$\chi_{21} = \frac{1}{\int_S -\nabla p \cdot \vec{n}\, dA} \int_S \rho_e(\mathbf{x}) \mathbf{u}^{(p)}(\mathbf{x}) \cdot \vec{n}\, dA \tag{4.13}$$

The symbols $\rho_e(\mathbf{x})$, $\mathbf{u}^{(e)}(\mathbf{x})$, and $-\nabla\phi_{\text{ext}}$, denote the free-charge density, electric-field-driven flow, and the electric field. In the above expressions, gradients in pressure and electrical potential are assumed uniform across the surface S.

The final term, χ_{22}, relates the area-averaged current to the applied electrical potential gradient. We refer to this as the conductivity term. In general form, we write this as:

$$\chi_{22} = \sigma_{\text{Ohmic}} + \sigma^{(\text{ex})}_{\text{Ohmic}} + \sigma^{(\text{ex})}_{\text{EO}} \tag{4.14}$$

We have separated the conductivity term into three components. The bulk conductivity, σ_{Ohmic}, represents the contribution from Ohmic conduction. Contributions to Ohmic conductivity from boundary effects are included in $\sigma^{(\text{ex})}_{\text{Ohmic}}$. We have used the superscript (ex) to indicate excess or surface contributions to the system conductivity. Finally, the electroosmotic contribution, $\sigma_{\mathrm{EO}}^{(\mathrm{ex})}$, represents the contribution by electroosmotic transport of current when a field is applied. In integral form:

$$\sigma_{\mathrm{Ohmic}} = \frac{1}{\int_S \nabla\phi_{\mathrm{ext}}\cdot\vec{n}\,dA} F \sum_i |z_i|\,\mu_i \int_S c_{i,\infty} \nabla\phi_{\mathrm{ext}} \cdot \vec{n}\,dA \tag{4.15}$$

$$\sigma_{\mathrm{Ohmic}}^{(\mathrm{ex})} = \frac{1}{\int_S \nabla\phi_{\mathrm{ext}}\cdot\vec{n}\,dA} F \sum_i |z_i|\,\mu_i \int_S \left(c_i(\mathbf{x}) - c_{i,\infty}\right) \nabla\phi_{\mathrm{ext}} \cdot \vec{n}\,dA \tag{4.16}$$

$$\sigma_{\mathrm{EO}}^{(\mathrm{ex})} = \frac{1}{-\int_S \nabla\phi_{\mathrm{ext}}\cdot\vec{n}\,dA} \int_S \rho_e(\mathbf{x})\mathbf{u}^{(e)}(\mathbf{x}) \cdot \vec{n}\,dA \tag{4.17}$$

The symbol μ_i represents the mobility of the i^{th} ion. In most microfluidic systems, the excess conductivities are small when the double layers are thin relative to the system size.

4.5 Coupling terms for systems with rigid interfaces

We present coupling terms for a parallel-plate system with bare rigid walls as a prelude to the porous layer geometry. These terms are dependent on the potential distribution and do not require explicit details of the flow as inputs, beyond boundary conditions and the forces applied to the fluid (pressure or electrical potential). Furthermore, simplifications and physical insight proceed quickly from the integral forms of the coupling terms. Here, the flow u proceeds along the x direction and varies across the half domain $0 \leq y \leq h$. At the solid boundary, we fix the potential, ϕ_o, and enforce a no-slip boundary condition. At the channel centerline, both velocity and potential obey a homogeneous Neumann condition. Equations (4.2) and (4.6) reduce from partial to ordinary differential equations:

$$\frac{dp}{dx} = \eta \frac{d^2u}{dy^2} \tag{4.18}$$

$$-\varepsilon\varepsilon_o \frac{d^2\phi}{dy^2} = \rho_e(y) \tag{4.19}$$

The hydraulic resistance term, χ_{11}, is determined from equations 4.18 and 4.11 along with no-slip boundary conditions:

$$\chi_{11}^{\text{(hard)}} = \frac{h^2}{3\eta} \tag{4.20}$$

The current density in response to a pressure gradient is computed from:

$$\chi_{21}^{\text{(hard)}} = \frac{1}{-\langle \nabla p \rangle A} \int_0^{2h} \int_0^{w} u^{(p)} \rho_e(y)\, dz dy \tag{4.21}$$

Here $0 \leq z \leq w$ is the channel width (into the page, in figure 4.1). We assume that the velocity, potential, and charge profiles are uniform in this direction. With $A = 2hw$,

$$\chi_{21}^{\text{(hard)}} = \frac{1}{-h\langle \nabla p \rangle} \int_0^{h} u \left(-\varepsilon\varepsilon_o \frac{d^2\phi}{dy^2} \right) dy \tag{4.22}$$

After integration by parts (twice), enforcing boundary conditions $u(0) = 0$ (no slip), $\phi(0) = \phi_o$, $\left.\frac{du}{dy}\right|_{y=h} = \left.\frac{d\phi}{dy}\right|_{y=h} = 0$ (symmetry), and finding the velocity gradient at the wall:

$$\chi_{21}^{\text{(hard)}} = -\frac{\varepsilon\varepsilon_o \phi_o}{\eta} \left[1 - \frac{1}{h} \int_0^{h} \frac{\phi(y)}{\phi_o}\, dy \right] \tag{4.23}$$

To find the flux density of volume in response to an applied electric field, absent pressure, we compute:

$$\chi_{12}^{\text{(hard)}} = \frac{2\int_0^h u^{(e)}\, dy}{-2wh\langle \nabla \phi_{\text{ext}} \rangle} = -\frac{1}{h\langle \nabla \phi_{\text{ext}} \rangle} \int_0^{h} u^{(e)}\, dy \tag{4.24}$$

The solution is most easily obtained by solving directly for the field $\mathbf{u}^{(e)}$ from the Stokes equations with zero pressure forcing, a no-slip boundary, and symmetrical velocity profiles about the centerline:

$$\chi_{12}^{\text{(hard)}} = -\frac{1}{h\langle \nabla \phi_{\text{ext}} \rangle} \int_0^{h} \frac{\varepsilon\varepsilon_o}{\eta} \langle \nabla \phi_{\text{ext}} \rangle \left(\phi_o - \phi(y) \right) dy \tag{4.25}$$

Or,

$$\chi_{12}^{\text{(hard)}} = -\frac{\varepsilon\varepsilon_o}{\eta} \phi_o \left[1 - \frac{1}{h} \int_0^{h} \frac{\phi}{\phi_o}\, dy \right] \tag{4.26}$$

The conductivity term is more complicated, owing to the convolution of the charge density and electroosmotic flow; both terms have a direct connection with the electrical potential. Using earlier results, we express the conductivity for our 1-D flow as:

$$\chi_{22}^{(\text{hard})} = F \sum_i |z_i| \mu_i \frac{1}{h} \int_0^h c_i(y)\, dy - \frac{\int_0^h \rho_e(y) u^{(e)}(y)\, dy}{h \langle \nabla \phi_{\text{ext}} \rangle} \tag{4.27}$$

The excess conductivity ($\sigma_{\text{EO}}^{(\text{ex})} + \sigma_{\text{Ohmic}}^{(\text{ex})}$) has been determined by Bikerman for $h \gg \lambda_D$ and a symmetric electrolyte [73], which we reproduce here under the additional assumption of balanced mobilities for the electrolyte pair:

$$\begin{aligned} \chi_{22}^{(\text{hard})} &= \sigma_{\text{Ohmic}} + \frac{\lambda_D}{h} \frac{2F^2 c_\infty z^2 D}{RT} \left(1 + \frac{3m}{z^2}\right) \left[\cosh\left(\frac{zF\phi_o}{2RT}\right) - 1\right] \\ &= \sigma_{\text{Ohmic}} + \frac{2\varepsilon\varepsilon_o D}{h} \left(1 + \frac{3m}{z^2}\right) \left[\cosh\left(\frac{zF\phi_o}{2RT}\right) - 1\right] \end{aligned} \tag{4.28}$$

Of critical significance is the parameter $m = \left(\frac{RT}{F}\right)^2 \frac{2\varepsilon\varepsilon_o}{3\eta D}$, which relates the relative contributions of excess Ohmic and electroosmotic conductivities: $\sigma_{\text{Ohmic}}^{(\text{ex})} = \frac{3m}{z^2} \sigma_{\text{EO}}^{(\text{ex})}$. Simplified relationships for the conductivity outside of the $h \gg \lambda_D$ limit are not available; in such cases we represent excess Ohmic and electroosmotic conductivities in integral form, written here assuming a Boltzmann distribution for the free-charge density:

$$\sigma_{\text{Ohmic}}^{(\text{ex})} = F \sum_i |z_i| \mu_i c_{i,\infty} \frac{1}{h} \int_0^h \left(e^{-\frac{z_i F \phi(y)}{RT}} - 1\right) dy \tag{4.29}$$

$$\begin{aligned} \sigma_{\text{EO}}^{(\text{ex})} &= \frac{(\varepsilon\varepsilon_o)^2}{\eta} \frac{1}{h} \int_0^h \left(\frac{d\phi}{dy}\right)^2 dy \\ &= 2 \frac{\varepsilon\varepsilon_o RT}{\eta h} \sum_i c_{i,\infty} \int_0^h \left(e^{-\frac{z_i F \phi(y)}{RT}} - e^{-\frac{z_i F \phi_{\text{mid}}}{RT}}\right) dy \end{aligned} \tag{4.30}$$

Outside the thin electrical double layer limit, the potential at the channel centerline is non-zero, represented here by ϕ_{mid}. We do not consider the conductivity further in this work.

4.5.1 Remarks on Coupling Terms for Rigid Interfaces

The results derived in this section are general: in χ_{11} we assume only that the fluid is Newtonian with no-slip boundaries. Examining the cross terms, χ_{12} and χ_{21}, we observe a term depending only on the electrical boundary condition, and an integral term representing the average channel potential; this integral term is proportional to the ratio $\frac{1}{h}$, and, since the potential varies appreciably only over λ_D, the contribution of this integral term will be minimal when $\lambda_D \ll h$. Finally, the χ_{12} and χ_{21} relations apply for *all forms* of the charge distribution – the relations do not require a point-charge or other approximation; hard-sphere corrections, for example, may be included. These remarks indicate that for systems with $h \gg \lambda_D$, χ_{12} and χ_{21} depend chiefly upon the boundary value, and details of the mobile/free charge distribution may be omitted.

The conductivity term, $\chi_{22}^{\text{(hard)}}$, is the least general, requiring free-charge and electroosmotic distributions that must be integrated. Because the excess conductivities are localized to regions near the charged surface, the importance of these excess conductivities diminish as the size of the system (i.e., h) increases.

4.6 Coupling Terms for Systems with Porous and Charged Interfaces

Porous and charged layers affect both electrical potential and momentum distributions. A system with a porous layer has increased hydraulic resistance in the porous region, as captured in the Stokes–Brinkman equation by the added term $-k\mathbf{u}$. Porous and charged layers contribute a fixed charge density term in the Poisson equation, $\rho_f(\mathbf{x})$. For the parallel-plate system considered here, the differential equations for the porous layer

$(0 \leq y \leq \delta)$ become:

$$0 = \eta \tfrac{d^2u}{dy^2} - ku - \tfrac{dp}{dx} - \tfrac{d\phi_{\text{ext}}}{dx}\rho_e \tag{4.31}$$

$$-\varepsilon\varepsilon_o \tfrac{d^2\phi}{dy^2} = \rho_e(y) + \rho_f(y) \tag{4.32}$$

Outside of the porous layer of thickness δ $(y \geq \delta)$, we solve equations (4.18) and (4.19). These equations are coupled by the boundary conditions presented in (4.4) and (4.8).

4.6.1 χ_{11} with Porous and Charged Interfaces

A porous layer reduces the hydraulic conductance of the channel. The porous layer exhibits a resistance beyond the viscous retardation of the fluid alone; this effect is captured in the $-ku$ term. Below, we solve for the velocity in the channel, and then describe the hydraulic conductance, $\chi_{11}^{(\text{soft})}$. For convenience and clarity, we work in the dimensionless variable $y^* = y/\delta$, and define $\beta = h/\delta$ which is the half-height of the channel normalized by the porous layer thickness. We introduce parameters $\lambda_o = \sqrt{\frac{\eta}{k}}$, a measure of the penetration of momentum from the pure fluid into the porous layer, $\alpha = \frac{\delta}{\lambda_o}$, to characterize the thickness of the porous layer relative to the penetration distance of momentum from the pure fluid into the porous layer, and $G = \frac{\delta^2}{\eta}\langle\nabla p\rangle$, a modified pressure gradient with units of velocity.

The shape of the velocity profiles are strong functions of α and β. Equations (4.33) and (4.34) show the nonlinear dependence in the parameter α:

$$u_1^{(p)} = \tfrac{G}{\alpha^2}\left(\cosh(\alpha y^*) - 1 - \tfrac{\sinh(\alpha y^*)}{\cosh(\alpha)}\left[\alpha(\beta - 1) + \sinh(\alpha)\right]\right) \tag{4.33}$$

$$u_2^{(p)} = \tfrac{G}{\alpha^2}\left(\tfrac{1}{\cosh(\alpha)} + \tfrac{\alpha^2}{2}(y^* - 1)(1 + y^* - 2\beta) - 1 - \alpha\,(\beta - 1)\tanh(\alpha)\right) \tag{4.34}$$

These equations are plotted in figure 4.2, showing the velocity profiles across the channel for small, moderate, and large resistance parameters (α). Perturbations induced by the porous layer on the momentum distribution are dependent on β, mostly by constriction effects, as α becomes large. For values of β approaching unity, nearly all non-vanishing values of α will have some effect on the velocity profiles.

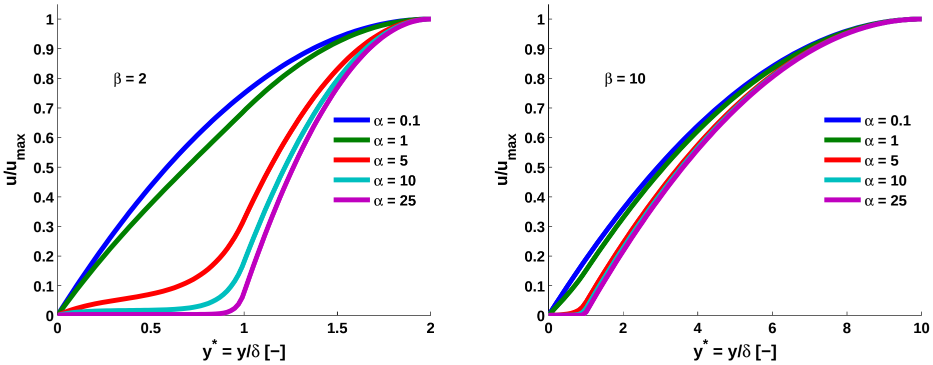

Figure 4.2: Velocity profiles about the channel centerline for varying layer resistance parameter α and relative channel height β. At left, $\beta = 2$, the velocity profile is strongly perturbed from parabolicity by large and moderate values of α. At right, $\beta = 10$, the channel is large relative to the porous layer thickness, and retarding effects are mainly confined to the porous layer and do not interfere strongly with momentum transport in the pure fluid region.

For the one-dimensional geometry considered, we compute $\chi_{11}^{(\text{soft})}$ from equation (4.11). This yields:

$$\chi_{11}^{(\text{soft})} = \frac{h^2}{3\eta}\left[1 - \frac{3\alpha^2\beta^2 - 3\alpha^2\beta + \alpha^2 - 6\beta + 3}{\alpha^2\beta^3} - \frac{6(\beta-1)}{\alpha^2\beta^3\cosh(\alpha)} + 3\left(\frac{(\beta-1)^2}{\alpha} - \frac{1}{\alpha^3}\right)\frac{\tanh(\alpha)}{\beta^3}\right] \tag{4.35}$$

In addition to the non-dimensional parameters α and β, equation (4.35) contains two dimensional parameters: the domain height, h, and the viscosity, η. The premultiplying dimensional term is the exact result for the hydraulic conductivity between two parallel plates; the additional bracketed terms represent corrections due to the thickness and resistivity of the porous layer.

Similar to the velocity profiles just described, $\chi_{11}^{(\text{soft})}$ is strongly dependent on α. For a porous region that is greatly resistive, $\alpha \gg 1$:

$$\frac{\chi_{11}^{(\mathrm{soft})}}{h^2/3\eta} = 1 - \frac{3\beta^2 - 3\beta + 1}{\beta^3} + \frac{3(\beta - 1)^2}{\alpha\beta^3} + O\left(\frac{1}{\alpha^2}\right) \tag{4.36}$$

In this limit, transport within the porous layer is diminished, and the porous layer serves to constrict the channel volume. If the porous layer becomes impenetrable ($\alpha \to \infty$),

$$\frac{\chi_{11}^{(\mathrm{soft})}}{h^2/3\eta} = 1 - \frac{3\beta^2 - 3\beta + 1}{\beta^3} \tag{4.37}$$

For a porous region that is weakly resistive, $\alpha << 1$, we describe this layer using a series expansion in the now-small parameter α:

$$\frac{\chi_{11}^{(\mathrm{soft})}}{h^2/3\eta} = 1 - \frac{3 - 5\beta(3 - 4\beta)}{20\beta^3}\alpha^2 + O(\alpha^4) \tag{4.38}$$

A vanishingly small resistance corresponds to a porous layer with no resistance beyond the viscosity of the working fluid, and is equivalent to the limit $\alpha \to 0$. In this case:

$$\frac{\chi_{11}^{(\mathrm{soft})}}{h^2/3\eta} = 1 \tag{4.39}$$

Both large- and small-α limits concur with physical intuition. For a very resistive layer, the channel is throttled by the impermeable porous layer and a reduced channel height. For a ‘porous’ layer with zero resistance, $\chi_{11}^{(\mathrm{soft})}$ has no dependence on the layer thickness δ, as the porous layer provides no additional resistance to the channel. Between these limits, the hydraulic conductivity varies smoothly across a large range of α. This behavior is shown in figure 4.3.

4.6.2 χ_{21} with Porous and Charged Interfaces

The current density in response to a pressure gradient is related through the coupling coefficient $\chi_{21}^{(\mathrm{soft})}$, which is a convolution of the pressure-driven velocity field and the total charge density formed by mobile ions. In the presence of a permeable layer with fixed

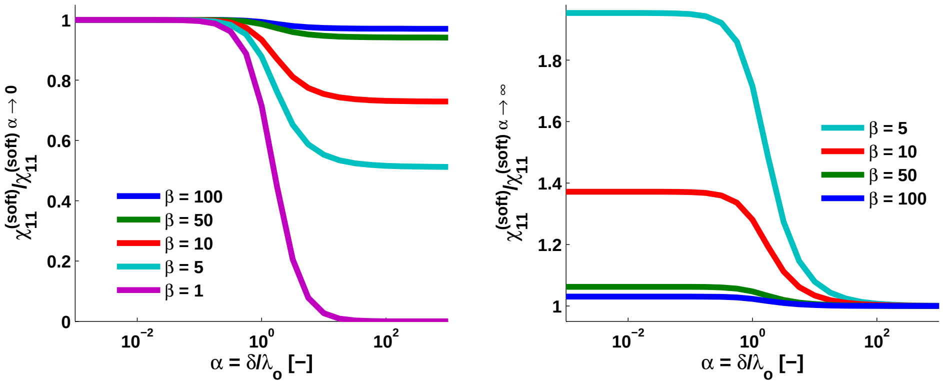

Figure 4.3: Plots of $\chi_{11}^{(\text{soft})}$ normalized by the $\alpha \to 0$ limit (left) and the $\alpha \to \infty$ limit (right). In both cases, porous layer effects are small when the channel height is large relative to the porous layer thickness ($\beta \gg 1$).

charge, the magnitude of convected charge can differ markedly from the rigid interface previously considered. There are two sources for this change: (1) the distribution of ions is perturbed by the porous and charged layer and (2) the distribution of momentum is perturbed by the porous and charged layer.

We derive $\chi_{21}^{(\text{soft})}$ in a general form accounting for a uniformly resistive porous layer. Our derivation places no requirements on the distribution of charge, nor do we assume a distribution (or magnitude) of potential (beyond that which solves a general Poisson equation). Thus, our formulation assumes only the existence of potential and fixed-charge distributions.

For the parallel-plate geometry, we derive $\chi_{21}^{(\text{soft})}$ by substituting in the Poisson equation and the known velocity solution, and repeatedly integrating by parts. We start with:

$$\chi_{21}^{(\text{soft})} = \frac{I/A}{-\langle \nabla p \rangle} = -\frac{1}{\beta \langle \nabla p \rangle} \int_0^{\beta} u^{(p)} \rho_e \, dy^* \tag{4.40}$$

Here, and in the following Poisson equation, we again scale the spatial coordinate y by the porous layer thickness δ:

$$-\frac{\varepsilon\varepsilon_o}{\delta^2}\frac{d^2\phi}{dy^{*2}} = \rho_e(y^*) + \rho_f(y^*) \tag{4.41}$$

By substituting out the charge density in (4.40) for the potential curvature and fixed charge density terms, we obtain:

$$-\frac{1}{\beta\langle\nabla p\rangle}\int_0^\beta u^{(p)}\left(-\frac{\varepsilon\varepsilon_o}{\delta^2}\frac{d^2\phi}{dy^{*2}} - \rho_f(y^*)\right)dy^* = \frac{1}{\beta\langle\nabla p\rangle}\left[\frac{\varepsilon\varepsilon_o}{\delta^2}\int_0^\beta u^{(p)}\frac{d^2\phi}{dy^2}\,dy^* + \int_0^1 u^{(p)}\rho_f(y^*)\,dy^*\right] \tag{4.42}$$

The limits of the last integral range only from $0 \le y^* \le 1$, because ρ_f vanishes outside the porous layer. After successive integrations by parts, and invoking the boundary conditions on velocity and potential,

$$\chi_{21}^{(\text{soft})} = \frac{\varepsilon\varepsilon_o}{\eta}\phi_o\left[\frac{1}{\beta G}\left.\frac{du_1^{(p)}}{dy^*}\right|_{y^*=0} + \frac{1}{\beta}\int_0^\beta \frac{\phi}{\phi_o}\,dy^* + \frac{1}{\beta}\int_0^1 \frac{u_1^{(p)}}{\alpha^2 G}\left(\frac{\phi}{\phi_o} + \frac{\delta^2}{\alpha^2\varepsilon\varepsilon_o}\frac{\rho_f}{\phi_o}\right)dy^*\right] \tag{4.43}$$

The velocity in the porous layer is known and described in the previous section. The velocity gradient at the boundary between the rigid wall and porous layer is $\left.\frac{du_1^{(p)}}{dy^*}\right|_{y^*=0} = G\left(\frac{1-\beta}{\cosh(\alpha)} - \frac{\tanh(\alpha)}{\alpha}\right)$. Including these terms gives:

$$\begin{aligned}\chi_{21}^{(\text{soft})} = -\frac{\varepsilon\varepsilon_o}{\eta}\phi_o\Bigg[&\frac{1-1/\beta}{\cosh(\alpha)} + \frac{\tanh(\alpha)}{\alpha\beta} - \frac{1}{\beta}\int_0^\beta \frac{\phi}{\phi_o}\,dy^* - \dots\\ &\frac{1}{\beta}\int_0^1\left(\cosh(\alpha y^*) - 1 - \frac{\sinh(\alpha y^*)}{\cosh(\alpha)}\left(\alpha(\beta-1)+\sinh(\alpha)\right)\right)\left(\frac{\phi}{\phi_o} + \frac{\delta^2}{\alpha^2\varepsilon\varepsilon_o}\frac{\rho_f}{\phi_o}\right)dy^*\Bigg]\end{aligned} \tag{4.44}$$

Presently, these equations are nondimensionalized in space only. By introducing the scales $\phi^* = \frac{\phi}{RT/F}$, $\rho_f^* = \frac{\rho_f\lambda_D^2}{\varepsilon\varepsilon_o\frac{RT}{F}} = \frac{\rho_f}{2FI_c}$, defining $\gamma = \frac{\lambda_D}{\delta}$, and noting $I_c = \frac{1}{2}\sum_j c_{j,\infty}z_j^2$ is the ionic strength of solution, the quantity contained within the square brackets is converted to dimensionless form:

$$\begin{aligned}\chi_{21}^{(\text{soft})} = -\frac{\varepsilon\varepsilon_o}{\eta}\phi_o\Bigg[&\frac{1-1/\beta}{\cosh(\alpha)} + \frac{\tanh(\alpha)}{\alpha\beta} - \frac{1}{\beta}\int_0^\beta \frac{\phi^*}{\phi_o^*}\,dy^* - \dots\\ &\frac{1}{\beta}\int_0^1\left(\cosh(\alpha y^*) - 1 - \frac{\sinh(\alpha y^*)}{\cosh(\alpha)}\left(\alpha(\beta-1)+\sinh(\alpha)\right)\right)\left(\frac{\phi^*}{\phi_o^*} + \frac{1}{\alpha^2\gamma^2}\frac{\rho_f^*}{\phi_o^*}\right)dy^*\Bigg]\end{aligned} \tag{4.45}$$

Lastly, grouping terms in the final integral into the function $H(y^*;\alpha,\beta)$:

$$\chi_{21}^{(\text{soft})} = -\frac{\varepsilon\varepsilon_o}{\eta}\phi_o\left[\frac{1-1/\beta}{\cosh(\alpha)} + \frac{\tanh(\alpha)}{\alpha\beta} - \frac{1}{\beta}\int_0^\beta \frac{\phi^*}{\phi_o^*}\,dy^* - \frac{1}{\beta}\int_0^1 H(y^*;\alpha,\beta)\left(\frac{\phi^*}{\phi_o^*} + \frac{1}{\alpha^2\gamma^2}\frac{\rho_f^*}{\phi_o^*}\right)dy^*\right] \tag{4.46}$$

$$H(y^*;\alpha,\beta) = \cosh(\alpha y^*) - 1 - \frac{\sinh(\alpha y^*)}{\cosh(\alpha)}\left(\alpha(\beta-1) + \sinh(\alpha)\right) \tag{4.47}$$

This result succinctly communicates the functional dependence of $\chi_{21}^{(\text{soft})}$ on the physicochemical parameters α, β, and γ, and the chemical properties ϕ^* and ρ_f^*.

Four terms contribute to the expression for $\chi_{21}^{(\text{soft})}$. The first two bracketed terms, $\frac{1-1/\beta}{\cosh(\alpha)} + \frac{\tanh(\alpha)}{\alpha\beta}$, represent the direct contribution from the solid charged boundary. This quantity is linearly related to the pressure-normalized velocity gradient at the interface, and is only reduced by the presence of the porous layer. The second contribution, $-\frac{1}{\beta}\int_0^\beta \frac{\phi^*}{\phi_o^*}\,dy^*$, is a correction to the previous boundary potential terms resulting from the integration of the normalized potential across the channel. This integral term is minimal when (1) the channel is large relative to the porous layer thickness ($\beta \gg 1$), or (2) the Debye length is small in comparison to all other electrical and boundary length scales in the system ($\gamma \ll 1$, $\gamma \ll \beta$). This term plays an identical role to the integrated potential terms in equations (4.23) and (4.26). The final term $-\frac{1}{\beta}\int_0^1 H(y^*;\alpha,\beta)\left(\frac{\phi^*}{\phi_o^*} + \frac{\rho_f^*}{\phi_o^*}\frac{1}{\alpha^2\gamma^2}\right)dy^*$ describes current transport within the porous layer. $H(y^*;\alpha,\beta)$ is a filter-like function that describes the relative penetration of momentum into the porous layer as a function of α and β (or, equivalently, δ, λ_D, and h). This function H is proportional to the pressure-driven velocity within the porous layer, $H(y^*;\alpha,\beta) = \frac{\alpha^2}{G}u_1^{(p)}$. The second term in this integral, $\frac{\phi^*}{\phi_o^*} + \frac{\rho_f^*}{\phi_o^*}\frac{1}{\alpha^2\gamma^2}$, is a modified representation of the free charge density within a porous layer bearing fixed charge.

The behavior of the filter-like function, shown in figure 4.4, is a strong nonlinear function of α, and a weak function of β. Here, plots of $-\frac{1}{\beta}H(y^*;\alpha,\beta)$ over y^* for varying α and β illustrate the weighting of $\frac{\phi^*}{\phi_o^*} + \frac{\rho_f^*}{\phi_o^*}\frac{1}{\alpha^2\gamma^2}$ at various points in the porous layer. For $\beta = 1$, the porous layer occupies the entire width of the channel, and transport varies from nearly parabolic flow profile (small α) to a top-hat like shape dominated by the Brinkman term at large α. For larger values of β and small values of α, transport within the porous layer layer again mimics the portion of the parabolic profile contained in the porous layer. As α increases, the dominant contribution is contributed by the porous layer edge, owing to strongly retarded flow toward the interior of the porous layer.

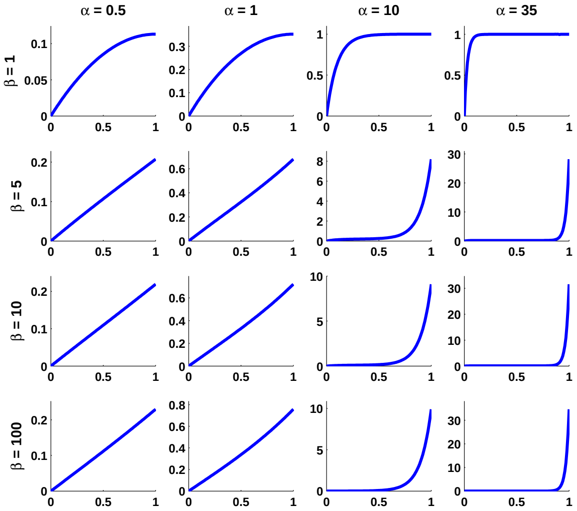

Figure 4.4: Behavior of the filter-like function $-\frac{1}{\beta}H(y^*;\alpha,\beta)$ as function of space over a range of α (columns) and β (rows). The horizontal axes in all plots range over $0 \le y^* \le 1$.

4.6.3 χ_{12} with Porous and Charged Interfaces

Although the coupling coefficient $\chi_{12}^{(\mathrm{soft})}$ is identical to $\chi_{21}^{(\mathrm{soft})}$ by Onsager reciprocity, the direct computation of $\chi_{12}^{(\mathrm{soft})}$ is substantially more difficult than $\chi_{21}^{(\mathrm{soft})}$ because the expressions for electroosmotic flow are more complicated than the corresponding pressure-driven flow relations. The generating formula for $\chi_{12}^{(\mathrm{soft})}$ in our one-dimensional system is:

$$\chi_{12}^{(\mathrm{soft})} = -\frac{1}{\beta\langle\nabla\phi_{\mathrm{ext}}\rangle}\int_0^\beta u^{(e)}\,dy^* \tag{4.48}$$

The field-driven fluid velocities are computed from the set of equations,

$$0 = \tfrac{d^2 u_1^{(e)}}{dy^{*2}} - \alpha^2 u_1^{(e)} + \tfrac{1}{\eta}\tfrac{d\phi_{\text{ext}}}{dx}\left(\varepsilon\varepsilon_o \tfrac{d^2\phi}{dy^{*2}} + \delta^2 \rho_f\right) \tag{4.49}$$

$$0 = \tfrac{d^2 u_2^{(e)}}{dy^{*2}} + \tfrac{1}{\eta}\tfrac{d\phi_{\text{ext}}}{dx}\varepsilon\varepsilon_o \tfrac{d^2\phi}{dy^{*2}} \tag{4.50}$$

along with the flow boundary conditions from equation (4.4). This set has the solution

$$\begin{aligned} u_1^{(e)} = C_1 e^{\alpha y^*} + C_2 e^{-\alpha y^*} - \int_0^{y^*} \frac{\langle \nabla \phi_{\text{ext}} \rangle e^{\alpha y^*} e^{-\alpha s}}{2\alpha\eta}\left(\delta^2 \rho_f(s) + \varepsilon\varepsilon_o \frac{d^2\phi}{ds^2}\right) ds \ + \dots \\ \int_0^{y^*} \frac{\langle \nabla \phi_{\text{ext}} \rangle e^{-\alpha y^*} e^{\alpha s}}{2\alpha\eta}\left(\delta^2 \rho_f(s) + \varepsilon\varepsilon_o \frac{d^2\phi}{ds^2}\right) ds \end{aligned} \tag{4.51}$$

$$u_2^{(e)} = C_3 + y^* C_4 - \frac{\varepsilon\varepsilon_o}{\eta}\langle \nabla \phi_{\text{ext}} \rangle \phi(y^*) \tag{4.52}$$

with constants:

$$C_1 = \tfrac{1}{2\cosh(\alpha)}\left[\int_0^1 \tfrac{\langle \nabla \phi_{\text{ext}} \rangle}{\alpha\eta} \cosh(\alpha(1-s))\left(\delta^2 \rho_f(s) + \varepsilon\varepsilon_o \tfrac{d^2\phi}{ds^2}\right) ds - \tfrac{\varepsilon\varepsilon_o}{\alpha\eta}\langle \nabla \phi_{\text{ext}} \rangle \phi'_\delta\right] \tag{4.53}$$

$$C_2 = -C_1 \tag{4.54}$$

$$C_3 = \int_0^1 \tfrac{\sinh(\alpha s)}{\cosh(\alpha)} \tfrac{\langle \nabla \phi_{\text{ext}} \rangle}{\alpha\eta}\left(\delta^2 \rho_f(s) + \varepsilon\varepsilon_o \tfrac{d^2\phi}{ds^2}\right) ds - \tfrac{\varepsilon\varepsilon_o}{\alpha\eta}\langle \nabla \phi_{\text{ext}} \rangle \left(\phi'_\delta \tanh(\alpha) - \alpha\phi_\delta\right) \tag{4.55}$$

$$C_4 = 0 \tag{4.56}$$

The coupling coefficient $\chi_{12}^{(\text{soft})}$ follows from a direct integration of the velocity expressions above. The process is tedious, but eventually yields the result $\chi_{12}^{(\text{soft})} = \chi_{21}^{(\text{soft})}$. See the supplementary information for further details on simplifying $\chi_{12}^{(\text{soft})}$.

4.7 Analysis and Limiting forms of $\chi_{21}^{(\text{soft})}$ and $\chi_{12}^{(\text{soft})}$

The coupling coefficients $\chi_{12}^{(\text{soft})}$ and $\chi_{21}^{(\text{soft})}$ (collectively written $\chi_{ij}^{(\text{soft})}$) presented in equations (4.46) and (4.47) are superior to alternate forms that depend on free charge, electrical potential slope, and electrical potential concavity terms. Our representation of $\chi_{ij}^{(\text{soft})}$

depends upon quantities that are known exactly in certain regions of the porous layer and are typically straightforward to approximate or bound in the remaining regions. These forms of $\chi_{ij}^{\text{(soft)}}$ depend solely on parameters α, β, γ, and spatial distributions of potential (ϕ) and fixed-charge density (ρ_f). Specifically, the fixed charge density may be approximated with information about the chemistry of the charge-generating mechanism. Typically, such bound charge is controlled by pH-dependent chemistry [58, 92, 170]. Regardless of the charging mechanism, the charge is a nonlinear function of the potential, and estimations of charge densities require estimations of potential, not potential curvature or slope. Using either exact, numerical, or approximate expressions for the potential potential and fixed-charge profiles, these expressions are used as inputs in the function $\chi_{ij}^{\text{(soft)}}$. Furthermore, using our form of $\chi_{ij}^{\text{(soft)}}$, we obtain physical limits by varying parameters α, β, and γ, absent specific information on the form of the potential and charge distributions.

Our analysis of $\chi_{ij}^{\text{(soft)}}$ is informed by the interactions between distributions of momentum, potential, and charge. The Stokes and Poisson equations couple directionally – distributions of charge and potential are unaffected by the transport of momentum, whereas the free-charge distribution strongly affects electroosmotic transport. The quantity α contributes only to hydrodynamics, affecting the degree to which flow is retarded within the porous region. The term γ controls the decay of the potential profile generated by the fixed charge embedded in the porous region and rigid boundary. Although this term does not affect the pressure-driven flow, it does have an effect on the electroosmotic flow. Finally, β contributes to both the momentum and charge distributions by adjusting the separation between momentum and electrical boundary conditions. Furthermore, regions of net free charge (and non-zero potential) are typically confined to the charged porous region plus a distance of several γ's into the pure fluid phase. In general, the parameters α and γ directly control the transport behavior of the system, whereas β indicates the relative magnitude of fluid transport within and outside of the porous region.

We implement analytical approximations and numerical solution methods to resolve the behavior of $\chi_{ij}^{\text{(soft)}}$ for varied parameters α, β, and γ. In our analyses, we assume the conventional Boltzmann forcing of the Poisson equation. The Poisson–Boltzmann equation is strongly nonlinear, and has no general closed-form solution for our geometry and boundary conditions. Thus, we implement approximate analytical solutions where the potential, ϕ^*, can be estimated. Outside of approximate limits, we perform numerical computations to determine $\chi_{ij}^{\text{(soft)}}$.

The parameter $\alpha = \frac{\delta}{\lambda_o}$ determines the penetration of velocity from the pure fluid into the porous region, strongly affecting the value of $\chi_{ij}^{\text{(soft)}}$. When $\alpha \to 0$, the resistance of the porous layer is minimal and momentum transfers freely from the fluid into the porous layer; conversely, $\alpha \to \infty$ implies that the porous layer is highly resistive, and transport in the porous layer is throttled. For $\alpha << 1$, we perform a series expansion in the small parameter α. Then, to zeroth order in α:

$$\frac{\chi_{ij}^{\text{(soft)}}}{-\frac{\varepsilon\varepsilon_o}{\eta}\phi_o} \approx 1 - \frac{1}{\beta}\int_0^\beta \frac{\phi^*}{\phi_o^*}\,dy^* + \int_0^1 \left(y^* - \frac{y^{*2}}{2\beta}\right)\frac{\rho_f^*}{\phi_o^*\gamma^2}\,dy^* \tag{4.57}$$

Equation (4.57) shows the limit for $\chi_{ij}^{\text{(soft)}}$ in system having a weakly resistive porous layer is equal to the sum of χ_{ij} for a hard surface (the first two terms, which are equivalent to equation (4.23)) and contributions from the fixed-charge-density term (the last integral). Further reducing this expression in the limit of $\beta \gg 1$ removes the second, overlap-correction term. In essence, then, the first *and* third terms are boundary terms, because they are wholly or partially in the limit where reductions by double layer overlap are minimized ($\beta \gg 1$):

$$\frac{\chi_{ij}^{\text{(soft)}}}{-\frac{\varepsilon\varepsilon_o}{\eta}\phi_o} \approx 1 + \int_0^1 \frac{\rho_f^*}{\phi_o^*}\frac{y^*}{\gamma^2}\,dy^* \tag{4.58}$$

All forms of $\chi_{ij}^{\text{(soft)}}$ remain bounded even when $\gamma \to 0$ or $\lambda_D \to 0$ in this limit because $\rho_f^* \sim \gamma^2 \sim \lambda_D^2$.

The small-α case offers insight into the importance of the solid-wall potential boundary condition versus the fixed-charge distribution in the porous region. For porous regions thick relative to the Debye length, $\gamma^2 << 1$, we expect that the solid boundary will contribute minimally because the wall charge is screened by the charge in the porous layer. For α and $\gamma \ll 1$, $\chi_{ij}^{\text{(soft)}}$ is heavily dependent on the porous layer charge, except when the boundary potential greatly exceeds the Donnan potential, $\phi_o^* > \frac{z \sinh(\phi_D^*)}{2z\gamma^2}$. Furthermore, thick porous layers exhibit minimal concavity in electrical potential far from porous layer edges, $\frac{d^2\phi}{dy^2} \approx 0$, implying $\rho_f^* = \frac{1}{z}\sinh(z\phi_D^*)$ for a $z : z$ electrolyte. Recall that ϕ_D^* is the Donnan potential. For a uniform fixed charge distribution within the porous layer, and using the Donnan potential relationship between charge and potential in the small-γ limit, we obtain:

$$\frac{\chi_{ij}^{\text{(soft)}}}{-\frac{\varepsilon\varepsilon_o}{\eta}\phi_o} \approx 1 + \frac{\sinh(z\phi_D^*)}{z\phi_o^*}\frac{1}{2\gamma^2} \tag{4.59}$$

As expected, the thick-layer limit of $\chi_{ij}^{\text{(soft)}}$ is heavily dependent on the porous layer charge, except when the boundary potential greatly exceeds the Donnan potential, $\phi_o^* > \frac{z \sinh(\phi_D^*)}{2z\gamma^2}$.

When $\beta \to 1$, transport occurs entirely within the porous region, and the only contribution to $\chi_{ij}^{\text{(soft)}}$ comes from the porous layer. Applying this condition in equation (4.57) yields, for uniform charge density:

$$\frac{\chi_{ij}^{\text{(soft)}}}{-\frac{\varepsilon\varepsilon_o}{\eta}\phi_o} \approx 1 - \int_0^1 \frac{\phi^*}{\phi_o^*}\,dy^* + \frac{1}{3}\frac{\rho_f^*}{\phi_o^*\gamma^2} \tag{4.60}$$

The term $\int_0^1 \frac{\phi^*}{\phi_o^*}\,dy^*$ can be approximated as $\frac{\phi_D^*}{\phi_o^*}$ when: (1) the wall potential matches identically with the potential in the porous layer (in which case this approximation is exact) or (2) $\gamma << 1$, relegating any perturbation in electrical potential to a small region of thickness $\sim 5\gamma$ near the wall. In either case,

$$\frac{\chi_{ij}^{(\text{soft})}}{-\frac{\varepsilon\varepsilon_o}{\eta}\phi_o} \approx 1 - \frac{\phi_D^*}{\phi_o^*} + \frac{1}{3}\frac{\rho_f^*}{\phi_o^*\gamma^2} \tag{4.61}$$

Thus, the dominant contribution for a channel completely filled by a porous layer is the charge carried by the porous layer. This limiting area of parameter space implies a zero when $\rho_f^* = 3\gamma^2 \int_0^1 (\phi^* - \phi_o^*)\, dy$, which can occur only when the porous layer and wall potentials have opposite sign.

Limiting forms of $\chi_{ij}^{(\text{soft})}$ for highly resistive porous layers ($\alpha \gg 1$) are more difficult to obtain than those for weakly resistive porous layers. A uniform limiting expression for the filter-like function $H(y^*;\alpha,\beta)$ is not available for the general case of large α. The difficulty of obtaining approximations of $\chi_{ij}^{(\text{soft})}$ as $\alpha \gg 1$ is well-motivated by figures 4.2 and 4.4: as α is increased for all $\beta > 1$, flow within the porous layer is zero nearly everywhere *except* the porous layer edge; similarly, $\frac{1}{\beta}H(y;\alpha,\beta)$ tends to zero in all regions but the porous layer edge, where the value of the function increases substantially. The first boundary term, however, can be approximated: the sustained absence of flow near the wall removes the contribution from the boundary term. Given restrictions on interchanging the limit and integration operations for the porous regions integral, we seek further simplifications to χ_{ij} by way of approximation for the quantity $\frac{\phi^*}{\phi_o^*} + \frac{\rho_f^*}{\phi_o^*}\frac{1}{(\alpha\gamma)^2}$. Approximate expressions are delicate at the interface between the porous layer and pure fluid: the potential and fluid velocity both change appreciably in a thin slice of the domain. We begin by considering $\chi_{ij}^{(\text{soft})}$ with $\alpha \gg 1$ and a uniform fixed charge density. Then:

$$\frac{\chi_{ij}^{(\text{soft})}}{-\frac{\varepsilon\varepsilon_o}{\eta}\phi_o} \approx -\frac{1}{\beta}\int_0^\beta \frac{\phi^*}{\phi_o^*}\, dy^* + \frac{\rho_f^*}{\phi_o^*}\left(\frac{1}{\alpha^2\gamma^2} + \frac{1/\beta - 1}{\alpha^2\gamma^2\cosh(\alpha)} - \frac{\tanh(\alpha)}{\alpha^3\gamma^2\beta}\right) - \frac{1}{\beta}\int_0^1 \frac{\phi^*}{\phi_o^*} H(y^*;\alpha,\beta)\, dy^* \tag{4.62}$$

Here, terms of $\frac{1}{\alpha^n}$, $n \geq 1$, have been omitted; we retain the term $O\left(\frac{1}{\alpha^2\gamma^2}\right)$ since $\alpha\gamma$ may be of order unity or smaller. In dimensional form, $\alpha\gamma = \lambda_D/\lambda_o$ – this combination of parameters controls the local convection of charge at the porous layer edge. This dependence of $\chi_{ij}^{(\text{soft})}$ on $(\alpha\gamma)^{-2}$ results from the coincidence of velocity and potential gradients near the porous layer edge. As λ_D decreases, the potential profile sharpens limiting to a function mimicking the fixed-charge distribution. Similarly, the velocity profile sharpens ($\left|\frac{du}{dy}\right|$ increasing) with increasing λ_o at the porous layer edge.

When $\gamma << 1$, the potential profile will mimic a step function, and the electrical potential everywhere within the porous layer can be bounded by two limits. Here, we estimate the electrical potential ϕ^* in the integral $-\frac{1}{\beta}\int_0^1 \frac{\phi^*}{\phi_o^*} H(y^*;\alpha,\beta)\,dy^*$: (1) a lower bound where the potential everywhere within the porous layer is greater than or equivalent to the potential at the porous layer edge ($\phi^*(1) = \phi(\delta)$ presented in the supplementary information), $\phi^* \geq \phi_\delta^*$, and (2) an upper bound where the potential everywhere within the porous layer is less than or equal to the Donnan potential of the porous layer, $\phi^* \leq \phi_D^*$. Then:

$$\left.\frac{\chi_{12}^{(\text{soft})}}{-\frac{\varepsilon\varepsilon_o}{\eta}\phi_o}\right|_{\min} = -\frac{1}{\beta}\frac{\phi_D^* + f(z,\phi_D^*)}{\phi_o^*} + \left(\frac{\rho_f^*}{\alpha^2\gamma^2\phi_o^*} + \frac{\phi_D^* + f(z,\phi_D^*)}{\phi_o^*}\right)\left(1 + \frac{1/\beta - 1}{\cosh(\alpha)} - \frac{\tanh(\alpha)}{\alpha\beta}\right) \tag{4.63}$$

$$\left.\frac{\chi_{12}^{(\text{soft})}}{-\frac{\varepsilon\varepsilon_o}{\eta}\phi_o}\right|_{\max} = -\frac{1}{\beta}\frac{\phi_D^*}{\phi_o^*} + \left(\frac{\rho_f^*}{\alpha^2\gamma^2\phi_o^*} + \frac{\phi_D^*}{\phi_o^*}\right)\left(1 + \frac{1/\beta - 1}{\cosh(\alpha)} - \frac{\tanh(\alpha)}{\alpha\beta}\right) \tag{4.64}$$

These relations are compared and evaluated later in frame (C) of figure 4.6 for $\alpha << 1$ and figure 4.7 for $\alpha >> 1$. In particular, we apply relations (4.63) and (4.64) over the entire range of α in figure 4.8 demonstrating the ability of the expressions to bound $\chi_{ij}^{(\text{soft})}$.

4.8 Numerical Representation of $\chi_{ij}^{(\text{soft})}$ for Arbitrary Values of α, β, γ, and Validation of Approximate Analytical Formulas

We implement numerical methods to determine $\chi_{ij}^{(\text{soft})}$ outside of the limits described in the previous section. Further, we use the numerical description of $\chi_{ij}^{(\text{soft})}$ to validate our approximate expressions. We numerically determine $\chi_{ij}^{(\text{soft})}$ in the parameter space spanned by the charge (or potential) in the porous layer, and quantities α, β, and γ. We assume the Boltzmann relation for the free charge density. The numerical quadrature of $\chi_{ij}^{(\text{soft})}$ is straightforward if $\phi^*(y^*)$ and $\rho_f^*(y^*)$ are known; this is a main feature of our form for $\chi_{ij}^{(\text{soft})}$ – we do not require computations of field gradients, which are prone to numerical errors given the spatially stiff nature of the Poisson–Boltzmann equation. All numerical representations of the potential presume a uniformly charged porous layer, as well as uniform fluid and electrical properties across the entire domain. The details of the numerical scheme are summarized the supplementary information.

We have compared numerical potential simulations to analytical expressions for the potential at the porous layer edge, with favorable results. At the porous layer edge, we use a Grahame-type formula (see supplementary information) to compare against our numerical calculations. These results, along with potential profiles across the domain for varying values of the parameter γ, are shown in figure 4.5, demonstrating quantitative agreement with theoretical predictions and scaling. As expected, and similar to the semi-infinite rigid interface solution, the length scale controlling the decay of the potential at the porous layer edge is strongly dependent upon the potential in the porous layer. This decay is illustrated in frame (A) of figure 4.5, and shown more clearly in frames (B) and (C). Although (B) and (C) are qualitatively similar, the length scale over which (B) decays is 1/10th of the scale in (C). This disparity in decay length is a direct result of the nonlinearity of the governing physics. In contrast to the linearized limit, at large potential the characteristic length scale is a strong function of the local potential. Furthermore, we directly compare numerical and analytical results (cf., equation (4.96) for the edge potential in the supplementary information) in (D) and (E), showing excellent agreement. Frames (D) and (E) demonstrate that the porous layer edge potential matches the analytical result, and also that the result is invariant to the value of γ. This invariance to γ is also demonstrated in panes (A) through (C). These favorable comparisons establish the validity of our numerical potential simulations to describe the potential and charge distribution within the porous layer system.

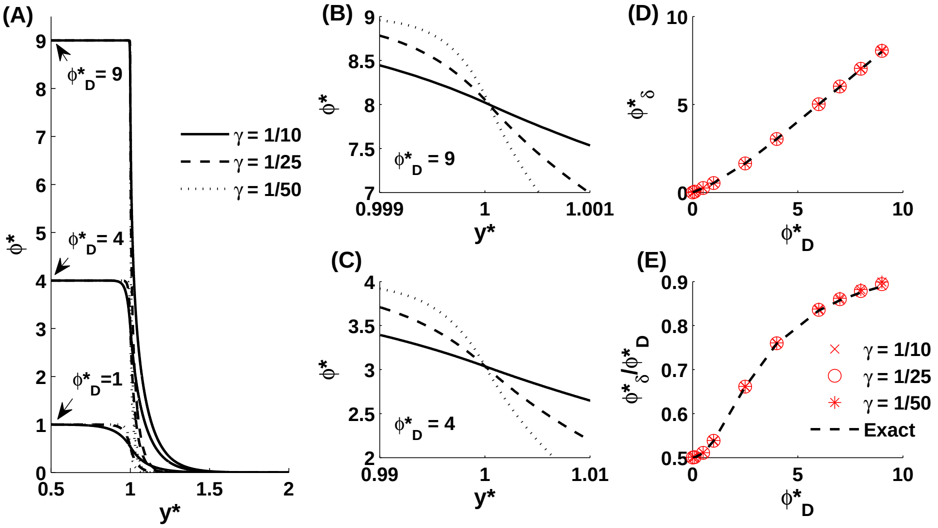

Figure 4.5: Numerical results for electrical potential distributions, and comparison against exact results. For all results, $\beta = 10$ with a $1 : 1$ electrolyte; the uniform porous layer terminates at $y = 1$. (A) Potential profiles for various values of potential and γ (as indicated); the extents of the data are truncated to highlight the porous layer edge. Panes (B) and (C) highlight the change in potential near the porous layer edge at $y = 1$. The legend in (A) also applies to (B) and (C). (D) and (E) display a comparison between the computed potential at the porous layer edge and the analytical result. The legend in (E) applies to (D) as well.

Parameters α, β, and γ have distinct effects on the electrokinetic coupling parameters $\chi_{ij}^{(\text{soft})}$. We explored the impact of these parameters on $\chi_{ij}^{(\text{soft})}$ previously with our analytical form (4.46) and here show a more complete picture via numerics. The parameter α

affects only the fluid mechanics of the system. As $\alpha \rightarrow \infty$, momentum transport in the porous region vanishes, throttling fluid transport. This restriction occurs independently of the potential profile. The limit of $\alpha \rightarrow 0$ represents the opposite extreme, where the porous layer exhibits no resistance beyond fluid viscous effects. For most systems, α is the dominating factor governing the magnitude of the coupling coefficients. This dominance is demonstrated in figure 4.6, showing the cross-coefficients (χ_{12} and χ_{21}) over seven decades of α, while β and γ are simultaneously varied. The results shown in figure 4.6A communicate the importance of transport within the porous layer. At low values of α, transport is permitted in the porous region and overall charge transport is enhanced by the coincidence of fluid motion and fixed charge density, with minimal sensitivity to the value of β. All results in figure 4.6 are shown for an interior (or Donnan) potential of $\phi_D^* = 5$ i.e., $\phi_D = 128$ mV. The boundary potential, ϕ_o, is assumed equal to the Donnan potential for these cases.

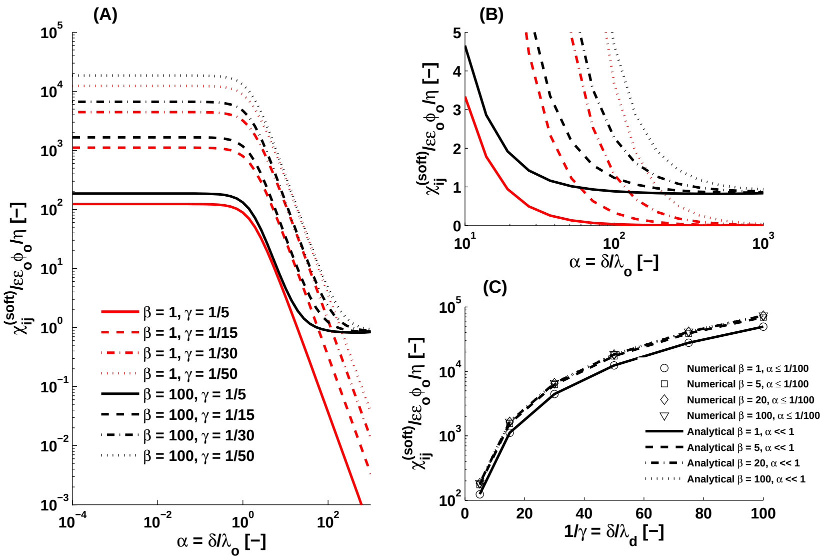

Figure 4.6: Behavior of the coupling coefficients $\chi_{12}^{(\text{soft})}$ and $\chi_{21}^{(\text{soft})}$ over 7 decades of α for $\beta = 1$ (red lines in (A) and (B)), $\beta = 100$ (black lines in (A) and (B)), and various values of γ, indicated with various line styles. Pane (C) compares numerical values and analytical approximations of $\chi^{(\text{hard})}$ in the $\alpha \ll 1$ limit as a function of γ (x-axis) and β for $\phi_D = 5$, showing excellent agreement.

The selections of $\beta = 1$ and 100 illustrate $\chi_{ij}^{(\text{soft})}$ for a porous layer completely filling the channel ($\beta = 1$) and a porous layer forming a thin region of fixed charge relative to the pure fluid phase ($\beta = 100$). Furthermore, we consider a range of γ indicating porous layers that are similar in size to the Debye length of the fluid (solid lines) to layers that are much larger than the Debye length (dash-dot and dotted lines). The discrepancy between the large- and small-β limit is attributable to convection of charge in the double layer beyond the edge of the porous region. This layer is not present in the $\beta = 1$ limit (as the porous region fills entirely the channel), and thus contributes neither fluid nor current flux. For strongly resistive layers, the data presented in figure 4.6C demonstrates that $\chi_{ij}^{(\text{soft})}$ exhibit greater sensitivity to the value of β when α becomes large. Here, the porous layer is strongly resistive and transport occurs mainly in the pure fluid region. For $\beta = 1$, the entire channel is filled with a strongly resistive layer; the flow is throttled, and the fluxes vanish.

The parameter γ affects the coupling coefficients $\chi_{12}^{(\text{soft})}$ and $\chi_{21}^{(\text{soft})}$ at nearly all values of α. When $\alpha \ll 1$, the coupling coefficients reach their limiting maximum form, and exhibit a scaling of $1/\gamma^2$. This behavior is shown most clearly in figure 4.6B, in which the coupling coefficient is plotted as a function of γ for $\alpha \ll 1$, while simultaneously varying the height of the channel (β). The γ^{-2} scaling is confirmed by the favorable comparison between our low-α analytical relation, equation (4.58), and the results of our numerical representations for the potential and coupling coefficients. These results display not only correct scaling, but also the accuracy of our analytical approximations in this region.

The value of γ does not affect the limiting result of the coupling coefficients as $\alpha \gg 1$. Rather, the parameter γ controls the value of α at which this limiting result is achieved, as illustrated in figure 4.6C. This behavior can be explained by considering the potential in regions with fluid transport. For a porous layer with $\alpha \ll 1$, transport occurs near and beyond the porous layer edge, having been diminished within the porous layer. In the context of pressure-driven flow, for the large-α limit, flow is relegated to a thin region of thickness order λ_o near the porous layer edge, or α in dimensionless space. Similarly, the fixed charges within the porous layer generate a potential whose decay length is equal to λ_D, or γ in dimensionless space. As γ decreases, the potential profile limits to the step function defined by the fixed charge in the porous layer (e.g., figure 4.5). This limiting case exhibits zero potential curvature everywhere in the porous layer *except* at the edge, and within the porous layer the free charge is equal and opposite to the fixed charge. Thus, any transport in this region necessarily depends on both α and γ — increasing values of α will decrease charge transport by reducing fluid velocities at the porous region edge, and decreasing values of γ will increase the charge transport by enhancing the amount of free charge that may be convected near the porous region edge.

Numerical simulations of $\chi_{ij}^{(\mathrm{soft})}$ show that the upper and lower limits for $\chi_{ij}^{(\mathrm{soft})}$ bound the cross-coupling coefficient at large α. Agreement is shown in figure 4.7 for $\alpha = 100$ and $\phi_o^* = 5$, over a range of β and γ. Furthermore, these results communicate that strong changes in the electrical potential profile and transport at the interface are responsible for variations in $\chi_{ij}^{(\mathrm{soft})}$. Both of these effects are apparent when comparing results for $\beta = 1$ to all other cases. When $\beta = 1$, gradients in fluid velocity occur at the solid boundary, and there are no gradients in electrical potential or charge; and the approximation matches the numerical data. For $\beta \neq 1$, there is a decay in potential from ϕ_D^* in the porous layer toward the bulk (midline) value; the decay length is governed by the parameter γ. As γ decreases, the dominant flux contribution is from the value of the fixed charge density. Conversely, when γ becomes large, the potential terms become dominant: Since the potential is estimated everywhere within the porous layer and at the boundary of the porous layer and fluid, the large–γ case yields the largest errors.

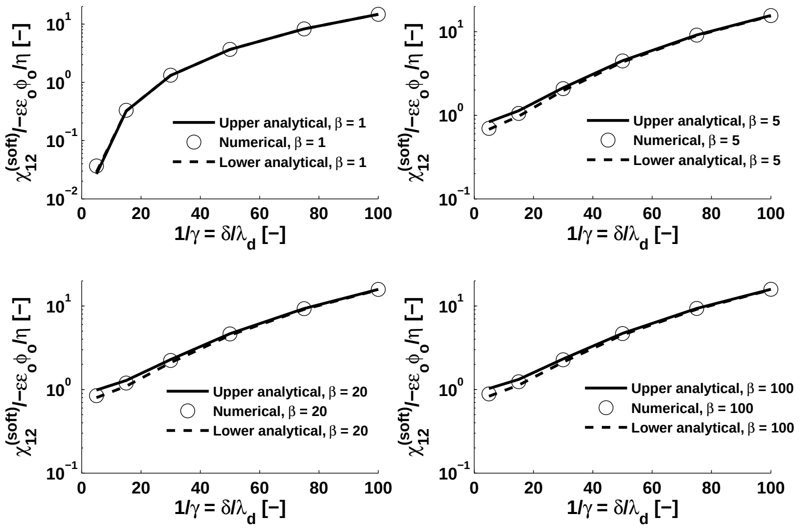

Figure 4.7: Upper and lower limit forms of $\chi_{12}^{(\mathrm{soft})}$ for $\alpha = 100$.

Furthermore, the upper and lower bounds derived for $\chi_{ij}^{(\mathrm{soft})}$ at large α (equations (4.63) and (4.64)) accurately approximate $\chi_{ij}^{(\mathrm{soft})}$ over a large range of α. This matching, and the associated errors, is shown in figure 4.8. The accuracy of these expressions over the entire range of α is somewhat surprising, as they were developed only for the large-α limit. Given our assumptions on the fixed charge distribution within the porous layer, however, we are able to exactly capture the contribution from each term containing ρ_f^*. Because this fixed charge density term is dominant at low α, the approximation for ϕ^* in the system does not contribute at small α, no matter the accuracy of the estimated value for α. As α is increased, the ϕ^* term in the integral contributes a greater amount as compared to the ρ_f^* term, and the estimated value of the potential in the porous layer *does* play an important role, as seen in figures 4.7 and 4.8. At large α the exact and approximated values of $\chi_{ij}^{(\mathrm{soft})}$ diverge, producing errors of about 10%.

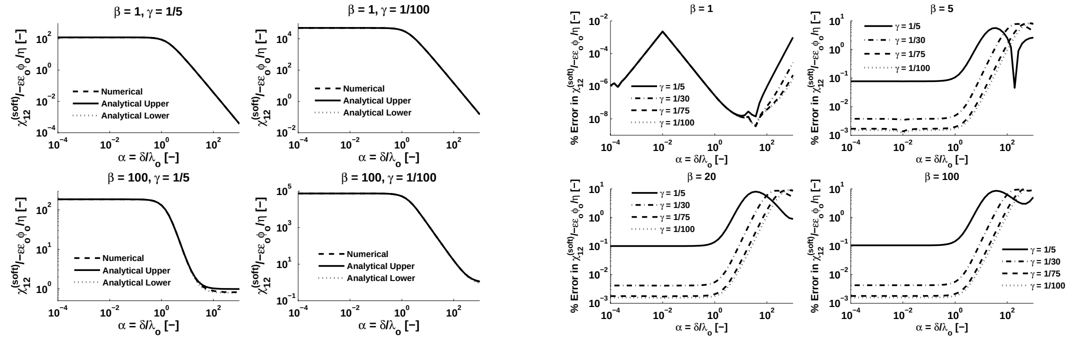

Figure 4.8: Leftmost four plots: Large α limit applied over the entire range of α. Rightmost four plots: Errors (as percent) in $\chi_{12}^{(\text{soft})}$ applied over the entire range of α. The non-monotonicity observed in the errors is results from taking the maximum error of the difference between the numerical value and upper and lower estimations of $\chi_{ij}^{(\text{soft})}$.

4.9 Conclusion

We have developed simplified analytical expressions for $\chi_{11}^{(\text{soft})}$ and $\chi_{ij}^{(\text{soft})}$ that are functions of known and/or estimable properties of a system with porous and charged layers. These expressions are improvements over earlier works on similar systems by removing the functional dependence on potential curvature and fluid velocity, which are typically not known. Prior workers have examined limiting regions of the parameter space that we consider in full.

Our results consider the limits of system parameters α, β, and γ rather than ϕ_D or ϕ_o, which extends the generality of our results. We have described the system using physical and chemical properties that can be measured or inferred: the solid wall potential (ϕ_o), fixed charge in the porous layer (ρ_f), porous layer thickness (δ), porous layer resistance (k), Debye length (λ_D), the system height (h), and the fluid viscosity (η). These properties can be further reduced to a set to dimensionless parameters, chiefly, the quantities α, β, and γ, which describe distributions of momentum and charge within the system.

With numerical solution of the governing equations, we have validated our approximate analytical forms of the coupling coefficients, and have shown that two simple analytical expressions, equations (4.63) and (4.64), faithfully describe the behavior of the terms $\chi_{ij}^{(\mathrm{soft})}$ to within 10%. Equations (4.63) and (4.64) make no assumptions on the magnitude of the potential or fixed charge density within the porous layer, but do assume that the fixed charge is uniformly distributed and the potential deep within the porous layer is gradient-free. Similarly, we have derived and validated expressions for $\chi_{ij}^{(\mathrm{soft})}$ when the parameter α is small, and the small-α limit applies more generally to systems with arbitrary distributions of fixed charge.

The theory, modeling, and analysis herein forms a structure through which systems with porous layers may be analyzed. If system parameters are known, expressions for $\chi_{11}^{(\mathrm{soft})}$ and $\chi_{ij}^{(\mathrm{soft})}$ give predictive capability for several phenomena. Conversely, if the coupling parameters are known from experimental measurements, system parameters may be determined.

4.10 Acknowledgments

The authors acknowledge support from the DOE PECASE program; ACB acknowledges support from the NSF Graduate Research Fellowship Program.

4.11 Supplementary Information

4.11.1 Brief Details on the Numerical Scheme

We implement a finite differencing scheme to solve the Poisson–Boltzmann equation. Specifically, we have used an implicit Crank–Nicholson scheme by introducing a pseudo-time variable to change the equation from elliptic-like to parabolic-like. Discretization of the Poisson–Boltzmann equation in space and time leads to an implicit set of equations that may be recast in matrix form, including a forcing term representing contributions from the fixed and nonlinear free charge density terms. We solve this matrix equation using a tridiagonal matrix algorithm, iterating and comparing successive solutions until convergence.

4.11.2 $\chi_{12}^{(\mathrm{soft})}$ for Porous and Charged Interfaces

Here, we show that the coupling coefficient computed from electroosmosis:

$$\chi_{12}^{(\mathrm{soft})} = -\frac{1}{\beta \nabla \phi_{\mathrm{ext}}} \int_0^{\beta} u^{(e)}\, dy^* \tag{4.65}$$

is identical to the coefficient $\chi_{21}^{(\mathrm{soft})}$ derived previously from streaming current.

The field-driven fluid velocities are computed from the set of equations,

$$0 = \frac{d^2 u_1^{(e)}}{dy^{*2}} - \alpha^2 u_1^{(e)} + \frac{\nabla \phi_{\mathrm{ext}}}{\eta} \left(\varepsilon \varepsilon_o \frac{d^2 \phi}{dy^{*2}} + \delta^2 \rho_f \right) \tag{4.66}$$

$$0 = \frac{d^2 u_2^{(e)}}{dy^{*2}} + \frac{\nabla \phi_{\mathrm{ext}}}{\eta} \varepsilon \varepsilon_o \frac{d^2 \phi}{dy^{*2}} \tag{4.67}$$

along with the flow boundary conditions for the Stokes–Brinkman equation. This set has the solution

$$\begin{aligned} u_1^{(e)} = C_1 e^{\alpha y^*} + C_2 e^{-\alpha y^*} - \int_0^{y^*} \frac{\nabla\phi_{\text{ext}} e^{\alpha y^*} e^{-\alpha s}}{2\alpha\eta} \left(\delta^2 \rho_f(s) + \varepsilon\varepsilon_o \frac{d^2\phi}{ds^2}\right) ds + \\ \int_0^{y^*} \frac{\nabla\phi_{\text{ext}} e^{-\alpha y^*} e^{\alpha s}}{2\alpha\eta} \left(\delta^2 \rho_f(s) + \varepsilon\varepsilon_o \frac{d^2\phi}{ds^2}\right) ds \end{aligned} \tag{4.68}$$

$$u_2^{(e)} = C_3 + y^* C_4 - \frac{\varepsilon\varepsilon_o}{\eta} \nabla\phi_{\text{ext}} \phi(y^*) \tag{4.69}$$

with constants:

$$C_1 = \frac{1}{2\cosh(\alpha)} \left[\int_0^1 \frac{\nabla\phi_{\text{ext}}}{\alpha\eta} \cosh(\alpha(1-s)) \left(\delta^2 \rho_f(s) + \varepsilon\varepsilon_o \frac{d^2\phi}{ds^2}\right) ds - \frac{\varepsilon\varepsilon_o}{\alpha\eta} \nabla\phi_{\text{ext}} \phi'_\delta \right] \tag{4.70}$$

$$C_2 = -C_1 \tag{4.71}$$

$$C_3 = \int_0^1 \frac{\sinh(\alpha s)}{\cosh(\alpha)} \frac{\nabla\phi_{\text{ext}}}{\alpha\eta} \left(\delta^2 \rho_f(s) + \varepsilon\varepsilon_o \frac{d^2\phi}{ds^2}\right) ds - \frac{\varepsilon\varepsilon_o}{\alpha\eta} \nabla\phi_{\text{ext}} \left(\phi'_\delta \tanh(\alpha) - \alpha\phi_\delta\right) \tag{4.72}$$

$$C_4 = 0 \tag{4.73}$$

Since the final result for $\chi_{21}^{(\text{soft})}$ is written in terms of potential concavity rather than potential, we integrate each constant expression by parts to convert from dependence on the concavity of potential to dependence on the potential. After integrating C_1 by parts twice, the first constant becomes:

$$C_1 = \int_0^1 \frac{\nabla\phi_{\text{ext}}}{2\alpha\eta} \frac{\cosh(\alpha(1-s))}{\cosh(\alpha)} \left(\delta^2 \rho(s) + \alpha^2 \varepsilon\varepsilon_o \phi(s)\right) ds - \frac{\varepsilon\varepsilon_o \nabla\phi_{\text{ext}}}{2\alpha\eta} \phi'_o - \frac{\varepsilon\varepsilon_o \nabla\phi_{\text{ext}}}{2\eta} \phi_o \tanh(\alpha) \tag{4.74}$$

We have removed the potential derivative (ϕ'_δ) at the boundary between the porous layer and the fluid, but gained terms in both the solid wall potential (ϕ_o) and potential derivative (ϕ'_o). We perform a similar procedure with the C_3 constant term, which becomes:

$$C_3 = \int_0^1 \frac{\sinh(\alpha s)}{\cosh(\alpha)} \nabla\phi_{\text{ext}} \frac{1}{\alpha\eta} \left(\delta^2 \rho_f(s) + \alpha^2 \varepsilon\varepsilon_o \phi(s)\right) ds + \nabla\phi_{\text{ext}} \frac{\varepsilon\varepsilon_o}{\eta} \frac{\phi_o}{\cosh(\alpha)} \tag{4.75}$$

With these modified constant terms, we compute the contributions to $\chi_{12}^{(\text{soft})}$ both inside ($I_1 = -\frac{1}{\beta\nabla\phi_{\text{ext}}} \int_0^1 u_1^{(e)}\, dy^*$) and outside of the porous layer ($I_2 = -\frac{1}{\beta\nabla\phi_{\text{ext}}} \int_1^\beta u_2^{(e)}\, dy^*$).

We begin with the outer portion:

$$I_2 = -\frac{1}{\beta\nabla\phi_{\text{ext}}}\int_1^{\beta}\left(C_3 - \frac{\varepsilon\varepsilon_o}{\eta}\nabla\phi_{\text{ext}}\phi(y^*)\right)dy^* \tag{4.76}$$

$$I_2 = \frac{C_3}{\nabla\phi_{\text{ext}}}\left(\frac{1}{\beta} - 1\right) + \frac{\varepsilon\varepsilon_o}{\eta}\frac{1}{\beta}\int_1^{\beta}\phi(y^*)\,dy^* \tag{4.77}$$

Finally,

$$\begin{aligned} I_2 = \int_0^1 \frac{\sinh(\alpha s)}{\cosh(\alpha)}\left(\frac{1}{\beta} - 1\right)\frac{1}{\alpha\eta}\left(\delta^2\rho_f(s) + \alpha^2\varepsilon\varepsilon_o\phi(s)\right)ds + \\ \frac{\varepsilon\varepsilon_o}{\eta}\frac{\phi_o\left(\frac{1}{\beta} - 1\right)}{\cosh(\alpha)} + \frac{\varepsilon\varepsilon_o}{\eta}\frac{1}{\beta}\int_1^{\beta}\phi(y^*)\,dy^* \end{aligned} \tag{4.78}$$

The first integral, I_1, requires significantly more manipulation. Before performing the integration, we combine the terms in equation (4.68) and the relation between C_1 and C_2 (equation (4.71)) to give:

$$\begin{aligned} u_1^{(e)} = 2C_1\sinh(\alpha y) - \int_0^{y^*}\frac{\nabla\phi_{\text{ext}}e^{\alpha y^*}e^{-\alpha s}}{2\alpha\eta}\left(\delta^2\rho_f(s) + \varepsilon\varepsilon_o\frac{d^2\phi}{ds^2}\right)ds \ + \ldots \\ \int_0^{y^*}\frac{\nabla\phi_{\text{ext}}e^{-\alpha y^*}e^{\alpha s}}{2\alpha\eta}\left(\delta^2\rho_f(s) + \varepsilon\varepsilon_o\frac{d^2\phi}{ds^2}\right)ds \end{aligned} \tag{4.79}$$

Then, I_1 becomes:

$$\begin{aligned} I_1 = \frac{2C_1}{\alpha\beta\nabla\phi_{\text{ext}}}(1 - \cosh(\alpha)) + \frac{1}{\beta}\int_0^1\int_0^{y^*}\frac{e^{\alpha y^*}e^{-\alpha s}}{2\alpha\eta}\left(\delta^2\rho_f(s) + \varepsilon\varepsilon_o\frac{d^2\phi}{ds^2}\right)ds\,dy^* - \ldots \\ \frac{1}{\beta}\int_0^1\int_0^{y^*}\frac{e^{-\alpha y^*}e^{\alpha s}}{2\alpha\eta}\left(\delta^2\rho_f(s) + \varepsilon\varepsilon_o\frac{d^2\phi}{ds^2}\right)ds\,dy^* \end{aligned} \tag{4.80}$$

We next place the latter two integral terms in equation (4.80) in the form seen in constant terms C_1, C_2, C_3, and I_2. First, we apply an integration by parts ($\int u\,dv = uv| - \int v\,du$) to the integral terms in (4.80) with $u = \pm\frac{1}{\beta}\int_0^{y^*}\frac{e^{\mp\alpha s}}{2\alpha\eta}\left(\delta^2\rho_f(s) + \varepsilon\varepsilon_o\frac{d^2\phi}{ds^2}\right)ds$ and $dv = \frac{1}{\beta}e^{\pm\alpha y^*}\,dy^*$. The sum of these terms become:

$$\frac{1}{\beta}\int_0^1\frac{\cosh(\alpha(1 - s)) - 1}{\alpha^2\eta}\left(\delta^2\rho_f(s) + \varepsilon\varepsilon_o\frac{d^2\phi}{ds^2}\right)ds \tag{4.81}$$

Following the removal of the double-integral terms, we convert the ϕ'' term to a ϕ term, again with integration by parts:

$$\begin{aligned}\frac{1}{\beta}\int_0^1 \frac{\cosh(\alpha(1-s))-1}{\alpha^2\eta}\varepsilon\varepsilon_o\frac{d^2\phi}{ds^2}\,ds = -\frac{\phi'_o}{\beta}\frac{\varepsilon\varepsilon_o}{\alpha^2\eta}(\cosh(\alpha)-1)-\frac{\phi_o}{\beta}\frac{\varepsilon\varepsilon_o}{\alpha\eta}\sinh(\alpha)+\dots\\ \frac{1}{\beta}\int_0^1\frac{\cosh(\alpha(1-s))-1}{\eta}\varepsilon\varepsilon_o\phi(s)\,ds+\frac{1}{\beta}\int_0^1\frac{\varepsilon\varepsilon_o}{\eta}\phi(s)\,ds\end{aligned}\tag{4.82}$$

Then I_1 becomes:

$$\begin{aligned}I_1 = \frac{2C_1}{\alpha\beta\nabla\phi_{\text{ext}}}(1-\cosh(\alpha))-\frac{\phi'_o}{\beta}\frac{\varepsilon\varepsilon_o}{\alpha^2\eta}(\cosh(\alpha)-1)-\frac{\phi_o}{\beta}\frac{\varepsilon\varepsilon_o}{\alpha\eta}\sinh(\alpha)+\frac{1}{\beta}\int_0^1\frac{\varepsilon\varepsilon_o}{\eta}\phi(s)\,ds+\dots\\ \frac{1}{\beta}\int_0^1\frac{\cosh(\alpha(1-s))-1}{\eta}\left(\delta^2\frac{\rho_f(s)}{\alpha^2}+\varepsilon\varepsilon_o\phi(s)\right)ds\end{aligned}\tag{4.83}$$

Incorporating the form of C_1 removes the ϕ'_o terms and becomes:

$$I_1 = -\varepsilon\varepsilon_o\frac{\phi_o}{\eta}\frac{\tanh(\alpha)}{\alpha\beta}+\frac{1}{\beta}\int_0^1\frac{\varepsilon\varepsilon_o}{\eta}\phi(s)\,ds+\frac{1}{\beta}\int_0^1\frac{1}{\eta}\left(\frac{\cosh(\alpha(1-s))}{\cosh(\alpha)}-1\right)\left(\delta^2\frac{\rho_f(s)}{\alpha^2}+\varepsilon\varepsilon_o\phi(s)\right)ds\tag{4.84}$$

Then, we combine I_1 and I_2:

$$\begin{aligned}I_1+I_2 = -\frac{\varepsilon\varepsilon_o}{\eta}\phi_o\left(\frac{\tanh(\alpha)}{\alpha\beta}+\frac{1-1/\beta}{\cosh(\alpha)}\right)+\frac{\varepsilon\varepsilon_o}{\eta}\phi_o\frac{1}{\beta}\int_0^\beta\frac{\phi(s)}{\phi_o}\,ds+\dots\\ \frac{1}{\beta}\int_0^1\frac{1}{\eta}\left(\frac{\cosh(\alpha(1-s))}{\cosh(\alpha)}-1\right)\left(\delta^2\frac{\rho_f(s)}{\alpha^2}+\varepsilon\varepsilon_o\phi(s)\right)ds+\dots\\ \int_0^1\frac{\sinh(\alpha s)}{\cosh(\alpha)}\left(\frac{1}{\beta}-1\right)\frac{1}{\alpha\eta}\left(\delta^2\rho_f(s)+\alpha^2\varepsilon\varepsilon_o\phi(s)\right)ds\end{aligned}\tag{4.85}$$

Which further becomes:

$$\begin{aligned}I_1+I_2 = -\frac{\varepsilon\varepsilon_o}{\eta}\phi_o\left(\frac{\tanh(\alpha)}{\alpha\beta}+\frac{1-1/\beta}{\cosh(\alpha)}\right)+\frac{\varepsilon\varepsilon_o}{\eta}\phi_o\frac{1}{\beta}\int_0^\beta\frac{\phi(s)}{\phi_o}\,ds+\dots\\ \frac{1}{\beta}\int_0^1\frac{\varepsilon\varepsilon_o}{\eta}\phi_o\left(\delta^2\frac{\rho_f(s)}{\alpha^2\varepsilon\varepsilon_o\phi_o}+\frac{\phi}{\phi_o}\right)\left[\cosh(\alpha s)-1-\frac{\sinh(\alpha s)}{\cosh(\alpha)}(\alpha(\beta-1)+\sinh(\alpha))\right]ds\end{aligned}\tag{4.86}$$

Finally,

$$\begin{gathered}\frac{\chi_{12}^{(\text{soft})}}{-\frac{\varepsilon\varepsilon_o}{\eta}\phi_o} = \frac{1-1/\beta}{\cosh(\alpha)} + \frac{\tanh(\alpha)}{\alpha\beta} - \frac{1}{\beta}\int_0^\beta \frac{\phi(s)}{\phi_o}\, ds - \dots \\ \frac{1}{\beta}\int_0^1 \left(\delta^2 \frac{\rho_f(s)}{\alpha^2\varepsilon\varepsilon_o\phi_o} + \frac{\phi}{\phi_o}\right)\left[\cosh(\alpha s) - 1 - \frac{\sinh(\alpha s)}{\cosh(\alpha)}\left(\alpha(\beta-1) + \sinh(\alpha)\right)\right] ds\end{gathered} \tag{4.87}$$

4.11.3 The Potential at the Porous Layer Boundary

Ohshima and Ohki [89] have derived a relationship between the potential at the edge of the porous layer and the Donnan potential deep within the porous layer. This estimation makes use of a Grahame-like [1] equation for the slope at the porous layer edge. We consider a uniformly charged porous layer in a system with total height much larger than the porous layer thickness $h >> \delta$ ($\beta >> 1$), and in a $z : z$ electrolyte. First, write the Poisson-Boltzmann equation with fixed charge multiplied by the quantity $\frac{1}{2}\frac{d\phi}{dy}$:

$$-\varepsilon\varepsilon_o \frac{1}{2}\frac{d\phi}{dy}\frac{d^2\phi}{dy^2} = \frac{1}{2}F\sum_j c_{j,\infty} z_j e^{-\frac{z_j F\phi}{RT}}\frac{d\phi}{dy} + \frac{1}{2}\rho_f \frac{d\phi}{dy} \tag{4.88}$$

This is equivalently,

$$-\varepsilon\varepsilon_o \frac{d}{dy}\left(\left(\frac{d\phi}{dy}\right)^2\right) = \frac{1}{2}F\sum_j c_{j,\infty} z_j e^{-\frac{z_j F\phi}{RT}}\frac{d\phi}{dy} + \frac{1}{2}\rho_f \frac{d\phi}{dy} \tag{4.89}$$

or, after transforming the differential operator ($\frac{d}{dy} = \frac{d\phi}{dy}\frac{d}{d\phi}$):

$$\int_{y_o}^{y} d\left(\left(\frac{d\phi}{dy}\right)^2\right) = -\int_{\phi_o}^{\phi} \frac{F}{2\varepsilon\varepsilon_o}\sum_j c_{j,\infty} z_j e^{-\frac{z_j F\phi}{RT}} d\phi - \int_{\phi_o}^{\phi} \frac{1}{2\varepsilon\varepsilon_o}\rho_f d\phi \tag{4.90}$$

These integrations are straightforward. In all cases, we choose the point y_o and ϕ_o deep within the porous layer where the electrical potential is given by the Donnan potential, ϕ_D. We also presume that electrical potential is locally uniform. These assumptions hold when the porous layer is uniformly charged, and the point in the porous layer is several Debye lengths away from the porous layer edge. In this way, we ensure that the perturbation introduced into to the electrical potential at the porous layer edge has no effect. We evaluate the second limit at the porous layer edge, indicated with the subscript δ. The result is:

$$\left(\frac{d\phi}{dy}\right)_{\delta}^{2} = \frac{RT}{2\varepsilon\varepsilon_o} \sum_j c_{j,\infty} \left(e^{-\frac{z_j F \phi_\delta}{RT}} - e^{-\frac{z_j F \phi_D}{RT}}\right) + \frac{\rho_f}{2\varepsilon\varepsilon_o} (\phi_D - \phi_\delta) \tag{4.91}$$

After nondimensionalizing this equation (taking the characteristic length scale as λ, and the Debye length as λ_d):

$$\left(\frac{\lambda_d}{\lambda}\right)^2 \left(\frac{d\phi^*}{dy^*}\right)_{\delta}^{2} = \frac{1}{4} \sum_j c^*_{j,\infty} \left(e^{-z_j \phi^*_\delta} - e^{-z_j \phi^*_D}\right) + \frac{\rho^*_f}{2} (\phi^*_D - \phi^*_\delta) \tag{4.92}$$

This equation relates the potential at the porous layer edge to the charge within the layer (ρ^*_f and ϕ_D) as well as the gradient in the electrical potential at the porous layer edge. To determine the potential at the porous layer edge, we simplify the above expression for a $z : z$ electrolyte:

$$\left(\frac{\lambda_d}{\lambda}\right)^2 \left(\frac{d\phi^*}{dy^*}\right)_{\delta}^{2} = \frac{1}{2z^2} \left(\cosh(z\phi^*_\delta) - \cosh(z\phi^*_D)\right) + \frac{\rho^*_f}{2} (\phi^*_D - \phi^*_\delta) \tag{4.93}$$

At the porous layer edge, we can express the gradient in terms of the charge density on the pure fluid side of the porous layer as:

$$\left(\frac{\lambda_d}{\lambda}\right)^2 \left(\frac{d\phi^*}{dy^*}\right)_{\delta}^{2} = \frac{1}{2z^2} \left(\cosh(z\phi^*_\delta) - 1\right) \tag{4.94}$$

Whence,

$$\frac{1}{2z^2} \left(\cosh(z\phi^*_\delta) - 1\right) = \frac{1}{2z^2} \left(\cosh(z\phi^*_\delta) - \cosh(z\phi^*_D)\right) + \frac{\rho^*_f}{2} (\phi^*_D - \phi^*_\delta) \tag{4.95}$$

Using the relation $\rho^*_f = 1/z \sinh(z\phi^*_D)$:

$$\phi^*_\delta = \phi^*_D + \frac{1 - \cosh(z\phi^*_D)}{z \sinh(z\phi^*_D)} = \phi^*_D + f(z, \phi^*_D) \tag{4.96}$$

The results presented to this point also include an expression for the slope at the interface:

$$\left(\frac{\lambda_d}{\lambda}\right)^2 \left(\frac{d\phi^*}{dy^*}\right)_{\delta}^{2} = \frac{1}{2z^2} \left(\cosh(z\phi^*_\delta) - 1\right) \tag{4.97}$$

When $\lambda = \lambda_d$:

$$\left.\frac{d\phi^*}{dy^*}\right|_{y=\delta} = \frac{1}{z}\sqrt{\frac{1}{2}\left(\cosh(z\phi^*_\delta) - 1\right)} = \frac{1}{z}\sinh\left(\frac{z\phi^*_\delta}{2}\right) \tag{4.98}$$

As the Donnan potential becomes very large ($\phi^*_D \geq 4$), the potential at the porous layer boundary limits nearly to the Donnan potential. Then:

$$\left.\frac{d\phi^*}{dy^*}\right|_{y=\delta} = \frac{1}{z}\sinh\left(\frac{z}{2}[\phi^*_D - 1]\right) \tag{4.99}$$

4.11.4 Additional Approximations for $\chi_{ij}^{\text{(soft)}}$

Weakly Resisting Porous Layer

In the limit of a weakly resisting porous layer, $\alpha \ll 1$, we expand equations (4.46) and (4.47) in a Taylor series with α as the small parameter:

$$\frac{\chi_{ij}^{\text{(soft)}}}{-\frac{\varepsilon\varepsilon_o}{\eta}\phi_o} \approx 1 + \alpha^2\left(\frac{1}{6\beta} - \frac{1}{2}\right) + O(\alpha^4) - \frac{1}{\beta}\int_0^\beta \frac{\phi^*}{\phi^*_o}\,dy^* \ + \ldots$$
$$\int_0^1 \left[\left(y^* - \frac{y^{*2}}{2\beta}\right)\left(\alpha^2\frac{\phi^*}{\phi^*_o} + \frac{\rho^*_f}{\phi^*_o\gamma^2}\right) + \alpha^2\frac{\rho^*_f}{\phi^*_o\gamma^2}\frac{4y^{*3}\beta - y^{*4} - 12\beta y^* + 4y^*}{24\beta} + O(\alpha^4)\right] dy^* \tag{4.100}$$

This equation is later simplified to zeroth order in the main document (equation (4.57)).

Strongly Resisting Porous Layer

In a system with a porous layer that strongly resists flow, $\alpha \gg 1$, the boundary terms in equation (4.46), $\frac{1-1/\beta}{\cosh(\alpha)} + \frac{\tanh(\alpha)}{\alpha\beta}$, contribute minimally and may be neglected. This yields:

$$\frac{\chi_{ij}^{\text{(soft)}}}{-\frac{\varepsilon\varepsilon_o}{\eta}\phi_o} \approx -\frac{1}{\beta}\int_0^\beta \frac{\phi^*}{\phi^*_o}\,dy^* - \frac{1}{\beta}\int_0^1 H(y^*;\alpha,\beta)\left(\frac{\phi^*}{\phi^*_o} + \frac{\rho^*_f}{\phi^*_o}\frac{1}{(\alpha\gamma)^2}\right) dy^* \tag{4.101}$$

In the main document, we continue by assuming a uniform free charge density everywhere within the film. This leads to equation (4.62). Continuing from here, we approximate the final term in expression (4.62). In this approximation, we assume the potential everywhere in the porous layer to be constant. The integral term is bounded from below using the edge potential (i.e., (4.96)), ϕ_δ, and above by the Donnan potential, ϕ_D:

$$-\frac{1}{\beta}\frac{\phi_\delta^*}{\phi_o^*}\int_0^1 H(y^*;\alpha,\beta)\,dy^* \leq -\frac{1}{\beta}\int_0^1 \frac{\phi^*}{\phi_o^*}H(y^*;\alpha,\beta)\,dy^* \leq -\frac{1}{\beta}\frac{\phi_D^*}{\phi_o^*}\int_0^1 H(y^*;\alpha,\beta)\,dy^* \tag{4.102}$$

Finally, for a strongly resisting porous layer with $\beta = 1$ and either $\gamma \ll 1$ or $\phi_o^* = \phi_D^*$, equations (4.63) and (4.64) become:

$$\frac{\chi_{ij}^{(\text{soft})}}{-\frac{\varepsilon\varepsilon_o}{\eta}\phi_o} \approx \frac{\alpha - \tanh(\alpha)}{\alpha^3\gamma^2}\frac{\rho_f^*}{\phi_o^*} \tag{4.103}$$

This quantity tends to zero as $\alpha \to \infty$, consistent with restricted transport everywhere in a channel under pressure or electric field forcing.

CHAPTER 5

SURFACE CONDUCTIVITY IN ELECTROKINETIC SYSTEMS WITH POROUS AND CHARGED INTERFACES: BENCHMARKING ANALYTICAL APPROXIMATIONS VS. NUMERICAL RESULTS

5.1 Abstract

We derive an approximate analytical representation of the conductivity for a one-dimensional system with porous and charged layers grafted onto parallel-plates. Our theory improves on prior work by considering porous and charged layers of moderate and weak mechanical resistance to flow, and by applying to porous layers with potentials large and small relative to the thermal voltage $\left(\frac{RT}{F}\right)$. We demonstrate the efficacy of our approximate expression with comparisons to numerical representations of the exact analytical conductivity. Finally, we utilize this conductivity expression, in concert with other components of the electrokinetic coupling matrix, to describe the streaming potential and electroviscous effect in systems with porous and charged layers.

5.2 Introduction

Porous and charged layers are present in a variety of natural [14, 171, 172] and synthetic [49, 122, 173] systems. These porous and charged layers are often utilized in micro- and nanofluidic systems to modify transport or electrokinetic properties of the coated surface [48, 50]. Understanding momentum and charge transport gives predictive capability

---

A manuscript based on the contents of this chapter have been submitted for publication in the journal *Physical Review E*. This is the pre-publication version of the following article: “Surface Conductivity in Electrokinetic Systems with Porous and Charged Interfaces: Benchmarking Analytical Approximations vs. Numerical Results”.

required to engineer systems with porous and charged layers.

Electrokinetic techniques are often implemented to characterize these porous and charged layers [163]. Streaming current [130, 133], streaming potential [100], and conductivity [127, 128] measurements have been performed to extract information on the state of the interface in these systems. These experimental efforts require an analytical [58, 93, 98, 108, 110, 162, 170] and/or numerical [92, 99, 134] framework through which the experimental data is analyzed and interpreted to extract fundamental parameters such as the density and fluid resistance of the porous and charged layer;

Cell conductivities in microfludic and nanofluidic systems are larger than that predicted by the conductivity of the working fluid alone because of the wetted interface. Perturbations of charge and electrical potential are introduced by the solid phases onto the fluid, resulting in two effects on the current flux when a field is applied. First, the electric field exerts a body force on the net charge , which actuates the fluid (electroosmotic flow) and generates a net flux of ions. Second, the charged boundary perturbs the concentration of ions local to the wall, which enhances the ion flux when an external potential is applied.

Relative to the linear field–flux relations, the electrical conductivity is often the most difficult to derive – the conductivity includes both Ohmic and electroosmotic conduction effects and is sensitive to local rather than integrated ion distributions, making most analytical treatments difficult because of the nonlinear nature of the Poisson–Boltzmann equation. In prior works (discussed below), analytical descriptions have required approximations either made from the outset (via a linearized Poisson–Boltzmann equation) or in later stages of analysis through simplified expressions for the charge, potential, and/or velocity distributions.

Previous efforts have created a limited analytical framework for evaluting the conductivity of porous and charged layers. Exact solutions have been obtained only in the limit of small potentials (e.g., using a linearized Poisson-Boltzmann equation) in simplifying geometries. Early works by Donath and Voigt [92] and then Ohshima and Kondo [97] examine streaming current and conductivity for porous and charged layers in semi-infinite rectangular capillaries. Donath and Voigt consider the low-potenital (linearized) limit of the Poisson-Boltzmann equation analytically, and develop a numerical representation of streaming current and conductivity in the nonlinear regime. In their work, Ohshima and Kondo develop approximate analytical descriptions of the conductivity and streaming current with estimated forms of the potential distribution. Keh and Liu [162] develop electrokinetic descriptions of a circular capillary coated with a porous and charged layer in the limit of small potentials, deriving hydraulic, electroosmotic, and electrical conductivities for the linearized limit ($\phi \ll \frac{RT}{F}$). More recently, Duval and van Leeuwen [98] and Duval [99] have extended the analyses by previous workers to porous and charged layers with variable densities of hydraulic resistance and charge, developing analytical linearized [98] and nonlinear [99] theories for charge and momentum transport. Dukhin and co-authors have developed conductivity expressions for porous and charged layers under a variety of conditions. Early analyses of these systems [58, 108] consider a porous layer with a uniform density of charged sites exhibiting a Darcian fluid resistance, but permitting variable site charging by potential-determining ions (e.g., H^+ for Brønsted acids). These results have been extended to consider salt condensation [170], and also the distribution of charge [110] (when combined with other electrokinetic measurements). Analytical simplifications in these theories are made under the assumption that the thickness of the porous layer is larger than the characteristic length scales over which fluid velocity varies within the porous layer (for both pressure- and electric field-driven forcing). Furthermore, these analyses are simplified in the limit of porous layer charges and potentials that are large in magnitude, as co-ions are assumed to be excluded from the porous and charged layer.

In this work, we develop an approximate analytical description of the conductivity applicable for porous and charged layers of arbitrary mechanical resistance and arbitrary electrical potential. We formulate our approximate analytical expression using a convenient set of dimensionless parameters to illustrate limiting behaviors of the conductivity. Both Ohmic and electroosmotic contributions to the conductivity are considered; we demonstrate the superiority and accuracy of our result through comparisons with numerically computed values of the conductivity. Finally, we combine our conductivity expression with our prior work [174], describing the hydraulic conductivity and streaming current coefficients in systems with porous and charged layers, to describe the streaming potential and electroviscous coefficients in these systems.

This paper is outlined as follows: In section two, we describe electrokinetic and transport properties of porous and charged layers, and develop a dimensionless integral relation for the electrical conductivity. In section three, we recount the Dukhin theory of conductivity in soft and charged layers; We then compare the Dukhin theory against numerical computations of the conductivity in section four. In section five, we present an analytical expression for system conductivity with a porous and charged layer, which demonstrates improved agreement with numerically computed values. In section six, we use the approximate analytical form of the conductivity to predict streaming potential and the electroviscous effect in systems with porous and charged layers.

5.3 Electrokinetic Descriptions of Systems with Porous and Charged Layers

Flows over and through charged regions give rise to several electrokinetic phenomena. The various phenomena are succinctly described by the electrokinetic coupling matrix (EKCM):

$$\begin{pmatrix} Q/A \\ I/A \end{pmatrix} = \begin{bmatrix} \chi_{11} & \chi_{12} \\ \chi_{21} & \chi_{22} \end{bmatrix} \begin{pmatrix} -\langle \nabla p \rangle \\ -\langle \nabla \phi_{\text{ext}} \rangle \end{pmatrix} \tag{5.1}$$

Here, Q/A and I/A are volume and current flux densities, which relate to the pressure and electric potential gradients $-\nabla p$ and $-\nabla \phi_{\text{ext}}$ through the various χ constants. These gradients may act alone or in concert – in which case fluxes result from the superposition of the applied gradients. The constant χ_{11} is the hydraulic conductance, communicating the ability of the system to transport a volume flux under the action of a pressure gradient, χ_{22} is the electrical conductance, describing the ability of the system to transport electrical charge under the application of an electrical potential gradient. Terms χ_{12} and χ_{21} are cross-coupling (or conjugate) coefficients that govern electroosmotic flow and streaming current, respectively. The cross-coupling coefficients are equal, $\chi_{12} = \chi_{21}$, following Onsager reciprocity. Additionally, we use angle brackets to denote area-averaged vector fluxes of pressure and electrical potential, i.e., $\langle \nabla p \rangle = \frac{1}{A} \int_S \nabla p \cdot \vec{n} \, dA$ and $\langle \nabla \phi_{\text{ext}} \rangle = \frac{1}{A} \int_S \nabla \phi_{\text{ext}} \cdot \vec{n} \, dA$, where $\vec{n}$ is the normal to the cross-sectional area A.

5.3.1 Momentum and Potential Distributions in Sytems with Porous and Charged Layers

Compared with a simple interface, interfaces with porous and charged layers exhibit different the distributions of momentum, charge, and potential. The porous layer contributes an additional resistance to the fluid percolating the pores, and the wetted area of the porous material can exhibit a fixed charge. We model the flow inside the porous layer with the Brinkman equation [104]. Outside the porous layer, the constant $k \to 0$ and the Stokes equation is recovered. The Brinkman approach is advantageous in that it permits modeling of the no-slip condition at the solid surface beneath the porous layer, as well as stress and velocity matching conditions at the boundary between the pure fluid and porous layer. The Brinkman approach is preferred to the Beavers-Joseph boundary condition [164], which also provides for a coupling between flow in a porous medium and flow in a bulk fluid. The Beavers-Joseph condition assumes a Darcian flow within the porous layer, and does not allow for the no-slip condition at the rigid boundary. Both the Brinkman equation and Beavers-Joseph condition are approximations of the flow at the interface between the porous layer and pure fluid; the validity and merit of these conditions has been widely discussed in the literature [107,148,165,166,168,169,175]. We write the Brinkman equation as:

$$0 = -\nabla p - k\mathbf{u} + \eta\nabla^2\mathbf{u} - \rho_e(\mathbf{x})\nabla\phi_{\text{ext}} \tag{5.2}$$

Here, $\mathbf{u}$, in the pure fluid and porous layer regions; in both parts of the domain, the fluid has viscosity η, but only the porous region exhibits a volumetric resistance, parameterized by k. This approximation captures both the resistance effects of the porous medium and the kinematic and stress conditions at the porous layer boundaries. The Brinkman equation includes forcing from a pressure gradient, ∇p, and localized momentum production as the free charge density, $\rho_e(\mathbf{x})$, responds to variations in an external potential,

$\nabla\phi_{\text{ext}}$.

The Poisson equation describes the distribution of potential, ϕ, in space, and depends upon the distributions of free, $\rho_e(\mathbf{x})$, and fixed, $\rho_f(\mathbf{x})$, charge:

$$\nabla \cdot (-\varepsilon\varepsilon_o \nabla\phi) = \rho_e(\mathbf{x}) + \rho_f(\mathbf{x}) \tag{5.3}$$

Terms ε_o and ε denote the vacuum permittivity and dielectric constant of the medium. When chemical equilibrium applies, the free charge density is written using a Boltzmann distribution for the ions:

$$\rho_e(\mathbf{x}) = F \sum_j c_{j,\infty} z_j e^{-\frac{z_j F \phi(\mathbf{x})}{RT}} \tag{5.4}$$

Where $c_{j,\infty}$ and z_j are the bulk concentration and valence of the j^{th} ionic component, R is the ideal gas constant, T is the absolute temperature, and F is Faraday's constant.

We introduce scales for many of the quantities in equations (5.2) and (5.3), to render several terms dimensionless. The system we consider (see figure 5.1) has a porous ($k \neq 0$) and charged ($\rho_f \neq 0$) layer of thickness δ, and we use δ as a characteristic length scale in equations (5.2) and (5.3). We nondimensionalize the charge densities by $2FI_c$, where $I_c = {}^1\!/_2 \sum_i z_i^2 c_{i,\infty}$ is the ionic strength of solution. Finally, we nondimensionalize ϕ by the thermal voltage to obtain $\phi^* = \frac{F\phi}{RT}$. With these modifications, the governing equations become:

$$0 = -\nabla p \frac{\delta^2}{\eta} - \frac{k\delta^2}{\eta}\mathbf{u} + \nabla^{*2}\mathbf{u} - 2FI_c\rho_e^*(\mathbf{x}^*)\nabla\phi_{\text{ext}} \tag{5.5}$$

$$\frac{\lambda_D^2}{\delta^2}\nabla^* \cdot (-\nabla^*\phi^*) = \rho_e^*(\mathbf{x}^*) + \rho_f^*(\mathbf{x}^*) \tag{5.6}$$

The fluid velocity, pressure, and external electric field are dimensional in this form. In equation (5.5), we define a penetration length $\lambda_o = \sqrt{\frac{\eta}{k}}$, representing the depth of momentum penetration from the pure fluid phase into the porous layer. Further, we define a dimensionless parameter $\alpha = \frac{\delta}{\lambda_o} = \sqrt{\frac{k\delta^2}{\eta}}$ to parameterize this behavior. Additionally, we recognize a ratio of length scales in equation (5.6), $\gamma = \frac{\lambda_D}{\delta}$, which relates the thickness of the electrical decay to the thickness of the porous layer.

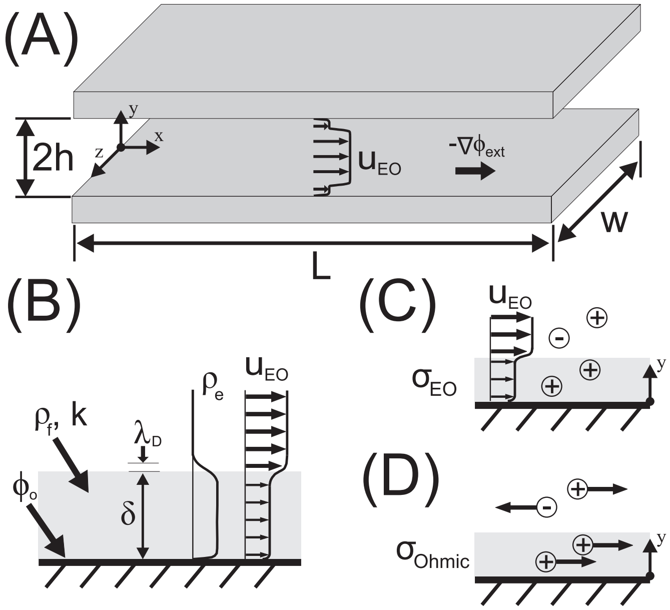

Figure 5.1: Schematic of the parallel-plate cell considered in this work. In (A), the geometric definition of the cell with sample electroosmotic velocity profile u_{EO} resulting from an applied potential gradient, $-\nabla\phi_{\text{ext}}$. The velocity profile is retarded near the wall by the the porous and charged layer, shown in (B) with associated lengths and the free charge density resulting from mobile charges in the bulk and porous and charged regions. In (C) and (D), diagrams of the electroosmotic and Ohmic conduction mechanisms, respectively. Electroosmotic conduction results from the transport of charge by bulk fluid motion, Ohmic conduction results by electrophoresis of the ions; excess free (positive) charges in the porous layer are balanced by bound fixed charge to maintain electroneutrality.

Discontinuous properties at the boundary between pure fluid ($k = 0, \rho_f = 0$) and porous regions ($k \neq 0, \rho_f \neq 0$) of the system require that equations (5.2) and (5.3) be solved separately in each domain and then connected via boundary conditions: No-slip at the rigid interface beneath the porous layer, no-slip at the interface between the porous layer and the pure fluid, stress matching at the interface between the porous layer and the pure fluid, and zero stress at the channel centerline along the direction of the flow. For a one-dimensional electrokinetic cell formed by infinite parallel plates of separation $2h$, or nondimensional separation $2\beta = \frac{2h}{\delta}$, and a porous layer of thickness $\delta^* = 1$, these conditions become:

$$u_1(0) = 0 \tag{5.7}$$

$$\left.\frac{du}{dy^*}\right|_{y^*=\beta} = 0 \tag{5.8}$$

$$u_1(1) = u_2(1) \tag{5.9}$$

$$\left.\frac{du_1}{dy^*}\right|_{y^*=1} = \left.\frac{du_2}{dy^*}\right|_{y^*=1} \tag{5.10}$$

Similar boundary conditions follow when solving equations (5.3) and (5.4):

$$\phi_1(0) = \phi_o \tag{5.11}$$

$$\left.\frac{d\phi_2}{dy^*}\right|_{y^*=1} = 0 \tag{5.12}$$

$$\phi_1(1) = \phi_2(1) \tag{5.13}$$

$$\varepsilon_1\left.\frac{d\phi_1}{dy^*}\right|_{y^*=1} = \varepsilon_2\left.\frac{d\phi_2}{dy^*}\right|_{y^*=1} \tag{5.14}$$

The boundary conditions in (5.7) through (5.10) and (5.11) through (5.14) close equations (5.5) and (5.6). Finally, the boundary conditions may be combined with assumptions about the porous layer to produce specific conditions on the potential within the system; chiefly, the Donnan and boundary potentials.

ϕ_D^*: The Donnan Potential A special case of (5.3) occurs when the gradient of potential vanishes within the porous layer. Typically, this will occur when the charged layer is uniformly charged and thick relative to the characteristic decay length of potential (the Debye length) in the solution. In this limit, the fixed and free charges balance:

$$0 = \rho_e^*(\mathbf{x}^*) + \rho_f^*(\mathbf{x}^*) \tag{5.15}$$

The potential satisfying the condition imposed in (5.15) is the Donnan potential, ϕ_D^*; for a $z : z$ electrolyte in which the Boltzmann distribution holds, the balance in (5.15) yields:

$$\phi_D^* = \frac{1}{z}\operatorname{arcsinh}\left(z\rho_f^*\right) \tag{5.16}$$

ϕ_δ^***: The Boundary Potential** The boundary potential, ϕ_δ^*, is the potential at the edge of the porous layer terminating into solution. Under certain conditions, depending upon the distribution of the fixed charge in the porous layer and the potential deep within the porous layer and far away from the boundary, this boundary potential can be written exactly. This was first done by Ohshima and Kondo [93], using a Grahame-equation-type approach. We repeat their result here, assuming that the charges of a $z:z$ electrolyte follow the Boltzmann distribution:

$$\phi_\delta^* = \phi_D^* + \frac{1}{z}\frac{1 - \cosh\left(z\phi_D^*\right)}{\sinh\left(z\phi_D^*\right)} \tag{5.17}$$

5.3.2 General Conductivity Expressions

Electroosmotic and electrophoretic transport determine the magnitude of conducted current, *viz*:

$$\left.\frac{I}{A}\right|_{\nabla p=0} = \chi_{22}\left(-\langle\nabla\phi_{\text{ext}}\rangle\right) \tag{5.18}$$

Where the proportionality constant χ_{22} contains both Ohmic and electroosmotic contributions:

$$\chi_{22} = \sigma_{\text{EO}} + \sigma_{\text{Ohmic}} \tag{5.19}$$

The electroosmotic transport contribution is determined by the integrated convolution of free-charge density and electroosmotic velocity:

$$\sigma_{\text{EO}} = \frac{1}{-\langle\nabla\phi_{\text{ext}}\rangle A}\int_S \rho_e(\mathbf{x})\mathbf{u}^{(e)}\cdot\vec{n}\,dA \tag{5.20}$$

The Ohmic component depends upon the concentrations, c_i, and mobilities, μ_i, of all ions everywhere in the domain:

$$\sigma_{\text{Ohmic}} = \frac{1}{\langle\nabla\phi_{\text{ext}}\rangle A}F\sum_i |z_i|\,\mu_i\int_S c_i\nabla\phi_{\text{ext}}\cdot\vec{n}\,dA \tag{5.21}$$

Here, we have expressed σ_{Ohmic} to permit a variable electric field, but in all future formulations we will assume $\nabla\phi_{\text{ext}}$ to be uniform.

For our parallel–plate system, we reduce these 3D equations to 1D, with $0 \leq y \leq h$ for one half of the channel. Then, for the electroosmotic component:

$$\sigma_{\text{EO}} = \frac{-1}{h\langle\nabla\phi_{\text{ext}}\rangle}\int_0^h \rho_e(y)u^{(e)}(y)\,dy \tag{5.22}$$

We convert to dimensionless variables using $\hat{u}^{(e)} = \frac{u^{(e)}}{\frac{\varepsilon\varepsilon_o}{\eta}\phi_o\langle-\nabla\phi_{\text{ext}}\rangle}$. Then,

$$\sigma_{\text{EO}} = \left(\frac{4}{3}FI_c\frac{\varepsilon\varepsilon_o}{\eta}\phi_o\right)\frac{1}{\beta}\int_0^\beta \frac{3}{2}\rho_e^*\hat{u}^{(e)}\,dy^* \tag{5.23}$$

The parenthetical factor in equation (5.23) serves as a scale for the electroosmotic conductivity, as a charge density multiplied by a Smoluchowski-like mobility using the wall potential. The fraction $\frac{4}{3}$ has been factored for convenience. Similarly, with the addition of a scale for the concentration, $c_i^* = \frac{c_i}{I_c}$, we write the Ohmic conductivity as:

$$\sigma_{\text{Ohmic}} = \frac{1}{\beta}FI_c\sum_i |z_i|\,\mu_i\int_0^\beta c_i^*\,dy^* \tag{5.24}$$

The Ohmic conductivity in equation (5.24) presents a similar charge scale (FI_c), but a mobility that is based on charge rather than potential [1]:

$$\mu_i = \frac{|z_i|e}{6\pi\eta r_i} \tag{5.25}$$

We can convert this mobility to a potential by considering a bare ion (e.g., Na$^+$) of valence z_i and radius r_i suspended in a solvent with dielectric constant ε. The bare ion generates an electric field $E(r) = \frac{1}{4\pi\varepsilon\varepsilon_o}\frac{ze}{r^2}$, and the potential at the isolated ion is $\phi_i = -\int_\infty^{r_i}\frac{1}{4\pi\varepsilon\varepsilon_o}\frac{z_ie}{r_i^2}\,dr$. Then,

$$\phi_i = \frac{1}{4\pi\varepsilon\varepsilon_o}\frac{z_ie}{r_i} = \frac{3}{2}\left(\frac{1}{6\pi\varepsilon\varepsilon_o}\frac{z_ie}{r_i}\right) = \frac{3}{2}\mu_i\frac{\eta}{\varepsilon\varepsilon_o}\frac{z_i}{|z_i|} \tag{5.26}$$

We tabulate this value for several ionic species in table 5.1. Introducing the ionic potential into equation (5.24) we obtain:

$$\sigma_{\text{Ohmic}} = \left(\frac{4}{3}FI_c\frac{\varepsilon\varepsilon_o}{\eta}\right)\frac{1}{\beta}\sum_i z_i\phi_i\int_0^\beta \frac{c_i^*}{2}\,dy^* \tag{5.27}$$

Ion	$\mu_i \times 10^7 \left[\frac{\text{m}^2}{\text{s-V}}\right]$	ϕ_{ion} [mV]	ϕ^*_{ion}[-]
H^+	3.625	790.06	30.76
K^+	0.762	166.05	6.46
Na^+	0.519	113.18	4.40
OH^-	2.050	-446.79	-17.39
Cl^-	0.791	-172.44	-6.75
NO_3^-	0.740	-161.36	-6.28

Table 5.1: Mobilities [1] and tabulated potentials for ions, at 25 [C]. $\phi^*_{\text{ion}} = \frac{F\phi_i}{RT}$

In equation (5.27) we again identify a parenthetical factor, absent a potential, which generally may not be factored out of the sum across the various ionic species. To resolve this, we introduce an average ionic potential:

$$\hat{\phi} = \frac{1}{n}\sum_i z_i\phi_i \tag{5.28}$$

Then, upon introducing this scale into the sum of equations (5.23) and (5.27) we obtain:

$$\chi^*_{22} = \frac{\chi_{22}}{\frac{4}{3}FI_c\frac{\varepsilon\varepsilon_o}{\eta}\hat{\phi}} = \frac{\sigma_{\text{EO}} + \sigma_{\text{Ohmic}}}{\frac{4}{3}FI_c\frac{\varepsilon\varepsilon_o}{\eta}\hat{\phi}} = \frac{1}{\beta}\frac{\phi_o}{\hat{\phi}}\int_0^\beta \frac{3}{2}\rho^*_e\hat{u}^{(e)}\,dy^* + \frac{1}{\beta}\sum_i \frac{\phi_i z_i}{\hat{\phi}}\int_0^\beta \frac{c^*_i}{2}\,dy^* \tag{5.29}$$

For a $z:z$ electrolyte, with $\phi_+ = -\phi_- = \phi_\pm$ equation (5.29) reduces to:

$$\frac{\chi_{22}}{\frac{4}{3}FI_c\frac{\varepsilon\varepsilon_o}{\eta}z\phi_\pm} = \frac{\sigma_{\text{EO}} + \sigma_{\text{Ohmic}}}{\frac{4}{3}FI_c\frac{\varepsilon\varepsilon_o}{\eta}z\phi_\pm} = \frac{1}{\beta}\frac{\phi_o}{z\phi_\pm}\int_0^\beta \frac{3}{2}\rho^*_e\hat{u}^{(e)}\,dy^* + \frac{1}{\beta}\int_0^\beta \cosh\left(\frac{z\phi F}{RT}\right)dy^* \tag{5.30}$$

In equation (5.30) we have produced an expression for the conductivity of the solvent–interface system accounting for electroosmotic and Ohmic conduction, in which the impact of the wall potential and mobility of the ionic components are readily evaluated.

5.3.3 The Dukhin Model for Conductivity in Systems with Porous and Charged Layers

Dukhin and co-workers [58, 108, 110, 170] have developed a theory for the conductivity of quasi-one-dimensional systems with porous and charged layers. Their work combines expressions for the Ohmic and electroosmotic conductivities within the porous and charged layer with the Bikerman result [73] outside of the porous and charged layer to describe the conductivity of entire channel. The primary assumptions in the Dukhin theory are (i) that the porous layer is thick relative to the Debye length, to justify a uniform potential within the porous layer, and (ii) the channel is large relative to the Debye length such that the potential at the channel center vanishes. Dukhin, *et al.* have also relaxed some of these assumptions, examining charge-bearing layers with pH-dependent charge densities [58, 108].

The conductivity consists of contributions from the surface and bulk:

$$\chi_{22} = \chi_{22}^{\text{bulk}} + \chi_{22}^{\text{surf}} \tag{5.31}$$

The bulk conductivity is described with the ionic mobility and concentration of ionic species unperturbed by the system boundaries,

$$\chi_{22}^{\text{bulk}} = F \sum_{j} |z_j| \mu_i c_{i,\infty} \tag{5.32}$$

Surface conductivity effects are denoted with superscipts 'i' and 'o' referring, respectively, to those occuring inside and outside of the porous and charged layer, and consist of Ohmic and electroosmotic conduction:

$$\chi_{22}^{\text{surf}} = \chi_{22}^{\text{surf,o}} + \chi_{22}^{\text{surf,i}} \tag{5.33}$$

$$\chi_{22}^{\text{surf,o}} = \sigma_{\text{EO}}^{\text{surf,o}} + \sigma_{\text{Ohmic}}^{\text{surf,o}} \tag{5.34}$$

$$\chi_{22}^{\text{surf,i}} = \sigma_{\text{EO}}^{\text{surf,i}} + \sigma_{\text{Ohmic}}^{\text{surf,i}} \tag{5.35}$$

In the Dukhin analysis [170], $\chi_{22}^{\text{surf,o}}$ is given by Bikerman's result [73] for a $z : z$ electrolyte bounded by well-spaced walls ($\lambda_D \ll h$) with potential ϕ_δ:

$$\chi_{22}^{\text{surf,o}} = 2\frac{\lambda_D}{h} z^2 F c_\infty \mu_\pm \left(1 + \frac{3m}{z^2}\right)\left[\cosh\left(\frac{zF\phi_\delta}{2RT}\right) - 1\right] \tag{5.36}$$

Here, $\mu_\pm$ is the mobility of the cation/anion pair, and c_∞ is the bulk concentration for each component. The parameter $m = \frac{RT}{F}\frac{2\varepsilon\varepsilon_o}{3\eta\mu_\pm}$ relates the relative contributions of excess Ohmic and electroosmotic conductivities: $\sigma_{\text{Ohmic}}^{\text{surf,o}} = \frac{3m}{z^2}\sigma_{\text{EO}}^{\text{surf,o}}$.

The inner Ohmic and electroosmotic conduction terms (equation (5.35)) are written assuming a uniformly charged porous layer. Further, the electroosmotic term assumes a porous layer flow dominated by the resistance of the porous material, rather than viscous effects, implying $\delta \gg \sqrt{\frac{\eta}{k}}$. Then,

$$\sigma_{\text{Ohmic}}^{\text{surf,i}} = 2\frac{\delta}{h}\mu_\pm z c_\infty F\left[\cosh\left(\frac{zF\phi_D}{RT}\right) - 1\right] \tag{5.37}$$

$$\sigma_{\text{EO}}^{\text{surf,i}} = \frac{\delta}{h}\frac{\rho_f^2}{k} \tag{5.38}$$

Finally, using the scalings developed in the previous section, we can write the dimensionless form of the Dukhin theory for a $z : z$ electrolyte:

$$\chi_{22,D}^{*} = \frac{1}{z^2}\left\{1 + \frac{\gamma}{\beta}(z + 3m)\left[\cosh\left(\frac{z}{2}\phi_\delta^{*}\right) - 1\right] + \frac{1}{\beta}\left[\cosh(z\phi_D^{*}) - 1\right] + \frac{1}{\beta}\frac{3}{2}\frac{\sinh^2(z\phi_D^{*})}{\alpha^2\gamma^2}\frac{1}{z\phi_\pm}\right\} \tag{5.39}$$

Equations (5.31) through (5.38) form Dukhin's theory for the conductivity of systems with porous and charged layers when (i) the porous layer is uniformly charged, (ii) the potential in the porous layer is uniform, (iii) the porous layer is uniformly resistive, (iv) transport in the porous layer is dominated by the resistance factor k, and (v) the characteristic channel dimension, h, is large relative to both the thickness of the charged layer and the Debye length ($h \gg \lambda_D$ and $h \gg \delta$).

The charging of a system depends upon the chemical nature of the porous layer. Many materials undergo pH-dependent association/dissociation of protons to generate charge, as with oxides [52, 69], and weak acidic and basic [176] groups attached to long-chain polymers. Polymers without easily identified reactive groups also exhibit pH dependence [53], although the charging mechanism for these polymers is not conclusively known [64]. To exhibit pH-independent charge, the charging mechanism of the porous layer must exhibit a pKa that is several units away from the pH of the working solution.

The potential is non-uniform for uniformly charged porous layers. If the porous layer is thin relative to the Debye length ($\delta < \lambda_D$), large variations in potential will exist across the layer. If the rigid wall opposite the fluid exhibits a potential ϕ_o different than ϕ_D, there will be a variation in potential of length $O(\lambda_D)$ near the wall. Finally, even for thick and uniformly charged layers in systems with $\phi_o = \phi_D$, the boundary potential given in equation (5.17) demonstrates that the value of the potential at the film edge is less than the potential within the porous layer. This is significant, because transport within the porous layer is localized to the edge region for porous layers with large hydrodynamic resistance (i.e., $\sqrt{\frac{\eta}{k}} \ll \delta$).

Additionally, it is not the case that every porous layer or film will exhibit transport dominated by the resistance term $-k\mathbf{u}$. When transport within the porous layer is not dominated by the term $-k\mathbf{u}$, equation (5.38) fails. Although it is convenient to estimate the electroosmotic velocity apparent within the porous region, assuming that viscosity has no impact within the porous layer will result in over-estimated electroosmotic velocities for small values of k, producing excessive electroosmotic ion currents.

The impact of these approximations on the estimated conductivity is illustrated best by a full analytical representation of the Ohmic and electroosmotic contriutions, which is not generally available. To resolve this difficulty, we perform numerical simulations of the potential and velocity fields, and compute the conductivity while varying the parameters α, β, γ, as well as the dimensionless charge density and porous layer potential. This approach is described in the next section.

5.4 Numerical Representation of the Conductivity

We implement a numerical representation of the conductivity by solving for the potential and velocity fields specified by equations (5.5) through (5.14) and then applying these fields to equation (5.29) via numerical quadrature. We solve the nonlinear Poisson-Boltzmann equation is solved using a pseudo-steady Crank-Nicholson finite difference scheme as described in [174]; the Brinkman equation, which is linear, is approximated numerically using central differencing and solved using the tridiagonal matrix algorithm.

5.4.1 Conductivity at Low Potential, $\phi^*_D, \phi^*_o \ll 1$

At very low potential everywhere, the porous layer contributes minimally to the overall conductivity. In the scaled units of equation (5.30), this implies a conductivity of unity for a $1 : 1$ electrolyte. We compute the numerical conductivity in this limit (figure 5.2), and observe close agreement with the predicted theoretical value. Agreement is best for channels large in comparison to the porous layer thickness ($\beta = 60$) where electroosmotic effects are mitigated further.

In the limit of very low potential everywhere, the Dukhin theory (equation (5.39)) reduces to the bulk conductivity to zeroth order:

$$\chi^*_{22,D} \to \frac{1}{z^2} + \left(\frac{1}{2\beta} + \frac{z\gamma}{32\beta} + \frac{3}{2z\alpha^2\gamma^2\phi^*_\pm} + \frac{3\gamma}{32\beta\phi^*_\pm}\right){\phi^*_D}^2 + O\left({\phi^*_D}^3\right) \tag{5.40}$$

The porous layer potential has a vanishingly small perturbative effect on the conduc-

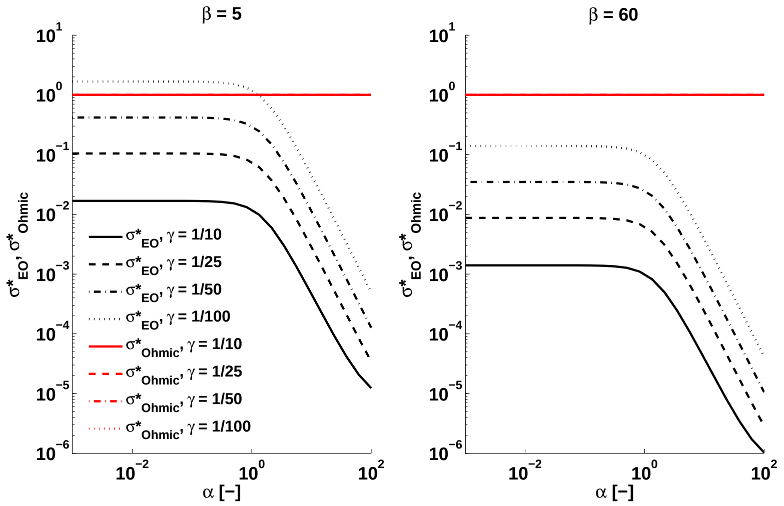

Figure 5.2: Ohmic and electroosmotic conductivies for $\phi_o^* = \phi_D^* = {}^1/_{10}$ for $\beta = 5$ and 60 as a function of α and γ. The computed Ohmic conductivity in all cases is equal to 1, and is invariant to α, β, and γ. The legend at left applies for both plots.

tivity; Excess effects exist only to second order in ϕ_D^*, and are further reduced under the stipulation that $\beta \gg 1$. Equation (5.40) does, however, predict a divergence in the conductivity for $\alpha \to 0$ ($k \to 0$), which is consistent with our earlier observations. In figure 5.2 we do not observe a divergence in the conductivity for small α.

5.4.2 Conductvity at High Potential, $\phi_D^*, \phi_o^* > 1$

The conductivity is increased by excess Ohmic and electroosmotic effects at larger values of the potential in the porous layer. In figure 5.3 we show the numerically computed values of χ_{22}^* for a $1:1$ electrolyte, while varying the parameters α, β, and γ. In particular, figure 5.3 demonstrates stark enhancements in the conductivity for small values of α, γ, and β. Limits of the conductivity as a function of these parameters will be explored in later sections.

The divergence between the Dukhin and numerical representations of the conduc-

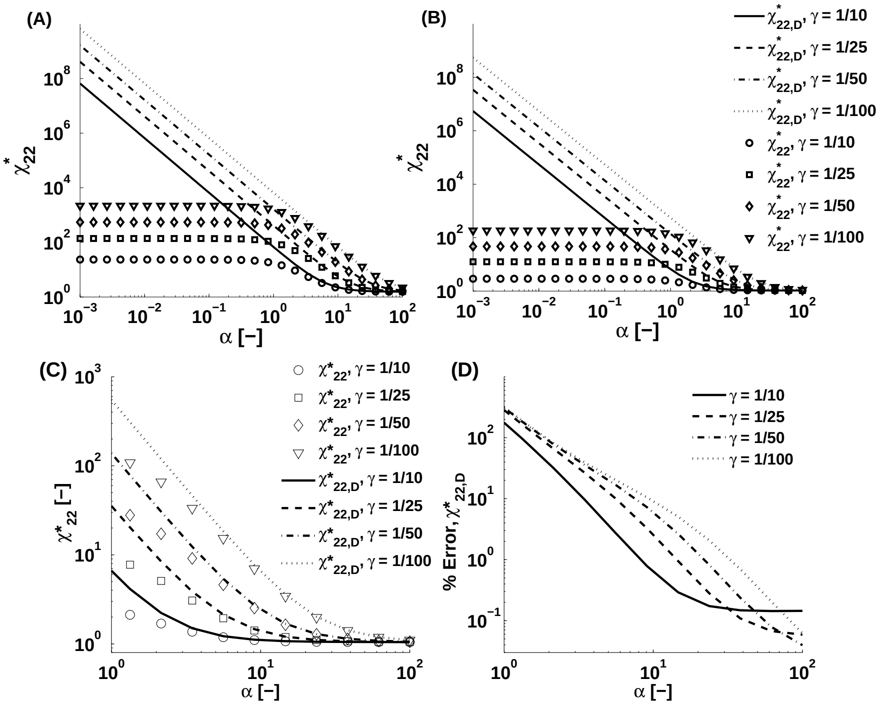

Figure 5.3: Above: χ^*_{22} computed numerically and from the Dukhin theory ($\chi^*_{22,D}$, equation (5.39)) for a 1 : 1 electrolyte with $\phi^*_o = \phi^*_D = 2$ over a range of α and γ. $\beta = 5$ for frame (A), and $\beta = 60$ for (B). In (C), a selection of the data in (B) for $10^0 \leq \alpha \leq 10^2$, with the percent error between the Dukhin and numerically computed conductivities in (D). Note the logarithmic scale.

tivity for $\alpha \ll 1$ is clearly seen in figure 5.3. This divergence between the theories continues until about $\alpha \gtrsim 5$, at which point the porous layer resistance begins to dominate over viscous resistance and the theories exhibit improved agreement. The quality of the match depends upon other parameters as well; Since the Dukhin theory was developed for porous layer much smaller than the cell height ($\beta \gg 1$), the Dukhin theory at $\beta = 60$ matches better than the same theory for $\beta = 5$. In frame (D) of figure 5.3, we quantify the error between the numerical and Dukhin representations of the conductivity for $\beta = 60$ and moderate to large values of α. The errors in this region clearly indicate that the value of α must be large to predict the conductivity with reasonable accuracy.

These comparisons motivate our development of an approximate analytical form for the conductivity proposed in the next section. Our result provides an improved analytical approixmation of the conductivity in all regions of the parameter α. Further, our result is quantitatively adherent to the conductivity beyond the region of the parameter space in which the expression was first derived.

5.5 An Improved Conductivity Approximation

In contrast with the approximate form of χ_{22}^* above, the present work considers both the Darcian and the viscous term when computing the flow profile within the porous and charged layer. Full consideration of viscous effects modifies the electroosmotic term inside of the porous and charged layer; electroosmotic conduction outside of the porous layer, along with Ohmic conduction inside and outside of the charged layer, are not modified.

The electroosmotic condction within the porous and charged layer is:

$$\left(\sigma_{\text{EO}}^{\text{surf,i}}\right)^* = \frac{1}{\beta}\frac{\phi_o^*}{\hat{\phi}^*}\int_0^1 \frac{3}{2}\rho_e^* \hat{u}^{(e)}\, dy^* \tag{5.41}$$

This equation is a dimensionless version of equation (5.23) with integral bounds over the porous and charged layer only. The veocity profile is given from the solution to equations (5.5) through (5.14), since the free charge density must be known to determine the local velocity. Since the Poisson-Boltzmann equation is not soluble in general, we solve equation (5.5) for an arbitrary distribution of fixed charge. We present this result in appendix 5.8.1; a more thorough description of this process is available in [174].

Despite the availability of the function $\hat{u}^{(e)}$, ρ_e^* is unknown and prevents direct integration of (5.41). We then approximate the free charge density within the porous layer as uniform, but still pemit the velocity to be non-uniform:

$$\left(\sigma_{\text{EO}}^{\text{surf,i}}\right)^* \approx \frac{1}{\beta}\frac{\phi_o^*}{\hat{\phi}^*}\frac{3}{2}\rho_e^* \int_0^1 \hat{u}^{(e)}\, dy^* \tag{5.42}$$

This integral of velocity is computed in the appendix. Including this result gives:

$$\left(\sigma_{\text{EO}}^{\text{surf,i}}\right)^* \approx \frac{\phi_o^*}{\hat{\phi}_\pm^*}\frac{3}{2}\rho_e^*\left[-\frac{\tanh(\alpha)}{\alpha\beta} + \frac{1}{\beta}\int_0^1 \frac{\phi^*(s)}{\phi_o^*}\,ds + \frac{1}{\beta}\int_0^1 \left(\frac{\cosh(\alpha(1-s))}{\cosh(\alpha)} - 1\right)\left(\frac{\rho_f^*(s)}{\alpha^2\gamma^2\phi_o^*} + \frac{\phi^*(s)}{\phi_o^*}\right) ds\right] \tag{5.43}$$

We will explore two limiting cases for equation (5.43). In the first approximation, we will assume that the potential everywhere is equal to the Donnan potential, ϕ_D^*. This limit corresponds to the maximum possible electroosmotic conductivity, as it assumes the potential at the porous layer edge (ϕ_δ^*) does not diminish from the potential in the middle of the porous layer. Further, this approximation neglects any possible potential concavity in the porous layer, which is consistent with our earlier approximation of constant ρ_e^*, and implies $\rho_f^* = -\rho_e^*$. Then,

$$\left(\sigma_{\text{EO}}^{\text{surf,i}}\right)^*_{\text{max}} = -\frac{1}{\beta}\frac{3}{2}\frac{\phi_o^*}{\hat{\phi}^*}\rho_f^*\left[\frac{\phi_D^*}{\phi_o^*} - \frac{\tanh(\alpha)}{\alpha} + \left(\frac{\tanh(\alpha)}{\alpha} - 1\right)\left(\frac{\rho_f^*}{\alpha^2\gamma^2\phi_o^*} + \frac{\phi_D^*}{\phi_o^*}\right)\right] \tag{5.44}$$

Finally, we take the boundary potential equal to the Donnan potential, $\phi_o^* = \phi_D^*$,

$$\left(\sigma_{\text{EO}}^{\text{surf,i}}\right)^*_{\text{max}} = \frac{1}{\beta}\frac{3}{2}\left(1 - \frac{\tanh(\alpha)}{\alpha}\right)\frac{{\rho_f^*}^2}{\alpha^2\gamma^2\hat{\phi}^*} \tag{5.45}$$

Similarly, we can write a mimimum bound for the electroosmotic conductivity in the porous and charged layer by assuming a potential within the porous layer that is everywhere equal to the edge potential, ϕ_δ^*. The minimum bound still assumes a fixed charge based on the Donnan potential, but the free charge density is then a function of the edge potential. Thus, $\rho_e^*\left(\phi_\delta^*\right) \neq \rho_f^*$, although ρ_e^* and ρ_f^* are of opposite sign. The minimum is then:

$$\left(\sigma_{\text{EO}}^{\text{surf,i}}\right)^*_{\text{min}} = \frac{1}{\beta}\frac{3}{2}\left(\frac{\tanh(\alpha)}{\alpha} - 1\right)\frac{\rho_e^*\left(\phi_\delta^*\right)\rho_f^*}{\alpha^2\gamma^2\hat{\phi}^*} \tag{5.46}$$

The porous layer contributions to the excess Ohmic conductivity is calculated under the same assumptions used in the electroosmotic conductivity. Starting from equation

(5.27) these limits become,

$$\left(\sigma^{\text{surf,i}}_{\text{Ohmic}}\right)^*_{\text{max}} = \frac{1}{\beta}\sum_i \frac{\phi_i^* z_i}{\hat{\phi}^*}\int_0^1 \frac{1}{2} c^*_{i,\infty} e^{-z_i \phi_D^*}\, dy^* \tag{5.47}$$

$$\left(\sigma^{\text{surf,i}}_{\text{Ohmic}}\right)^*_{\text{min}} = \frac{1}{\beta}\sum_i \frac{\phi_i^* z_i}{\hat{\phi}^*}\int_0^1 \frac{1}{2} c^*_{i,\infty} e^{-z_i \phi_\delta^*}\, dy^* \tag{5.48}$$

Each pair of equations in the porous and charged layer ((5.45) and (5.47) for the maximum, and (5.46) and (5.48) for the minimum) can be combined with expressions for the bulk and Bikerman conductivities to describe the conductivity of a system with porous and charged interfaces. While similar, the descriptive ability of the maximum and minium approximations are wildly different. The maximum approximation is quantitatively superior to the minimum approximation over a wide range of parameter space. This behavior is shown in appendix 5.8.2. Here, we discuss only the maximum approximation, which, for a 1 : 1 electrolyte, is given by:

$$\chi^*_{22,\text{max}} = 1 + \frac{\gamma}{\beta}\left(1 + \frac{1}{\phi^*_\pm}\right)\left[\cosh\left(\frac{\phi^*_\delta}{2}\right) - 1\right] + \frac{1}{\beta}\left[\cosh\left(\phi^*_D\right) - 1\right] + \frac{1}{\beta}\frac{3}{2}\left(1 - \frac{\tanh(\alpha)}{\alpha}\right)\frac{\sinh^2\left(\phi^*_D\right)}{\alpha^2\gamma^2\phi^*_\pm} \tag{5.49}$$

The superiority of our result, equation (5.49), is shown in figure 5.4. We achieve agreement between the numerical and approximate analytical forms of the conductivity for $\alpha \ll 1$, due to the inclusion of viscous effects within the porous layer. Further, at moderate values of α, the approximate analytical form is also superior to the earlier theory, by comparing the magnitude of the errors in figures 5.3D and 5.4D.

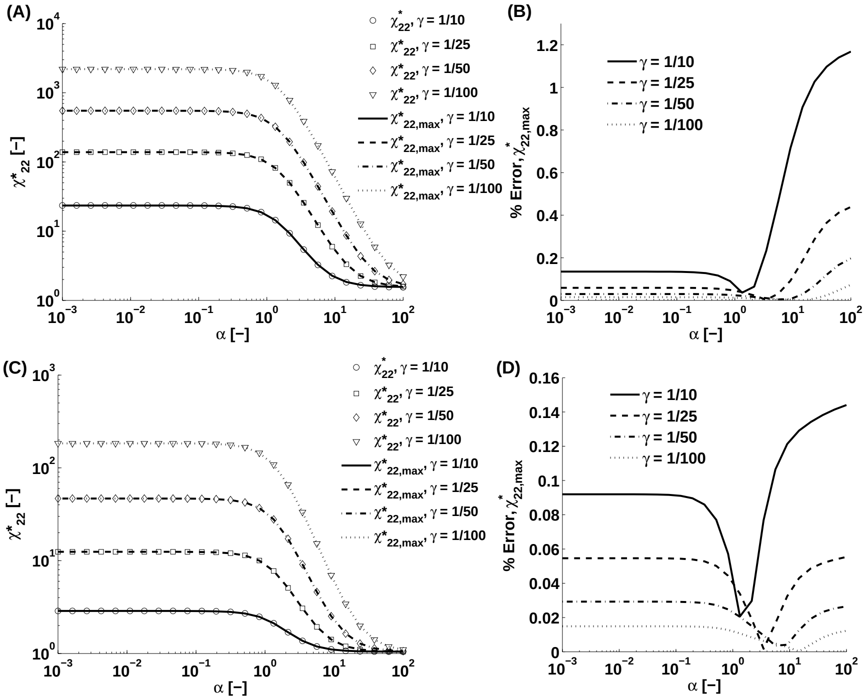

Figure 5.4: Comparison of the improved analytical aproximation (equation (5.49)) for $\beta = 5$ ((A) and (B)) and $\beta = 60$ ((C) and (D)). The fits in both limits of β show excellent agreement over the entire range of α and γ. Computed errors between the approximate and exact numerical results in (C) and (D) are superior to the errors reported in figure 5.3

5.6 Streaming Potential and Electroviscosity in Systems with Porous and Charged Layers

The results derived in the earlier sections, combined with our prior work on χ_{11} and χ_{12} enable quantitative descriptions of all electrokinetic coupling matrix outputs for systems with porous and charged interfaces. Further, our results provide an excellent framework for describing and interpreting these outputs, as we have developed a dimensionless parameter space to describe the EKCM coupling coefficients. The EKCM describes several electrokinetic phenomena:

1. **Pressure-driven flow:** $\left.\frac{Q}{A}\right|_{\langle\nabla\phi_{\text{ext}}\rangle=0} = \chi_{11}\langle-\nabla p\rangle$ A pressure source generates a flow across the channel, with reservoirs at electrical isopotential.
2. **Electroosmotic flow:** $\left.\frac{Q}{A}\right|_{\langle\nabla p\rangle=0} = \chi_{12}\langle-\nabla\phi_{\text{ext}}\rangle$ An electrical potential difference between two channels establishes a flow, with the pressure held constant between the reservoirs (open to atmosphere at both ends).
3. **Streaming current:** $\left.\frac{I}{A}\right|_{\langle\nabla\phi_{\text{ext}}\rangle=0} = \chi_{21}\langle-\nabla p\rangle$ A pressure source generates a flow and convection of ions, in the absence of an electrical potential gradient.
4. **Conductivity:** $\left.\frac{I}{A}\right|_{\langle\nabla p\rangle=0} = \chi_{22}\langle-\nabla\phi_{\text{ext}}\rangle$ An electrical potential difference is applied across the channel generating a current flux in the absence of a pressure gradient.
5. **Streaming Potential:** $\left.\frac{\langle\nabla\phi_{\text{ext}}\rangle}{\langle\nabla p\rangle}\right|_{I=0} = -\frac{\chi_{21}}{\chi_{22}}$ Typically, a pressure is applied across a channel generating an electrical current. Since the ends (reservoirs) of the channel are isolated, a potential is established and back-conduction of current results via the conductivity, χ_{22}. The ratio of current generation, χ_{21}, to conduction defines the streaming potential.
6. **Pressure-driven flow retarded by electroosmosis:** $\left.\frac{Q}{A}\right|_{I=0} = \chi_{11}\left(1 - \frac{\chi_{12}^2}{\chi_{11}\chi_{22}}\right)\langle-\nabla p\rangle$ Often referred to as electroviscosity, pressure driven flow produces a net transport of ions establishing a potential difference opposite the pressure gradient. The potential difference establishes an electroosmotic flow counter to the pressure driven flow. Often, this backflow is referred to as electroviscosity, since it may be interpreted by an enhanced viscosity, although the viscosity of the working fluid does not change.
7. **Conductivity reduced by streaming potential:** $\left.\frac{I}{A}\right|_{Q=0} = \chi_{22}\left(1 - \frac{\chi_{12}^2}{\chi_{11}\chi_{22}}\right)\langle-\nabla\phi_{\text{ext}}\rangle$ Analogous to the previous case, conduction with the absence of a mean flow results in a backflow which manifests as a reduced conductivity.

Three types of phenomena are enumerated above. The first kind, items 1 through 4, consist of phenomena which depend on individual coupling coefficients, having set one gradient term to zero. This set of phenomena is full described by our present (χ_{22}) and prior work [174] (χ_{11}, χ_{12}, and χ_{21}). The second and third set relate forces in fluxes with multiple coupling coefficients. The second set, consisting of item 5, represents conditions where a flux is set to zero, leaving a relation between gradient terms. Finally, the third set, items 6 and 7, permits both gradient terms, but requires either current or flow to vanish, resulting in inteference by flow onto conduction and *vice versa*. We will describe the second and third types of phenomena in systems with porous and charged layers, using the dimensionless parameters ϕ^*, ρ_f^*, α, β, and γ.

5.6.1 Streaming Potential in Systems with Porous and Charged Layers

The streaming potential method is important in micro- and nanoscale flows. Streaming potential measurements are used to characterize the electrokinetic properties of materials and inform device performance; accurate models are required to relate the measured electrical potential and pressure gradients to system properties such as ρ_f and χ_{12}. Consistent with our present and prior [174] work, we apply the scales $\chi_{12} = a_{12}\chi_{12}^*$ and $\chi_{22} = a_{22}\chi_{22}^*$ where $a_{12} = \frac{\varepsilon\varepsilon_o\phi_o}{\eta}$ and $a_{22} = \frac{4}{3}FI_c\frac{\varepsilon\varepsilon_o}{\eta}\hat{\phi}$. These scalings leave the χ terms dimensionless, but since the ratio potential to pressure gradients is dimensional, a factor persists with same units of $\frac{\nabla\phi_{\text{ext}}}{\nabla p}$. Finally, then, we normalize $-\frac{a_{21}}{a_{22}}\frac{\chi_{21}^*}{\chi_{22}^*}$ by the streaming potential of a reference system, choosing a rigid surface at potential ϕ_o and infinite separation, $-\frac{\varepsilon\varepsilon_o}{\eta}\phi_o$. This yields:

$$\left(\left.\frac{\nabla\phi_{\text{ext}}}{\nabla p}\right|_{I=0}\right)^* = \frac{\chi_{21}^*}{\chi_{22}^*} \tag{5.50}$$

We detail the outputs of this analytical expression in figure 5.5 over a range of system parameters.

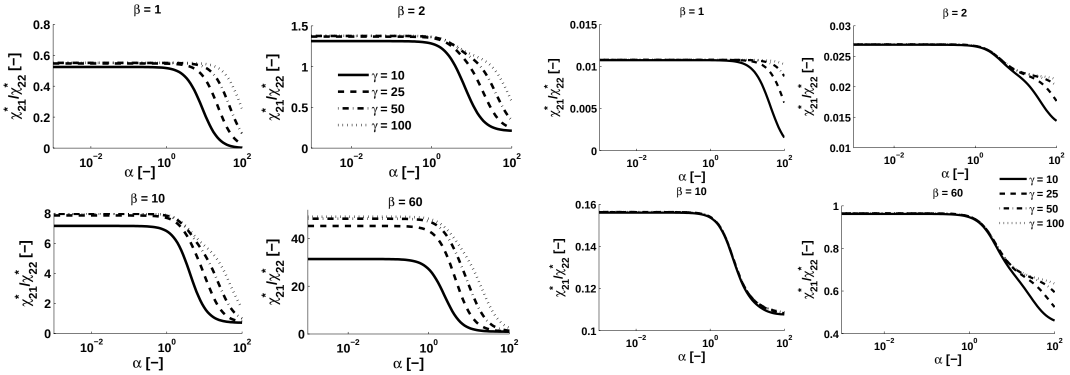

Figure 5.5: The streaming potential ratio, equation (5.50), for $\phi^*_D = 2$ (left four plots) and $\phi^*_D = 5$ (right four plots) over a range of parameters α, β, and γ, as indicated.

The streaming potential is a strong function of the fixed- and free-charge densities. Comparing the leftmost and rightmost four plots in figure 5.5 reveals that increasing the Donnan potential within the porous layer from $\phi^*_D = 2$ to 5 (a factor of 2.5) *decreases* the streaming potential by a factor of ~ 50. This result has strong implications for laboratory measurements – highly charged porous layers will exhibit much smaller voltage drops when compared to rigid surfaces at the same potential for an identically applied pressure. This follows directly from the scaling of the streaming current coefficient, χ^*_{21}, and conductivity with the free charge density: The conductivity term is quadratic in the charge density, while the streaming potential term is only linear. These results further reveal the importance of the parameter α in the behavior of the streaming potential, which is similar to its role in determining χ^*_{22} and χ^*_{21} [174].

5.6.2 Electroviscosity in Systems with Porous and Charged Layers

In the third-class phenomena, the tabulated quantity is not the output produced (fluxes of volume and current), but the amount to which the outputs are reduced by backflows from the surface charge and/or potential. Retarding effects manifest in the multiplicative factor $\Gamma = 1 - \frac{\chi_{12}^2}{\chi_{11}\chi_{22}}$, which is inherently dimensionless. Applying a similar approach as was performed above, now with $a_{11} = \frac{h^2}{3\eta}$, we arrive at:

$$\Gamma = 1 - \frac{\chi_{12}^2}{\chi_{11}\chi_{22}} = 1 - \frac{9}{2}\frac{\gamma^2}{\beta^2}\frac{\phi_o^{*2}}{\hat{\phi}^*}\frac{\chi_{12}^{*\ 2}}{\chi_{11}^*\chi_{22}^*} \tag{5.51}$$

The form on the right hand side of equation (5.51), consisting of entirely dimensionless paramters, is convenient given the framework we have developed to describe the coupling coeffficients. The quantity Γ ranges from zero (fully retarded/frustrated transport) to unity (no retarding/backflow effects).

We plot the electroviscous coefficient Γ in figures 5.6 and 5.7 for moderate $\phi_D^* = 2$ and large $\phi_D^* = 8$ Donnan potentials, as compared to the thermal voltage. To explore this phenomena, we vary the domain extents ($\beta = 1$, 2, 10, 60), the momentum penetration (α) within the layer, along with the characteristic dimension of electrical potential decay relative to the porous layer thickness, γ. The magnitude of electroviscous effects depends on all constants probed; Small channels (β near unity) are most strongly perturbed by electroviscous effects, as the extents of the charged porous layer equal or exceed the extents of the pure fluid region. Electroviscous effects are further enhanced when α is small (as charge trasport is increased in the porous layer) and when $\frac{1}{\gamma} \ll 1$ (charging effects in porous layer persist over a greater distance into the pure fluid). These trends are consistent with our prior description of electroviscosity - the forced motion of ions through the channel establishes a potential, driving a backflow that appears to retard the fluid, or give the appearance of an enhanced fluid viscosity.

The strongest electroviscous effects are realized when $\alpha, \gamma \to 0$ and β is near one. Figure 5.6 suggets this limit is a function of β for small values of α and γ. By expanding Γ with α and γ as small parameters, we can estimate this value:

$$\Gamma_{\alpha,\gamma \ll 1} \sim 1 - \frac{(3\beta - 1)^2}{4\beta^3} + O(\alpha^2) + O(\gamma^2) \tag{5.52}$$

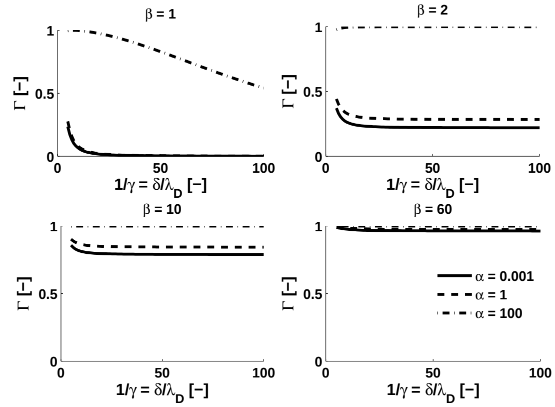

Figure 5.6: The magnitude of electroviscous effects for $\phi_D^* = 2$ plotted over $\frac{1}{\gamma}$ for a range of α (weakly resisting, moderately resisting, and strongly resisting) and β.

Thus, the lower bound for Γ depends chiefly on β. All other parameter (including porous layer charge and potential) are second order effects in α and γ. In particular, the fixed and free charge densities of the porous layer do not contribute. This result follows from the scaling of the coupling coefficients at small α and γ: ${\chi_{21}^*}^2 \sim \rho_e^{*2}$ and $\chi_{22}^* \sim \hat{u}_1^{(e)}\rho_e^* \sim \rho_e^{*2}$, so that the ratio of the two terms does not contain a scaling in the charge density. This behavior is supported by the calculated behavior of the electroviscous coefficient for a porous and charged layer with $\phi_D^* = 8$ shown in figure 5.7, which shows nearly identical behavior in comparison to the data in figure 5.6.

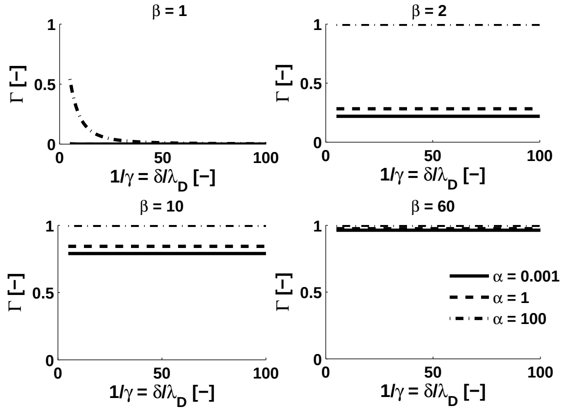

Figure 5.7: Magnitude of the electroviscous coefficient for a porous and charged layer with $\phi_D^* = 8$ plotted over the same parameters as in figure 5.6. The limiting behavior of $\Gamma\left(\phi_D^* = 8\right)$ is nearly identical to $\Gamma\left(\phi_D^* = 2\right)$.

5.7 Conclusion

In this work, we have developed an improved analytical expression for the electrokinetic conductivity of a system with porous and charged interfaces in the presence of an ionic solution. Our results improve upon past efforts, by incorporating the viscous effects within the porous and charged layer. Accounting for these effects enables predictive capability across the entire range of the parameter α, which parameterizes the flow properties of the porous layer. We validate our theory via comparisons with numerical results, where we observe excellent agreement over a wide range of parameter space.

Further, the present work, coupled with our earlier work developing coupling coefficients χ_{11}, χ_{12}, and χ_{21} for the same system, form a coherent framework for evaluating electrokinetic behaviors contained within the electrokinetic coupling matrix (equation (5.1)). To demonstrate this, we consider the electroviscosity and streaming potential and demonstrate the behavior of each using our analytical formulas. The ability to predict these quantities with analytical tools improves the ability of scientists and engineers to design and understand physicochemical systems; our analytical results obviate the need for time consuming numerical modeling.

5.8 Supplementary Information

5.8.1 Electroosmotic velocity and flow in the porous layer

The electroosmotic fluid velocities are computed from the set of equations,

$$0 = \frac{d^2 u_1^{(e)}}{dy^{*2}} - \alpha^2 u_1^{(e)} + \frac{\nabla\phi_{\text{ext}}}{\eta}\left(\varepsilon\varepsilon_o \frac{d^2\phi}{dy^{*2}} + \delta^2\rho_f\right) \tag{5.53}$$

$$0 = \frac{d^2 u_2^{(e)}}{dy^{*2}} + \frac{\nabla\phi_{\text{ext}}}{\eta}\varepsilon\varepsilon_o \frac{d^2\phi}{dy^{*2}} \tag{5.54}$$

Equations (5.53) and (5.54) each apply in distinct parts of the domain, and are coupled with the various boundary conditions discussed in the main document. This set has the solution

$$\begin{aligned} u_1^{(e)} = C_1 e^{\alpha y^*} + C_2 e^{-\alpha y^*} - \int_0^{y^*} \frac{\nabla\phi_{\text{ext}} e^{\alpha y^*} e^{-\alpha s}}{2\alpha\eta}\left(\delta^2\rho_f(s) + \varepsilon\varepsilon_o \frac{d^2\phi}{ds^2}\right) ds + \\ \int_0^{y^*} \frac{\nabla\phi_{\text{ext}} e^{-\alpha y^*} e^{\alpha s}}{2\alpha\eta}\left(\delta^2\rho_f(s) + \varepsilon\varepsilon_o \frac{d^2\phi}{ds^2}\right) ds \end{aligned} \tag{5.55}$$

$$u_2^{(e)} = C_3 + y^* C_4 - \frac{\varepsilon\varepsilon_o}{\eta}\nabla\phi_{\text{ext}}\phi(y^*) \tag{5.56}$$

with constants:

$$C_1 = \int_0^1 \frac{\nabla\phi_{\text{ext}}}{2\alpha\eta}\frac{\cosh(\alpha(1-s))}{\cosh(\alpha)}\left(\delta^2\rho(s) + \alpha^2\varepsilon\varepsilon_o\phi(s)\right) ds - \frac{\varepsilon\varepsilon_o\nabla\phi_{\text{ext}}}{2\alpha\eta}\phi_o' - \frac{\varepsilon\varepsilon_o\nabla\phi_{\text{ext}}}{2\eta}\phi_o \tanh(\alpha) \tag{5.57}$$

$$C_2 = -C_1 \tag{5.58}$$

$$C_3 = \int_0^1 \frac{\sinh(\alpha s)}{\cosh(\alpha)}\nabla\phi_{\text{ext}}\frac{1}{\alpha\eta}\left(\delta^2\rho_f(s) + \alpha^2\varepsilon\varepsilon_o\phi(s)\right) ds + \nabla\phi_{\text{ext}}\frac{\varepsilon\varepsilon_o}{\eta}\frac{\phi_o}{\cosh(\alpha)} \tag{5.59}$$

$$C_4 = 0 \tag{5.60}$$

We then compute $I_1 = -\frac{1}{\beta}\int_0^1 u_1^{(e)}\, dy^*$. Using the relationships between the constants, (5.55) becomes:

$$\begin{aligned} u_1^{(e)} = 2C_1\sinh(\alpha y) - \int_0^{y^*} \frac{\nabla\phi_{\text{ext}} e^{\alpha y^*} e^{-\alpha s}}{2\alpha\eta} \left(\delta^2\rho_f(s) + \varepsilon\varepsilon_o \frac{d^2\phi}{ds^2}\right) ds \ + \ldots \\ \int_0^{y^*} \frac{\nabla\phi_{\text{ext}} e^{-\alpha y^*} e^{\alpha s}}{2\alpha\eta} \left(\delta^2\rho_f(s) + \varepsilon\varepsilon_o \frac{d^2\phi}{ds^2}\right) ds \end{aligned} \tag{5.61}$$

I_1 is then:

$$\begin{aligned} I_1 = \frac{2C_1}{\alpha\beta\nabla\phi_{\text{ext}}}(1-\cosh(\alpha)) + \frac{1}{\beta}\int_0^1\int_0^{y^*} \nabla\phi_{\text{ext}} \frac{e^{\alpha y^*} e^{-\alpha s}}{2\alpha\eta} \left(\delta^2\rho_f(s) + \varepsilon\varepsilon_o \frac{d^2\phi}{ds^2}\right) ds\, dy^* - \ldots \\ \frac{1}{\beta}\int_0^1\int_0^{y^*} \nabla\phi_{\text{ext}} \frac{e^{-\alpha y^*} e^{\alpha s}}{2\alpha\eta} \left(\delta^2\rho_f(s) + \varepsilon\varepsilon_o \frac{d^2\phi}{ds^2}\right) ds\, dy^* \end{aligned} \tag{5.62}$$

This form of I_1 is not ideal, instead, we will manipulate the double integrals by repeatedly applying an integration by parts ($\int u\,dv = uv| - \int v\,du$) . First with $u = \pm\frac{1}{\beta}\int_0^{y^*} \nabla\phi_{\text{ext}} \frac{e^{\mp\alpha s}}{2\alpha\eta}\left(\delta^2\rho_f(s) + \varepsilon\varepsilon_o \frac{d^2\phi}{ds^2}\right) ds$ and $dv = \frac{1}{\beta}e^{\pm\alpha y^*}\, dy^*$. The sum of which become:

$$\frac{1}{\beta}\int_0^1 \nabla\phi_{\text{ext}} \frac{\cosh(\alpha(1-s)) - 1}{\alpha^2\eta} \left(\delta^2\rho_f(s) + \varepsilon\varepsilon_o \frac{d^2\phi}{ds^2}\right) ds \tag{5.63}$$

Integration by parts is then applied to convert the ϕ'' term to a ϕ term:

$$\begin{aligned} \frac{1}{\beta}\int_0^1 \frac{\cosh(\alpha(1-s)) - 1}{\alpha^2\eta} \varepsilon\varepsilon_o \frac{d^2\phi}{ds^2}\, ds = -\frac{\phi_o'}{\beta}\frac{\varepsilon\varepsilon_o}{\alpha^2\eta}(\cosh(\alpha) - 1) - \frac{\phi_o}{\beta}\frac{\varepsilon\varepsilon_o}{\alpha\eta}\sinh(\alpha) + \ldots \\ \frac{1}{\beta}\int_0^1 \frac{\cosh(\alpha(1-s)) - 1}{\eta}\varepsilon\varepsilon_o\phi(s)\, ds + \frac{1}{\beta}\int_0^1 \frac{\varepsilon\varepsilon_o}{\eta}\phi(s)\, ds \end{aligned} \tag{5.64}$$

Then I_1 becomes:

$$\begin{aligned} I_1 = \frac{2C_1}{\alpha\beta}(1-\cosh(\alpha)) - \nabla\phi_{\text{ext}}\frac{\phi_o'}{\beta}\frac{\varepsilon\varepsilon_o}{\alpha^2\eta}(\cosh(\alpha)-1) - \nabla\phi_{\text{ext}}\frac{\phi_o}{\beta}\frac{\varepsilon\varepsilon_o}{\alpha\eta}\sinh(\alpha) + \ldots \\ \frac{1}{\beta}\int_0^1 \nabla\phi_{\text{ext}}\frac{\varepsilon\varepsilon_o}{\eta}\phi(s)\, ds + \ldots \\ \frac{1}{\beta}\int_0^1 \nabla\phi_{\text{ext}}\frac{\cosh(\alpha(1-s)) - 1}{\eta}\left(\delta^2\frac{\rho_f(s)}{\alpha^2} + \varepsilon\varepsilon_o\phi(s)\right) ds \end{aligned}$$

Further simplifications follow after substituting for the C_1 term, yielding:

$$\begin{aligned} I_1 = -\varepsilon\varepsilon_o\nabla\phi_{\text{ext}}\frac{\phi_o}{\eta}\frac{\tanh(\alpha)}{\alpha\beta} + \frac{1}{\beta}\int_0^1 \nabla\phi_{\text{ext}}\frac{\varepsilon\varepsilon_o}{\eta}\phi(s)\, ds \\ + \frac{1}{\beta}\int_0^1 \nabla\phi_{\text{ext}}\frac{1}{\eta}\left(\frac{\cosh(\alpha(1-s))}{\cosh(\alpha)} - 1\right)\left(\delta^2\frac{\rho_f(s)}{\alpha^2} + \varepsilon\varepsilon_o\phi(s)\right) ds \end{aligned} \tag{5.65}$$

We make I_1 fully dimensionless by diviging through by the scale $\frac{\varepsilon\varepsilon_o}{\eta}\phi_o\nabla\phi_{\text{ext}}$. Then,

$$\frac{I_1}{\frac{\varepsilon\varepsilon_o}{\eta}\phi_o\nabla\phi_{\text{ext}}} = -\frac{\tanh(\alpha)}{\alpha\beta}+\frac{1}{\beta}\int_0^1 \frac{\phi(s)}{\phi_o}\,ds+\frac{1}{\beta}\int_0^1\left(\frac{\cosh(\alpha(1-s))}{\cosh(\alpha)}-1\right)\left(\delta^2\frac{\rho_f(s)}{\varepsilon\varepsilon_o\alpha^2\phi_o}+\frac{\phi(s)}{\phi_o}\right)ds \tag{5.66}$$

Introducing scales for the charge density, normalizing the potentials, and recognizing the formation of the dimensionless group γ finally yields:

$$\frac{I_1}{\frac{\varepsilon\varepsilon_o}{\eta}\phi_o\nabla\phi_{\text{ext}}} = -\frac{\tanh(\alpha)}{\alpha\beta}+\frac{1}{\beta}\int_0^1 \frac{\phi^*(s)}{\phi_o^*}\,ds+\frac{1}{\beta}\int_0^1\left(\frac{\cosh(\alpha(1-s))}{\cosh(\alpha)}-1\right)\left(\frac{\rho_f^*(s)}{\alpha^2\gamma^2\phi_o^*}+\frac{\phi^*(s)}{\phi_o^*}\right)ds \tag{5.67}$$

5.8.2 Descriptive Ability of the Maximum and Minimum Approximations for χ_{22}^*

In section 5.5 we describe limiting approximations of the conductivity in porous and charged layers, and assert the superiority of the maximum expression, equation (5.49) for a 1 : 1 electrolyte. In figure 5.8, we compare the maximum and minimum limits demonstrating the efficacy of the maximum limit via direct comparison with numerical results.

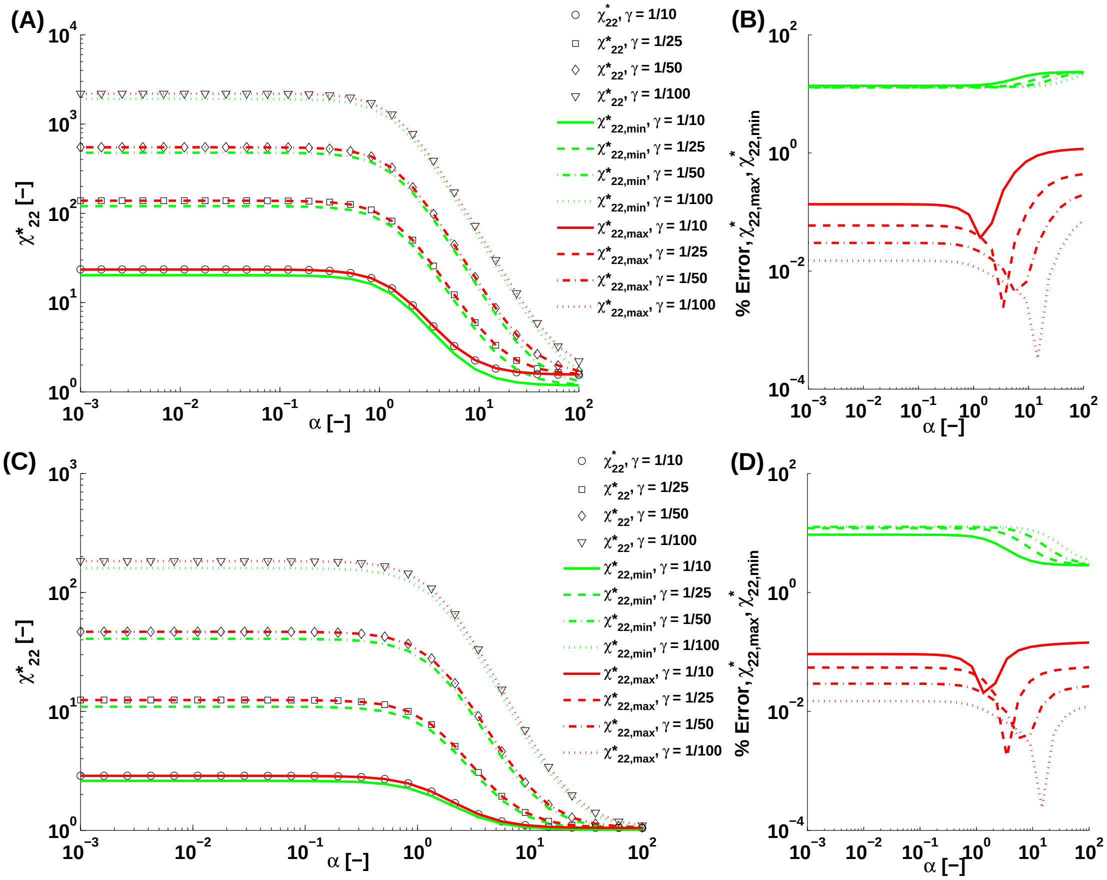

Figure 5.8: Plots of the maximum and minimum estimates of the conductivity vs. numerically computed values as a function of the parameters α, β, and γ for $\phi_D^* = 2$. In pane (A), χ_{22}^* for $\beta = 5$ with associated errors in (B). In pane (C), χ_{22}^* for $\beta = 60$ with errors in (D). In both cases, the maximum limit displays suprior perforamance. Note the logarithmic scale in panes (B) and (D).

CHAPTER 6

ELECTROKINETIC CHARACTERIZATION OF THIN NAFION FILMS

6.1 Abstract

We perform an electrokinetic characterization of $\sim$ 300 nanometer Nafion films deposited on glass slides over a relatively unexplored region of ionic strength and pH. Owing to the small pore size of the Nafion, we probe the Nafion–fluid interface with the streaming potential measurement, and we probe ionic transport through the entire thickness of the Nafion film with the conductivity measurements. By applying a transport model for each of these measurements, we show that the inferred fixed charge density and characteristic fluid resistance length is different in each case. Analyzing our results with data from the literature, we suggest that our result is consistent with a thin Nafion film that is both nonuniform and weakly hydrated. Our regimen of experimentation and analysis may be generalized to characterize other porous and charged layers.

6.2 Introduction

Electrokinetic phenomena, typically characterized by the ζ-potential [52, 53, 60], reveal information on the physicochemical state of an interface in contact with an electrolytic solution. Electrokinetic parameters, like the ζ-potential , are dependent upon the chemistry of the solid–liquid interface; the pKa of acidic and basic groups, ionic nature of the solution [177], and the presence of surfactants [146], contribute strongly to observed electrokinetic effects. The morphology of the interface is also important; in contrast to

---

A manuscript based on the contents of this chapter have been submitted for publication in the journal *Langmuir*. This is the pre-publication version of the following article: “Electrokinetic Investigations of Thin Nafion Films”.

a system with charged rigid walls, systems with porous and charged layers can exhibit increased fluxes of mass and current [163].

The electrokinetic response of a material or system is described by the electrokinetic coupling matrix (EKCM). The EKCM characterizes the response of a system to linear forcing by pressure (∇p) and electrical potential ($\nabla \phi_{\text{ext}}$) gradients:

$$\begin{pmatrix} Q/A \\ I/A \end{pmatrix} = \begin{bmatrix} \chi_{11} & \chi_{12} \\ \chi_{21} & \chi_{22} \end{bmatrix} \begin{pmatrix} -\langle \nabla p \rangle \\ -\langle \nabla \phi_{\text{ext}} \rangle \end{pmatrix} \tag{6.1}$$

The angled brackets take the area average of the component of the gradient normal to the channel cross-section, i.e., $\langle \nabla \phi_{\text{ext}} \rangle = \frac{1}{A} \int_A \nabla \phi_{\text{ext}} \cdot \vec{n} \, dA$. Area-averaged fluxes of volume,$\frac{Q}{A}$, and current, $\frac{I}{A}$, are related to the gradients via coupling coefficients: The hydraulic capacitance, χ_{11}, relates the ease with which flow is actuated by pressure, the electrical conductivity, χ_{22}, relates the applied electric field to the driven current, and the off-diagonal terms χ_{12} and χ_{21} communicate the ability of the system to generate flow from an applied potential gradient and current from an applied pressure; These off-diagonal terms are equal by Onsager reciprocity.

Electrokinetic techniques are often used to measure physical and chemical properties of porous and charged layers [163]. Typically, streaming current, streaming potential, and conductivity measurements are coupled with physical measurements of the porous layer and a numerical [92,93,99] or approximate analytical [58,92,98,108,162,174,178] models of the transport in the layer. Zimmermann, et al. [179] performed a combined analysis to study protein adsorption within a planar electrokinetic cell [67] designed to extract information from streaming current/potential and conductivity measurements. Cordeiro, et al. [131] executed a similar set of experiments with the same electrokinetic cell to measure electrokinetic effects with a thermo-responsive polymer layer. In these and other studies, transport models are applied to the collected data to determine charge densities and other physicochemical properties.

Here, we examine a Nafion polymer film in a pseudo-1D configuration. Nafion is important in a variety of industrial applications, most notably as a cation exchange membrane in fuel cells and in electrolytic filtration [121] assemblies. Further, porous polymers are often used as coatings in capillaries to modify the electrokinetic response of the base material [48–50], and on electrodes to modify transport properties [180]. In these and other applications, the response of the porous and charged polymer to applied fields, imposed flows, and solutions of different compositions is essential to engineer device performance. In this study, we systematically examine a Nafion thin film deposited on a rigid substrate over a range of pH and salt concentrations using the electrokinetic methods of streaming potential and conductivity. Additionally, we execute XPS, ellipsometry, and profilometry measurements to further characterize chemical and physical attributes of the Nafion.

In comparison with most materials used in characterization of porous and charged polymer layers [127, 131, 179], Nafion is expected to exhibit a larger hydraulic resistance. The generally accepted structure of bulk Nafion consists of a percolation network of aqueous blobs and channels lined with hydrophilic sulfonate groups (as described by the Gierke model [15, 181]) interspersed with phases of hydrophobic perfluorinated polymer. Transport occurs in the hydrophilic phase of the material, with a characteristic pore dimension of 1-2 [nm].

We perform streaming potential and conductivity measurements to characterize the electrokinetic behavior of the Nafion–fluid system. Although conductivity measurements are commonly performed on Nafion samples in a variety of electrolytes, these measurements are normally performed in mixtures of [dM] or [M] ionic strength. Our work expands available results in concentration space down to 10 [μM] for conductivity measurements and 100 [μM] for streaming potential measurements.

Further, when performing streaming potential measurements, our electrokinetic cell preferentially probes the surface of the Nafion layer. The streaming potential is a result of ions advected by the flow; For a porous material with large mechanical resistance to flow, like Nafion, we expect that pressure-driven flow will actuate a thin region of fluid within Nafion film at the boundary between the porous layer and pure fluid. As the actuated charge is localized to a thin region of the interface, any properties inferred from the measurement may be attributed to this same thin region.

The significance of measuring Nafion both at the interface and throughout the bulk is reinforced by independent interfacial studies of Nafion. Studying the Nafion-air and Nafion-water interface, Bass, et al. [182] observe a roughening of the Nafion surface (via AFM) when in contact with water, which they attribute to the re-organization of hydrophobic and hydrophilic polymer. This study [182] further observed a change from hydrophobicity to hydrophilicity of the Nafion surface upon hydration, which was also reported by Goswami, et al. [183]. At the solid–Nafion boundary, Dura, et al. [184] observe multilamellar structures at the interface between Nafion and SiO_2 in hydrated films; these multilamellar structures increase in number and thickness as the humidity is increased. Dura, et al. [184] do not observe lamellar structures for similarly prepared films on metal (Au and Pt) surfaces.

Despite their unique ability to infer a localized charge density ρ_f and penetration length λ_o of the Nafion, electrokinetic studies in a planar configuration have not been pursued to date. Instead, researchers have reported the phenomenological zeta potential or the coupling coefficient χ_{21} in a configuration where the flow proceeds through the Nafion polymer [7, 185–187]. Limited results have been obtained in dispersions of Nafion polymer in a mixture of water and aliphatic alcohols by Zhang, et al. [188]; they measure a value of $\zeta^* = -2.807$ in a solution at pH = 3. Daiko, et al. [189] perform layer-by-layer assembly of Nafion and poly(allyamine hydrochloride) and claim a pH-dependent zeta potential (via laser-light scattering of tracer particles) for Nafion, although direct conclusions about Nafion are obscured by the presence of a second material. Abebe, et al. [190] perform layer-by-layer assembly of Nafion with various polymers on .5[μm] particles and claim a pH-dependent charge based upon zeta potential measurements and a color changes attributed to dye uptake in the Nafion capping layer; specifically, values of $\zeta^* = -2.203$ at pH$= 11$ and a value of $\zeta^* = 0$ at $1.2 \leq$pH≤ 1.3. The porous nature of the material appears to be neglected in these [188–190] electrokinetic analyses of Nafion.

Although many studies report on the conductivity through [2, 2, 3, 7, 185, 191] and along [4, 192–195] Nafion membranes, we know of no measurements characterizing the conductivity of Nafion in parallel with an ion-containing fluid. Conductivity measurements have been made with Nafion membranes immersed in liquid, and in controlled atmosphere with varying amounts of humidity [191–193]. In nearly all instances, the role of hydration [192–194, 196] (often cited as water molecules per charge) along with the diffusivity/mobility [4, 7, 191, 195, 197] of the cations has been identified as a controlling factor in the conductivity. Often, the conductivity is expressed [4, 198] with an effective mobility of the cationic species, as it may differ from the bulk value. Peckham and Holdcroft [198] provide a review of the structure/morphology properties of ionic conductors, and their relation to the overall conductivity of the material.

This paper is organized as follows. We first describe our electrokinetic cell in detail, and outline the program of measurements, which we perform to characterize the physical and chemical properties of the thin Nafion films. Then, we present results from our streaming potential and conductivity measurements that we interpret using a model [174, 178] to predict the charge density and resistive properties of the Nafion film. We then compare these results with available data from other electrokinetic studies on Nafion (performed in different configurations), and propose an explanation for our observed data.

6.3 Materials and Methods

Sample Preparation Glass microscope slides (75mm x 25mm x 1mm, VWR) were sonicated for 20 minutes in mixtures of soap and water, then a 1:1 mixture of methanol and ethanol, rinsed with de-ionized (DI) water, and dried with N_2. The slides were further cleaned in a solution of 3:1 H_2SO_4:H_2O_2 at 50 C for 20 minutes, rinsed several times with DI water, and dried in an N_2 stream.

We coated the cleaned slides with a silane layer to promote adhesion with the Nafion polymer [199]. Following the procedure of Luzinov, et al. [200], slides were immersed in a solution of 1% v/v 3-Glycidoxypropyltrimethoxysilane in toluene for 22 hours. Care was taken to minimize exposure of the slides to water vapor by performing the silane deposition in a closed container over a desiccant with a gentle N_2 purge. Following immersion, slides were soaked in toluene for 20 minutes, rinsed in anhydrous ethanol, sonicated in anhydrous ethanol for twenty minutes, then dried in a stream of nitrogen gas. After the silane deposition, slides are stored in a closed container over a desiccant and used within 48 hours. All solvents used are of ACS Reagent grade.

We implement a solution-casting technique [199,201,202] with spinning to generate nanometer-thick Nafion polymer layers. A solution of 20% Nafion resin in aliphatic alcohols and water (Sigma-Aldrich No. 663492) was diluted to 3% in 200-proof ethanol. This solution was applied to the silane-treated slides at an area density of 1 mL per 75mm x 25mm slide surface, and spun at 1000 RPM for 7 seconds. Following spinning, slides were placed beneath large pyrex petri dishes on a level surface and cured in a 150-C oven (air atmosphere) for 1 hour. This temperature was selected by the observation that higher curing temperatures lead to more stable films [201, 202] Following the 1-hour cure, the slides are left covered to cool to room temperature on a lab bench. The samples appeared slightly yellowed at the slide edges (i.e., on the edge bead).

Following Nafion deposition and oven curing, we wash the samples in (70%) nitric acid for 1 hour at room temperature, then rinse in DI water and dry in a nitrogen stream. Acid washing ensures the Nafion is in proton form (e.g., -SO_3H vs. -SO_3Na); X-ray photoelectron spectra of the Nafion films after the acid wash do not contain a sodium peak (see supplementary information). Additionally, the slight yellowing observed following curing is removed by this acid treatment.

Profilometry Measurements Mechanical film thickness measurements were performed in wet and dry states. Measurements were performed with a Dektak 6m profilometer (Veeco) and a stylus with a 12 [μm] diameter tip. The films were mechanically abraded in three positions along the sample centerline, corresponding to upstream, middle, and downstream positions. Four measurements were made at each position. This procedure was performed on a set of three samples at the dry state and each pH and salt concentration condition tested, to characterize the swelling response that we later apply to our electrokinetic samples under similar conditions.

Ellipsometry Measurements Ellipsometric film thickness and optical property measurements were made on dry Nafion films using a Woollam Spectroscopic Ellipsometer (J. A. Woollam Co., Inc.). Measurements were made on a rectangular silicon substrate with a deposited layer of 1μm thermal oxide. Processing conditions for Nafion on silicon are identical to films deposited on glass slides, with the amount of 3% resin used adjusted to keep the surface coverage uniform between the two substrates. The silicon surface was used to eliminate backside reflection of the glass substrate. Measurements were taken at incident angles of 65, 70, 75, and 80 degrees, over incident light at wavelengths between 300 and 1000 [nm] in 5 [nm] increments (see supplementary information for graphical output). Modeling was performed using WVase32 software (J. A. Woollam Co., Inc.).

XPS Measurements Survey and narrow scans were performed on the Nafion samples to determine atomic composition and bonding information (Surface Science Instrument, SSX-100). A flood gun was used to reduce charging effects on the polymer. All XPS measurements were performed in an evacuated (ultra-high vacuum) chamber.

Electrode Fabrication Silver chloride electrodes were prepared using an electrolytic method [203]. Silver wire of .5mm diameter and 5mm length were installed in Nanoport fittings (IDEX Health and Science) with an ethylene tetrafluoroethylene sleeve. Pairs of silver wire electrodes were anodes in a cell opposite a platinum anode in a solution of .1 [mol/L] HCl, through which a current density of 2 [mA/cm^2] is supplied for 30 minutes. After the deposition, the electrodes are stored with leads shorted in a .1 [mol/L] HCl solution until used.

Experiment Solutions Sodium chloride solutions (concentrations 1, 5, 10, 50 and 100 [mM]) are prepared at pH 3, 4, and 5 using hydrochloric acid, sodium chloride salt, and DI water. We measure the pH, temperature, and conductivity of each solution before and after each set of electrokinetic experiments (Mettler Toledo model SevenMulti). Solutions are not purged with inert gas, and the concentration of bicarbonate and carbonate ions are small as compared to the added ionic species.

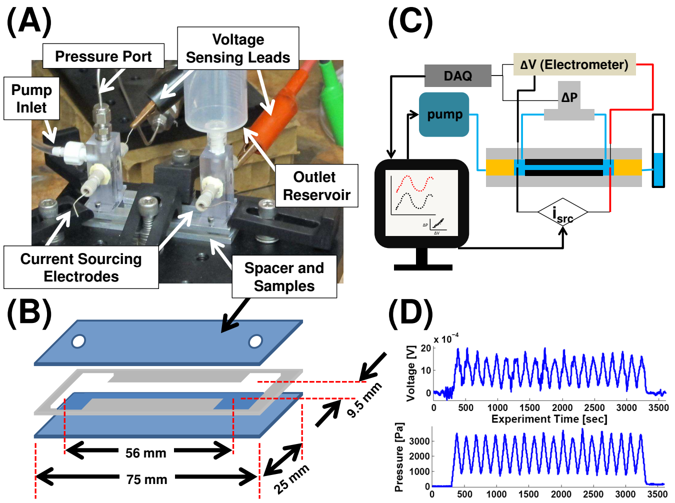
(A)
Pressure Port
Voltage Sensing Leads
Pump Inlet
Outlet Reservoir
Current Sourcing Electrodes
Spacer and Samples
(B)
56 mm
75 mm
9.5 mm
25 mm
(C)
DAQ
ΔV (Electrometer)
ΔP
pump
ΔP
ΔV
i_src
(D)
x 10^-4
Voltage [V]
20
10
0
0 500 1000 1500 2000 2500 3000 3500
Experiment Time [sec]
Pressure [Pa]
3000
2000
1000
0
0 500 1000 1500 2000 2500 3000 3500

Figure 6.1: Picture and schematic of the electrokinetic cell with sample data. The assembled cell is shown in (A), with current leads disconnected for clarity, highlighting the various inputs and outputs of the device. The dimensions of the sample slides and shim are shown diagrammatically in (B); the plate separation (cell height, $2h$) is approximately 57 [μm]. In (C), we present a component-level diagram of the components involved in the streaming potential and conductivity experiments, with sample data from a streaming potential experiment shown in pane (D).

The flat plate cell and electrokinetic measurements Electrokinetic measurements (streaming potential and conductivity) are performed in a home-built flat plate streaming potential apparatus, similar to designs presented by Van Wagenen, et al. [68] and Scales, et al. [66]. A schematic of this device is presented in figure 6.1. A pair of Nafion-coated slides form the channel floor and ceiling separated by a thin (nominally 50 [μm]) Teflon shim having a cut-out region with length 56 [mm] and width 9.5 [mm]. Holes ($\frac{1}{8}$" diameter) drilled in the top slide permit access to the channel formed by the Teflon shim. We position an instrument pillar above each drilled hole. In addition to establishing a connection to the sample slides, the upstream pillar contains two electrodes (one current sourcing, one voltage sensing), a pressure port, and an inlet port which connects to a syringe pump (KD Scientific). Similarly, the downstream pillar contains a complimentary pair of electrodes, and connection to an outlet reservoir. Voltage sensing is performed using a Keithley Electrometer (model 6514), current is sourced from a Keithley Sourcemeter (model 2400), and pressure is measured using an Omega Engineering 0-5 psi pressure transducer (model PX409). All instruments are connected to a computer and are controlled (or monitored by) a LabView script.

We implement phase-sensitive streaming potential measurements [65] to determine the streaming current coupling coefficient (χ_{21}) of the Nafion–fluid system at each salt concentration and pH. The syringe pump provides a triangular waveform with minimum and maximum flowrates of .1 and .5 [mL/min] over a peak-to-peak time of 150 seconds. The generated pressure and voltage waveforms are collected and dominant peaks from their Fourier transform are used to calculate the streaming potential coupling coefficient:

$$\chi_{21} = -\chi_{22} \frac{\mathcal{F}\left(\nabla \phi_{\text{ext}}\right)}{\mathcal{F}\left(\nabla p\right)} \tag{6.2}$$

Here, χ_{22} is the cell conductivity (measured in our electrokinetic device), and ∇p and $\nabla \phi_{\text{ext}}$ are the generated pressure and electrical potential gradients along the direction of flow. The scripted operator, $\mathcal{F}$, denotes the amplitude of the peak (i.e., driving) frequency in each Fourier spectrum.

The cell conductivity is measured with a four-electrode technique to prevent polarization effects [75]. The sourcemeter provides a sequence of currents (maximum .1 [μA]) for 5 seconds each, and the electrometer measures the potentials required to drive the currents. Ohm's law is used to compute the conductance of the cell, which we convert to a conductivity with knowledge of the cell geometry. The width and length of the cell are measured with a digital caliper, and the cell height is determined from hydraulic resistance measurements.

Samples are repeatedly measured at each combination of pH and salt concentration. Prior to the initial measurement, each pair of Nafion coated slides is soaked in a solution of pH 3, 4, or 5 (0 [mM] NaCl) for a minimum of four days with the solution exchanged at least once per day. Each pair of slides is examined in a solution containing only HCl followed by analysis in solutions of HCl and 1, 5, 10, 50 and 100 [mM] NaCl. Experiments at a given pH and salt concentration consist of two streaming potential measurements, four conductance measurements, and one hydraulic resistance measurement. This set of experiments is repeated a minimum of four times at each combination of pH and salt concentration. The first set of experiments at each pH and salt concentration is neglected in our presented data, as these experiments contain a mixture of experiment solutions (i.e., in changing from 1 to 5 [mM] a mixture of the two exists in the electrokinetic cell). An average of 5 sets of experiments are performed on each pair of slides at a given pH and salt concentration, and two pairs of slides are used for each pH. Each pair of slides is tested at one pH only. At the end of each experiment, we obtain the streaming potential coefficient χ_{21}, the cell conductivity, χ_{22}, the hydraulic conductivity, χ_{11}, as well as the bulk conductivity and pH of the working fluid measured on a separate, benchtop, meter.

6.4 Results and Discussion

6.4.1 Streaming Potential

We present streaming potential data over three decades of pH and NaCl concentration in figure 6.2. The streaming-current-coupling parameter, χ_{21}, and the phenomenological zeta potential, $\zeta = -\chi_{21}\frac{\eta}{\varepsilon\varepsilon_o}$, are plotted as a function of the ionic strength of solution, $I_c = 1/2\sum_i z_i^2 c_{i,\infty}$, where z_i and $c_{i,\infty}$ are the valence and bulk concentration of the i^{th} component. These data reveal a strong inverse dependence on the logarithm of I_c, and show χ_{21} and ζ to be insensitive to the pH. The pH insensitivity is expected based upon the chemistry of the material — Kreuer [15] estimates a pKa of −6 for the sulfonate groups in Nafion. The scaling of χ_{21} and ζ with the ionic strength of solution is expected based on the Donnan theory of membrane potentials [77]. Inside the membrane, a local balance exists between the charge of the sulfonate groups and mobile cations from solution. This balance predicts a potential difference between the film interior and bulk fluid, which, for a $z : z$ electrolyte is:

$$\phi_D = \frac{RT}{zF}\operatorname{arcsinh}\left(\frac{\rho_f}{2FI_c}\right) \tag{6.3}$$

Here, ϕ_D is the Donnan potential [70] in [V], F is Faraday's constant, R the ideal gas constant, T the absolute temperature, and ρ_f is the fixed charge density in [coul/L]. This scaling predicts a decrease in the Donnan potential for constant ρ_f and increasing I_c.

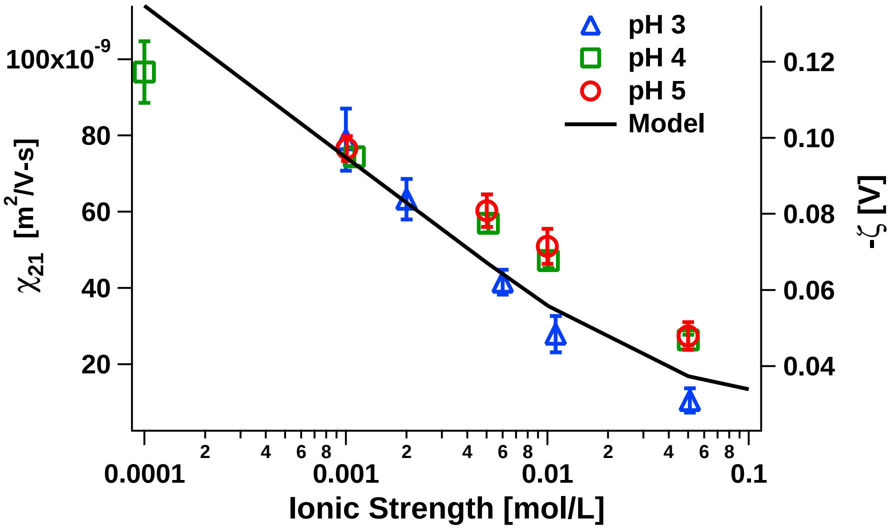

Figure 6.2: Data and model fit (from equation (6.5)) for χ_{21} and ζ as a function of pH and ionic strength. The model is a function of ionic strength, charge density, and the momentum penetration length λ_o, only.

The phenomenological ζ-potential and Donnan potentials are not equivalent in the Nafion–solution system. The phenomenological ζ-potential is the surface potential at the plane of shear [59,60], and relates to χ_{21} as $\zeta = -\chi_{21}\frac{\eta}{\varepsilon\varepsilon_o}$ when $h >> \lambda_D$ and the shear plane and solid boundary coincide. Thus, the phenomenological ζ-potential assumes that the surface of polymer is rigid and impermeable; this is inconsistent with our understanding of Nafion as a porous material, and violates equation (6.3), which requires a fixed charge density and cannot exist in a planar surface. In a previous publication, we derive an approximate form of the coefficient χ_{21} for a porous and charged layer grafted on a rigid surface in a parallel-plate configuration [174]. Our result is written in terms of dimensionless ratios, many of which are known for our thin Nafion films:

$$\zeta^* = \frac{\chi_{21}}{-\frac{\varepsilon\varepsilon_o}{\eta}\frac{RT}{F}} = -\frac{1}{\beta}\phi_D^* + \left(\frac{\rho_f^*}{\alpha^2\gamma^2} + \phi_D^*\right)\left(1 + \frac{1/\beta - 1}{\cosh(\alpha)} - \frac{\tanh(\alpha)}{\alpha\beta}\right) \tag{6.4}$$

Here, $\alpha = \frac{\delta}{\lambda_o}$ parameterizes the hydraulic resistance of Nafion, where δ is the thickness of the Nafion film and λ_o is the characteristic penetration distance of momentum from the bulk fluid into the Nafion film. The parameter $\beta = \frac{h}{\delta}$ is a dimensionless cell height, with h representing the half-height of the cell (see figure 6.1), and $\gamma = \frac{\lambda_D}{\delta}$ compares the thickness of the Debye length, $\lambda_D = \sqrt{\frac{\varepsilon\varepsilon_o RT}{2F^2 I_c}}$ to the thickness of the Nafion film (ε and ε_o are the solvent dielectric constant and vacuum permittivity, respectively). The remaining terms, $\phi^* = \frac{\phi F}{RT}$ and $\rho_f^* = \frac{\rho_f}{2F^2 I_c}$, are potentials and charge densities made dimensionless by the thermal voltage (for ϕ) and the charge in solution via the ionic strength (for ρ_f).

Very basic information about the Nafion film simplifies (6.4) considerably. Our measurements of the Nafion film thickness, coupled with hydraulic capacitance measurements to characterize the cell height, and reported literature on the small pore size (less than $\sim$ 3 [nm]) of the Nafion polymer [15, 181], indicate that α and $\beta \gg 1$. Profilometric film thickness measurements yield an approximate hydrated thickness of 320 [nm]; with a cell height of $2h = 57[\mu\text{m}]$ and an *a priori* estimate of 5 [nm] for λ_o, $\alpha = 64$ and $\beta = 89$ so we can safely approximate (6.4) as:

$$\zeta^* = \frac{\chi_{21}}{-\frac{\varepsilon\varepsilon_o}{\eta}\frac{RT}{F}} = \phi_D^*\left(1 - \frac{1}{\beta}\right) + \frac{\rho_f^*}{\alpha^2\gamma^2} = \operatorname{arcsinh}\left(\rho_f^*\right)\left(1 - \frac{1}{\beta}\right) + \frac{\rho_f^*}{(\lambda_D/\lambda_o)^2} \tag{6.5}$$

The free parameters are ρ_f^* and λ_o; β is known from independent measurements of the film thickness and height of the electrokinetic cell. We fit the parameters λ_o and ρ_f^*

by finding the combination of ρ_f^* and λ_o that minimize the error between the predicted and experimental values of χ_{21}. During this search process, we restrict ρ_f^* and λ_o to be identical in each film.

Our model (equation (6.5)) and data (figure 6.2) predicts a charge density of .0582 $\left[\frac{\text{mol}[-\text{SO}_3^-]}{\text{L}}\right]$, which is less than the accepted value of 1.6727 $\left[\frac{\text{mol}[-\text{SO}_3^-]}{\text{L}}\right]$ for a 1100 EW Nafion film with a dry density of 1.84 [g/cm^3]. The fitted penetration length is $\lambda_o = 1.57$ [nm], suggesting that the Nafion film is weakly permeable to fluid flow. The penetration depth is on the same order as the Debye length in solution, and both are much smaller than the thickness of the Nafion film, $\sim$ 300 [nm]. Thus, the streaming potential measurement constitutes a local probe of the Nafion–fluid interface; free charge a distance $O(\lambda_o)$ into the Nafion is actuated by the flow, with the remaining free charge essentially motionless and neglected in the magnitude of χ_{21}. This value of the penetration length is comparable to the reported pore size based upon the Gierke model of Nafion [15, 181].

Based upon literature descriptions of electroosmotic and Ohmic conductivity through the Nafion polymer, we may anticipate a trend in χ_{21} as a function of pH for solutions of identical ionic strength. Work by Okada, et al. [195] describes a dependence of water permeability (average velocity through the membrane per applied pressure) that varies with the type of cationic species in a Nafion membrane. Their data demonstrates that water permeability through the Nafion membrane increases as the proportion of protons in solution. They further show [4, 195] that the transference coefficient for water varies in inverse proportion with the concentration of protons in the membrane. The water permeability measure the resistance of flow to pressure, and the transference coefficient indicates the number of water molecules transported by the application of an electric field. Thus, both the mechanical resistance and electroosmotic resistance to flow are expected to change as a function of pH and ionic strength. Based upon the permeability and transference observations of Okada, et al. [4, 195], we would expect a trend where solutions with the same ionic strength and different pH are ordered: $\chi_{21}^{\mathrm{pH=3}} > \chi_{21}^{\mathrm{pH=4}} > \chi_{21}^{\mathrm{pH=5}}$. This trend is not observed in our data, suggesting that solution-dependent permeability and transference are minimally present at the Nafion–solution interface, or that these effects are small as compared to other sources of variability in our measurements (e.g., variations from sample to sample). Absence of this trend does not indicate lessened interaction between the fluid and the Nafion film; XPS results (see supplementary information) suggest cation exchange by the appearance of a sodium peak in proton-form Nafion films that have been immersed in a solution containing sodium chloride.

6.4.2 Conductivity

We perform conductivity measurements in concert with the streaming potential measurements. The conductivity is a measure of ionic charge transport everywhere within the electrokinetic cell. In contrast to the χ_{21} measurement, in which a pressure-driven flow penetrates a characteristic distance $\lambda_o \ll \delta$ into the porous layer, the field applied during the conductivity measurements ($\nabla\phi_{\mathrm{ext}}$) actuates a body force ($-\rho_e\nabla\phi_{\mathrm{ext}}$) on the free charge density (ρ_e) everywhere in the domain. Thus, the conductivity measurements represent the ability of the system to transport ions averaged over the entire domain, in contrast to the local probing of the χ_{21} measurement.

Our conductivity data are presented in figure 6.3. We show the conductivity as measured in the electrokinetic cell (the cell conductivity, χ_{22}), and a ratio of cell to bulk conductivities $\left(\frac{\sigma_{\mathrm{cell}}}{\sigma_{\mathrm{bulk}}}\right)$ as a function of ionic strength and pH. The cell conductivity is an intrinsic measure of the ability of the cell (Nafion and ion-carrying bulk fluid) to transport current; as such, these values are not directly comparable to literature values of Nafion conductivity (presented later).

The observed cell conductivity varies with the pH and ionic strength of solution. These variations reflect differences in the mobilities [1] of the ions H^+, Na^+, and Cl^-. Comparing solutions of the same (or similar) ionic strength but different pH, the solution with lower pH has a larger concentration of high-mobility protons ($\mu_{H^+} \approx 7\mu_{Na^+}$). At larger ionic strengths (by the addition of NaCl), this mobility difference is overcome by increased concentrations of lower-mobility salt ions relative to the protons.

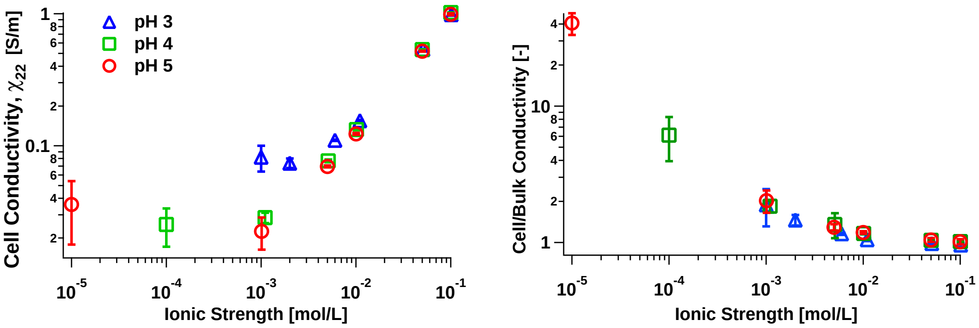

Figure 6.3: Left: Cell conductivity as a function of solution pH and ionic strength measured using the four-electrode technique. Right: Cell to bulk conductivity ratio. Bulk conductivities are obtained using a commercial conductivity meter in a 50 [mL] flask, absent surface effects.

The ratio of the cell to the bulk conductivity indicates that cell effects, owing to the Nafion films, diminish as the ionic strength of the working fluid increases. This trend is expected based upon an equivalent circuit model of the cell conductivity: $\chi_{22} = \sigma_{\text{bulk}}\left(1 - \frac{1}{\beta}\right) + \frac{1}{\beta}\sigma_{\text{Nafion}}$ where σ_{bulk} and σ_{Nafion} are the conductivities in the bulk fluid and Nafion, respectively. This relation can be re-arranged to yield the conductivity of the thin Nafion film:

$$\sigma_{\text{Nafion}} = \sigma_{\text{bulk}} + \beta\left(\chi_{22} - \sigma_{\text{bulk}}\right) \tag{6.6}$$

The cell conductivity, χ_{22}, includes all conduction mechanisms in the Nafion and fluid portions of the electrokinetic cell. We plot the Nafion conductivity from equation (6.6) in figure 6.4 as a function of ionic strength. These data reveal a relatively uniform conductivity in the Nafion, although the magnitude of the errors preclude definitive conclusions as to the scaling with solution properties. In particular, the 50 and 100 [mM] data points at pH 5 exhibit a negative conductivity, which is non-physical. These negative conductivity data points are not considered further in our analysis. Despite this noise, we are able to extract parameters that inform the state of the Nafion film.

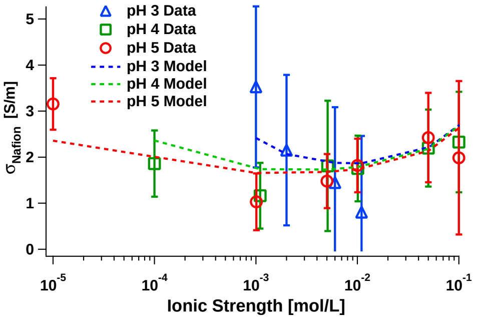

Figure 6.4: Experimental conductivity data (symbols, as indicated) in the Nafion film with lines from the model presented in equation (6.10). The error bars represent propagation of standard deviations from the various measurements determining σ_{Nafion}.

We implement a conductivity model [178] to determine the fixed charge density, ρ_f, and penetration length, λ_o in the Nafion film. Our model incorporates conduction from the bulk, as well as excess Ohmic and electroosmotic conduction in the Nafion layer, $\chi_{22} = \sigma_{\mathrm{bulk}} + \sigma_{\mathrm{Ohmic}} + \sigma_{\mathrm{EO}}$. Like the bulk term, the Ohmic and electroosmotic (EO) subscripted terms account for conduction effects throughout the domain, not just in the thin Nafion film. We neglect Ohmic and electroosmotic conduction outside of the Nafion film, and validate this simplification by application of the Bikerman [58, 73] conductivity formula with inputs derived from our χ_{21} analysis. The estimated contribution from Ohmic and electroosmotic conduction in the bulk fluid is several orders of magnitude lower than the conductivity within the Nafion layer, which validates our simplification. For efficiency, we work in dimensionless conductivities with the scaling $\frac{4}{3}FI_c\frac{\varepsilon\varepsilon_o}{\eta}\hat{\phi}$. The parameter $\hat{\phi}$ in the conductivity scale is a measure of the mobility of the current-carrying ions (see the supplementary information for a brief description). We discuss this parameter at length elsewhere [178].

Our model for the conductivity accounts for conduction in the bulk (driven by the electrophoretic motion of ions) along with Ohmic and electroosmotic excess conductivities within the Nafion film:

$$\chi^*_{22} = \sigma^*_{\text{bulk}} + \sigma^*_{\text{Ohmic}} + \sigma^*_{\text{EO}} \tag{6.7}$$

$$\sigma^*_{\text{Ohmic}} = \frac{1}{\beta}\sum_i \frac{\phi^*_i z_i}{2\hat{\phi}^*} c^*_i \left(e^{-z_i\phi_D} - 1\right) \tag{6.8}$$

$$\sigma^*_{\text{EO}} = \frac{1}{\beta}\frac{3}{2}\left(1 - \frac{\tanh(\alpha)}{\alpha}\right)\frac{{\rho^*_f}^2}{\alpha^2\gamma^2\hat{\phi}^*} \tag{6.9}$$

Here, ϕ^*_i is the ionic potential of the i$^{\text{th}}$ species, z_i is the valence, $c^*_i = \frac{c_i}{I_c}$ is the bulk concentration normalized by the ionic strength, and the remaining symbols have the same meaning as in equation (6.5). Manipulating equations (6.8) and (6.9) to predict the Nafion conductivity is straightforward. We combine equations (6.6) and (6.7) through (6.9) to yield:

$$\sigma^*_{\text{Nafion}} = \sigma^*_{\text{bulk}} + \frac{3}{2}\left(1 - \frac{\tanh(\alpha)}{\alpha}\right)\frac{{\rho^*_f}^2}{\alpha^2\gamma^2\hat{\phi}^*} + \sum_i \frac{\phi^*_i z_i}{2\hat{\phi}^*} c^*_i \left(e^{-z_i\phi_D} - 1\right) \tag{6.10}$$

This result depends only upon the parameters α, γ, ρ^*_f, and the ionic potentials ϕ^*_i which may be calculated [178] from values in the literature for a variety of electrolytes, including ions within Nafion film [195].

We apply equation (6.10) to our conduction data, and perform a regression analysis to determine the values of λ_o and ρ_f, which are the only free parameters. The domains of the parameter space are defined by $10^{-2} \leq \frac{\rho_f}{\rho_f^{(1100\text{EW})}} \leq 1$ and $10^{-10} \leq \lambda_o \leq 10^{-8}$ [m], where $\rho_f^{(1100\text{EW})}$ is the charge density of a 1100 EW Nafion membrane. A family of ρ_f and λ_o pairs yield extrema *within* the domain that minimize the error between the model and experimental data; a single point on the boundary of the parameter space gives a global minimum. This is in contrast to the regression performed on χ_{21}, which gave a unique minimum on the interior of the ρ_f–λ_o space. Neither the family of ρ_f and λ_o pairs, nor the minimum on the domain boundary intersect with the minimum identified in the χ_{21} analysis.

Nafion film properties, from the boundary extremum, yield a charge density of $1.6727 \left[\frac{\mathrm{mol}[-\mathrm{SO}_3^-]}{\mathrm{L}}\right]$ and a penetration length $\lambda_o = 2.58{\times}10^{-10}$ [m]. The match between the data and experiment is shown in figure 6.4. The theory and data agree reasonably well, when the errors in the measurement are taken into account. In extracting the parameters ρ_f and λ_o from the boundary extremum, we assume that the average charge density in the Nafion thin film is equivalent to the charge density for commercial Nafion membranes. This assumption is reasonable, provided there is enough water in the Nafion film for the charged domains to form a well-connected network, which will allow conduction of cations through the film. Our conductivity measurements are within the range of values obtained for Nafion immersed in water with multiple cations, although our measurements are made in a range of ionic strength that has not been extensively explored. We present a comparison between our data and literature values in figure 6.5.

The compilation of data in figure 6.5 illustrates several points about the conductivity available in the literature and the physicochemical nature of Nafion. There is a large spread in these data – even at the same ionic strength, variations are observed for identical or similar materials among researchers. Two reasons are identified in the literature for this spread. First, the cationic composition in the Nafion and solution govern the conductivity by affecting the hydration in the Nafion membrane. This is readily seen in figure 6.5 by comparing the filled markers, where protons are the only cations in solution, to data represented by open and wired markers where the protons and univalent alkali metal ions are present in the Nafion membrane and solution (all are Na^+

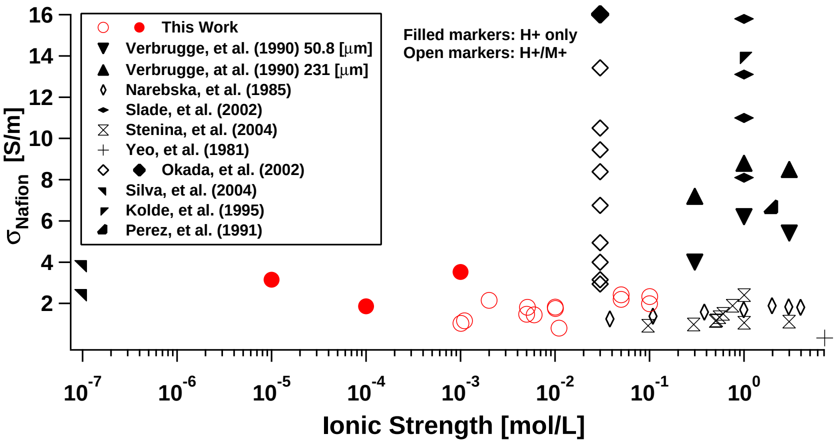

Figure 6.5: A comparison of conductivities measured in Nafion membranes as a function of ionic strength, with the nature of the electrolyte indicated in the marker type. Shown are the data of Slade, et al. [2], Verbrugge, et al. [3] (for two thicknesses), Kolde, et al.(from Slade [2]), Perez, et al.(from Slade [2]), Okada, et al. [4], Yeo, et al. [5], Stenina, et al. [6], Narebska, et al. [7], and Silva, et al. [8]

except for Yeo, et al. [5] which is K^+). Although decreased conductivity for mixed cation electrolytes is consistent within each dataset presented, there are disagreements between datasets, as, for example, between the data of Okada, et al. [4, 195] and Verbrugge, et al. [3]. Secondly, the data by Slade, et al. [2] and Verbrugge, et al. [3] reveal a dependence on the thickness of the Nafion layer. This is surprising, because the conductivity is an intrinsic transport property, and should not be dependent on material extents. The four conductivity values from the Slade data are proportional to the thickness of the membrane studied; the highest conductivity (15.8 [S/m]) is observed for a 208 [μm] membrane, with thinner membranes (161, 111, and 58 [μm]) exhibiting a monotonic decrease in the conductivity. The two sets of Verbrugge data show a similar trend, although the decrease is not as strong as in the Slade data. Not all data sets show size-dependent conductivity for varying thickness; Okada, et al. [4] studied Nafion membranes of type 115 (125 [μm] dry) and 117 (175 [μm] dry) using an HCl/NaCl electrolyte, and observed no appreciable thickness dependence. In the context of our results, this literature survey suggests that we should observe a decrease in the conductivity for mixed cation electrolytes relative to proton-only electrolytes, as well as a decrease in the conductivity for thin Nafion films relative to thick Nafion films. Although there is appreciable scatter in the data found in the literature, these patterns are apparent in figure 6.5.

6.5 Conclusions

In this study, we have combined streaming potential and conductivity measurements to analyze thin Nafion films in contact with an electrolyte solution. We explored a relatively untested region of ionic strength, taking these measurements over three decades of pH at six different values of salt concentration. We coupled our measurements with a theory to extract the fixed charge density, ρ_f, and penetration length, λ_o, as predicted by both the streaming potential and conductivity techniques.

Our results are consistent with a Nafion film that is dehydrated and nonuniform along the film thickness δ. The observed χ_{21} data follow from the advection of mobile charge; in the Nafion film, a volume of fluid with thickness on the order of λ_o is actuated by the flow. Thus, χ_{21} measurements constitute a localized probing of the Nafion–fluid interface. In contrast, our conductivity measurements average transport of free charge over the entire Nafion film. Because of the values derived from these measurements do not coincide, our results suggest that the Nafion film in our experiments is nonuniform. Specifically, our results are consistent with a Nafion film that is poorly hydrated at the interior. Although we do not explore the source of the hydration in detail, the temperature at which we bake the Nafion during film preparation has been correlated with decreased conductivity measurements on non-wetted Nafion films [193].

Even with this nonuniformity, we underpredict the expected Nafion charge with our streaming potential measurements. The literature [182,183] indicates that the Nafion–air interface is less hydrophilic than the bulk, and conductivity measurements are consistent with a hydrophobic interfacial region for a wetted Nafion film. Following observations of decreasing Nafion conductivity with Nafion membrane thickness, Verbrugge, et al. [3] hypothesized that the interfacial regions of the Nafion film are of higher ionic resistance than the bulk. As increased hydration and increased percolation of aqueous domains in the Nafion drive conduction [181, 196, 198, 204], higher ionic resistance is consistent with an interface that is more mechanically resistive and less permeable to flow.

Finally, we have applied two commonly used electrokinetic techniques in an uncommon configuration for a widely studied material. This combination of technique and geometry has enabled us to probe an interface in an uncommon way – we have taken direct measures of the Nafion–liquid interface, and our results suggest that this interface behaves differently than may be assumed if the material were identical to the properties of a bulk Nafion film. Further studies using our technique on this interface, varying, for example, the Nafion thickness, type of electrolyte, or environmental variables such as temperature and pressure, are likely to yield enriching results on the Nafion–fluid interface. Although we have identified several follow-on studies to the material studied presently, this approach is not limited to Nafion surfaces, and would be of great utility for any porous material where the surface structure is posited to exhibit a form or function different from its bulk properties.

6.6 Acknowledgemens

The authors thank the Department of Energy (PECASE) for support. ACB acknowledges fellowship support from the NSF Graduate Research Fellowship Program.

6.7 Supplementary Information

6.8 XPS

Here, we present XPS spectra and atomic percentages of a Nafion film after treatment with nitric acid (the datum state of the Nafion samples for our measurements) in figure 6.6. Additionally, we show XPS spectra and atomic percentages for a Nafion film after treatment with a solution of 100 [mM] NaCl (figure 6.7). These results show that the acid treatment leaves the surface of the film free of metal cations, and that the film does participate in an exchange of cations when placed in contact with a solution containing sodium chloride.

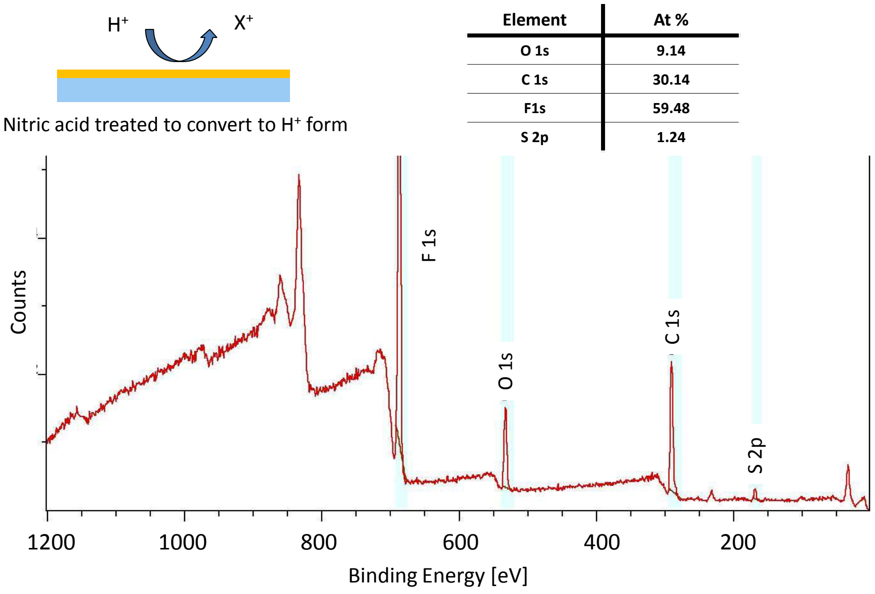

Element	At %
O 1s	9.14
C 1s	30.14
F1s	59.48
S 2p	1.24

Figure 6.6: XPS spectra of a thin Nafion film following treatment in 70% nitric acid.

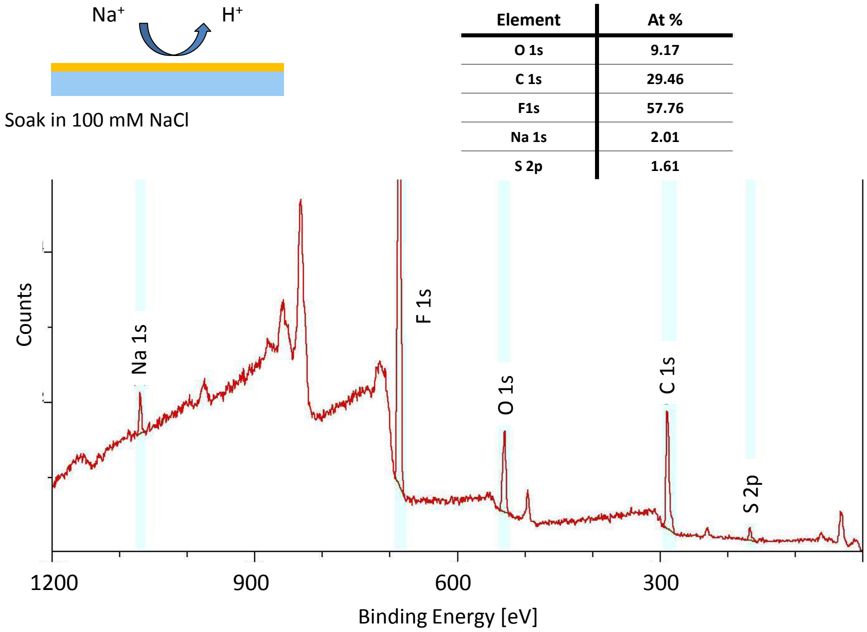

Element	At %
O 1s	9.17
C 1s	29.46
F1s	57.76
Na 1s	2.01
S 2p	1.61

Figure 6.7: XPS spectra of a Nafion film after contact with a 100 [mM] NaCl solution. The film was initially in proton form.

6.8.1 XPS spectra showing removal of sodium peak with acid treatment

6.9 Ellipsometry

Ellipsometry measurements of the prepared Nafion film and application of an optical model reveal a dry thickness of 250.594 ± 1.36[nm] and an index of refraction as a function of wavelength. These data are extracted using a Cauchy dispersion model for the real index of refraction, and display excellent agreement (see figure 6.8). In our model, the film thickness and Cauchy parameters (A, B, and C) are free variables:

$$n(\lambda) = A + \frac{B}{\lambda^2} + \frac{C}{\lambda^4} \tag{6.11}$$

The wavelength, λ, is referenced in microns. Our extracted optical constants are similar to those reported by Zudans, et al. [205] for Nafion layers on glass, as we show in table

6.1.

	Present Work	Zudans, et al. [205]
A	$1.3555 \pm .00179$	1.353
B	$2.2408 \times 10^{-3} \pm .456 \times 10^{-3}$	1.8×10^{-3}
C	$-1.0565 \times 10^{-4} \pm 4.33 \times 10^{-5}$	0

Table 6.1: Optical constants extracted from ellipsometry data and model of Nafion film.

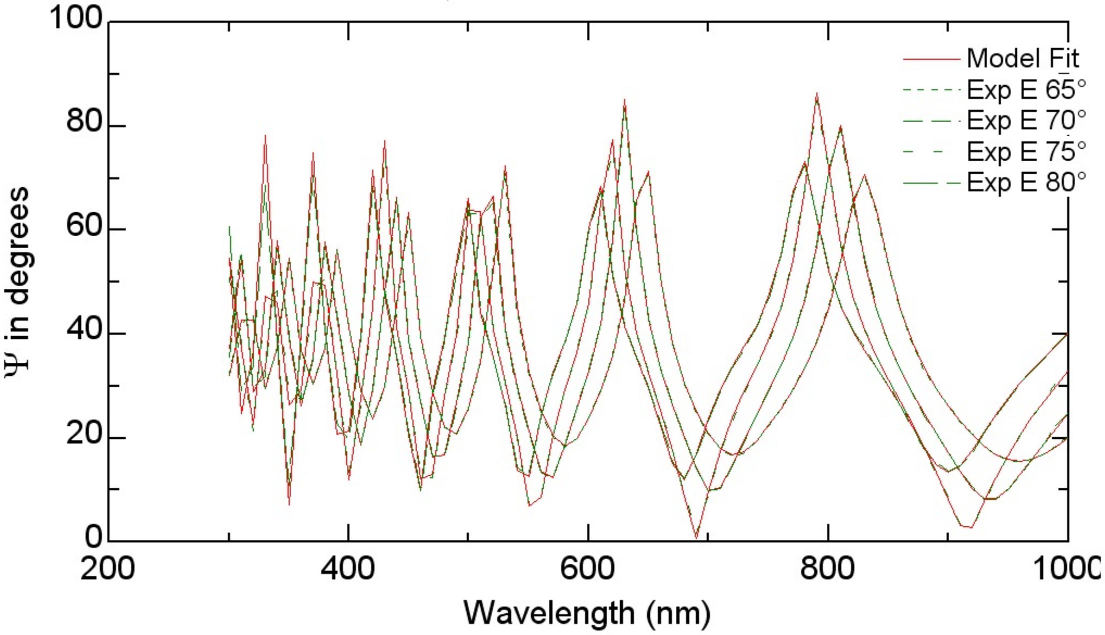

Figure 6.8: Psi (amplitude) of measured light as a function of wavelength [nm] for a nanoscale Nafion polymer film. The data at various incident angles (green lines) shows an excellent match to the model (red lines).

6.10 Ionic Mobilities Expressed as Potentials

In developing a nondimensional form of the conductivity, we convert ionic mobilities to potentials. The Ohmic conductivity is dependent upon the mobilities, μ_i, of the various ionic components in an electrolyte, while the electroosmotic conductivity is dependent upon the charge density, which dependes on the potential through the Poisson-Boltzmann equation. In order to relate these two conduction mechanisms coherently, we

Ion	$\mu_i \times 10^7 \left[\frac{\text{m}^2}{\text{s-V}}\right]$	ϕ_{ion} [mV]	ϕ^*_{ion}[-]
H^+	3.625	790.06	30.76
Na^+	0.519	113.18	4.40
Cl^-	0.791	-172.44	-6.75

Table 6.2: Mobilities [1] and tabulated potentials for ions, at 25 [C]. $\phi^*_{\text{ion}} = \frac{F\phi_i}{RT}$

relate the mobilities of ions to the potential difference that the ions generate in a solvent. We describe this procedure in detail elsehwere [178], although some values of the ionic potential are shown in table 6.2. Finally, the quantity $\hat{\phi}$ is defined as:

$$\hat{\phi} = \frac{1}{n} \sum_{i=1}^{n} z_i \phi_i \tag{6.12}$$

This term represents the average ionic potential of the various components in an electrolyte.

CHAPTER 7

CONCLUSION

In this work, we have described the application of microfluidics to problems in biology and interface science. These efforts are connected by their dependence on transport phenomena, considerations about which permeate both works.

In chapter two we presented a novel microdevice for cell seeding, coherent growth, and observation of rat hippocampal neurons. Our device design and methodology exploits biological insecurities of the neurons to direct their growth toward specific regions of our device. The construction of the device enables the observation of cells at very high (100x) magnification, which is necessary to observe the transport of intracellular components in the neurons. Finally, we present an analysis of solute delivery via convection and diffusion, and the concomitant shear stresses, and develop a straightforward way to account for design tradeoffs imposed by both shear stress and solute delivery requirements.

The literature survey in chapter three describes state-of-the-art techniques for the analysis and experimentation of porous and charged layers. Our coherent analysis of work in this field highlights the advantages and limitations of present theoretical and experimental approaches. As a result of this survey, we identified areas for improvement in the understanding of porous and charged layers, which were considered in subsequent works. In chapters four and five, we proposed an improved framework for the description of forces and fluxes in systems with porous and charged layers. In comparison with prior approaches, our contributions apply for systems regardless of the magnitude of the interfacial potential within the porous and charged layer. The approximate analytical formulas we developed were benchmarked against numerical results of the full govern equations, demonstrating excellent agreement. Further, we presented our results using a set of dimensionless parameters, which is convenient for both system design and analysis of experimental systems with porous and charged layers.

Finally, in chapter six, we incorporate the studies from chapters three, four, and five and described our effort toward the electrokinetic characterization of thin Nafion films. Using a home-built electrokinetic cell, we have described the streaming current and conductivity of thin Nafion films in a new region of parameter space (defined by the pH and ionic strength of an aqueous solution). With input from the studies in chapters four and five, we presented properties of the Nafion film (fixed charge density and fluid penetration depth) derived from our experiments. Our results are consistent with an anisotropic Nafion film, possible due to dehydration of the film interior. In addition to the experimental work and analysis performed, we have suggested several follow-on studies to further interrogate thin Nafion layers.

BIBLIOGRAPHY

[1] Allen J. Bard and Larry R. Faulkner. *Electrochemical Methods - Fundamentals and Applications*. Wiley, 2001.

[2] S. Slade, S. A. Campbell, T. R. Ralph, and F. C. Walsh. Ionic conductivity of an extruded nafion 1100 ew series of membranes. *Journal of the Electrochemical Society*, 149:A1556–A1564, 2002.

[3] M. W. Verbrugge and R. F. Hill. Analysis of promising perflurosulfonic acid membranes for fuel-cell electrolytes. *Journal of the Electrochemical Society*, 137:3770–3777, 1990.

[4] T. Okada, S. Moller-Holst, O. Gorseth, and S. Kjelstrup. Transport and equilibrium properties of nafion membranes with h+ and na+ ions. *Journal of Electroanalytical Chemistry*, 442:137–145, 1998.

[5] R. S. Yeo, S. F. Chan, and J. Lee. Swelling behavior of nafion and radiation-grafted cation exchange membranes. *Journal of Membrane Science*, 9:273–283, 1981.

[6] I. A. Stenina, P. Sistat, A. I. Rebrov, G. Pourcelly, and A. B. Yaroslavtsev. Ion mobility in nafion-117 membranes. *Desalination*, 170:49–57, 2004.

[7] A. Narebska, S. Koter, and W. Kujawski. Ions and water transport across charged nafion membranes. irreversible thermodynamics approach. *Desalination*, 51:3–17, 1984.

[8] R. F. Silva, M. De Francesco, and A. Pozio. Solution-cast nafion ionomer membranes: preparation and characterization. *Electrochimica Acta*, 49:3211–3219, 2004.

[9] Todd M. Squires and Stephen R. Quake. Microfluidics: Fluid physics at the nanoliter scale. *Rev. Mod. Phys.*, 77:977–1026, Oct 2005.

[10] Jacob Israelachvili. *Intermolecular and Surface Forces*. Academic Press, 2nd edition, 1991.

[11] Reto B. Schoch, Jongyoon Han, and Philippe Renaud. Transport phenomena in nanofluidics. *Rev. Mod. Phys.*, 80:839–883, Jul 2008.

[12] Younan Xia and George M. Whitesides. Soft lithography. *Annual Review of Materials Science*, 28(1):153–184, 1998.

[13] Thomas M. Keenan and Albert Folch. Biomolecular gradients in cell culture systems. *Lab Chip*, 8:34–57, 2008.

[14] Melody A. Swartz and Mark E. Fleury. Interstitial flow and its effects in soft tissues. *Annual Review of Biomedical Engineering*, 9:229–256, 2007.

[15] K. D. Kreuer. On the development of proton conducting polymer membranes for hydrogen and methanol fuel cells. *Journal of Membrane Science*, 185:29–39, 2001.

[16] H. Strathmann. Electrodialysis, a mature technology with a multitude of new applications. *Desalination*, 264(3):268 – 288, 2010.

[17] Thomas M. Pearce and Justin C. Williams. Microtechnology: Meet neurobiology. *Lab Chip*, 7:30–40, 2007.

[18] Kurt J. De Vos, Andrew J. Grierson, Steven Ackerley, and Christopher C.J. Miller. Role of axonal transport in neurodegenerative diseases. *Annual Review of Neuroscience*, 31(1):151–173, 2008.

[19] Rita Selvatici, Maurizio Previati, Silvia Marino, Luca Marani, Sofia Falzarano, Irene Lanzoni, and Anna Siniscalchi. Sodium azide induced neuronal damage invitro: Evidence for non-apoptotic cell death. *Neurochemical Research*, 34:909–916, 2009. 10.1007/s11064-008-9852-0.

[20] Csaba Szabo, Harry Ischiropoulos, and Rafael Radi. Peroxynitrite: biochemistry, pathophysiology and development of therapeutics. *Nat Rev Drug Discov*, 6(8):662–680, August 2007.

[21] Michael P. Murphy. How mitochondria produce reactive oxygen species. *Biochemical Journal*, 417:1–13, 2009.

[22] DC Wallace. A mitochondrial paradigm of metabolic and degenerative diseases, aging, and cancer: A dawn for evolutionary medicine. *Annual Review of Genetics*, 39:359–407, 2005.

[23] Anthony A. Oliva, Conrad D. James, Caroline E. Kingman, Harold G. Craighead, and Gary A. Banker. Patterning axonal guidance molecules using a novel strat-

egy for microcontact printing. *Neurochemical Research*, 28:1639–1648, 2003. 10.1023/A:1026052820129.

[24] Stefanie Kaech and Gary Banker. Culturing hippocampal neurons. *Nature Protocols*, 1(5):2406–2415, 2006.

[25] R. B. Campenot. Local control of neurite development by nerve growth-factor. *Proceedings of the National Academy of Sciences of the United States of America*, 74(10):4516–4519, 1977.

[26] R. B. Campenot. Development of sympathetic neurons in compartmentalized cultures 1. local-control of neurite growth by nerve growth-factor. *Developmental Biology*, 93(1):1–12, 1982.

[27] R. B Campenot. Development of sympathetic neurons in compartmentalized cultures 2. local-control of neurite survival by nerve growth-factor. *Developmental Biology*, 93(1):13–21, 1982.

[28] Stephanie P. Lacour, Raghied Atta, James J. FitzGerald, Mark Blamire, Edward Tarte, and James Fawcett. Polyimide micro-channel arrays for peripheral nerve regenerative implants. *Sensors and Actuators A - Physical*, 147(2):456–463, OCT 3 2008.

[29] Jean-Michel Peyrin, Berangere Deleglise, Laure Saias, Maeva Vignes, Paul Gougis, Sebastien Magnifico, Sandrine Betuing, Mathea Pietri, Jocelyne Caboche, Peter Vanhoutte, Jean-Louis Viovy, and Bernard Brugg. Axon diodes for the reconstruction of oriented neuronal networks in microfluidic chambers. *Lab on a Chip*, 11(21):3663–3673, 2011.

[30] Anne M. Taylor, Seog Woo Rhee, Christina H. Tu, David H. Cribbs, Carl W. Cotman, and Noo Li Jeon. Microfluidic multicompartment device for neuroscience research. *Langmuir*, 19(5):1551–1556, 2003.

[31] Anne M Taylor, Mathew Blurton-Jones, Seog Woo Rhee, David H Cribbs, Carl W Cotman, and Noo Li Jeon. A microfluidic culture platform for cns axonal injury, regeneration and transport. *Nature Methods*, 2(8):599–605, August 2005.

[32] Anja Kunze, Robert Meissner, Serena Brando, and Philippe Renaud. Co-pathological connected primary neurons in a microfluidic device for alzheimer studies. *Biotechnology and Bioengineering*, 108(9):2241–2245, 2011.

[33] C. Joanne Wang, Xiong Li, Benjamin Lin, Sangwoo Shim, Guo-li Ming, and

Andre Levchenko. A microfluidics-based turning assay reveals complex growth cone responses to integrated gradients of substrate-bound ecm molecules and diffusible guidance cues. *Lab Chip*, 8:227–237, 2008.

[34] D Kleinfeld, KH Kahler, and PE Hockberger. Controlled outgrowth of dissociated neurons on patterned substrates. *The Journal of Neuroscience*, 8(11):4098–4120, 1988.

[35] C.D. James, R. Davis, M. Meyer, A. Turner, S. Turner, G. Withers, L. Kam, G. Banker, H. Craighead, M. Issacson, J. Turner, and W. Shain. Aligned microcontact printing of micrometer-scale poly-l-lysine structures for controlled growth of cultured neurons on planar microelectrode arrays. *Biomedical Engineering, IEEE Transactions on*, 47(1):17 –21, jan. 2000.

[36] G. Banker and K. Goslin, editors. *Culturing Nerve Cells*. MIT Press, 1998.

[37] Ivar Meyvantsson and David J. Beebe. Cell culture models in microfluidic systems. *Annual Review of Analytical Chemistry*, 1(1):423–449, 2008.

[38] Pamela G. Gross, Emil P. Kartalov, Axel Scherer, and Leslie P. Weiner. Applications of microfluidics for neuronal studies. *Journal of the Neurological Sciences*, 252(2):135 – 143, 2007.

[39] Jinyi Wang, Li Ren, Li Li, Wenming Liu, Jing Zhou, Wenhao Yu, Denwen Tong, and Shulin Chen. Microfluidics: A new cosset for neurobiology. *Lab Chip*, 9:644–652, 2009.

[40] Brian J. Kirby. *Micro- and Nanoscale Fluid Mechanics Transport in Microfluidic Devices*. Cambridge University Press, 2011.

[41] Larry J. Millet, Matthew E. Stewart, Jonathan V. Sweedler, Ralph G. Nuzzo, and Martha U. Gillette. Microfluidic devices for culturing primary mammalian neurons at low densities. *Lab Chip*, 7:987–994, 2007.

[42] Jennifer Monahan, Andrew A. Gewirth, and Ralph G. Nuzzo. A method for filling complex polymeric microfluidic devices and arrays. *Analytical Chemistry*, 73(13):3193–3197, 2001.

[43] Stefanie Kaech, Chun-Fang Huang, and Gary Banker. Short-term high-resolution imaging of developing hippocampal neurons in culture. *Cold Spring Harbor Protocols*, 2012(3):pdb.prot068247, 2012.

[44] M C van Loosdrecht, J Lyklema, W Norde, G Schraa, and A J Zehnder. Electrophoretic mobility and hydrophobicity as a measured to predict the initial steps of bacterial adhesion. *Applied and Environmental Microbiology*, 53(8):1898–1901, 1987.

[45] Huub H.M. Rijnaarts, Willem Norde, Edward J. Bouwer, Johannes Lyklema, and Alexander J.B. Zehnder. Reversibility and mechanism of bacterial adhesion. *Colloids and Surfaces B: Biointerfaces*, 4(1):5 – 22, 1995.

[46] Albert T. Poortinga, Rolf Bos, Willem Norde, and Henk J. Busscher. Electric double layer interactions in bacterial adhesion to surfaces. *Surface Science Reports*, 47(1):1 – 32, 2002.

[47] F. Gaboriaud, M. L. Gee, R. Strugnell, and J. F. L. Duval. Coupled electrostatic, hydrodynamic, and mechanical properties of bacterial interfaces in aqueous media. *Langmuir*, 24:10988–10995, 2004.

[48] D. Belder, H. Husmann, and J. Warnke. Directed control of electroosmotic flow in nonaqueous electrolytes using poly(ethyleneglycol) coated capillaries. *Electrophoresis*, 22:666–672, 2001.

[49] Detlev Belder and Martin Ludwig. Surface modification in microchip electrophoresis. *ELECTROPHORESIS*, 24(21):3595–3606, 2003.

[50] Grégoire Danger, Michel Ramonda, and Hervé Cottet. Control of the eof in ce using polyelectrolytes of different charge densities. *Electrophoresis*, 28(6):925–931, 2007.

[51] W. B. Russel, D. A. Saville, and W. R. Schowalter. *Colloidal Dispersions*. Cambridge University Press, 1st edition, 1989.

[52] B. J. Kirby and E. F. Hasselbrink. Zeta potential of microfluidic substrates: 1. theory, experimental techniques, and effects on separations. *Electrophoresis*, 25(2):187–202, January 2004.

[53] Brian J. Kirby and Ernest F. Hasselbrink. Zeta potential of microfluidic substrates: 2. data for polymers. *Electrophoresis*, 25(2):203–213, 2004.

[54] Hans-Jrgen Butt, Brunero Cappella, and Michael Kappl. Force measurements with the atomic force microscope: Technique, interpretation and applications. *Surface Science Reports*, 59(16):1 – 152, 2005.

[55] Antoine Pallandre, Bertrand de Lambert, Rafaele Attia, Alain M. Jonas, and Jean-Louis Viovy. Surface treatment and characterization: Perspectives to electrophoresis and lab-on-chips. *Electrophoresis*, 27(3):584–610, 2006.

[56] M. Zembala. Electrokinetics of heterogeneous interfaces. *Advances in Colloid and Interface Science*, 112:59 – 92, 2004.

[57] Z. Adamczyk, K. Sadlej, E. Wajnryb, M. Nattich, M.L. Ekiel-Jezewska, and J. Blawzdziewicz. Streaming potential studies of colloid, polyelectrolyte and protein deposition. *Advances in Colloid and Interface Science*, 153(12):1 – 29, 2010.

[58] Stanislav S. Dukhin, Ralf Zimmermann, and Carsten Werner. Intrinsic charge and donnan potentials of grafted polyelectrolyte layers determined by surface conductivity data. *Journal of Colloid and Interface Science*, 274(1):309 – 318, 2004.

[59] Brian J. Kirby. *Micro- and Nanoscale Fluid Mechanics Transport in Microfluidic Devices*. Cambridge University Press, 2010.

[60] Robert J. Hunter. *Zeta Potential in Colloid Science: Principles and Applications*. Academic Press, 1981.

[61] A.V. Delgado, F. Gonzlez-Caballero, R.J. Hunter, L.K. Koopal, and J. Lyklema. Measurement and interpretation of electrokinetic phenomena. *Journal of Colloid and Interface Science*, 309(2):194 – 224, 2007. ¡ce:title¿Elkin 06, International Electrokinetics Conference, June 25-29, Nancy, France¡/ce:title¿.

[62] Christine Schwer and Ernst Kenndler. Electrophoresis in fused-silica capillaries: the influence of organic solvents on the electroosmotic velocity and the .zeta. potential. *Analytical Chemistry*, 63(17):1801–1807, 1991.

[63] W. Schutzner and E. Kenndler. Electrophoresis in synthetic organic polymer capillaries - variation of electroosmotic velocity and zeta potential with ph and solvent composition. *Analytical Chemistry*, 64(17):1991–1995, September 1992.

[64] V. Tandon, S. K. Bhagvatula, W. C. Nelson, and B. J. Kirby. Zeta potential and electroosmotic mobility in microfluidic devices fabricated from hydrophobic polymers: 1. the origins of charge. *Electrophoresis*, 29:1092–1101, 2008.

[65] V. Tandon, S. K. Bhagavatula, and B. J. Kirby. Transient zeta-potential

measurements in hydrophobic, topas microfluidic substrates. *Electrophoresis*, 30(15):2656–2667, 2009.

[66] P. J. Scales, F. Grieser, T. W. Healy, L. R. White, and D. Y. C. Chan. Electrokinetics of the silica-solution interface: A flat plate streaming potential study. *Langmuir*, 8:965–974, 1992.

[67] Carsten Werner, Heinz Korber, Ralf Zimmermann, Stanislav Dukhin, and Hans-Jorg Jacobasch. Extended electrokinetic characterization of flat solid surfaces. *Journal of Colloid and Interface Science*, 208(1):329 – 346, 1998.

[68] R.A Van Wagenen and J.D Andrade. Flat plate streaming potential investigations: Hydrodynamics and electrokinetic equivalency. *Journal of Colloid and Interface Science*, 76(2):305 – 314, 1980.

[69] J. Th. G. Overbeek. *Colloid Science*, volume 1. Elsevier, 1952.

[70] J. T. Davies and E. K. Rideal. *Interfacial Phenomena*. Academic Press, 1963.

[71] J. J. Bikerman. Ionic theory for electroosmosis, the current flow and the surface conductivity. *Z. Physikalische Chemie A*, A163:378–394, 1933.

[72] J. J. Bikerman. Scientific and technical collected essays - surface conductivity and its significance. *Kolloid-Zeitschrift*, 72:100–108, 1935.

[73] J. Lyklema. *Fundamentals of Interface and Colloid Science: Volume II Solid-Liquid Interfaces*. Elsevier, 1995.

[74] J Lyklema and M Minor. On surface conduction and its role in electrokinetics. *Colloids and Surfaces A: Physicochemical and Engineering Aspects*, 140(13):33 – 41, 1998.

[75] H. P. Schwan and C. D. Ferris. Four electrode null techniqes for impedance measurements with high resolution. *Review of Scientific Instruements*, 39:481–485, 1968.

[76] R. J. Gross and J. F. Osterle. Membrane transport characteristics of ultrafine capillaries. *The Journal of Chemical Physics*, 49(1):228–234, 1968.

[77] T. Teorell. *Transport Processes and Electrical Phenomena in Ionic Membranes*, volume 3 of *Progress in Biophysics and Biophysical Chemistry*, chapter 9, pages 305–369. Pergamon Press, 1953.

[78] H. Ohshima. Electrophoresis of soft particles. *Advances in Colloid and Interface Science*, 62:189–235, 1995.

[79] Jrme F. L. Duval and Hiroyuki Ohshima. Electrophoresis of diffuse soft particles. *Langmuir*, 22(8):3533–3546, 2006.

[80] J. Lyklema. *Fundamentals of Interface and Colloid Science: Soft Colloids*. Academic Press, 2005.

[81] M. A. Cohen Stuart, F. H. W. H. Waajen, and S. S. Dukhin. Electrokinetic effects of adsorbed neutral polymers. *Colloid & Polymer Science*, 262:423–426, 1984. 10.1007/BF01410263.

[82] MA Cohen Stuart and J. W. Mulder. Adsorbed polymers in aqueous media the relation between zeta potential, layer thickness and ionic strength. *Colloids and Surfaces*, 15(0):49 – 55, 1985.

[83] R. Zimmermann, S. Dukhin, and C. Werner. Electrokinetic measurements reveal interfacial charge at polymer films caused by simple electrolyte ions. *Journal of Physical Chemistry B*, 105:8544–8549, 2001.

[84] J. K. Beattie. The intrinsic charge on hydrophobic microfluidic substrates. *Lab on a Chip*, 6:1409–1411, 2006.

[85] E. Donath and V. Pastushenko. Electrophoretical study of cell surface properties. the influence of the surface coat on the electric potential distribution and on general electrokinetic properties of animal cells. *Bioelectrochemistry and Bioenergetics*, 6:543–554, 1979.

[86] E. Donath and V. Pastushenko. Electrophoretic study of cell surface properties theory and experimental applicability. *Biochemistry and Bioenergetics*, 7:31–40, 1980.

[87] P. C. Hiemenz. *Principles of Colloid and Surface Chemistry*. Marcel Dekker, 1977.

[88] Hiroyuki Ohshima and Tamotsu Kondo. Relationship among the surface potential, donnan potential and charge density of ion-penetrable membranes. *Biophysical Chemistry*, 38(12):117 – 122, 1990.

[89] H. Ohshima and S. Ohki. Donnan potential and surface potential of a charged membrane. *Biophysical Journal*, 47(5):673 – 678, 1985.

[90] H. Ohshima and T. Kondo. Double-layer interaction regulated by the donnan potential. *Journal of Colloid and Interface Science*, 123:136–142, 1988.

[91] R. W. Wunderlich. The effects of surface structure on the electrophoretic mobilities of large particles. *Journal of Colloid and Interface Science*, 88:385–397, 1982.

[92] E. Donath and A. Voigt. Streaming current and streaming potential on structured surfaces. *Journal of Colloid and Interface Science*, 109:122–139, 1986.

[93] H. Ohshima and T. Kondo. Electrokinetic flow between two parallel plates with surface charge layers: Electro-osmosis and streaming potential. *Journal of Colloid and Interface Science*, 135:443–448, 1990.

[94] V. M. Starov and Y. E. Solomentsev. Influence of gel layers on electrokinetic phenomena: 1. streaming potential. *Journal of Colloid and Interface Science*, 158:159–165, 1993.

[95] V. M. Starov and Y. E. Solomentsev. Influence of gel layers on electrokinetic phenomena: 2. effects of ions interaction with gel layer. *Journal of Colloid and Interface Science*, 158:166–170, 1993.

[96] H. C. Brinkman. A calculation of the viscous force exerted by a flowing fluid on a dense swarm of particles. *Applied Sci. Research*, A1:27–34, 1947.

[97] Hiroyuki Ohshima and Tamotsu Kondo. Approximate analytic expression for the electrophoretic mobility of colloidal particles with surface-charge layers. *Journal of Colloid and Interface Science*, 130(1):281 – 282, 1989.

[98] J. F. L. Duval and H. P. van Leeuwen. Electrokinetics of diffuse soft interfaces. 1. limit of low donnan potentials. *Langmuir*, 20:10324–10336, 2004.

[99] Jrme F. L. Duval. Electrokinetics of diffuse soft interfaces. 2. analysis based on the nonlinear poissonboltzmann equation. *Langmuir*, 21(8):3247–3258, 2005. PMID: 15807561.

[100] LP Yezek, JFL Duval, and HP van Leeuwen. Electrokinetics of diffuse soft interfaces. iii. interpretation of data on the polyacrylamide/water interface. *Langmuir*, 21(14):6220–6227, JUL 5 2005.

[101] P. Debye and A. M. Bueche. Intrinsic viscosity, diffusion, and sedimentation rate of polymers in solution. *The Journal of Chemical Physics*, 16:573–579, 1948.

[102] Adrian E. Scheidegger. *The physics of flow through porous media*. University of Toronto Press, 1974.

[103] John Happel and Howards Brenner. *Low Reynolds number hydrodynamics*. Kluwer, 1983.

[104] Stanislav S. Dukhin, Ralf Zimmermann, Jrme F.L. Duval, and Carsten Werner. On the applicability of the brinkman equation in soft surface electrokinetics. *Journal of Colloid and Interface Science*, 350(1):1 – 4, 2010.

[105] H. Ohshima and T. Kondo. Electrophoresis of large colloidal particles with surface charge layers. position of the slipping plane and surface layer thickness. *Colloid & Polymer Science*, 264:1080–1084, 1986.

[106] H. Ohshima and T. Kondo. Electrophoretic mobility and donnan potential of a large colloidal particle with a surface charge layer. *Journal of Colloid and Interface Science*, 116:305–311, 1987.

[107] L. Durlofsky and J. F. Brady. Analysis of the brinkman equation as a model for flow in porous media. *Physics of Fluids*, 30:3329–3341, 1987.

[108] S. S. Dukhin, R. Zimmermann, and C. Werner. Electrokinetic phenomena at grafted polyelectrolyte layers. *Journal of Colloid and Interface Science*, 286:761–773, 2005.

[109] Hiroyuki Ohshima. Electrophoretic mobility of soft particles. *Colloids and Surfaces A: Physicochemical and Engineering Aspects*, 103(3):249 – 255, 1995. ¡ce:title¿3rd Australia/Japan Symposium¡/ce:title¿.

[110] S. S. Dukhin, R. Zimmermann, and C. Werner. Charge density distribution at interfaces between polyelectrolyte layers and aqueous solutions - experimental access and limitations of traditional electrokinetics. *Journal of Colloid and Interface Science*, 328:217–226, 2008.

[111] P. H. Elworthy, A. T. Florence, and A. Rahman. Conductivity of sodium chloride and potassium chloride in polymer solutions and the obstruction effect. *The Journal of Physical Chemistry*, 76(12):1763–1767, 1972.

[112] Henry Carrison Thomas and Alan G. Langdon. Self-diffusion studies of gel hydration and the obstruction effect. *The Journal of Physical Chemistry*, 75(12):1821–1826, 1971.

[113] A L Iordanskii, A L Shterenzon, Yu V Moiseev, and Gennadii E Zaikov. Diffusion of electrolytes in polymers. *Russian Chemical Reviews*, 48(8):781, 1979.

[114] L Masaro and X.X Zhu. Physical models of diffusion for polymer solutions, gels and solids. *Progress in Polymer Science*, 24(5):731 – 775, 1999.

[115] T. Odijk. Depletion theory of protein transport in semi-dilute polymer solutions. *Biophysical Journal*, 79:2314–2321, 2000.

[116] R. I. Cukier. Diffusion of brownian spheres in semidilute polymer solutions. *Macromolecules*, 17(2):252–255, 1984.

[117] P. G. De Gennes. Dynamics of entangled polymer solutions. i. the rouse model. *Macromolecules*, 9(4):587–593, 1976.

[118] F. Booth. The dielectric constant of water and the saturation effect. *The Journal of Chemical Physics*, 19(4):391–394, 1951.

[119] J. B. Hasted. *Aqueous Dielectrics*. Champan and Hall, 1973.

[120] R. Paul and S.J. Paddison. The phenomena of dielectric saturation in the water domains of polymer electrolyte membranes. *Solid State Ionics*, 168(34):245 – 248, 2004. ¡ce:title¿Proceedings of the Workshop on Hydrogen: Ionic, Atomic and Molecular Motion¡/ce:title¿.

[121] Ronald F. Probstein. *Physicochemical Hydrodynamics*. John Wiley, 2003.

[122] G. Karimi and X. Li. Electroosmotic flow through polymer electrolyte membranes in pem fuel cells. *Journal of Power Sources*, 140:1–11, 2005.

[123] G. Xie and T. Okada. Water transport behavior in nafion 117 membranes. *Journal of the Electrochemical Society*, 142:3057–3062, 1995.

[124] Menachem Elimelech, William H. Chen, and John J. Waypa. Measuring the zeta (electrokinetic) potential of reverse osmosis membranes by a streaming potential analyzer. *Desalination*, 95(3):269 – 286, 1994.

[125] B. Teychene, P. Loulergue, C. Guigui, and C. Cabassud. Development and use of a novel method for in line characterization of fouling layers electrokinetic properties and for fouling monitoring. *Journal of Membrane Science*, 370:45–57, 2011.

[126] T. Y. Chiu and A. E. James. Electrokinetic characterization techniques on asymmetric microfiltration membranes. *Colloids and Surfaces A: Physicochemical and Engineering Aspects*, 301:281–288, 2007.

[127] LP Yezek. Bulk conductivity of soft surface layers: Experimental measurement and electrokinetic implications. *Langmuir*, 21(22):10054–10060, OCT 25 2005.

[128] L. P. Yezek and H. P. van Leeuwen. An electrokinetic characterization of low charge density cross-linked polyacrylamide gels. *Journal of Colloid and Interface Science*, 278:243–250, 2004.

[129] Uwe Freudenberg, Ralf Zimmermann, Kati Schmidt, Sven Holger Behrens, and Carsten Werner. Charging and swelling of cellulose films. *Journal of Colloid and Interface Science*, 309(2):360 – 365, 2007. ¡ce:title¿Elkin 06, International Electrokinetics Conference, June 25-29, Nancy, France¡/ce:title¿.

[130] J. F. L. Duval, R. Zimmermann, A. L. Cordeiro, N. Rein, and C. Werner. Electrokinetics of diffuse soft interfaces. iv. analysis of streaming current measurements at thermoresponsive thin films. *Langmuir*, 25:10691–10703, 2009.

[131] Ana L. Cordeiro, Ralf Zimmermann, Stefan Gramm, Mirko Nitschke, Andreas Janke, Nicole Schafer, Karina Grundke, and Carsten Werner. Temperature dependent physicochemical properties of poly(n-isopropylacrylamide-co-n-(1-phenylethyl) acrylamide) thin films. *Soft Matter*, 5:1367–1377, 2009.

[132] Ralf Zimmermann, Willem Norde, Martien A. Cohen Stuart, and Carsten Werner. Electrokinetic characterization of poly(acrylic acid) and poly(ethylene oxide) brushes in aqueous electrolyte solutions. *Langmuir*, 21(11):5108–5114, 2005.

[133] R. Zimmermann, D. Kuckling, M. Kaufmann, C. Werner, and J. F. L. Duval. Electrokinetics of a poly(n-isopropylacrylamid-co-carboxyacrylamid) soft thin film: Evidence of diffuse segment distribution in the swollen state. *Langmuir*, 26:18169–18181, 2010.

[134] J. F. L. Duval, D. Kuttner, M. Nitschke, C. Werner, and R. Zimmermann. Interrelations between charging, structure and electrokinetics of nanometric polyelectrolyte films. *Journal of Colloid and Interface Science*, 362:439–449, 2011.

[135] Jerome F. L. Duval, David Kuettner, Carsten Werner, and Ralf Zimmermann. Electrohydrodynamics of soft polyelectrolyte multilayers: Point of zero-streaming current. *Langmuir*, 27(17):10739–10752, SEP 6 2011.

[136] E. Donath, A. Budde, E. Knippel, and H. Baumler. ”hairy surface layer” concept of electrophoresis combined with local fixed surface charge density isotherms: Application to human erythrocyte electrophoretic fingerprinting. *Langmuir*, 12(20):4832–4839, 1996.

[137] M. D. Afonso. Surface charge on loose nanofiltration membranes. *Desalination*, 191:262–272, 2006.

[138] M. J. Ariza and J. Benavente. Streaming potential along the surface of polysulfone membranes: a comparative study between two different experimental systems and determination of electrokinetic and adsorption parameters. *Journal of Membrane Science*, 190:119–132, 2001.

[139] P Fievet, M Sbai, A Szymczyk, and A Vidonne. Determining the zeta-potential of plane membranes from tangential streaming potential measurements: effect of the membrane body conductance. *Journal of Membrane Science*, 226:227 – 236, 2003.

[140] A. Voigt, S. Wolf, S. Lauckner, G. Neumann, R. Becker, and L. Richter. Electrokinetic properties of polymer and glass surfaces in aqueous solutions: Experimental evidence for swollen surface layers. *Biomaterials*, 4:299–304, 1983.

[141] A. L. Pidot and J. M. Diamond. Streaming potentials in a biological membrane. *Nature*, 201:701–702, 1964.

[142] E. H. Frank and A. J. Grodzinsky. Cartilage electromechanics - i. electrokinetic transduction and the effects of electrolyte ph and ionic strength. *Journal of Biomechanics*, 20:615–619, 1987.

[143] E. H. Frank and A. J. Grodzinsky. Cartilage electromechanics - ii. a continuum model of cartilage electrokinetics and correlation with experiments. *Journal of Biomechanics*, 20:629–639, 1987.

[144] T. Ishido and H. Mizutani. Experimental and theoretical basis of electrokinetic phenomena in rock-water systems and its application to geophysics. *Journal of Geophysical Research*, 86:1763–1775, 1981.

[145] Neil B. McKeown and Peter M. Budd. Exploitation of intrinsic microporosity in polymer-based materials. *Macromolecules*, 43(12):5163–5176, 2010.

[146] C. A. Lucy and R. S. Underhill. Characterization of the cationic surfactant in-

duced reversal of electroosmotic flow in capillary electrophoresis. *Analytical Chemistry*, 68:300–305, 1996.

[147] K. E. Markides, B. J. Tarbet, C. L. Woolley, C. M. Schregenberger, J. S. Bradshaw, M. L. Lee, and K. D. Bartle. Deactivation of fused silica capillary columns with phenylhydroxiloxanes. *Journal of High Resolution Chromotography and Chromatography Communications*, 8:378–384, 1985.

[148] P. G. Saffman. On the boundary condition at the surface of a porous medium. *Studies in Applied Mathematics*, 2:93–101, 1971.

[149] G. K. Batchelor. *An Introduction to Fluid Dynamics*. Cambridge University Press, 1967.

[150] Lars Onsager. Reciprocal relations in irreversible processes i. *Physical Review*, 37:405–426, 1931.

[151] Lars Onsager. Reciprocal relations in irreversible processes ii. *Physical Review*, 38:2265–2279, 1931.

[152] S. R. de Groot and P. Mazur. *Non-Equlibrium Thermodynamics*. Dover, 1984.

[153] L. D. Landau and E. M. Lifshitz. *Statistical Physics*. Addison-Wesley, 1958.

[154] U. Saxen. Uber die reciprocitat dir electrischen endosmose und der stromungsstrome. *Annalen der Physik und Chemie*, 47:46–68, 1892.

[155] J. T. G. Overbeek and P. W. O. Wijga. On electro-osmosis and streaming-potentials in diaphragms. *Recueil des Travaux Chimiques des Pays-Bas*, 65:556–563, 1946.

[156] P. Mazur and J. T. G. Overbeek. On electro-osmosis and streaming-potentials in diaphragms. *Recl. Trav. Chim. Pays-Bas*, 70:83–91, 1951.

[157] Niels Asger Mortensen, Laurits H. Olesen, Fridolin Okkels, and Henrik Bruus. Mass and charge transport in micro and nanofluidic channels. *Nanoscale and Microscale Thermophysical Engineering*, 11:57–69, 2007.

[158] Staffan Wall. The history of electrokinetic phenomena. *Current Opinion in Colloid & Interface Science*, 15(3):119 – 124, 2010.

[159] Edouard Brunet and Armand Ajdari. Generalized onsager relations for electrokinetic effects in anisotropic and heterogeneous geometries. *Physical Review E*, 69:016306, 2004.

[160] Claudio L. A. Berli and Maria L. Olivares. Electrokinetic flow of non-newtonian fluids in microchannels. *Journal of Colloid and Interface Science*, 320:582–589, 2008.

[161] Herman P. van Leeuwen and Jerome F.L. Duval. Faradaic double layer depolarization in electrokinetics: Onsager relations and substrate limitations. *Journal of Colloid and Interface Science*, 309(2):350 – 359, 2007. ¡ce:title¿Elkin 06, International Electrokinetics Conference, June 25-29, Nancy, France¡/ce:title¿.

[162] H. J. Keh and Yung C. Liu. Electrokinetic flow in a circular capillary with a surface charge layer. *Journal of Colloid and Interface Science*, 172:222–229, 1995.

[163] Alexander C. Barbati and Brian J. Kirby. Soft diffuse interfaces in electrokinetics - theory and experiment for transport in charged diffuse layers. *Soft Matter*, 8:10598–10613, 2012.

[164] Gordon S. Beavers and Daniel D. Joseph. Boundary conditions at a naturally permeable wall. *Journal of Fluid Mechanics*, 30:197–207, 1967.

[165] R. E. Larson and J. J. L. Higdon. Microscopic flow near the surface of two-dimensional porous media. part 1. axial flow. *Journal of Fluid Mechanics*, 166:449–472, 1986.

[166] A. S. Sangani and S. Behl. The planar singular solutions of stokes and laplace equations and their application to transport processes near porous surfaces. *Physics of Fluids A*, 1:21–37, 1989.

[167] N. Rakotomalala, D. Salin, and Y. C. Yortsos. Viscous coupling in a model porous medium geometry: Effect of fluid contact area. *Applied Scientific Research*, 55:155–169, 1995.

[168] Mark F. Tachie, David F. James, and Iain G. Currie. Velocity measurements of a shear flow penetrating a porous medium. *Journal of Fluid Mechanics*, 493:319–343, 2003.

[169] D. F. James and Anthony M. Davis. Flow at the interface of a model fibrous porous medium. *Journal of Fluid Mechanics*, 426:47–72, 2001.

[170] S. S. Dukhin, R. Zimmermann, and C. Werner. Surface conductivity reveals counterion condensation within grafted polyelectrolyte layers. *Journal of Physical Chemistry B*, 111:979–981, 2007.

[171] Laurence Jouniauz and JeanpPierre Pozzi. Permeability dependence of streaming potential in rocks for various fluid conductivities. *Geophysical Research Letters*, 22:485–488, 1995.

[172] Saad F. Alkafeef and Abdullah F. Alajmi. The electrical conductivity and surface conduction of consolidated rock cores. *Journal of Colloid and Interface Science*, 309:253–261, 2007.

[173] Ralf Zimmermann, Toshihisa Osaki, Gnter Gauglitz, and Carsten Werner. Combined microslit electrokinetic measurements and reflectometric interference spectroscopy to study protein adsorption processes. *Biointerphases*, 2:159–164, 2007. 10.1116/1.2814066.

[174] A. C. Barbati and B. J. Kirby. Force and flux relations in systems with porous and charged layers. *In Press*, 2013.

[175] G. I. Taylor. A model for the boundary condition of a porous material. part 1. *Journal of Fluid Mechanics*, 49:319–326, 1971.

[176] Eric V. Anslyn and Dennis A. Dougherty. *Modern Physical Organic Chemistry*. University Science Books, 2006.

[177] F. H. J. van der Heyden, D. Stein, K. Beteman, S. G. Lemay, and C. Dekker. Charge inversion at high ionic strength studied by streaming currents. *Physical Review Letters*, 96:224502, 2006.

[178] A. C. Barbati and B. J. Kirby. Surface conductivity in electrokinetic systems with porous and charged layers. *Submitted*, 2013.

[179] Ralf Zimmermann, Toshihisa Osaki, Gnter Gauglitz, and Carsten Werner. Combined microslit electrokinetic measurements and reflectometric interference spectroscopy to study protein adsorption processes. *Biointerphases*, 2:159–164, 2007. 10.1116/1.2814066.

[180] Royce W Murray. Polymer modification of electrodes. *Annual Review of Materials Science*, 14(1):145–169, 1984.

[181] K. A. Mauritz and R. B. Moore. State of understanding of nafion. *Chemical Reviews*, 104:4535–4585, 2004.

[182] M. Bass, A. Berman, A. Singh, O. Konovalov, and V. Freger. Surface structure of nafion in vapor and liquid. *Journal of Physical Chemistry B*, 114:3784–3790, 2010.

[183] S. Goswami, S. Klaus, and J. Benziger. Wetting and absorption of water drops on nafion films. *Langmuir*, 24:8627–8633, 2008.

[184] J. A. Dura, V. S. Murthi, M. Hartman, S. K. Satija, and C. F. Majkrzak. Multilamellar interface structures in nafion. *Macromolecules*, 42:4769–4774, 2009.

[185] A. Narebska, S. Koter, and W. Kujawski. Irreversible thermodynamics of transport across charged membranes. part i - macroscopic resistance coefficients for a system with nafion 120 membrane. *Journal of Membrane Science*, 25:153–170, 1985.

[186] G. Sicbona, C. Botre, F. Botre, and G. Gavelli. Electrokinetic effects across nafion 120 membranes. *Electrochimica Acta*, 36:139–141, 1991.

[187] C. Fabiani, G. Scibona, and B. Scuppa. Correlations between electroomotic coefficients and hydraulic permeability in nafion membranes. *Journal of Membrane Science*, 115:51–61, 1983.

[188] H. Zhang, J. Pan, X. He, and M. Pan. Zeta potential of nafion molecules in isopropanol-water mixture solvent. *Journal of Applied Polymer Science*, 107:3306–3309, 2007.

[189] Y. Daiko, K. Katagiri, and A. Matsuda. Proton conduction in thickness-controlled ultrathin polycation/nafion multilayers prepared via layer-by-layer assembly. *Chemical Materials*, 20:6405–6409, 2008.

[190] D. G. Abebe and T. R. Farhat. Self-assembly of nafion/poly(vinyl alcohol) at ph=1.2 and nafion/poly(ally amine) at ph = 11. *Soft Matter*, 6:1325–1335, 2010.

[191] T. A. Zawodzinski, C. Derouin, S. Radzinski, R. J. Sherman, Van T. Smith, and Gottesfeld S. Sprinter, Thomas E. Water uptake by tranport through nafion 117 membranes. *Journal of the Electrochemical Society*, 149:1041–1047, 1993.

[192] J. J. Sumner, S. E. Creager, J. J. Ma, and D. D. DesMarteau. Proton conductivity

in nafion 117 and in a novel bis[(perfluoroalkyl)sulfonly]imide ionomer membrane. *Journal of the Electrochemical Society*, 145:107–110, 1998.

[193] Y. Sone, P. Ikdunge, and D. Simonsson. Proton conductivity of nafion 117 as measured by a four-electrode ac impedance method. *Journal of the Electrochemical Society*, 143:1254–1259, 1996.

[194] T. A. Zawodzinski, M. Neeman, L. O. Sillerud, and S. Gossesfeld. Determination of water diffusions coefficients in perfluorosulfonate ionomeric membranes. *Journal of Physical Chemistry*, 95:6040–6044, 1991.

[195] T. Okada, H. Satou, M. Okuno, and M. Yuasa. Ion and water transport characteristics of perflurorosulfonated ionomer membranes with h+ and alkali metal cations. *Journal of Physical Chemistry B*, 106:1267–1273, 2002.

[196] W. Y. Hsu and T. D. Gierke. Ion transport and clustering in nafion perfluorinated membranes. *Journal of Membrane Science*, 13:307–326, 1983.

[197] A. Goswami, A. Acharya, and A. K. Pandey. Setudy of self-diffusion in monovalent and divalent cations in nafion-117 ion-exchage membrane. *Journal of Physcal Chemistry: B*, 105:9196–9201, 2001.

[198] T. J. Peckham and S. Holdcroft. Structure-morphology-property relationships of non-perfluorinated proton-conducting membranes. *Advanced Materials*, 22:4667–4690, 2010.

[199] Marilyn N. Szentirmay, Leigh F. Campbell, and Charles R. Martin. Silane coupling agens for attaching nafion to glass and silica. *Analytical Chemistry*, 58:661–662, 1986.

[200] I. Luzinov, D. Julthongpiput, A. Liebmann-Vinson, T. Cregger, M. D. Foster, and V. V. Tsukruk. Epoxy-terminated self-assembled monolayers: Molecular glues for polymer layers. *Langmuir*, 16(2):504–516, 2000.

[201] R. B. Moore and C. R. Martin. Procedure for preparing solution-cast perfluorosulfonate ionomer films and membranes. *Analytical Chemistry*, 58:2569–2570, 1986.

[202] R. B. Moore and C. R. Martin. Chemical and morphological properties of solution-cast perfluorosulfonate ionomers. *Macromolecules*, 21:1334–1339, 1988.

[203] David J. G. Ives and George J. Janz. *Reference Electrodes Theory and Practice*. Academic Press, 1961.

[204] M. A. Hickner. Water-mediated transport in ion-containing polymers. *Journal of Polymer Science Part B: Polymer Physics*, 50:9–20, 2012.

[205] I. Zudans, W. R. Heineman, and C. J. Seliskar. In situ measurements of chemical sensor film dynamics by spectroscopic ellipsometry. partitioning of a chromophore. *Journal of Physical Chemistry B*, 108:11521–11528, 2004.